Abschlußbericht über das F+E Vorhaben

im BMBF-Förderschwerpunkt:

Nanoelektronische Halbleiterstrukturen für die Quanteninformations-technologie (nanoQUIT)

Teilvorhaben:

„Ferromagnet/Halbleiter-Heterostrukturen für die Magnetologik und Spintronik“

Förderkennzeichen: 01BM463
Förderzeitraum: 01.01.2005 – 31.12.2008
Projektleiter: Dr. Achim Trampert

zusammengestellt von
Dr. Jens Herfort, Prof. Reinhold Koch und Dr. Achim Trampert

Paul-Drude-Institut für Festkörperelektronik
Hausvogteiplatz 5-7, 10117 Berlin

Berlin, 30.06.2009

I. Kurze Darstellung

1. Aufgabenstellung

Ziel des Forschungsvorhabens war es, Ferromagnet/Halbleiter-Nanostrukturen zu entwickeln, die in neuartigen multifunktionalen Logikkonzepten zur Anwendung kommen und die zur Verbesserung der Spininjektion in den Halbleiter führen. Erfolgversprechende ferromagnetische Materialien sind die halbmetallischen Heusler-Legierungen, die im Volumen einen hohen Spinpolarisationgrad der Leitungselektronen bis zu 100% aufweisen. Für GaAs- und Si-Substrate geeignete gitterangepasste Heusler-Verbindungen sind u. a. Fe_3Si, Co_2MnGe, Co_2MnSi und Co_2FeSi, die sich durch eine geringe Gitterfehlanpassung und Curie-Temperaturen deutlich oberhalb der Raumtemperatur auszeichnen. Die Ziele des Forschungsprojektes waren:

(1) Entwicklung von Ferromagnet/Halbleiter-Hetero- und Nanostrukturen mit scharfer Grenzfläche, die eine hohe Curie-Temperatur und eine hohe Spinpolarisation besitzen

(2) Untersuchung der Spininjektionseffizienz der unter (1) hergestellten Ferromagnet/Halbleiter-Hetero- und Nanostrukturen

(3) Herstellung eines magnetoresistiven Elements mittels der Ferromagnet/Halbleiter-Heterostrukturen aus (1)

(4) Aufbau eines Demonstrators für ein frei-programmierbares magnetologisches Bauelement mit (N)AND- und (N)OR-Funktionalität

2. Voraussetzungen

International wird sehr intensiv sowohl an der möglichen Realisierung von Bauelementen, die den Spin der Elektronen ausnutzen, als auch an der Weiterentwicklung und Verbesserung von Ferromagnet/Halbleiter-Hybridstrukturen gearbeitet. Daher war es notwendig, im Projektverlauf ständig den Vergleich mit dem internationalen Stand der Forschung zu ziehen und das Forschungsprogramm zu modifizieren. Die erzielten Ergebnisse wurden zeitnah, d.h. bereits vor Projektablauf, in einschlägigen Fachzeitschriften veröffentlicht und auf internationalen Konferenzen präsentiert. Das Wachstum der Ferromagnet/Halbleiter-Hybridstrukturen wurde in bereits vorhandenen Mehrkammer-Molekularstrahlepitaxie-Anlagen (III-V-Halbleiter- Molekularstrahlepitaxie (MBE), Ferromagnet-MBE, Schleusen- und Ladekammer) durchgeführt. Durch Investitionen, finanziert aus den Vorgängerprojekten 01BM907 und 13N8255, wurden im Vorfeld des Projektes die experimentellen Voraussetzungen geschaffen, die magnetischen Eigenschaften der Schichten sowohl *in-situ* (Kerr-Effekt-Messaufbau in der MBE-Kammer) als auch *ex-situ* mittels eines SQUID-Magnetometers zu untersuchen. Im Rahmen dieses Projektes waren keine weiteren Investitionen vorgesehen. Da die ursprünglich beantrage Wissenschaftlerstelle in eine Technikerstelle umgewandelt wurde, war es für die erfolgreiche Durchführung dieses Projektes notwendig, zusätzliches wissenschaftliches Personal aus den laufenden Mitteln des Instituts zu finanzieren.

3. Planung und Ablauf

Planung und Verlauf des Vorhabens erfolgten weitgehend in Übereinstimmung mit dem in der Antragformulierung aufgestellten Balkenplan. Der überwiegende Teil der im Antrag formulierten Ziele ist verwirklicht, womit das Projekt als erfolgreich abgeschlossen eingestuft werden kann. Im Einzelnen wurden detaillierte Untersuchungen zu Wachstum und Struktur von Fe, Fe_3Si und Co_2FeSi Schichten auf GaAs(001) und/oder GaAs(113) Substraten

durchgeführt [(1), (2), (5), (6) im Balkenplan] und deren magnetischen Eigenschaften charakterisiert [(3) im Balkenplan]; siehe Abschnitte II, 2. 3. und 7; außerdem wurde die magnetische Domänenstruktur von lithographisch hergestellten MnAs-Nanostrukturen untersucht, siehe Abschnitte II, 6. Auf die Untersuchung anderer im Antrag erwähnten Heusler-Legierungen wurde verzichtet, da die geforderte strukturelle Qualität und magnetischen Eigenschaften bereits mit Co_2FeSi Schichten erreicht wurde. Mit optimierten Co_2FeSi Schichten wurden im Verlauf des Projekt Spininjektionsexperimente durchgeführt [(4), (7) im Balkenplan]. Dabei wurde gegenüber früheren Ergebnissen eine deutliche Erhöhung der Spininjektionseffizienz vom Ferromagneten in den Halbleiter erzielt; siehe Abschnitt II, 4. Des Weiteren wurden auch Untersuchungen zu Wachstum, Struktur und magnetische Eigenschaften von Co_2FeSi Schichten auf Si(001) und Si(111) Substraten durchgeführt [(2), (3), (5), (6) im Balkenplan]; siehe Abschnitt II, 5. Die Entwicklung einer Ferromagnet-Halbleiter Heterostruktur mit verkippter Magnetisierung erwies sich nach dem am PDI entwickelten Verfahren zum Betrieb eines magnetologischen Elements als nicht notwendig und wurde daher aufgegeben. Die Untersuchungen von Fe_3Si auf den intrinsisch gestuften GaAs(113) Substraten haben auch keinen Hinweis auf eine verkippte Magnetisierung ergeben.

Da der ursprüngliche Projektleiter, Herr Koch, auf einen Lehrstuhl an der Johannes-Kepler-Universität Linz berufen wurde und das Paul-Drude-Institut für Festkörperelektronik im November 2006 verlassen hat, wurde die Entwicklung einer magnetoresistiven Technik zur in situ Bestimmung des Magnetowiderstandes ferromagnetischer Heterostrukturen [(4), (8) im Balkenplan] und der Aufbau eines Demonstrators für ein frei-programmierbares magnetologisches Element [(9) im Balkenplan] als Unterprojekt an die Johannes-Kepler-Universität Linz vergeben. Das in situ Verfahren ist mittlerweile realisiert und an ersten Proben ausgetestet; siehe Abschnitt II, 7. Der Aufbau eines Demonstrators für ein frei-programmierbares magnetologisches Element wurde im Projektverlauf in der Literatur bereits realisiert [J. Wang et al., J. Appl. Phys. **97**, 10D509 (2005)]. Zudem wurden durch die Markteinführung des 4 MBit MRAM-Chips Ende 2006 durch Freescale, heute Everspin Technologies [www.everspin.com] und der Weiterentwicklung zum 16 MBit MRAM-Chip im Jahr 2009 mittlerweile wesentliche Schritte des technologischen Prozesses für frei-programmierbare magnetologische Elemente gelöst, deren Aufbau der MRAM-Speicherzelle sehr ähnlich ist. Daher wurde im Rahmen dieses Projektes die Entwicklung eines Demonstrators zurückgestellt.

4. Wissenschaftlich technischer Stand an den angeknüpft wurde

Das Vorhaben knüpfte an den wissenschaftlich technischen Stand an, der in den vom BMBF geförderten Vorhaben 01BM907 „Quantendrähte und Quantenpunkte auf strukturierten, hochindizierten Substraten im Verbund mit metallischen und magnetischen Schichten“ und 13N8255 „Spininjektion, Spintransport, und Spinköhärenz für neuartige Spintronik-Bauelemente bei Raumtemperatur“ erreicht wurde. Zum Zeitpunkt der Antragstellung wurden vom Paul-Drude-Institut für Festkörperelektronik auch zwei Patente auf dem Gebiet der frei-programmierbaren Logik eingereicht. (i) „Magnetische Logikeinrichtung:“ Deutsches Patent Nr. DE 102 55 857 erteilt, Europäische Patentanmeldung Nr. 03789091 und PCT-Anmeldung PCT/EP2003/013318; (ii) „Magnetische Logikeinrichtung, Logikschaltung, Verfahren zu deren Betrieb und deren Verwendung:“ Deutsches Patent Nr. DE 103 11 717 und Europäisches Patent Nr. 04719995 erteilt. An Fachliteratur wurden die einschlägigen Fachzeitschriften, der Informations- und Dokumentationsdienst INSPEC genutzt.

5. Zusammenarbeit mit anderen Stellen

Unterprojekt an die Johannes-Kepler-Universität Linz, Institut für Halbleiter- und Festkörperphysik: Entwicklung einer magnetoresistiven Technik zur in situ Bestimmung des Magnetowiderstandes von ferromagnetischen Heterostrukturen und der Aufbau eines Demonstrators für ein frei-programmierbares magnetologisches Element

Universität Hamburg, Institut für Angewandte Physik, AG Prof. Merkt (Partner im nano-QUIT-Verbund): Bestimmung der Spinpolarisation von Heusler-Legierungen mit dem Andreev-Punktkontaktverfahren

II. Eingehende Darstellung

Im Folgenden werden einige der wichtigsten Ergebnisse, die im Verlauf des Projekts erzielt wurden, ausführlicher dargestellt. Für eine umfassende und tiefergreifende Darstellung der Ergebnisse wird auf die im Anhang zusammengestellten Originalarbeiten verwiesen.

1. Motivation

Im Rahmen dieses Projektes wurden Ferromagnet/Halbleiter-Nanostrukturen entwickelt, die für die Umsetzung neuartiger multifunktionaler Logikkonzepte geeignet sind und eine erhöhte Effizienz der Spininjektion in den Halbleiter in Aussicht stellen.

Die Integration ferromagnetischer Materialien in Halbleiterbauelemente stellt einen Schwerpunkt weltweiter Forschungsaktivitäten dar. Dies beruht auf dem Fakt, dass die Ausnutzung des Spins der Ladungsträger für logische Operationen in der Spin- und Magnetoelektronik als vielversprechend erachtet wird. In Bezug auf potentielle Anwendungen sollten zur Auswahl ferromagnetischer Materialien folgende wichtige Kriterien herangezogen werden: eine hohe Curie-Temperatur oberhalb von Raumtemperatur, ein hoher Spinpolarisationsgrad der freien Elektronen, eine ausreichend hohe thermische Stabilität und die Kompatibilität mit passenden Halbleitersubstraten. Dabei sind zwei Klassen von ferromagnetischen Materialsystemen von Allgemeinen Interesse. Einerseits handelt es sich um Hybridstrukturen, die aus einem ferromagnetischen Metall und einem Halbleiter bestehen, und andererseits um reine Halbleiterstrukturen, in denen ein verdünnter, magnetischer Halbleiter integriert ist. Im vorliegenden Projekt kamen dabei ausschließlich Hybridstrukturen, die aus einen ferromagnetischen Metall und einen Halbleiter bestehen, zum Einsatz.

Erfolgversprechende ferromagnetische Materialien sind die halbmetallischen Heusler-Legierungen, die im Volumen einen hohen Spinpolarisationgrad der Leitungselektronen bis zu 100% aufweisen. Für GaAs- und Si-Substrate geeignete Heusler-Verbindungen sind u. a. Fe_3Si und Co_2FeSi, die sich durch eine geringe Gitterfehlanpassung und Curie-Temperaturen deutlich oberhalb der Raumtemperatur auszeichnen.

2. Fe_3Si/GaAs(113)-Hybridstrukturen

2.1. Wachstum, strukturelle and magnetische Eigenschaften

Unsere Untersuchungen im Rahmen eines vom BMBF geförderten Vorgängerprojekts (Kennzeichen 13N8255) am binären Heusler-System Fe_3Si/GaAs(001) hatten gezeigt, dass es möglich ist, Fe_3Si-Schichten mit hoher epitaktischer Güte herzustellen. Trotz der für $Fe_{3+x}Si_{1-x}$/GaAs(001)-Hybridstrukturen hohen optimalen Wachstumstemperatur (T_G im Bereich von 150–250 °C) ist die Ferromagnet/Halbleiter-Grenzfläche scharf und Grenzflächenreaktionen sind vernachlässigbar. Diese verbesserte thermische Stabilität ist ein entscheidender Vorteil gegenüber z. B. Fe, Co, und Fe_xCo_{1-x}, auf GaAs(001) mit T_G < 50 °C, da nachfolgende Prozessschritte oftmals Temperaturzyklen deutlich oberhalb Raumtemperatur erfordern. Die Fe_3Si-Schichten sind bei Raumtemperatur ferromagnetisch und weisen zwei leichte Magnetisierungsachsen in der Filmebene entlang der [100]- und [010]-Richtung auf. Die Koerzitivfeldstärke ist kleiner als 1 Oe, was die hohe strukturelle Perfektion der Schichten unterstreicht.

Entsprechend den im Projektantrag formulierten Zielen haben wir die Wachstumsstudien von Fe_3Si auf eine höherindizierte GaAs-Oberfläche, nämlich GaAs(113), ausgedehnt, um neue magnetische Anisotropien gegebenenfalls mit einer aus der Filmebene gekippten leichten Magnetisiertungsachse zu stabilisieren. Die Herstellung der Schichten erfolgte in einer MBE-Anlage mit separaten Kammern für die GaAs-Präparation und das Wachstum von Fe_3Si, um die Kontamination der Fe_3Si-Schichten mit As aus der Gasphase zu verhindern. Als Substrat diente die wie üblich präparierte As-reiche GaAs(113)A-Oberfläche, Fe_3Si wurde durch zeitgleiches Abscheiden von Fe und Si aus Hochtemperatureffusionszellen hergestellt.

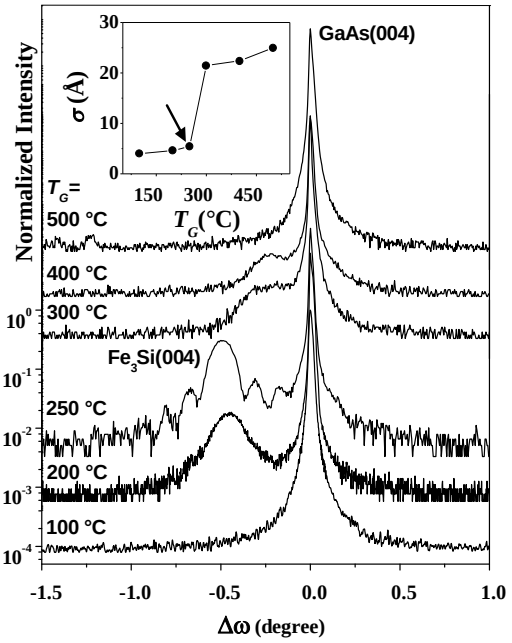

Abb. 1: ω–2θ-Röntgenbeugungsspektren bei verkippter Probe von Fe_3Si/GaAs(113)A, hergestellt bei Wachstumstemperaturen T_G zwischen 100 und 500 °C; die Spektren sind bezüglich des GaAs(004)-Peaks normiert und zur besseren Übersichtlichkeit gegeneinander verschoben. Das Insert zeigt die mit AFM ermittelte rms-Rauigkeit σ der Filme als Funktion von T_G.

Die optimalen Wachstumsbedingungen wurden durch systematische Variation der Wachstumsparameter ermittelt.

Abbildung 1 fasst die Ergebnisse von Röntgenbeugungsexperimenten an $Fe_{3+x}Si_{1-x}$/ GaAs(113)-Hybridstrukturen mit konstantem Fe/Si Verhältnis bei verschiedenen Wachstums-

temperaturen (T_G) zusammen. Ein für die $Fe_{3+x}Si_{1-x}$-Schichten charakteristischer Beugungspeak ergibt sich nur für Wachstumstemperaturen zwischen 200 und 400° C. Die optimale Wachstumstemperatur liegt bei etwa 250 °C. Wie bereits beim System Fe_3Si/GaAs(001) beobachtet, treten zusätzlich zu dem schmalen $Fe_{3+x}Si_{1-x}$-Peak auch Interferenz-Oszillationen bis zur 5. Ordnung auf, was auf die hohe strukturelle Güte der Filme und eine scharfe Grenzfläche hinweist. Die epitaktische Orientierung der Filme ist $Fe_3Si(113) \parallel GaAs(113)$ und $Fe_3Si[33\bar{2}] \parallel GaAs[33\bar{2}]$. Oberhalb von 400 °C treten zusätzliche Beugungspeaks auf, die auf die Ausbildung von Grenzflächenverbindungen (z. B. Fe_2As) zurückzuführen sind.

Das Insert von Abb. 1 zeigt die mittels Kraftmikroskopie (AFM) bestimmte rms-Rauhigkeit der Filme als Funktion von T_G. Unterhalb von T_G = 250 °C (Pfeil) beträgt die Rauhigkeit der Filme ca. 5–6 Å und nimmt oberhalb von 250 °C sprunghaft zu. Parallel dazu ist auch eine Degradation der Filmqualität in den Röntgenbeugungsspektren zu erkennen. Durch die Erniedrigung der Wachstumsrate von 0.26 nm/s (wie in Abb. 1) auf 0.13 nm/s kann die Oberflächenrauhigkeit bei 250 °C sogar auf 1.6 Å reduziert werden.

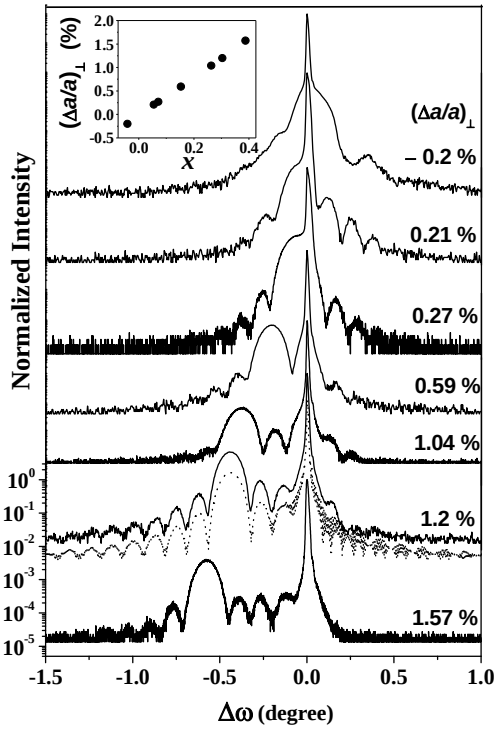

Abb. 2: ω–2θ-Röntgenbeugungsspektren bei verkippter Probe von $Fe_{3+x}Si_{1-x}$/GaAs(113)A mit unterschiedlichem Si-Gehalt und T_G = 250 °C; die Spektren sind bezüglich des GaAs(004)-Peaks normiert und zur besseren Übersichtlichkeit gegeneinander verschoben. Das Insert zeigt die senkrechte Verzerrung $(\Delta a/a)_\perp$ in Abhängigkeit von *x*.

Abbildung 2 zeigt Röntgenbeugungsspektren von $Fe_{3+x}Si_{1-x}$/GaAs(113)-Hybridstrukturen unterschiedlicher Si-Konzentration, die alle bei derselben Wachstumstemperatur von 250 °C und einer Aufdampfrate von 0.13 nm/s hergestellt wurden. Die Position des $Fe_{3+x}Si_{1-x}$-Peaks verschiebt sich deutlich bezüglich des GaAs(004)-Peaks, was sich durch unterschiedliche Gitterabstände in den jeweiligen Schichten erklärt. Für eine quantitative Auswertung wurden die Rocking-Kurven auch mit der Tagaki-Taupin-Methode zur Bestimmung der senkrechten Verzerrung und der Schichtdicke simuliert (Beispiel: gestrichelte Kurve in Abb. 2). Die Übereinstimmung mit dem Experiment ist hervorragend. Entsprechend unserer Analyse erstreckt sich der Si-Gehalt der in Abb. 2 aufgeführten Filme von 15 bis 26%. Das

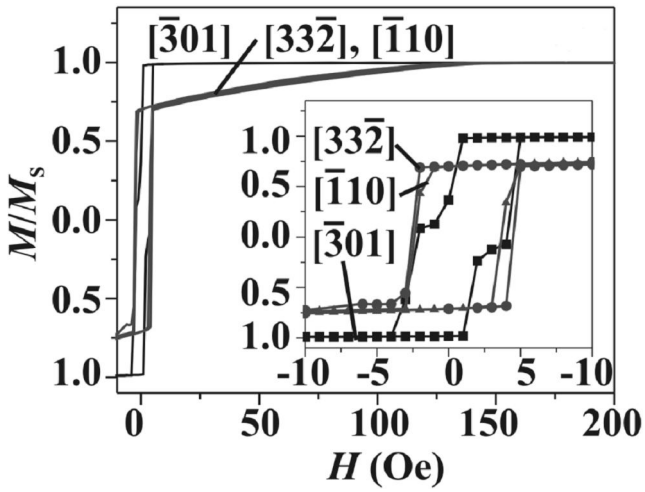

Abb. 3: Mittels SQUID-Magnetometrie gemessene Hysteresekurven einer Fe_3Si-Probe entlang verschiedener kristallographischer Richtungen; T_G = 250 °C, Wachstumsrate 0.13 nm/s

Insert zeigt die lineare Abhängigkeit der senkrechten Verzerrung $(\Delta a/a)_\perp$ von der Si-Konzentration.

Zur Untersuchung der magnetischen Eigenschaften wurden Messungen mit einem SQUID-Magnetometer bei Raumtemperatur durchgeführt. Abbildung 3 zeigt Hysteresekurven des um 1.2% verzerrten Filmes aus Abb. 2 entlang verschiedener, in der Filmebene liegender kristallographischer Richtungen. Die Probe ist bei Raumtemperatur ferromagnetisch mit einer Sättigungsmagnetisierung von 1300±200 emu/cm^3. Wie das magnetische Sättigungsverhalten zeigt, liegen die leichten Magnetisierungsrichtungen entlang der $\langle \bar{3}01 \rangle$-Richtungen und nicht entlang $\langle 100 \rangle$ wie bei Fe_3Si/GaAs(001). Dieses Ergebnis wird durch SQUID-Messungen mit dem Magnetfeld senkrecht zur Filmebene bestätigt. Die Koerzitivfeldstärke ist ähnlich zu Fe_3Si/GaAs(001) sehr klein und liegt bei ca. 5 Oe. Die Probe weist eine ausgeprägte vierfache magnetische Anisotropie in der Filmebene auf. Wie im Einschub von Abb. 3 zu sehen, erfolgt die Ummagnetisierung entlang der $[\bar{3}01]$-Richtung über einen Zwischenschritt, in dem die Magnetisierung in die zur $[\bar{3}01]$-Richtung senkrechten, ebenfalls in der Filmebene liegenden $[0\bar{3}1]$-Richtung klappt. Die beiden gegenüber $\langle \bar{3}01 \rangle$ um ±45° in der Filmebene rotierten Richtungen, $[\bar{1}10]$ und $[33\bar{2}]$, stellen mittelschwere Magnetisierungsrichtungen mit einem identischen Sättigungsfeld von etwa 130 Oe dar.

2.2. Magnetotransport in Fe_3Si/GaAs(001)- und Fe_3Si/GaAs(113)A-Hybridstrukturen

Wir haben weiterhin umfangreiche Studien zum Magnetotransport im System $Fe_{3+x}Si_{1-x}$/ GaAs(001) und Fe_3Si/GaAs(113)A durchgeführt. In magnetischen Materialien gibt es zusätzlich zum konventionellen Hall Effekt auch noch den Beitrag des anomalen Hall Effekts. Außerdem bewirkt auch ein Magnetfeld in der Filmebene eine Hall-Spannung, was als planarer Hall-Effekt bezeichnet wird. Unsere Hall-Effekt-Untersuchungen der Fe_3Si/GaAs(113)-Schichten zeigen, dass die in den Hysteresekurven äquivalenten Richtungen[$\bar{1}10$] und [$33\bar{2}$] bezüglich des Magnetotransportes nicht äquivalent sind. Während der planare Hall-Effekt, wie üblich, entlang der [$\bar{1}10$]-Richtung symmetrisch ist, tritt in der [$33\bar{2}$]-Richtung eine starke antisymmetrische Komponente auf (vergleiche Abb. 4a und Abb. 5a). In Abb. 4b und 5b ist die Abhängigkeit des planaren Hall-Widerstandes ρ_{xy} vom Magnetisierungswinkel θ_M der Probe dargestellt, die in einen symmetrischen und antisymmetrischen Beitrag aufgespalten werden kann (Abb. 4c und 5c). Der Kurvenverlauf des symmet-

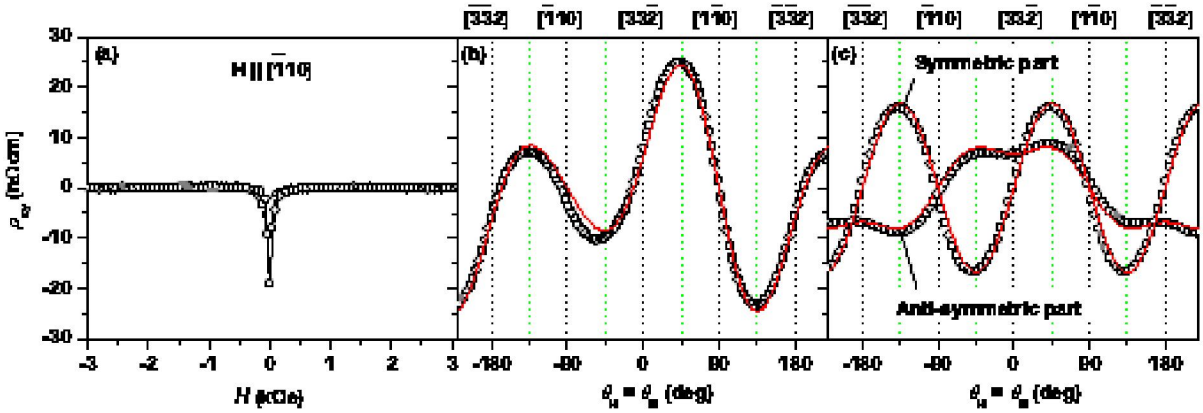

Abb. 4: Planarer Hall-Effekt in $Fe_{3-x}Si_{1+x}$/GaAs(113) bei 300 K (x = 0.07): a) ρ_{xy} mit dem Magnetfeld H parallel zur [$\bar{1}10$]-Richtung, b) Winkelabhängigkeit von ρ_{xy} bei H = 1 kOe, d.h. $\theta_H = \theta_M$, c) symmetrische und antisymmetrische Komponente von ρ_{xy}; die durchgezogenen Kurven illustrieren die zu erwartende $\sin(2\theta_M)$-Abhängigkeit für den symmetrischen Beitrag bzw. eine $\rho\cos(\theta_M) + \rho\cos^3(\theta_M)$-Abhängigkeit für die antisymmetrische Komponente.

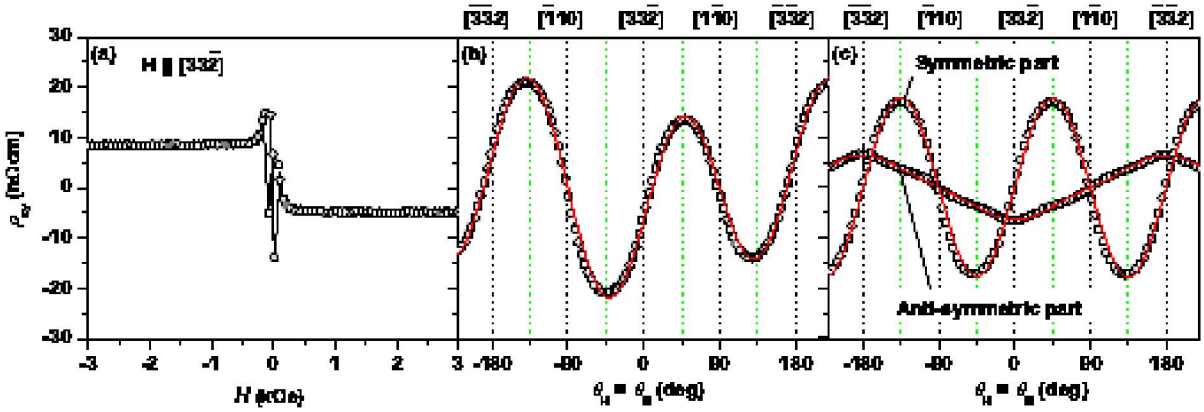

Abb. 5: Planarer Hall-Effekt in $Fe_{3-x}Si_{1+x}$/GaAs(113) bei 77 K (x = 0.07): a) ρ_{xy} mit dem Magnetfeld H parallel zur [$33\bar{2}$]-Richtung, b) Winkelabhängigkeit von ρ_{xy} bei H = 1 kOe, d.h. $\theta_H = \theta_M$, c) symmetrische und antisymmetrische Komponente von ρ_{xy}; die durchgezogenen Kurven illustrieren die zu erwartende $\sin(2\theta_M)$-Abhängigkeit für den symmetrischen Beitrag bzw. eine $\rho\cos(\theta_M) + \rho\cos^3(\theta_M)$-Abhängigkeit für die antisymmetrische Komponente.

rischen Beitrages entspricht erwartungsgemäß einer $\sin(2\theta_M)$-Abgängigkeit, die antisymmetrische Komponente wird durch eine $[\rho_0\cos(\theta_M) + \rho_1\cos^3(\theta_M)]$-Abhängigkeit beschrieben. Der Vergleich mit einer phänomenologischen Theorie weist die Magnetfeld-induzierte Anisotropie des Magnetowiderstandes in der (113)-Ebene als einen Beitrag zweiter Ordnung zum planaren Hall-Effekt aus. Die zusätzliche antisymmetrische Komponente hängt zudem von der Temperatur und der Zusammensetzung der $Fe_{3-x}Si_{1+x}$-Filme ab. Bei einer Si-Konzentration von 21% findet ein Vorzeichenwechsel statt.

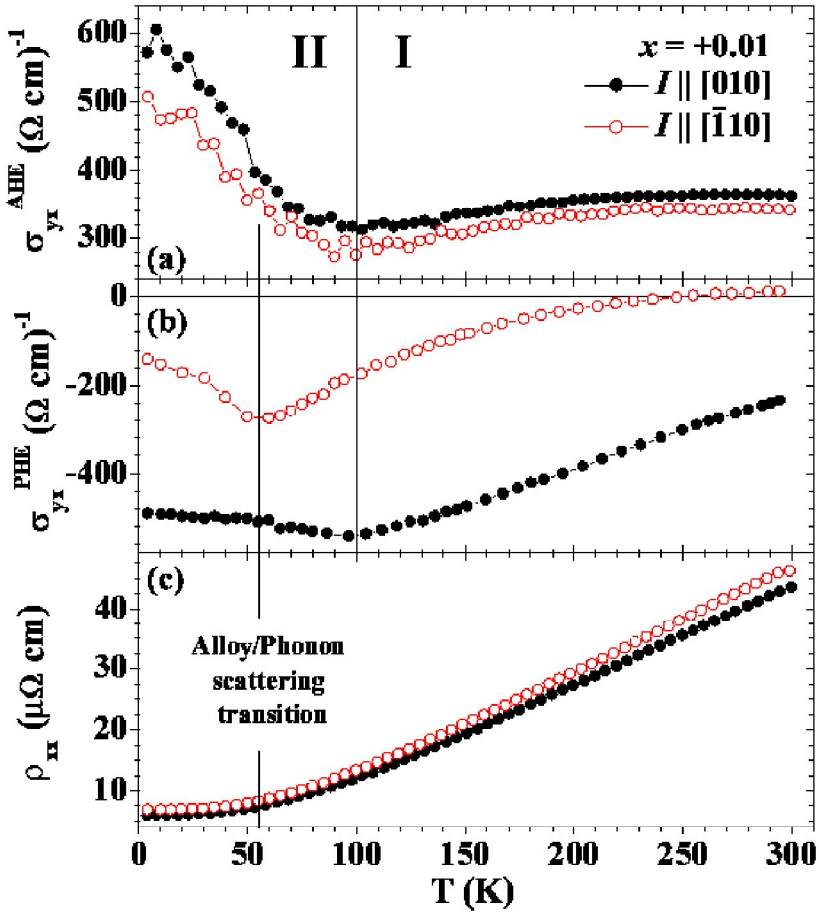

Abb. 6: Temperaturverlauf des (a) anomalen (σ_{yx}^{AHE}) und (b) planaren (σ_{yx}^{PHE}) Hall-Effekts, sowie (c) des Filmwiderstandes (ρ_{xx}) von stöchiometrischem $Fe_{3+x}Si_{1-x}$/ As(001) mit x = +0.01.

Abb. 6 zeigt den Temperaturverlauf von anomalem und planarem Hall-Effekt, sowie des Filmwiderstandes von stöchiometrischem $Fe_{3+x}Si_{1-x}$/GaAs(001) mit x = +0.01. Während der Filmwiderstand nahezu linear mit der Temperatur abnimmt, bis bei ca. 50 K der Übergang von Phonon- zu Legierungsstreuung stattfindet, nimmt der anomale Hall-Effekt unterhalb von 100 K wieder stark zu. Auch der planare Hall-Effekt mit dem Strom parallel zur $[\bar{1}10]$-Richtung weist ein Minimum bei 100 K auf, für die Stromrichtung entlang [010] liegt das Minimum bei 50 K.

Eine detaillierte Analyse zeigt nun, dass der Temperaturverlauf von anomalem und planarem Hall-Effekt vollständig durch das Auftreten von kohärenten Spin-Fluktuationen zwischen den Fe(*A*) und Fe(*C*)-Untergittern (siehe Abb. 7) eines strukturell geordneten Fe_3Si-Film verstanden werden kann. Mit dem Erscheinen dieser Fluktuationen bei ca. 100 K wird die Symmetrie des Magnetowiderstandstensors reduziert, was sowohl den starken Anstieg des anomalen Hall-Effekts bei Temperaturen unterhalb von 100 K, als auch die Unterschiede im

planaren Hall-Effekt für die beiden Stromrichtungen erklärt. Die experimentell ermittelte Einsatztemperatur für die kohärenten Spin-Fluktuationen stimmt gut mit der experimentell von Stearns [Phys. Rev. B 168, 588 (1968)] bestimmten Austauschenergie $J_{ex}[(A,C)\leftrightarrow(A,C)] = 80 \pm 20$ K zwischen den Fe(*A*,*C*)-Untergittern überein. Diese Interpretation wird durch Hall-Effekt-Untersuchungen von $Fe_{3+x}Si_{1-x}$/As(001) in der Nähe der stöchiometrischen Zusammensetzung bestätigt. Beispielsweise weist der anomale Hall-Effekt in $Fe_{3+x}Si_{1-x}$-Filmen mit $x = +0.09$ aufgrund der strukturellen Unordnung einen ähnlichen Temperaturverlauf auf wie der Filmwiderstand in Abb. 6.

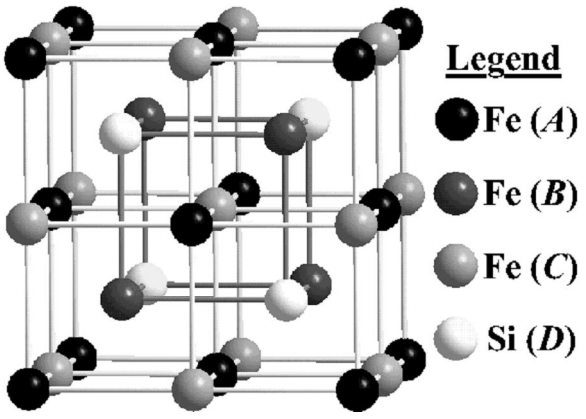

Abb. 7: *D0*$_3$-Struktur von Fe_3Si, zentriert um einen *C*-Platz, bestehend aus drei Fe und einem Si fcc-Untergitter. Die (*A*,*C*)-Plätze haben *F23*-Symmetrie, die (*B*,*D*)-Plätze hingegen eine $Fm\bar{3}m$ -Symmetrie.

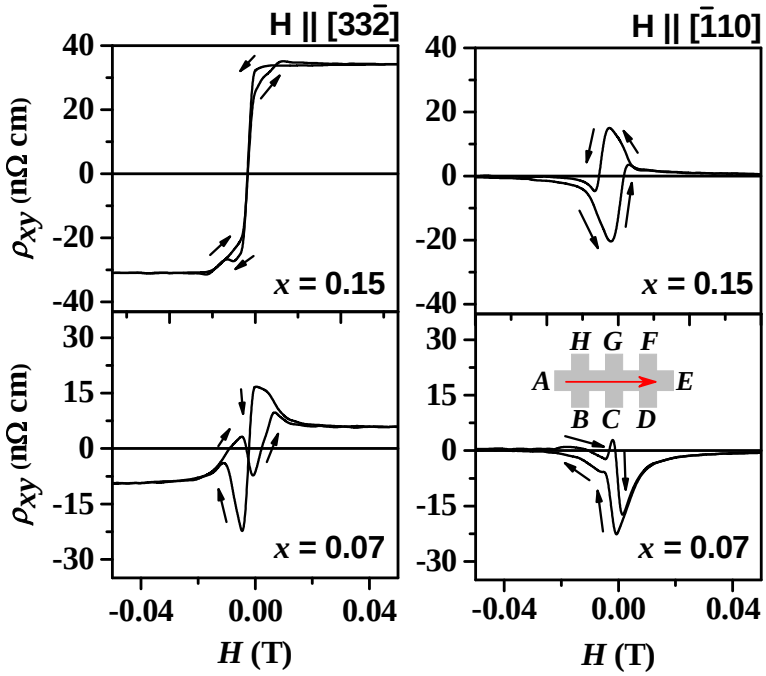

Abb. 8: Magnetfeldabhängigkeit des planaren Hallwiderstands ρ_{yx} von $Fe_{3+x}Si_{1-x}$/GaAs(113)A-Schichten (gemessen bei 300 °C). Der Einschub im unteren rechten Bild zeigt schematisch die Kontakte und die Geometrie der planaren Hall-Effektsmessung. Der Pfeil gibt die Richtung des eingeprägten Stromes (entlang der [33-2]-Richtung) an.

In Fortführung der Untersuchungen zum Magnetotransport im System Fe_3Si/GaAs(113)A haben wir die magnetische Anisotropie und das magnetische Umkehrverhalten dieser Schichten mittels des planaren Hall-Effekts bestimmt. Der planare Hall-Effekt in dieser Orientierung zeigt eine antisymmetrische Komponente zusätzlich zur gewöhnlichen symmetrischen Komponente. Der relative Anteil der symmetrischen und antisymmetrischen Komponente im planaren Hall-Effekt hängt von der Komposition der $Fe_{3+x}Si_{1-x}$-Filme sowie der Schichtdicke ab. Das führt zu einem komplexen Verhalten des planeren Hallwiderstands im Bereich geringer Magnetfelder (unterhalb der Sättigungsfeldstärke der Magnetisierung).

Abbildung 8 zeigt die Magnetfeldabhängigkeit des planaren Hallwiderstands für zwei $Fe_{3+x}Si_{1-x}$-Filme, die sich in der Zusammensetzung *x* voneinander unterscheiden. Im Bereich geringer Magnetfelder verhält sich der planare Hallwiderstandstand in beiden Proben sehr unterschiedlich. Das könnte darauf hindeuten, dass der Mechanismus der magnetischen Umkehr völlig unterschiedlich ist. Mittels detaillierter Modellrechnungen (Ergebnisse in Abb. 8 und 9) zeigt sich jedoch, dass dieses unterschiedliche Verhalten eine Konsequenz des Auftretens der antisymmetrischen Komponente ist, die sich mit der Richtung des angelegten Magnetfelds und der Zusammensetzung der Schichten ändert. Der Mechanismus der magnetischen Umkehr bleibt dabei unverändert und kann dabei qualitativ mittels des einfachen Stoner-Wolfahrt-Modells im Einzeldomänenbild erklärt werden. Damit ergibt sich die Möglichkeit, die magnetische Anisotropie der Fe_3Si/GaAs(113)A-Schichten aus den Messungen des planaren Hall-Effekts zu bestimmen. Hierbei finden wir eine sehr gute Übereinstimmung der experimentellen Ergebnisse aus Halleffekt-, Magnetowiderstands- und SQUID-Magnetometriemessungen.

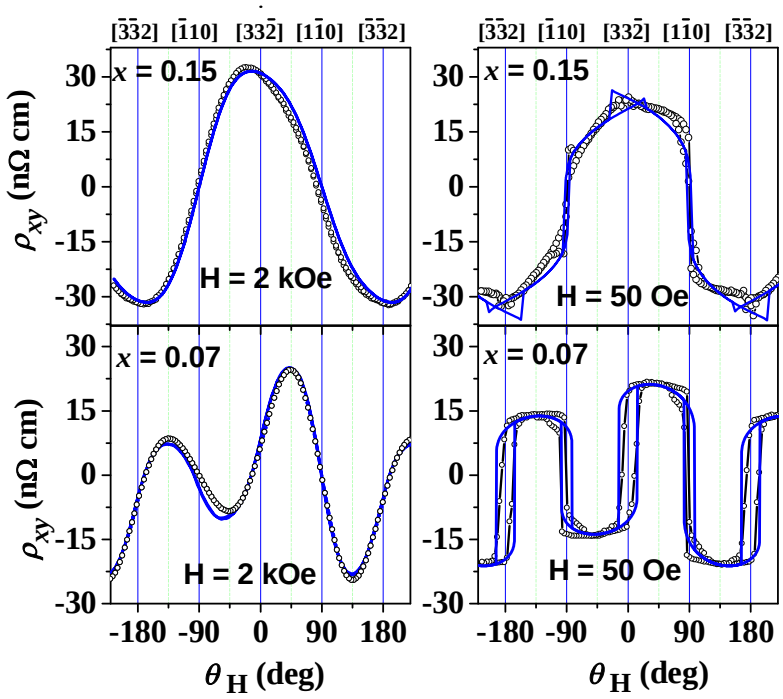

Abb. 9: Experimentelle (Symbole) und berechnete (dicke Linien) Winkelabhängigkeit des planaren Hall-Effekts für zwei verschiedene $Fe_{3+x}Si_{1-x}$/GaAs(113)A-Schichten. Hierbei entspricht $\theta_H = 0°$ der [33-2]-Richtung, was auch der Stromrichtung entspricht.

3. Co_2FeSi/GaAs(001)-Hybridstrukturen

3.1. Wachstum, strukturelle und elektrische Eigenschaften

Einen zweiten wesentlichen Schwerpunkt des Projekts stellen unsere Wachstumsuntersuchungen zu ternären Heusler-Verbindungen auf GaAs(001) dar. Hierbei fiel die Auswahl auf Co_2FeSi, das eine vollständige Heusler-Legierung mit einer Kristallstruktur darstellt, die aus vier ineinander geschachtelten fcc-Teilgittern besteht. Der Gitterabstand beträgt 5.658 Á und weist gegenüber dem GaAs(001)-Substrat (a_{GaAs} = 5.653 Á) die sehr kleine Fehlanpassung von 0.08% auf. Zusammen mit seinem großen magnetischen Moment (5.91 μ_B) und der hohen Curie-Temperatur (980 K) erfüllt Co_2FeSi damit wesentliche Voraussetzungen für ein Materialsystem der Spintronik. Theoretische Untersuchungen haben gezeigt, dass Co_2FeSi ein halbmetallischen Verhalten zeigt, d. h. die Spinpolarisation an der Fermi-Energie beträgt 100%. Deshalb wird Co_2FeSi ein sehr hohes Potential als möglicher Spininjektor zugeschrieben.

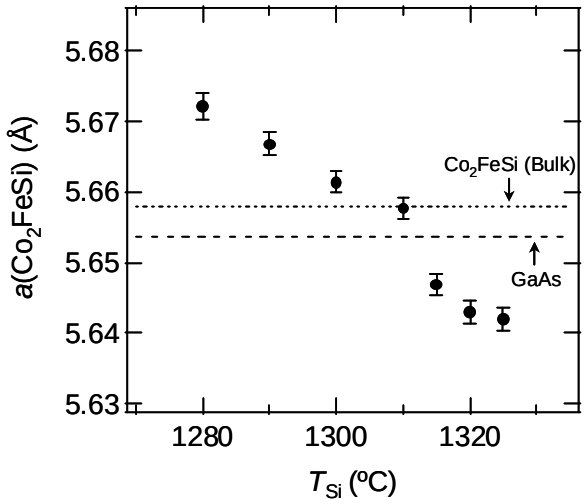

Abb. 10: Der aus Röngenbeugungsdaten ermittelte Gleichgewichtsgitterabstand der unverspannten Co_2FeSi-Legierungsfilme als Funktion der Quellentemperatur von Si.

Wie schon bei Fe_3Si erfolgte die Herstellung der Schichten mittels MBE in einer Anlage mit separaten Kammern für die GaAs-Präparation und das Metallwachstum. Als Substrat diente die As-reiche *c*(4×4)-Überstruktur von GaAs(001). Co, Fe und Si wurden aus Effusionszellen verdampft. In einem ersten Schritt wurden die Quellentemperaturen von Co und Fe für die Präparation der binären Legierung $Co_{0.66}Fe_{0.34}$ optimiert. Dann wurde Si mitverdampft und der Gitterabstand der aufgewachsenen Legierung mittels Röntgenbeugung ermittelt. Der Vergleich mit dem Gitterabstand der stöchiometrischen Verbindung (siehe Abb. 10) liefert die geeignete Quellentemperatur.

Abbildung 11 zeigt Röntgenbeugungsspektren von Filmen, die bei Wachstumstemperatur von 100–350 °C hergestellt wurden. Wie bereits bei Fe_3Si beobachtet, treten zusätzlich zum Co_2FeSi-Peak auch Interferenz-Oszillationen höherer Ordnung auf, die Aufschluss über die Qualität der Grenzfläche geben. Die besten Ergebnisse mit Oszillationen bis zur 5. Ordnung werden bereits bei niedrigen Wachstumstemperaturen von 100 °C erzielt [Abb. 11(b)]. Oberhalb von 250 °C verschlechtert sich das Beugungsbild, was auf Grenzflächenreaktionen zwischen dem Co_2FeSi-Film und dem GaAs-Substrat zurückzuführen ist. Diese Interpretation wird durch einen zusätzlichen Beugungspeak beim 350 °C-Film bestätigt (Abb. 7a), der einem $(Co, Fe)_2As$(110)-Reflex zugeordnet werden kann.

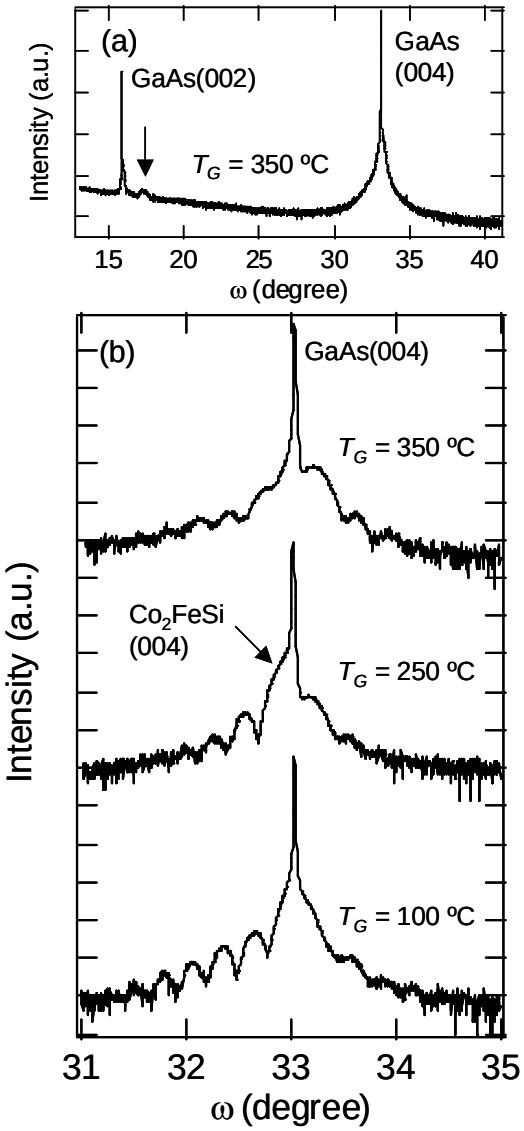

Abb. 11: Röntgenbeugungsspektren von Co_2FeSi/GaAs(001) bei verschiedenen Wachstumstemperaturen: a) ω–2θ-Kurve bei 350 °C; b) hochaufgelöste ω–2θ-Kurven bei verkippter Probe mit schönen Interferenz-Oszillationen (Pendellösungen); die Spektren sind bezüglich des GaAs(004)-Peaks normiert und zur besseren Übersichtlichkeit gegeneinander verschoben.

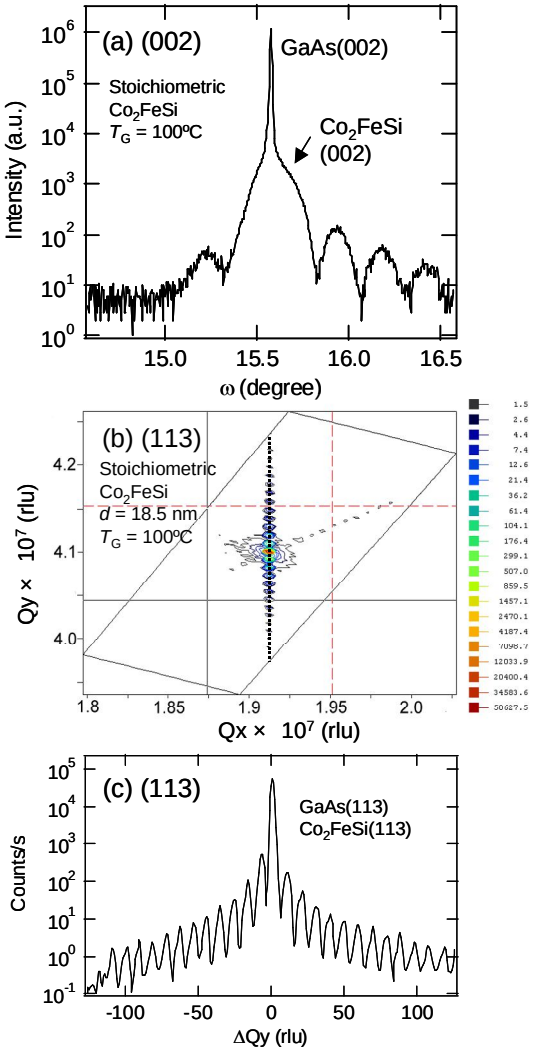

Abb. 12: a) Hochaufgelöste ω–2θ-Röntgenbeugungskurve am Co_2FeSi(002)-Reflex bei verkippter Probe, b) Co_2FeSi(113)-Reflex; c) Linienprofil entlang der gepunkteten Linie in b).

Zur Aufklärung der strukturellen Ordnung der Co_2FeSi-Filme entsprechend dem Heusler-Kristallgitter wurden auch andere Beugungsreflexe im Detail ausgemessen. So gibt der Co_2FeSi(002)-Reflex Aufschluss über den Ordnungsgrad der Fe- und Si-Untergitter und verschwindet bei deren völligen Unordnung. Bei vollständiger Unordnung zwischen allen Untergittern fehlt der Co_2FeSi(113)-Reflex. Tatsächlich treten beide Reflexe mit hoher Intensität auf, begleitet durch zusätzliche Interferenz-Oszillationen (siehe Abb. 12), was eindeutig auf eine hohe strukturelle Ordnung der drei atomaren Spezies entsprechend dem Kristallgitter von Heusler-Legierungen hinweist und die hohe Güte der Grenzfläche zum Substrat untermauert.

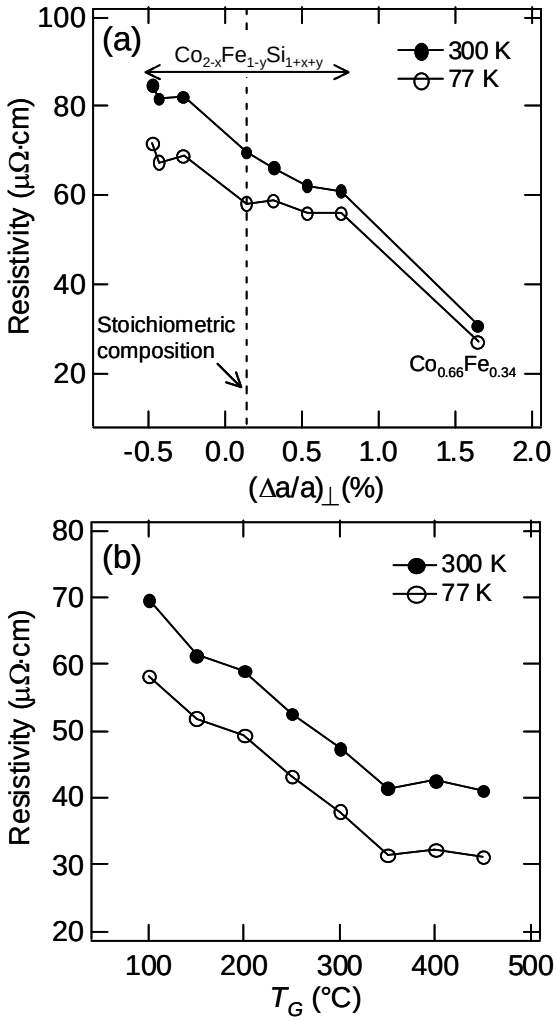

Abb. 13: Elektrischer Widerstand von Co_2FeSi-Filmen: a) mit unterschiedlichem Si-Gehalt und b) als Funktion der Wachstumstemperatur.

Abbildung 13a zeigt die Abhängigkeit des elektrischen Widerstands der Filme als Funktion der Zusammensetzung. Mit zunehmendem Si-Gehalt steigt der Widerstand an, wobei kein Minimum bei der stöchiometrischen Zusammensetzung auftritt. Dies legt den Schluss nahe, dass ein Teil der Si-Atome auch auf den Gitterplätzen der anderen Legierungskomponenten sitzt und damit für eine erhöhte Streuung der Elektronen Anlass gibt. Wie in Abb. 13b für den stöchiometrischen Film gezeigt, sinkt der Widerstand bei Erhöhung der Wachstumstemperatur. Offensichtlich erfordert die Wahl der optimalen Wachstumstemperatur einen Kompromiss zwischen einerseits vernachlässigbaren Grenzflächenreaktionen, d.h. niedriges T_G, und andererseits verbesserter struktureller Ordnung bei höhere Wachstumstemperaturen.

3.2. Magnetische Eigenschaften

Die magnetischen Eigenschaften von Co_2FeSi/GaAs(001) wurden mittels SQUID untersucht, mit dem externen Magnetfeld entlang der [110]-, [$1\bar{1}0$]- und [100]-Richtungen. Alle hergestellten Co_2FeSi-Filme sind bei Raumtemperatur ferromagnetisch. Beim stöchiometrischen Film (Abb. 14) liegt die Sättigungsmagnetisierung bei 1250±120 emu/cm^3, was innerhalb des experimentellen Fehlers mit dem Wert der Volumenphase übereinstimmt (1124 emu/ cm^3).

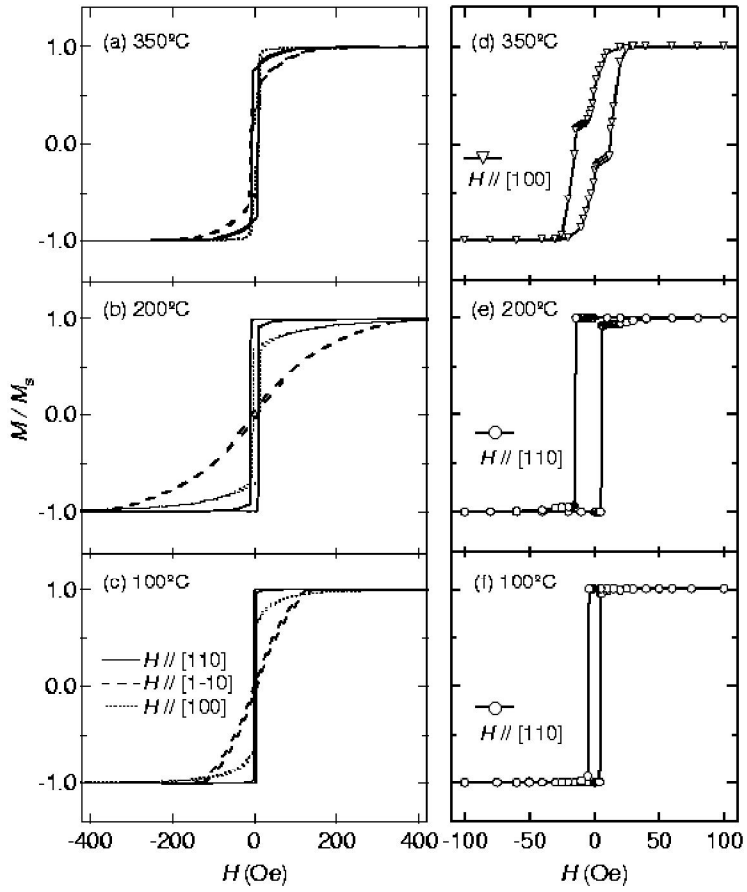

Abb. 14: SQUID-Hysteresekurven mit dem Magnetfeld entlang der [110]-, [$1\bar{1}0$]- und [100]-Richtungen von verschiedener, bei den angegebenen Wachstumstemperaturen hergestellten Co_2FeSi/GaAs(001)-Schichten; der diamagnetische Beitrag des Substrats ist subtrahiert.

Den Einfluss der Wachstumstemperatur auf die magnetischen Eigenschaften von Co_2FeSi/ GaAs(001) illustriert Abb. 14. Die Hysteresekurven wurden bei Raumtemperatur mit dem externen Magnetfeld entlang der [110]-, [$1\bar{1}0$]- und [100]-Richtungen gemessen. Für Wachstumstemperaturen unterhalb von 300°C liegt die leichte Magnetisierungsachse entlang der [110]-Richtung. Beim 100°C-Film beträgt die Koerzitivfeldstärke nur 4.5 Oe, was die hohe strukturelle Güte untermauert. Die [$1\bar{1}0$]- und [100]-Richtungen stellen mittelschwere bzw. schwere Magnetisierungsachsen dar. Dieses Ergebnis ist überraschend und weicht von der üblicherweise in Heusler-Legierungen beobachteten magnetischen Anisotropie mit leichten Magnetisierungsachsen entlang ⟨100⟩ ab. Die uniaxiale Anisotropie (UMA) der Co_2FeSi-Filme ist dabei als dominant grenzflächenrelevanter Term auf die Asymmetrie der Grenzfläche zum GaAs(001)-Substrat zurückzuführen. Die leichte Magnetisierungsachse des 350°C-Films scheint wie im Volumen entlang der [100]-Richtung zu liegen, wobei die Anisotropie in

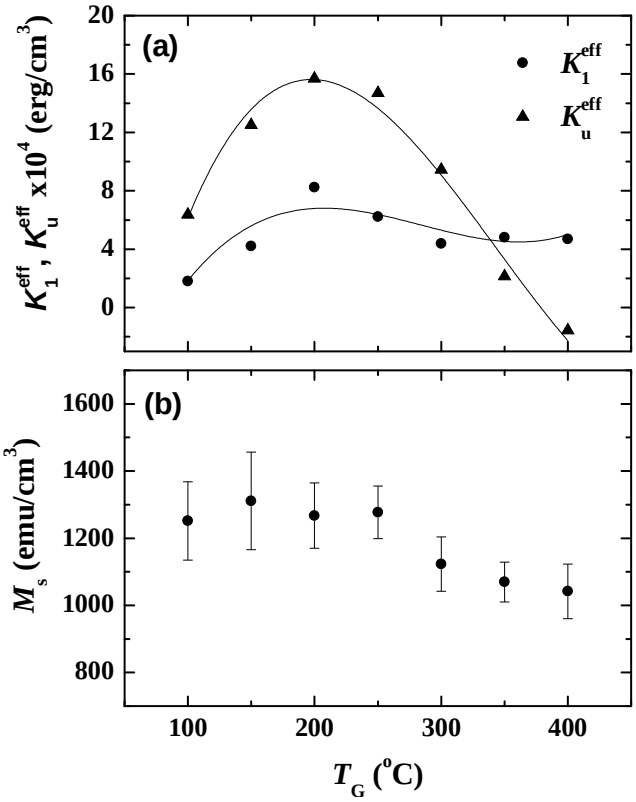

Abb. 15: Wachstumstemperaturabhängigkeit der (a) uniaxialen magnetischen Anisotropiekonstante K_U^{eff} (Dreiecke) und der kubischen magnetischen Anisotropiekonstante K_1^{eff} (Kreise) und (b) der Sättigungsmagnetisierung M_S der Co_2FeSi/GaAs(001)-Schichten. Die Linien dienen der Orientierung.

der Filmebene deutlich kleiner ist als bei den bei niedrigeren Temperaturen hergestellten Filmen.

Abbildung 15(a) zeigt die zwei effektiven magnetischen Anisotropiekonstanten in der Schichtebene, die man aus der Anpassung der reversiblen (harten) Magnetisierungskurven entlang der $[1\bar{1}0]$-Richtung erhält. Beide Anisotropiekonstanten K_U^{eff} (uniaxiale Komponente) und K_1^{eff} (kubische Komponente) haben ein Maximum bei 200 °C. Das ist ein weiterer Hinweis darauf, dass die optimale Wachstumstemperatur, um eine abrupte, geordnete Grenzfläche zu erhalten, bei ca. 200 °C liegt. Die Abnahme von K_U^{eff} oberhalb von 200 °C ist auf das fortschreitende Einsetzen der Grenzflächenreaktion zurückzuführen. Der simultane Abnahme von K_1^{eff} ist möglicherweise durch die atomare Unordnung bedingt, die durch die Co-Diffusion in das GaAs-Substrat hervorgerufen wird. Gleichzeitig verringert sich die Sättigungsmagnetisierung für Wachstumstemperaturen oberhalb 250 °C [Abb.15(b)].

3.3. Untersuchungen mittels Transmissionselektronenmikroskopie

Unsere Untersuchungen mittels Röntgenbeugung (XRD) zeigten (Abschnitt 3.1.), dass die optimale Wachstumstemperatur einen Kompromiss darstellt zwischen einerseits vernachlässigbaren Grenzflächenreaktionen, die bei niedrigen Wachstumstemperaturen unterdrückt sind, und andrerseits einer guten strukturellen Ordnung der Heusler-Legierung, wofür höhere Wachstumstemperaturen erforderlich sind. Die Qualität der Interferenzoszillationen (Pendellösung), die Aufschluss über die Güte der Grenzfläche geben, weist auf eine optimale Wachstumstemperatur im Bereich von ca. 200°C.

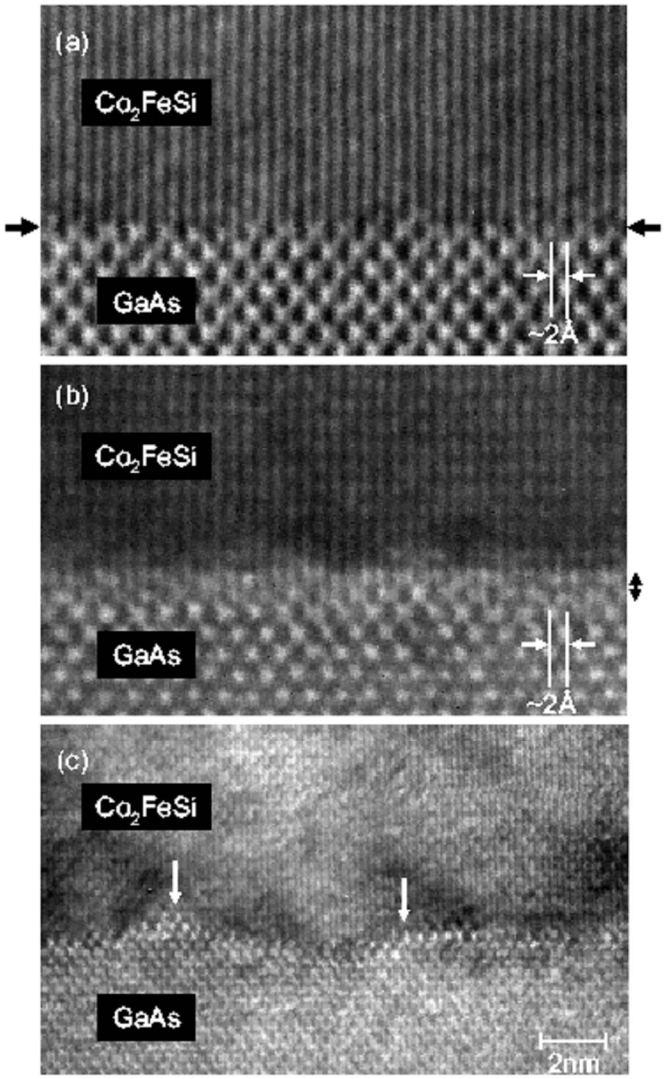

Abb. 16: HRTEM-Querschnittsaufnahmen von Co_2FeSi/GaAs(001) entlang der [110]-Richtung: Die Wachstumstemperaturen sind in a) 100°C, b) 200°C und c) 350°C; man beachte den größeren Bildausschnitt von c) gegenüber a) und b).

Zur detaillierten Charakterisierung der Grenzfläche, die für die Spin-Injektion eine entscheidende Rolle spielt, wurden Untersuchungen mittels hochauflösender Transmissionselektronenmikroskopie (HRTEM) durchgeführt. Abbildung 16 zeigt Querschnitt-HRTEM-Aufnahmen von Co_2FeSi/ GaAs(001) entlang der [110]-Richtung bei verschiedenen Wachstumstemperaturen (100, 200 und 350°C). In Übereinstimmung mit den XRD-Ergebnissen ist die Grenzfläche bei 100°C scharf [markiert durch Pfeile in Abb. 16(a)], d.h. der Übergang vom GaAs- zum Heusler-Kristallgitter erfolgt abrupt. Beide Kristallgitter sind perfekt angepasst und da-

mit ist der Co_2FeSi-Film einheitlich verspannt. Bei einer Wachstumstemperatur von 350°C hingegen ist die Grenzfläche im Nanometerbereich rau [Abb. 16(c)], was auf eine starke Reaktion im Grenzflächenbereich hinweist. Diese Interpretation wird durch XRD-Untersuchungen bestätigt, die einen zusätzlichen Beugungspeak beim 350 °C-Film zeigen, der einem $(Co, Fe)_2As$(110)-Reflex zugeordnet werden kann. Bei 200°C ist ein 1–2 Atomlagen dicker Übergangsbereich zu erkennen [Abb. 16(b)], in dem sich der Bildkontrast sowohl vom GaAs als auch vom Co_2FeSi-Film unterscheidet, was auf den Einsatz der Grenzflächenreaktionen hinweist.

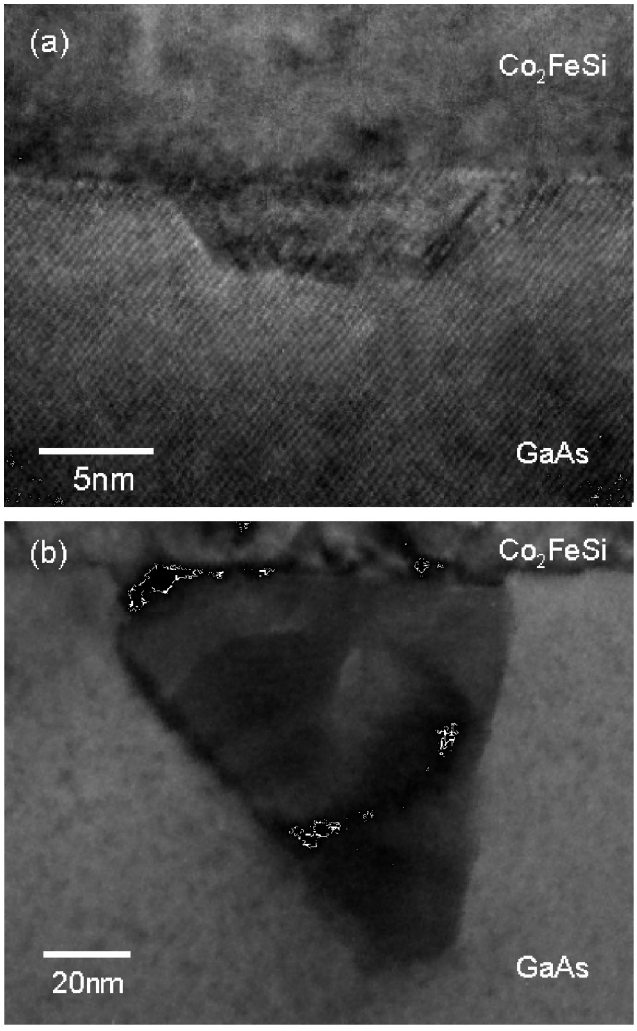

Abb. 17: TEM-Aufnahme im Querschnitt in der Umgebung von Reaktionsprodukten für eine Co_2FeSi/GaAs(001)-Schicht, die bei 250 °C gewachsen wurde. (b) Hellfeldaufnahme eine Co_2FeSi/GaAs(001)-Schicht, die bei 400 °C gewachsen wurde.

Die Einsatztemperatur für Grenzflächenreaktionen ist wesentlich höher als bei Hybridstrukturen, die aus reinen Fe oder Co bestehen. Die Grenzflächereaktion findet vorwiegend durch eine Co-Diffusion in das GaAs-Substrat statt. Das führt zu Formierung isolierter Körner im GaAs wie man in Abb. 17 erkennen kann. Durch umfangreiche Röntgenbeugungsdiffraktometrie- sowie TEM-Untersuchungen können wir nachweisen, dass die bei diesem Prozess gebildeten Reaktionsprodukte sich vom ternären Co_2GaAs (250 – 300 °C) zum binären CoAs (350 – 400 °C) ändern.

Es wurden weiterführende Untersuchungen an den Co_2FeSi/GaAs(001) Hybridstrukturen durchgeführt, um Aussagen über atomare Ordnung der Schichten in vertikaler Richtung

zu erzielen. Abbildung 18 (oben) zeigt eine hochaufgelöste Transmissionselektronenmikroskopieaufnahme (HRTEM-Aufnahme) im Querschnitt einer bei 200 °C gewachsenen Co_2FeSi Schicht. Die Schicht enthält 2 unterschiedliche Kristallphasen, die durch ein Linien-Ball-Interferenzmuster sowie ein netzartiges Interferenzmuster charakterisiert sind, wobei das Letztere hauptsächlich an der Grenzfläche zwischen dem GaAs und der Co_2FeSi Schicht beobachtet wird. Um die jeweiligen Interferenzmuster zu identifizieren haben wir Kontrastsimulationen für drei verschiedene Ordnungssysteme der Co_2FeSi Schicht sowie für das GaAs-Substrat durchgeführt. Von Bedeutung für die in Abb. 18 gezeigte Schicht sind dabei (i) die *B2*-Struktur (Unordnung zwischen dem Fe und Si Untergitter), (ii) die atomar geordnete $L2_1$-Struktur der Heuslerlegierung und (iii) die Zinkblendestruktur des GaAs-Substrats. Durch sehr sorgfältige Vergleiche der Dicken-Defokussierungs-Karten der einzelnen Strukturen mit

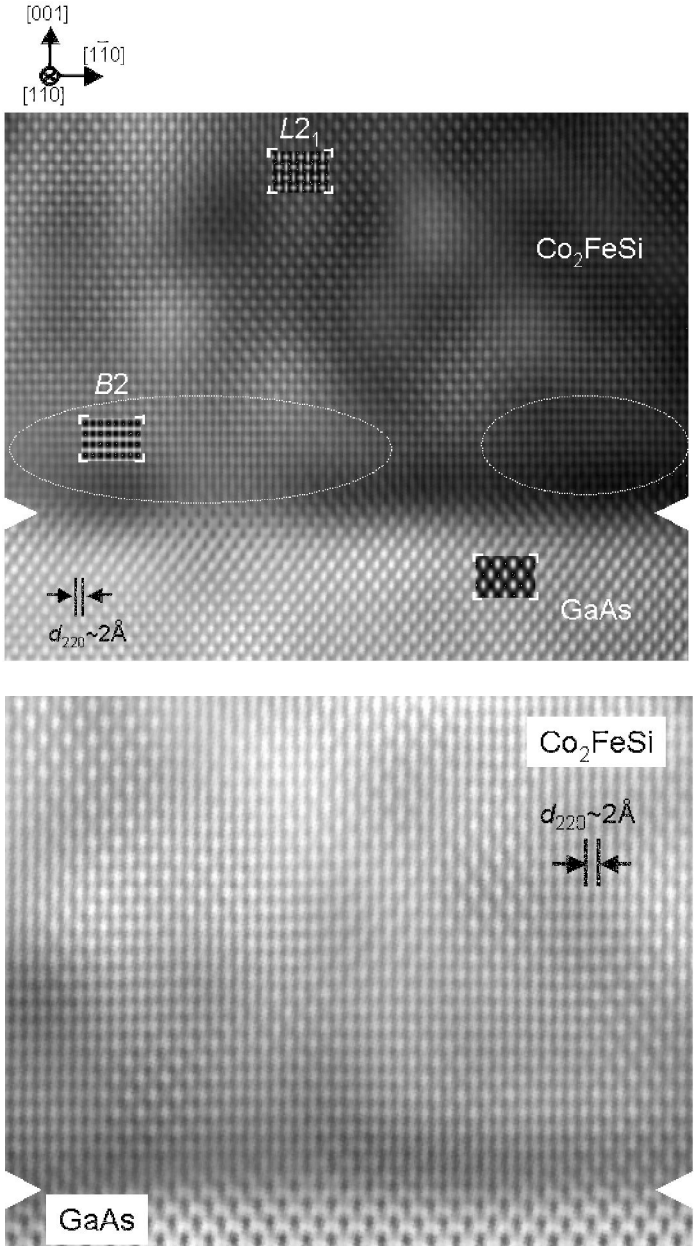

Abb. 18: Fouriergefilterte HRTEM-Aufnahmen im Querschnitt entlang der [110]-Richtung für Co_2FeSi/GaAs(001)-Schichten, die bei 200 °C (oberes Bild) und 100 °C (unteres Bild) gewachsen wurden. Die Simulationen der $L2_1$- und der *B2*-Struktur sind als Einschübe zum Vergleich gezeigt.

den experimentellen Ergebnis finden wir, dass das Linien-Ball-Interferenzmuster mit dem simulierten Muster der $L2_1$-Struktur übereinstimmt. Andererseits lässt sich das netzartige Interferenzbild der weniger geordneten *B2*-Struktur zuordnen. Dieses Ergebnis zeigt, dass unabhängig von der abrupten und scharfen Grenzfläche der bei 200 °C gewachsenen Schicht, beide Phasen zusammen auftreten. Insbesondere die weniger geordnete *B2*-Phase nahe der Grenzfläche kann zu einer Reduzierung der Spinpolarisation der Co_2FeSi Schicht führen. Die Koexistenz der $L2_1$/*B2*-Phasen wurde auch in Filmen beobachtet, die bei 100 °C gewachsen wurden (unteres Bild in Abb. 18).

Die HRTEM-Aufnahme einer bei 300 °C gewachsenen Schicht zeigt ein schachbrettartiges Muster (Abb. 19). Dieses Muster gehört zur $L2_1$-Struktur mit einer im Vergleich zur Schicht in Abb. 18 leicht veränderten Schichtdicke. Die einheitliche Verteilung der $L2_1$-Phase

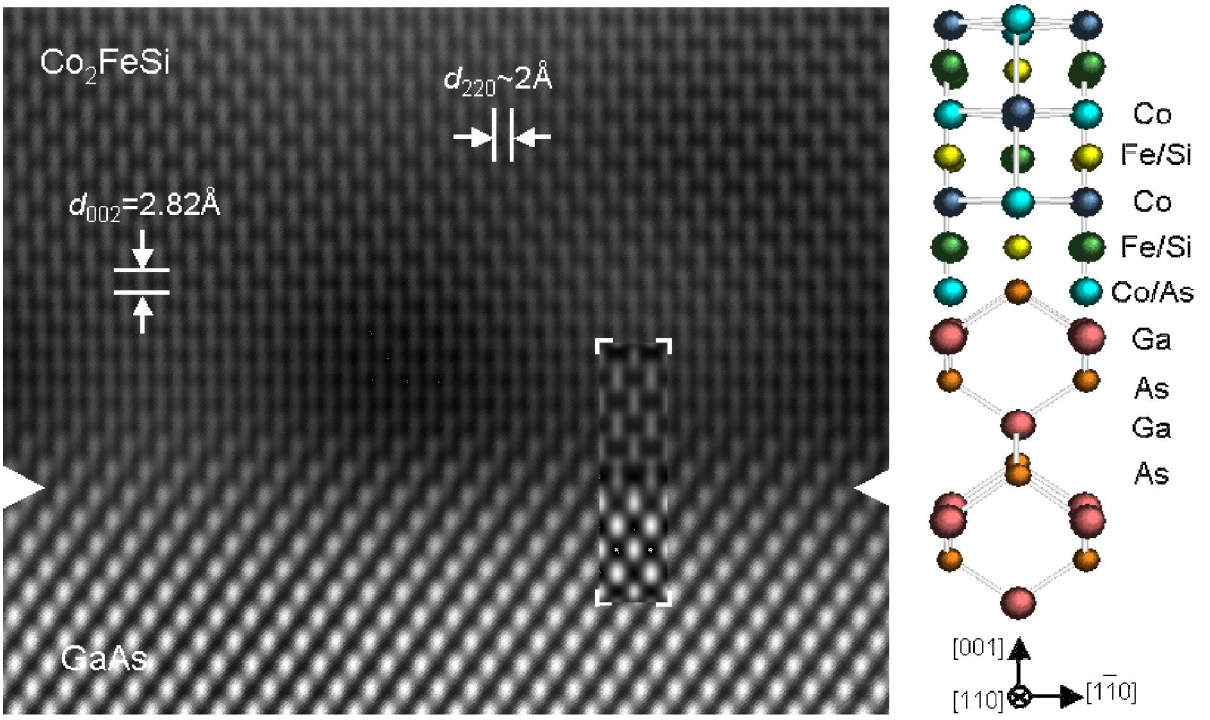

Abb. 19: Fouriergefilterte HRTEM-Aufnahmen im Querschnitt entlang der [110]-Richtung für eine Co_2FeSi/GaAs(001)-Schicht, die bei 300 °C gewachsen wurden. Die Simulationen der Grenzflächenanordnung mit einer Durchmischung von einer Atomlage (Modell rechts) ist als Einschub zum Vergleich gezeigt.

über den gesamten Bildausschnitt zeigt, dass ein Wachstum bei 300 °C ausreichend ist, um eine einheitlich geordnete Co_2FeSi Schicht zu erhalten. Andererseits zeigen unsere TEM-Untersuchungen auch, dass bei einer Wachstumstemperatur von 250 °C Grenzflächenreaktionen einsetzen.

Die atomare Anordnung der Co_2FeSi/GaAs-Grenzfläche wurde für eine bei 300 °C gewachsene Schicht untersucht. Auch die atomare Anordnung an der Grenzfläche wird als entscheidend für die Effizienz der Spininjektion in einen Halbleiter betrachtet. Auch hierfür wurden Kontrastsimulationen für drei verschiedene Modelle der $L2_1$-Co_2FeSi/As-terminierte-GaAs(001)-Grenzfläche durchgeführt. Hierbei handelt es sich um: (i) keine Durchmischung, (ii) Durchmischung in einer Atomlage und (iii) Durchmischung in zwei Atomlagen zwischen Co_2FeSi und GaAs. Im Ergebnis unserer Untersuchungen haben wir gefunden, dass das Interferenzbild der Grenzfläche am besten durch das Modell (ii) reproduziert wird (siehe Einschub

von Abb. 19). Dabei wird die unterste Atomlage des Co_2FeSi-Schicht mit der obersten As-Atomlage der GaAs-Schicht durchmischt. Schematisch ist das im rechten Teil der Abb. 19 dargestellt. In diesem Interferenzbild entspricht der weiße Kontrast den atomaren Positionen und der perfekten Anpassung der Co_2FeSi(220) und der GaAs(220) atomaren Ebenen. Das kann über die gesamte Grenzfläche gesehen werden. Solch eine Durchmischung kann einen starken Einfluss auf die Effizienz der Spininjektion haben und erfordert weitere experimentelle und theoretische Untersuchungen.

3.4. Temperung von Co_2FeSi/GaAs(001)-Hybridstrukturen

Der Einfluss einer nachträglichen Temperung auf die Eigenschaften der Co_2FeSi/GaAs(001)-Hybridstrukturen wurde detailliert untersucht. Hierzu wurde die stoichiometrische Co_2FeSi-Schicht bei einer Temperatur von 100°C gewachsen. Die Schichtdicke betrug 16 nm. Nach dem Wachstum wurden die Schichten in mehrere Teile gespalten und in einer Stickstoffatmosphäre bei Temperaturen zwischen 275 und 500 °C ex-situ getempert. Die Temperzeiten betrugen dabei 10, 30, 60 und 180 min.

Die Morphologie der Co_2FeSi-Oberfläche wurde mittels AFM untersucht. Abbildung 20 zeigt AFM-Aufnahmen der *as-grown* sowie der getemperten Schichten. Die Temperzeit betrug hierfür 10 min.

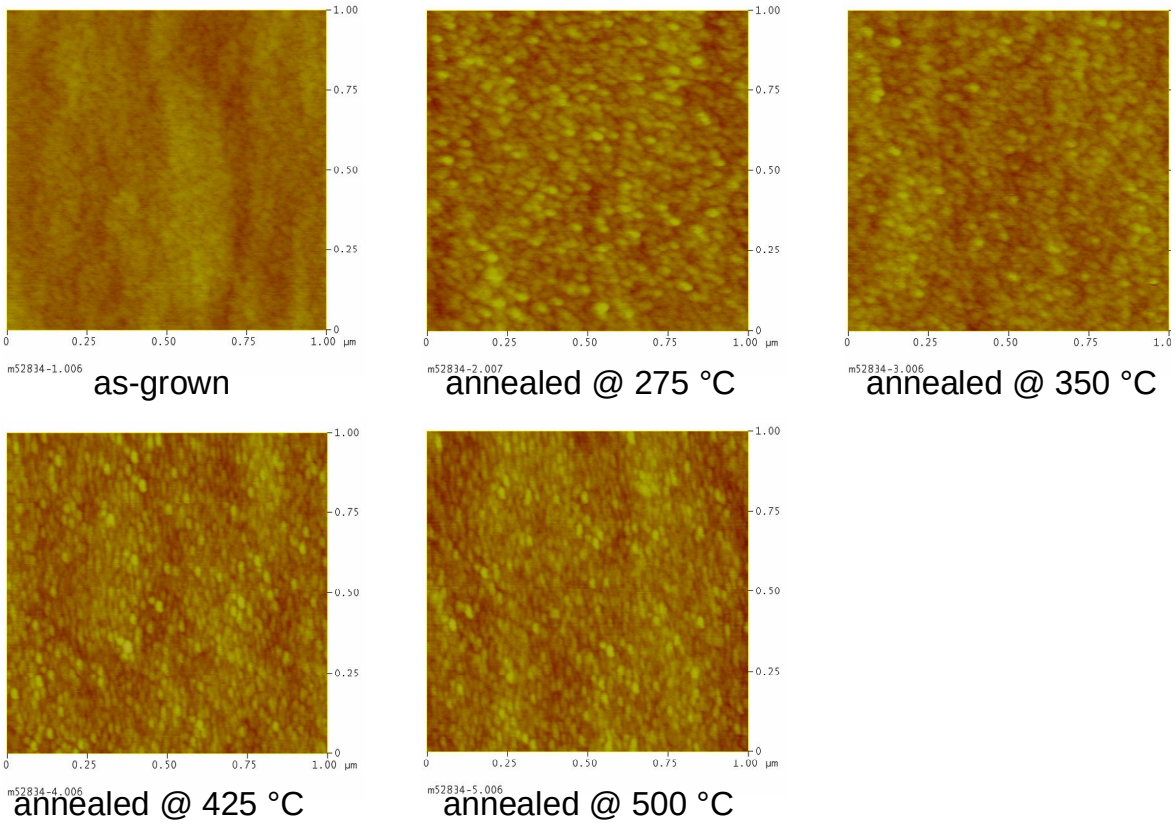

Abb. 20: AFM Aufnahmen von as-grown und getemperten Co_2FeSi-Oberflächen.

In den getemperten Schichten erkennt man kleine Partikel mit einem Durchmesser von ca. 20 nm. Die rms-Werte betragen 0.32 nm für die as-grown Probe und 0.45 nm für die getemperten Schichten. Obwohl die Rauhigkeit mit dem Temperschritt zunimmt, wird keine starke Beeinträchtigung der Oberfläche in Abhängigkeit von der Tempertemperatur beobachtet (zumindestens für eine Temperzeit von 10 min). Die rms-Werte für die bei 275 und bei 500°C getemperten Proben sind nahezu identisch.

Abbildung 21 zeigt Ergebnisse von XRD-Messungen, die mit offenen Detektor über einen weiten Winkelbereich durchgeführt wurden. Aufgrund der geringen Gitterfehlanpassung zwischen der Co_2FeSi- und der GaAs-Schicht (0.08%) überlappen die jeweiligen (002) und (004) Peaks. Bis auf die Kurve der bei 500°C getemperten Schicht sind alle Beugungsprofile identisch. Im Beugungsprofil der bei 500°C getemperten Probe tritt zusätzlich ein Peak bei $\omega = 17.3°$ (Pfeil) auf, der auch bei Proben auftrat, die bei Temperaturen über 350°C

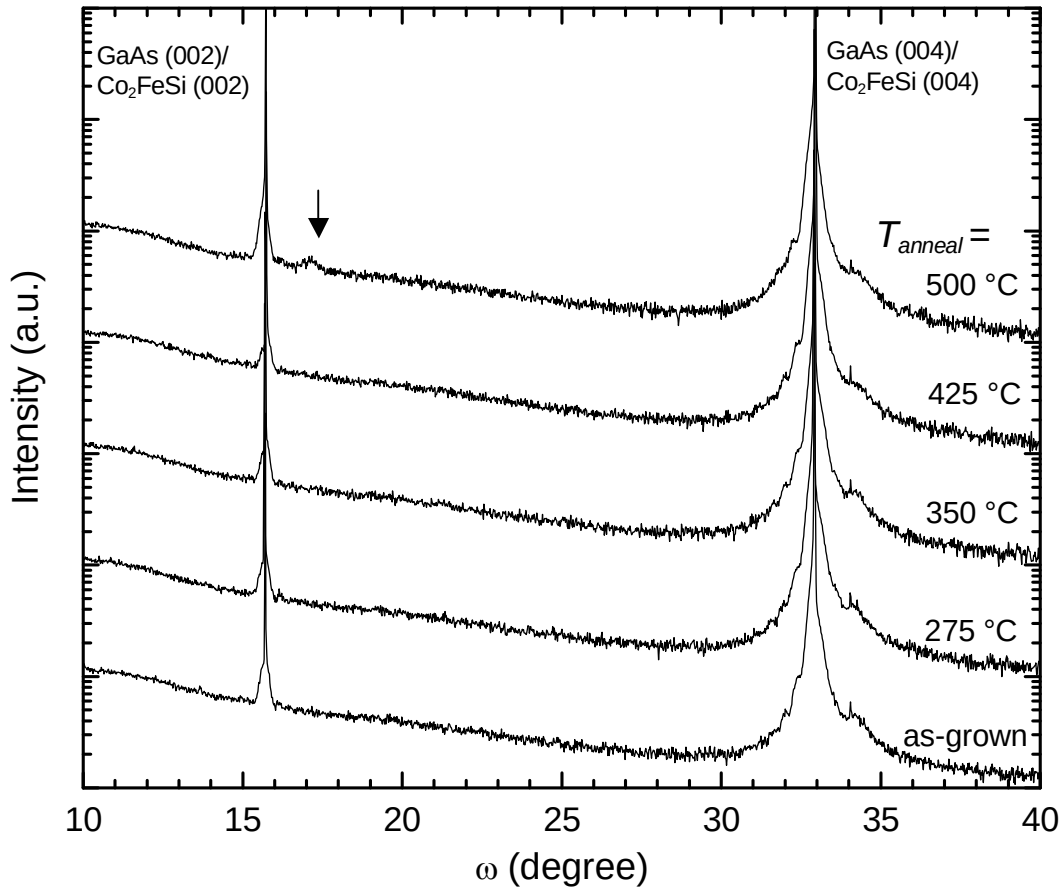

Abb. 21: Röntgenbeugungsprofile von as-grown und getemperten Co_2FeSi/GaAs-Hybridstrukturen.

gewachsen wurden. Wie im vorangegangenen Abschnitt gezeigt wurde, ist dieser Peak auf die Bildung von Reaktionsprodukten (CoAs) an der Grenzfläche zurückzuführen. Die Ergebnisse zeigen, dass die Co_2FeSi/GaAs(001)-Hybridstrukturen thermisch stabil bis zu ca. 475°C Temperung (10 min) sind. Allerdings sind Röntgenbeugungsexperimente nicht ausreichend um Grenzflächenreaktionen im Bereich von 1-2 Monolagen zu detektieren. Hierzu sind weitere TEM-Untersuchungen notwendig.

Zusätzliche Informationen kann man aus Widerstandmessungen der getemperten Schichten erhalten, da der Schichtwiderstand von der atomaren Ordnung der Schichten und von der Konzentration an Defekten abhängt. Der Schichtwiderstand wurde mittels van der Pauw-Proben bei Raumtemperatur (RT) und bei 77 K gemessen. Abbildung 22 zeigt die Abhängigkeit des Schichtwiderstands von der Tempertemperatur. Der Schichtwiderstand verringert sich leicht bei einer Tempertemperatur über 275°C. In vorausgegangenen Berichten hatten wir gezeigt, dass der Schichtwiderstand mit der atomaren Ordnung innerhalb der Co_2FeSi-Schicht korreliert ist. Die leichte Abnahme des Schichtwiderstands bei höheren Tempertemperaturen könnte deshalb ein Hinweis auf eine leicht erhöhte atomare Ordnung der Schicht sein. Hierzu sind jedoch weitere Untersuchungen zur Bestimmung der atomaren Ordnung notwendig.

Abbildung 23 zeigt die Abhängigkeit des Schichtwiderstands von der Temperzeit bei 425 und 500°C. Es zeigt sich, dass mit Zunahme der Temperzeit der Schichtwiderstand der Co_2FeSi-Schichten bei einer Tempertemperatur von 425°C konstant ist und bei 500°C nach der anfänglichen Verringerung wieder ansteigt. In Übereinstimmung mit den XRD-Untersuchungen zeigt das, dass bei einer Tempertemperatur von 500°C die Grenzflächenreaktionen mit

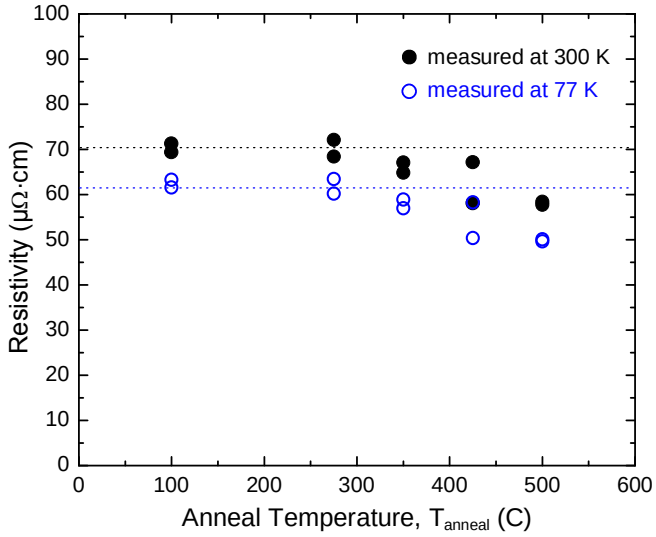

Abb. 22: Elektrischer Schichtwiderstand von as-grown und getemperten Co_2FeSi/GaAs-Hybridstrukturen. Die Temperzeit betrug 10 min.

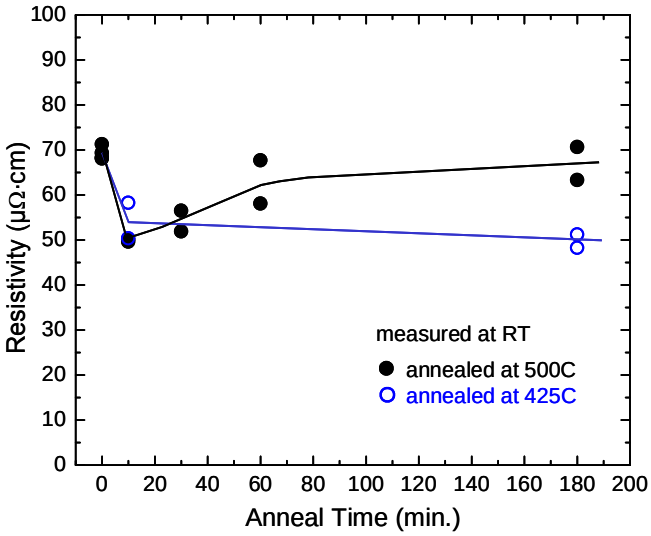

Abb. 23: Elektrischer Schichtwiderstand getemperten Co_2FeSi/GaAs-Hybridstrukturen in Abhängigkeit von der Temperzeit.

Zunahme der Temperzeit fortschreiten. Bezüglich der elektrischen Eigenschaften sind Co_2FeSi-Schichten, die bei 100°C gewachsen wurden, thermisch bei 425°C bis zu 180 min stabil.

Die magnetischen Eigenschaften der getemperten Schichten wurden mittels SQUID-Magnetometrie bei Raumtemperatur untersucht. Abbildung 24 zeigt die normierten Magnetisierungskurven der (a) as-grown Co_2FeSi/GaAs-Schicht und der bei 425°C (b) und 500°C getemperten Schichten. Das externe Magnetfeld wurde entlang der kristallographischen [110] und [-110]-Richtungen angelegt. Nach Abzug des diamagnetischen Beitrags der GaAs-

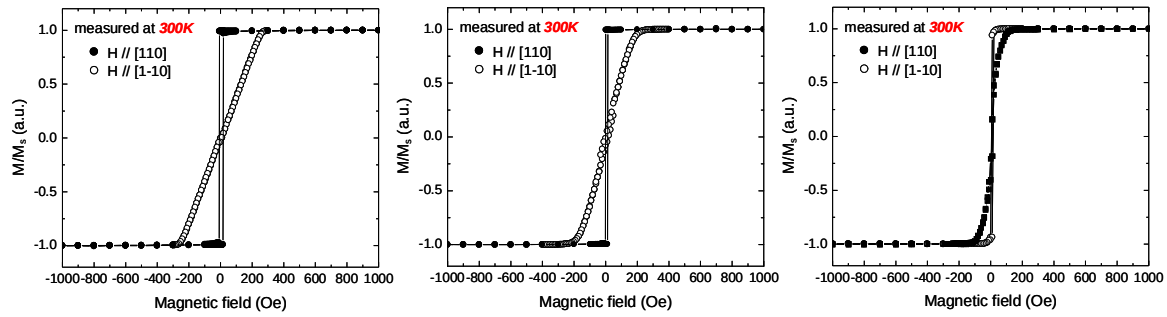

Abb. 24: Normierte Magnetisierungskurven der as-grown Co_2FeSi/GaAs-Schichten (links) sowie der jeweils 10 min getemperten Schichten bei 425 °C (Mitte) und 500 °C (rechts).

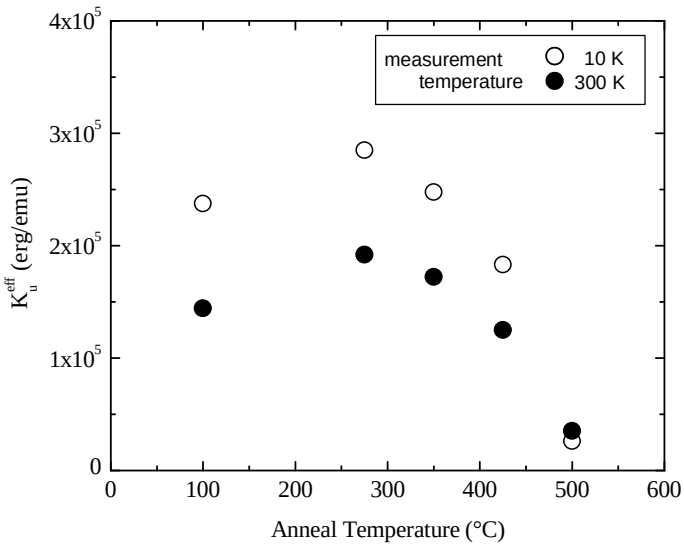

Abb. 25: Uniaxiale Anisotropiekonstante als Funktion der Tempertemperatur.

Schicht wurden die Kurven auf den Wert der Sättigungsmagnetisierung normiert. Die Magnetisierungskurven der Co_2FeSi/GaAs-Schichten unterhalb von 425°C sind rechteckig und zeigen ein klare Anisotropie, wobei die leichte (schwere) Achse der Magnetisierung entlang der [110]- ([-110]-) Richtung liegt. Auch bei den magnetischen Eigenschaften zeigen sich deutliche Änderungen erst bei der höchsten Tempertemperatur von 500°C, wo ein stärker isotropes Verhalten beobachtet wird.

Aus der Anpassung der Magnetisierungskurven kann man quantitativ die Anisotropiekonstanten für die uniaxiale Komponente K_U^{eff} und für die kubische Komponente K_1^{eff} unter der Annahme kohärenter Rotation des Ummagnetisierungsprozess bestimmen. Besonders interessant dabei ist K_U^{eff}, da sie ein reiner Grenzflächenterm ist, wie wir in den vorangegangenen Berichten zeigen konnten. Abbildung 25 zeigt die uniaxiale Anisotropiekonstante als Funktion der Tempertemperatur. Der Wert für K_U^{eff} ist nahezu konstant bis 425°C und verringert sich bei 500°C deutlich, wobei die Reduzierung wieder auf das Einsetzen der Grenzflächenreaktionen zurückzuführen ist.

Sekundärionen-Massenspektroskopie (SIMS) Untersuchungen sind durchgeführt worden, um den möglichen Diffusionsprozess von Co, Fe und/oder Si in das Substrat infolge des Temperns aufzuklären. Es zeigt sich (siehe Abschnitt 4), dass der Diffusionsprozess einen starken Einfluss auf die Ergebnisse zur Spininjektion hat.

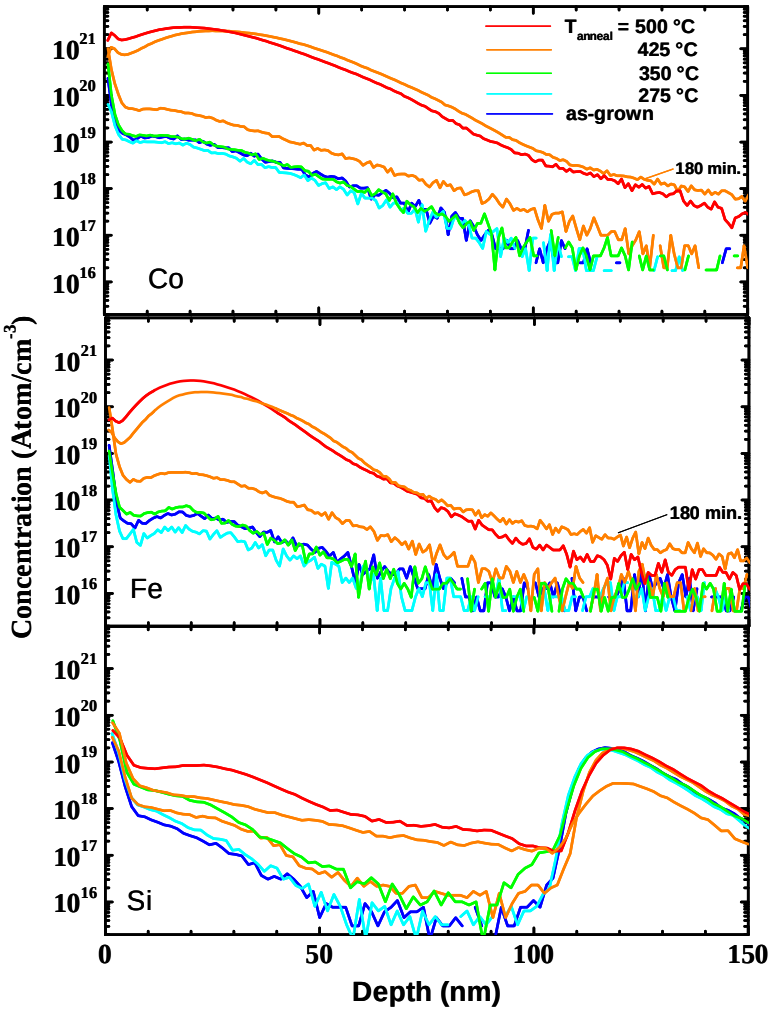

Abb. 26: Konzentrations-Tiefenprofil von Co (a), Fe (b) und Si (c) in Co_2FeSi-Schichten (bei 100 °C gewachsen) für verschiedene Temper-Temperaturen und -Zeiten. Die Messungen wurden mittels SIMS durchgeführt.

Das Ergebnis der SIMS-Messungen (Abb. 26) zeigt in Übereinstimmung mit vorhergehenden Untersuchungen, dass erst bei einer Temper-Temperatur von 425 °C ein leicht erhöhte Diffusion aller drei Elemente einsetzt, die sich bei weiterer Erhöhung der Temperatur oder einer Verlängerung der Temperzeit weiter verstärkt. Das zeigt, dass Co_2FeSi/GaAs(001)-Hybridstrukturen mindestens bis 350 °C thermisch stabil gegenüber einer Temperung sind.

Im Ergebnis der strukturellen, elektrischen und magnetischen Charakterisierung der getemperten Schichten kann festgestellt werden, dass die Schichten thermisch bis ca. 400°C stabil sind. Weitere Untersuchungen sind jedoch notwendig, um die tatsächliche Grenzflächenstruktur und den möglichen Diffusionsprozess von Co, Fe und/oder Si in das Substrat infolge des Temperns näher zu untersuchen. Es hat sich gezeigt, dass auch der Diffusionsprozess einen starken Einfluss auf die Ergebnisse zur Spininjektion hat.

4. Experimente zur Spininjektion mit Co_2FeSi als Injektormaterial

Die Untersuchungen im Abschnitt 3 haben gezeigt, dass infolge des Auftretens von Grenzflächenreaktionen für Wachstumstemperaturen über 250°C, die optimale Wachstumstemperatur von Co_2FeSi auf GaAs-Substraten um eine hohe Spininjektionseffizienz zu erzielen, bei ca. 200°C liegen sollte. Um den direkten Einfluss der Wachstumstemperatur der Co_2FeSi-Schicht auf die Effizienz zu untersuchen, haben wir mehrere *n-i-p* SpinLEDs mit Co_2FeSi-Injektor unterschiedlicher Wachstumstemperatur mittels MBE hergestellt. Die Proben bestehen aus einen Spindetektor, einen GaAs Quantengraben, der mit *n*- bzw. *p*-dotierten $Al_{0.1}Ga_{0.9}As$-Barriern umgeben ist und einer 9 nm dicken Co_2FeSi-Schicht, die bei 100°C (Probe 1), 200°C (Probe 2) und 300°C (Probe 3) gewachsen wurde.

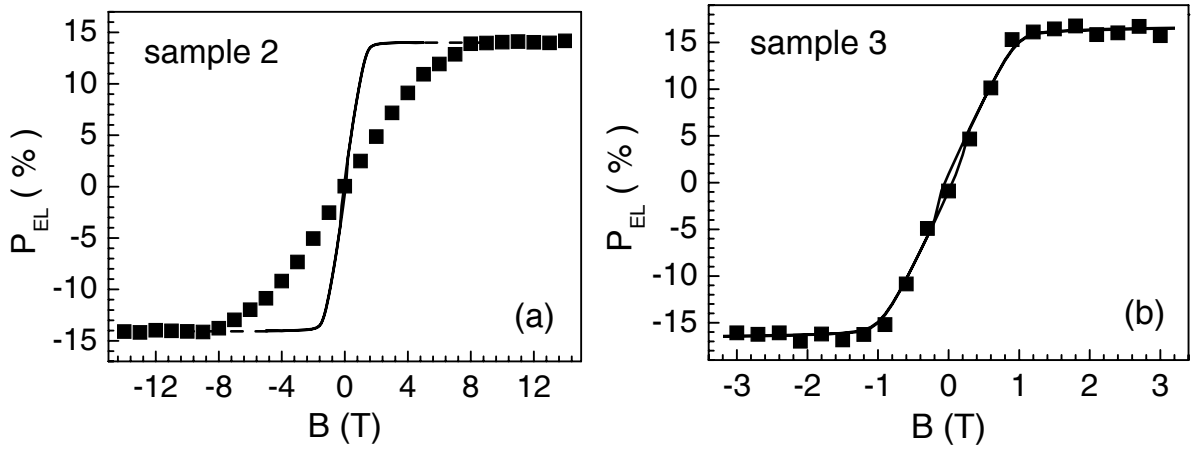

Abb. 27: .Zirkularer EL-Polarisationsgrad (Quadrate) als Funktion des externen Magnetfelds bei 20 K. Die Magnetisierung senkrecht zur Schichtebene (Linien) ist als Vergleich in beliebigen Einheiten hinzugefügt.

Die drei Proben zeigen stärkere Unterschiede in ihren elektro-optischen Charakteristika als man von den strukturellen Daten (TEM) erwarten konnte. Die Intensität der Elektrolumineszenz (EL) von Probe 1 war zu schwach um die Polarisation zu bestimmen. Die EL-Intensität der Proben 2 und 3 sind mehrere Größenordnungen höher, aber ihre Polarisationsdaten unterscheiden sich deutlich. Abbildung 27(a) und (b) zeigt den zirkularen Polarisationsgrad der EL der Proben 2 und 3. Die Magnetisierung senkrecht zur Schichtebene wurde unabhängig mittels SQUID-Magnetometrie bestimmt. Die Polarisation von Probe 2 folgt nicht dem Verlauf der Magnetisierungskurve der Co_2FeSi-Schicht und sättigt erst bei einem deutlich höheren Magnetfeld (8 T). Das könnte ein Indiz für einen paramagnetischen Injektor sein. Im Gegensatz dazu weist Probe 3 deutlich eine ferromagnetische Response auf, da die Polarisation der Magnetisierung im gesamten Magnetfeldbereich folgt. Der zirkulare Polarisationsgrad beträgt 17%. Eine Temperung von Probe 1 bei 300°C für 30 min führt zu einer EL-Intensität und einem Polarisationsverhalten, was nahezu identisch mit dem der ungetemperten Probe 3 ist.

Das komplexe Verhalten könnte im folgenden Bild verstanden werden. Bei einer Wachstumstemperatur von 100°C werden nichtstrahlende Defekte an der Grenzfläche generiert und verbleiben dort aufgrund der geringen Mobilität bei dieser tiefen Temperatur. Bei einer Wachstumstemperatur von 200°C setzt eine Diffusion von Co und Fe in die $Al_{0.1}Ga_{0.9}As$-Barriere ein. Abbildung 28 zeigt SIMS-Untersuchungen der tatsächlichen LED-Strukturen. Hierzu wurde zuvor die Co_2FeSi-Injektorschicht nasschemisch weggeätzt. Man erkennt eine deutliche Zunahme der Eindiffusion von Co, Fe und Si mit Erhöhung der Wachs-

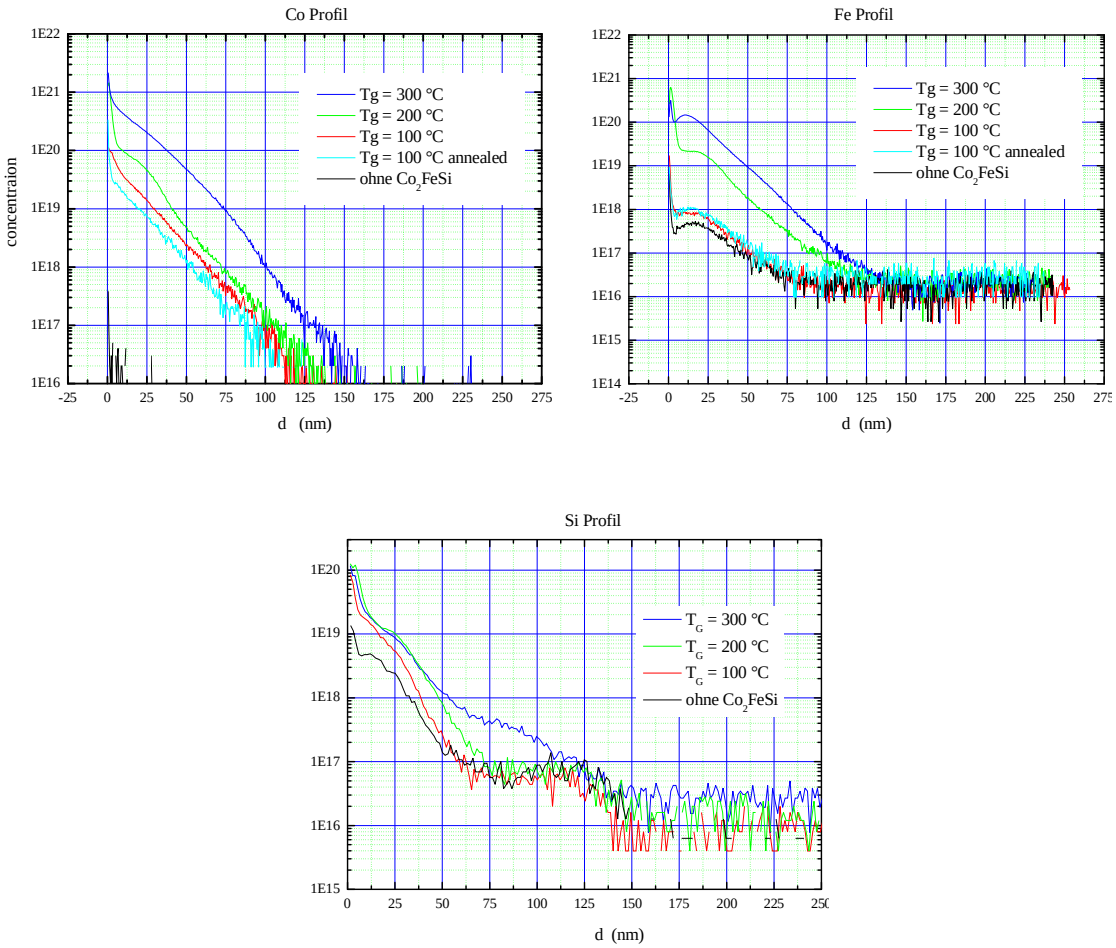

Abb. 28: SIMS-Profile der SpinLEDs, die bei unterschiedlichen Bedingungen hergestellt wurden.

tumstemperatur. Eine nachträgliche Temperung bei 300°C der bei 100°C gewachsenen Probe führt jedoch nicht zur einer erhöhten Diffusion. Bei Probe 2 besteht die Möglichkeit, dass die obere $Al_{0.1}Ga_{0.9}As$-Barriere infolge der stärkeren Diffusion in einen verdünnten magnetischen Halbleiter mit paramagnetischen Verhalten verwandelt wird. Bei einer Wachstumstemperatur von 300°C werden durch die beträchtliche Co-Diffusion CoAs Ausscheidungen gebildet (Siehe Abschnitt 3.3), was zu einem Entzug des Co aus der Matrix des verdünnten magnetischen Halbleiters führt und das ferromagnetische Verhalten erklären könnte. Weitere Untersuchungen sind jedoch notwendig um das beobachtete Verhalten besser verstehen zu können.

Um die tatsächliche Spininjektionseffizienz zu bestimmen, haben wir zeitaufgelöste Photoluminesenzuntersuchungen (PL) durchgeführt. Dazu wurde eine *n*-*i*-*n*-Referenzprobe mit identischer aktiver Region wie die SpinLEDs mittels MBE hergestellt. Abbildung 29(a) zeigt die polarisierten und unpolarisierten PL-Transienten dieser Probe. Der zirkulare Polarisationsgrad der Probe ist in Abb. 29(b) gezeigt. Die Analyse der Daten mit einem Model, dass Spinflip-Prozesse der Excitonen, der Elektronen und der Löcher berücksichtigt, ergibt für den Polarisationsgrad P = 17% eine Spininjektionseffizienz S = 51%. Dieser Wert ist niedriger als der theoretisch mögliche für ein perfektes Halbmetall (100%), ist jedoch eine Größenordnung höher als in unseren früheren Experimenten mit Fe-, MnAs- oder Fe_3Si-Spininjektoren. Ursache dafür kann auch hier die bereits oben erwähnte Diffusion magnetischer Verunreinigungen (Co, Fe) in die obere $Al_{0.1}Ga_{0.9}As$-Barriere sein. Diese Verunreinigungen stellen effiziente

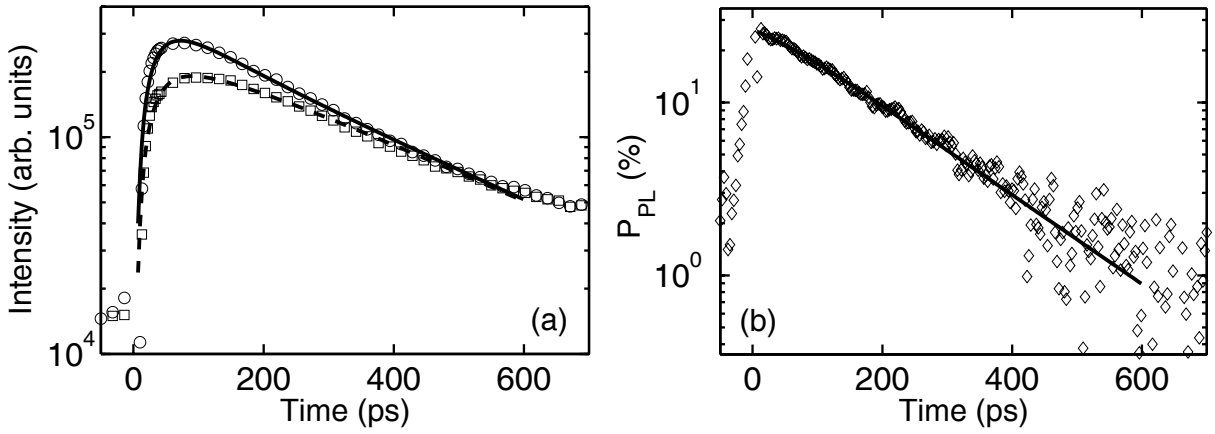

Abb. 29: (a) Polarisierte (Kreise) und unpolarisierte (Quadrate) PL Transienten der Referenzprobe bei zirkular polarisierter Anregung in der Barriere bei 20 K. (b) Abfall der zirkularen PL-Polarisation der Referenzprobe. Die Linien geben die simultane Anpassung des Messkurven mittels des im Text beschriebenen Modells.

Streuzentren für die spinpolarisierten Elektronen dar und können die ursprüngliche Spinpolarisation verringern bevor die Ladungsträger im Quantengraben rekombinieren.

5. Wachstum von Co_2FeSi-Schichten auf Si-Substraten

In Erweiterung zu den Wachstumsstudien von epitaktischen Co_2FeSi-Schichten auf GaAs(001) wurde das Wachstum auf Si(111)- und Si(001)-Substraten untersucht. Aufgrund der geringen Spin-Bahn-Streuung und der Inversionssymmetrie des Kristallgitters besitzt Si eine lange Spin-Lebensdauer und eine große Diffusionslänge der Elektronen. Diese Transportparameter bestimmen die Größenordnung der Kohärenz in Spintronik-Bauelementen. Mit seiner enormen Bedeutung in der Halbleiterindustrie ist Si daher auch für Spintronik-Anwendungen gut geeignet. Erst kürzlich (2007) gelang es, Spininjektion in Si nachzuweisen. Der Gitterabstand von Co_2FeSi (5.658 Å) weist gegenüber dem Si(001)-Substrat (5.431Å) allerdings eine recht große Fehlanpassung von 4% auf.

5.1. Wachstum auf Si(111)-Substraten

Die Si(111)-Substrate wurden vor dem Wachstum *in-situ* bei T_S = 500 °C für eine Minute mit Ga bedampft [Wright *et al.*, Appl. Phys. Lett. 36, 210 (1980)] behandelt. Hierbei reduziert ein Galliumatomstrahl Siliziumoxid auf der Siliziumoberfläche: $SiO_2 + 4\ Ga \Rightarrow Si + 2\ Ga_2O$ und bildet flüchtiges Galliumoxid. Anschließend wurden die Substrate für fünf Minuten bei T_S = 700 °C geheizt und dann auf die jeweilige Wachstumstemperatur abgekühlt. Bei allen Proben war vor Beginn des Wachstums im RHEED deutlich die für Si(111) typische 7×7-Rekonstruktion zu sehen. Auch das Wachstum wurde *in-situ* mittels RHEED überwacht. Die beobachteten Reflexe liegen nicht auf Laue-Kreisen sondern auf einer Geraden, was auf ein dreidimensionales Inselwachstum hinweist (Abb.30).

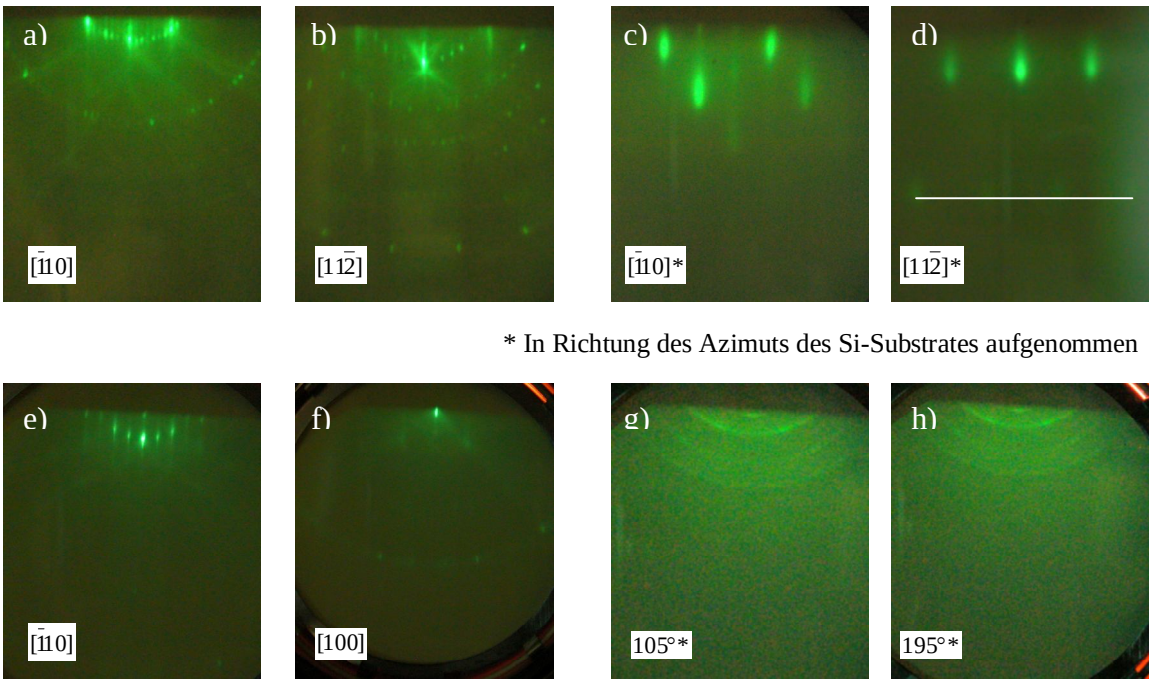

Abb. 30: RHEED Aufnahmen des Wachstums von Co_2FeSi auf Si(111) bzw. Si(001) bei T_S=200°C: a) und b) Si-(7x7)-Rekonstruktion vor dem Wachstum von Co_2FeSi auf Si(111); c) und d) Co_2FeSi nach dem Wachstum; e) und f) Si-(2x1)-Rekonstruktion vor dem Wachstum von Co_2FeSi auf Si(001). Nach dem Wachstum sieht man in g) und h) Ringe, welche auf polykristallines Co_2FeSi hinweist.

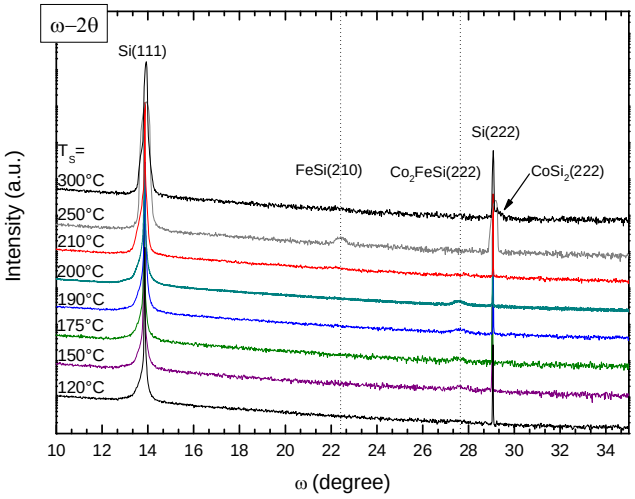

Abb. 31: XRD-Kurven des symmetrischen (222)-Reflexes in Abhängigkeit von der Wachstumstemperatur T_S. Für die Proben bei Wachstumstemperaturen zwischen $T_S = 150$ °C und $T_S = 200$ °C sind deutlich Co_2FeSi(222)-Reflexe zu erkennen. Dies weist auf Ordnung mindestens in der *B2*-Struktur hin.

Untersuchungen mittels Röntgenbeugung (XRD) zeigen, dass nur in einem relativ schmalen Temperaturfenster zwischen $T_S = 150$ °C und $T_S = 200$ °C geordnete Co_2FeSi-Schichten aufwachsen (Abb. 31). Das Auftreten des Co_2FeSi(222)-Reflexes weist auf eine Ordnung mindestens in der *B2*-Struktur hin. Bei höheren Wachstumstemperaturen setzen starke Grenzflächenreaktionen ein. Beim 250 °C-Film ist ein zusätzlicher Beugungsreflex zu sehen, der einem FeSi(210)-Reflex zugeordnet werden kann. Beim 300 °C-Film tritt ein Beugungsreflex des $CoSi_2$(222) auf. Bei niedriger Temperatur ($T_S = 120$ °C) konnte keine gute strukturelle Ordnung der Heusler-Legierung erreicht werden, was sich in der Abwesenheit des Beugungsreflexes der Schicht zeigt. Die gemessene Differenz zwischen den Co_2FeSi(222)- und den Si(222)-Reflexen betrug $\Delta\Theta_B \approx 1{,}43°$ und war somit größer als die theoretische Differenz von $\Delta\Theta_B = 1{,}29°$. Das bedeutet, dass die Schichten in vertikaler Richtung zwar teilweise relaxiert aber immer noch verspannt sind.

Der Einfluss der Wachstumstemperatur auf die Oberflächenmorphologie der gewachsenen Schichten wurde mittels AFM untersucht (Abb. 32). Alle Aufnahmen zeigen einen Größenbereich von 1,5×1,5 µm². Man erkennt deutlich, dass bei höheren Wachstumstemperaturen $T_S = 250$ °C und $T_S = 300$ °C höhere Rauigkeiten und damit einhergehend starke Grenzflächenreaktionen einsetzen. Die bei $T_S = 200$ °C gewachsene Schicht hat die niedrigste Rauigkeit mit rms = 0,765 nm. Diese Ergebnisse werden von den XRD-Untersuchungen bestätigt.

Den Einfluss der Wachstumstemperatur auf die magnetischen Eigenschaften von Co_2FeSi/Si(111) illustriert Abb. 33. Die Hysterese-Kurven wurden bei $T = 10$ K mit einem SQUID-Magnetometer mit dem externen Magnetfeld entlang der $[2\bar{1}\bar{1}]$- und $[0\bar{1}\bar{1}]$-Richtungen gemessen. Alle Schichten zeigen ferromagnetisches Verhalten. Eine Bestimmung der Sättigungsmagnetisierung ist aufgrund des schwer bestimmbaren Volumens der Schichten schwierig. Aufgrund der einsetzenden Grenzflächenreaktionen ist die Form der Hysterese-Kurve für die Schicht mit $T_S = 300$ °C gegenüber denen der Schichten bei $T_S \leq 200$ °C deutlich verändert und zeigt eine stärkere Temperaturabhängigkeit.

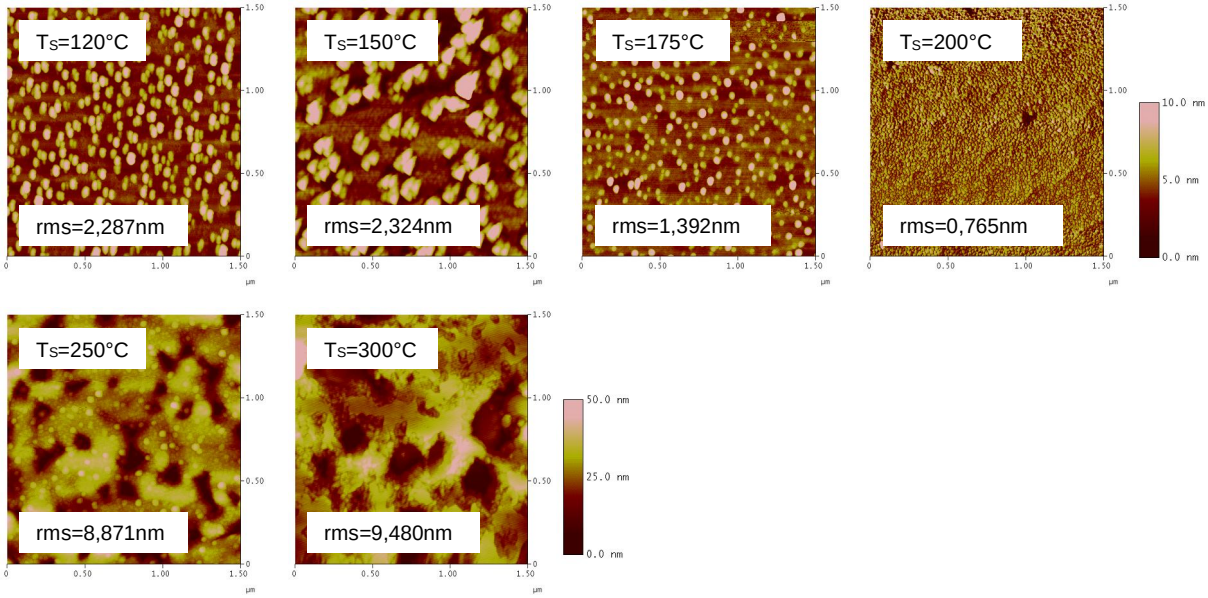

Abb. 32: AFM-Aufnahmen nach dem Wachstum von Co_2FeSi auf Si(111) in Abhängigkeit von der Wachstumstemperatur T_S. Man erkennt deutlich, dass bei höheren Wachstumstemperaturen T_S = 250 °C und T_S = 300 °C starke Grenzflächenreaktionen einsetzen. Die bei T_S = 200 °C gewachsene Schicht hat die niedrigste Rauhigkeit mit rms = 0,765 nm.

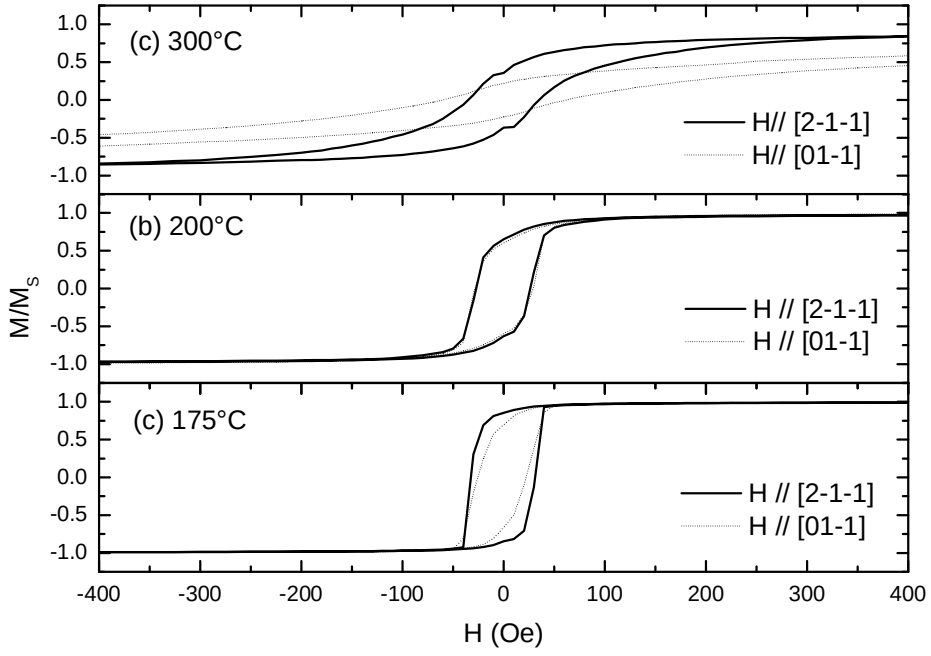

Abb. 33: SQUID-Hysteresekurven aufgenommen bei T = 10 K mit dem Magnetfeld entlang der $[2\bar{1}\bar{1}]$- und $[01\bar{1}]$-Richtungen von verschiedenen, bei den angegebenen Wachstumstemperaturen hergestellten Co_2FeSi/Si(111)-Schichten. Der diamagnetische Betrag des Substrates ist subtrahiert. Man erkennt ein ferromagnetisches Verhalten der Schichten. Bei T_S = 300 °C ist die Hysterekurve gegenüber denen der Schichten bei $T_S \leq 200$ °C deutlich verändert.

5.2. Wachstum auf Si(001)-Substraten

Die Si(001)-Substrate wurden vor dem Wachstum zweimal *in-situ* bei T_S = 500 °C eine Minute mit Ga behandelt und anschließend fünf Minuten bei T_S = 900 °C geheizt. Nach dem Abkühlen auf die Wachstumstemperatur war bei allen Proben im RHEED die für Si(001) typische (2×1)-Rekonstruktion zu erkennen. Das Wachstum wurde *in-situ* mit RHEED überwacht. Nach fünfminütigem Wachstum waren Ringe zu sehen, die auf ein polykristallines Wachstum hinweisen (Abb.30).

Der Einfluss der Wachstumstemperatur auf die Oberflächenmorphologie der gewachsenen Co_2FeSi-Schichten wurde mittels AFM untersucht (Abb. 34). Alle Aufnahmen zeigen einen Größenbereich von 1,5×1,5 μm².

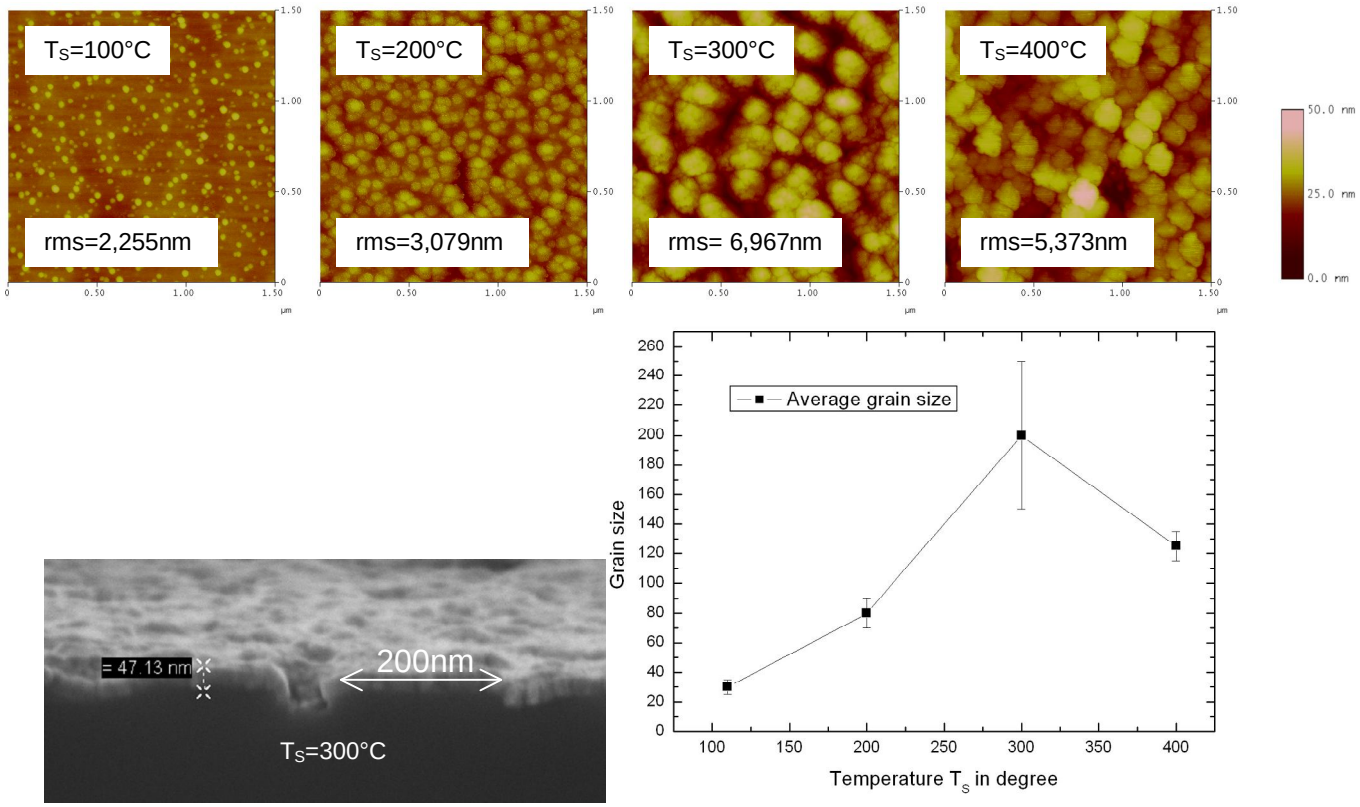

Abb. 34: AFM-Aufnahmen nach dem Wachstum von Co_2FeSi auf Si(001) in Abhängigkeit von der Wachstumstemperatur T_S. Die Rauhigkeit der gewachsenen Schichten ist wesentlich höher als bei den auf Si(111)-Substraten ($T_S \leq 200$ °C) gewachsenen Proben. Die Größe der polykristallinen Körner nimmt bis T_S = 300 °C mit der Wachstumstemperatur zu.

Die Rauhigkeit der Co_2FeSi/Si(001)-Schichten ist wesentlich höher als bei den auf Si(111)-Substraten ($T_S \leq 200$°C) gewachsenen Proben. Die Größe der polykristallinen Körner nimmt bis T_S = 300 °C mit der Wachstumstemperatur zu.

Untersuchungen mittels XRD zeigten, dass nur bei niedriger Wachstumstemperatur (T_S = 100 °C) ein Co_2FeSi(220)-Beugungsreflex auftritt (Abb. 35).

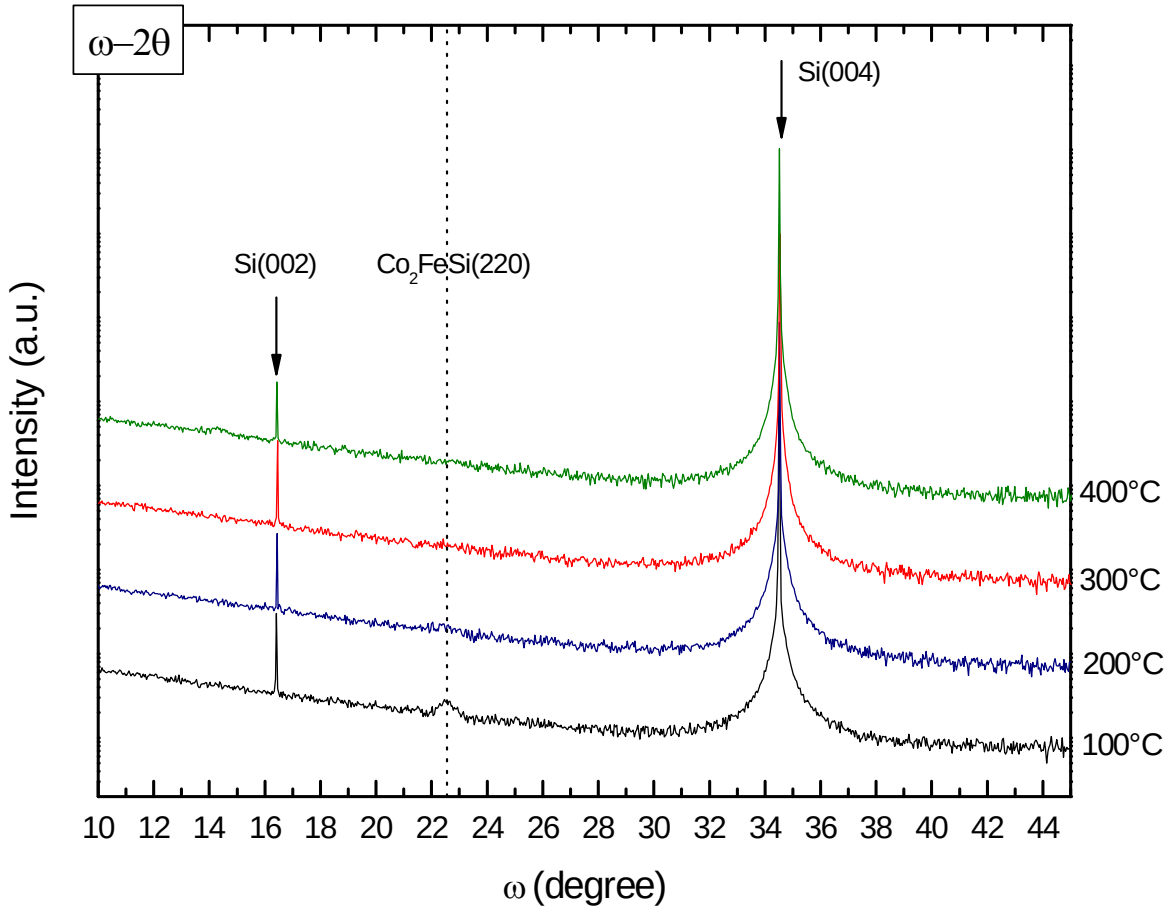

Abb. 35: XRD-Kurven des symmetrischen (004)-Reflexes in Abhängigkeit von der Wachstumstemperatur T_S. Für T_S = 100 °C ist ein Co_2FeSi(220)-Reflex zu erkennen.

6. Magnetische Nanostrukturen

Einen weiteren Schwerpunkt dieses Forschungsprojekts stellte die Herstellung und Charakterisierung von regelmäßigen Anordnungen magnetischer Nanostrukturen dar. In Fortführung der Studien von lithographisch präparierten Fe-Nanostrukturen (BMBF-Projekt 13N8255) wurden MnAs-Nanostrukturen präpariert und bezüglich ihrer magnetischen Eigenschaften charakterisiert. MnAs Filme auf GaAs(001) stellen vielerlei Hinsicht ein Modellsystem in dar. Zum einen weisen sie eine sehr starke uniaxiale Anisotropie in der Filmebene auf, die besonders in technologischen Anwendungen angestrebt wird. Zum anderen liegt magnetische Ordnungstemperatur etwa bei 40°C, was die Untersuchung phasenübergangs-relevanter Phänomene erleichtert. Eine zusätzliche Besonderheit von MnAs ist die Kopplung des magnetischen Phasenübergangs an einen strukturellen, die eine selbstorganisierte Musterbildung in dünnen Filmen zur Folge hat. Der gekoppelte Phasenübergang verläuft nach erster Ordnung und ist für magnetische Phasenübergänge unüblich.

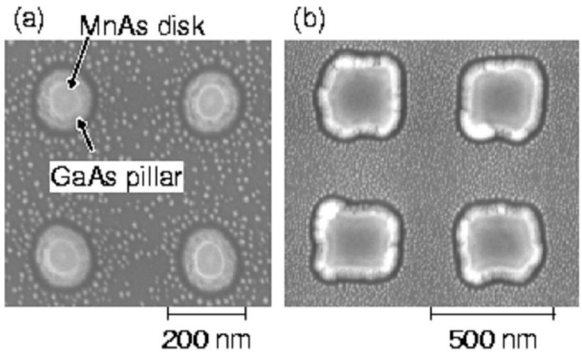

Abb. 36: Rasterelektronenmikroskopische Aufnahmen von MnAs-Quantenpunkten, die aus einem 50 nm dicken Film auf GaAs(001) hergestellt wurden. Der Teilchendurchmesser beträgt in a) 100 nm und b) 200 nm; man beachte, dass die Nanostrukturen auf kleinen GaAs-Säulen sitzen.

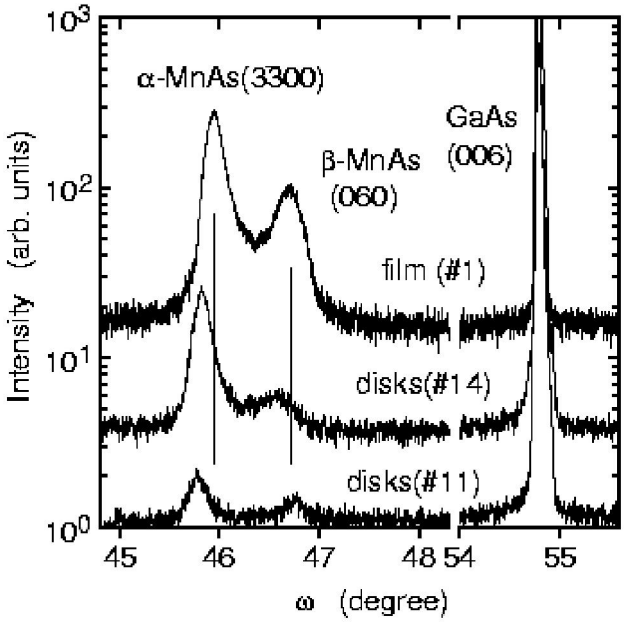

Abb. 37: ω–2θ-Röntgenbeugungskurven eines 50 nm dicken MnAs-Filmes auf GaAs(001) (Probe #1) sowie von daraus lithographisch hergestellten MnAs-Nanostrukturen: Der Teilchendurchmesser beträgt 430 nm für Probe #14 und 100 nm für Probe #11.

Abbildung 36 zeigt zwei Beispiele von MnAs-Nanostrukturen auf GaAs(001), die mittels Elektronenstrahllithographie und Ar-Sputtern aus einem 50 nm dicken MnAs/GaAs(001)-

Film hergestellt wurden. Die mittlere Teilchengröße beträgt 100 nm in Abb. 36a und 200 nm in Abb. 36b (man beachte, dass die Nanostrukturen auf kleinen GaAs-Säulen sitzen). Für alle untersuchten Proben weisen die bei 29°C aufgenommenen ω–2θ-Röntgenbeugungskurven Maxima von ferromagnetischem, hexagonalem α-MnAs und antiferromagnetischem, orthorhombischem β-MnAs auf (vgl. Abb. 37), die bei dieser Temperatur koexistieren. Die Verschiebung der Position des α-MnAs-Maximums im Falle der Nanostrukturen weist auf eine teilweise Relaxation der mit dem strukturellen Phasenübergang verbundenen Gitterverzerrungen hin.

Abbildung 38(b) zeigt Magnet-Kraftmikroskopie (MFM)-Aufnahmen einer Anordnung von 170 nm großen MnAs-Nanostrukturen nach Abkühlen von 60°C, wo MnAs in der antiferromagnetischen β-Phase vorliegt. Die Struktur der Teilchen ist zum Vergleich in Abb. 38(a) dargestellt. Aus dem hell/dunkel-Kontrast der MFM-Aufnahmen lässt sich die in Abb. 38(c) illustrierte magnetische Domänenstruktur ableiten. Die 170 nm großen Teilchen weisen eine oder zwei magnetische Domänen auf, wobei die leichte Magnetisierungsachse wie in den dünnen MnAs-Filmen parallel zur *a*-Achse in der Filmebene liegt. Von 44 Teilchen waren 23 in der antiparallelen zweidomänigen Konfiguration, 20 weitere waren eindomänig mit der Magnetisierung von je 10 Teilchen nach links bzw. rechts gerichtet, ein Teilchen zeigte keinen Kontrast mit MFM (siehe unten). Das einheitliche Höhenprofil der Teilchen in den Kraftmikroskopie (AFM)-Aufnahmen legt den Schluss nahe, dass die mit XRD detektierte

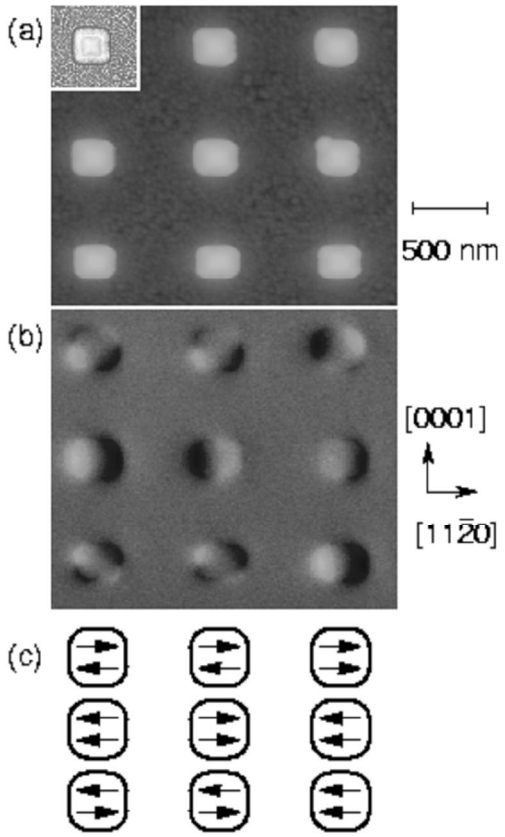

Abb. 38: a) Kraftmikroskopie- und b) Magnet-Kraftmikroskopie-Aufnahmen einer Anordnung von 170 nm großen MnAs-Nanostrukturen bei 25°C; das Bild links/oben zeigt eine typische Rasterelektronenmikroskopie-Aufnahme eines MnAs-Teilchens. c) Die aus dem hell/dunkel-Kontrast von b) ableitbare magnetische Domänenstruktur.

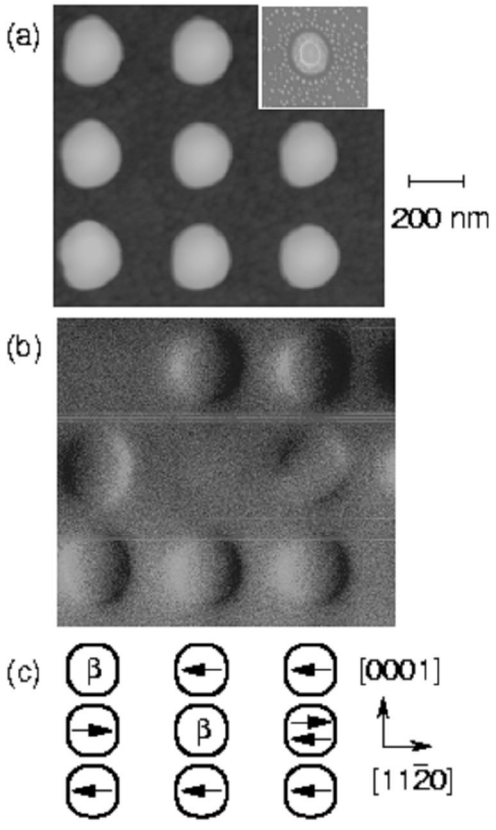

Abb. 39: a) Kraftmikroskopie- und b) Magnet-Kraftmikroskopie-Aufnahmen einer Anordnung von 100 nm großen MnAs-Nanostrukturen bei 25°C; das Bild rechts/oben zeigt eine typische Rasterelektronenmikroskopie-Aufnahme eines MnAs-Teilchens. c) Die aus dem hell/dunkel-Kontrast von b) ableitbare magnetische Domänenstruktur.

antiferromagnetische β-Phase nicht an der Oberfläche vorliegt sondern im Innern der Teilchen eingebettet ist.

Wenn die Teilchengröße auf 100 nm reduziert wird (Abb. 39), steigt die Zahl der eindomänigen Teilchen drastisch an. Von 50 ausgewerteten Teichen waren 32 Teilchen eindomänig und nur 10 zweidomänig. Obwohl deutlich in den AFM-Aufnahmen sichtbar (Abb. 39a), erscheinen einige der Teilchen in den MFM-Aufnahmen nicht [Abb. 39(b)]. Offensichtlich weisen diese Teilchen keinen magnetischen Kontrast auf und repräsentieren MnAs-Teilchen in der antiferromagnetischen β-Phase. Der Anteil dieser Teilchen entspricht etwa 2/3 des mit XRD detektierten β-MnAs. Wir schließen daraus, dass auch die eindomänigen magnetischen Teilchen überwiegend aus reinem α-MnAs bestehen. Sobald die Teilchengröße unterhalb von 100 nm liegt, wird der Phasenkoexistenz offensichtlich durch einphasige Nanostrukturen Rechnung getragen, die entweder aus reinem α-MnAs oder aus reinem β-MnAs bestehen und nebeneinander vorliegen. Das beobachtete Verhalten ist übrigens durch den Phasenübergang erster Ordnung von MnAs bedingt, bei dem bekanntlich die Kinetik durch den Keimbildungsprozess bestimmt wird.

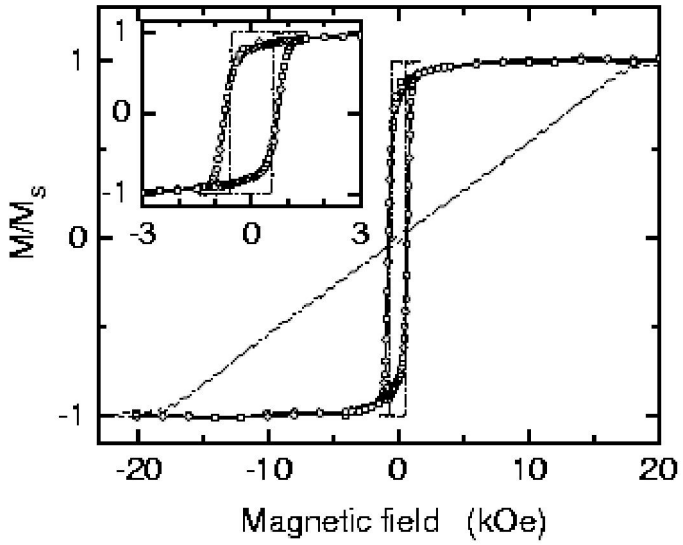

Abb. 40: SQUID-Hysteresekurven entlang der leichten Magnetisierungsrichtung (*a*-Achse in der Filmebene) einer Anordnung von MnAs-Nanostrukturen mit einer Teilchengröße von 100 nm (ausgezogene Linie mit Kreisen). Zum Vergleich sind auch die Hysteresekurven des für die Lithographie verwendeten 50 nm dicken MnAs-Films entlang der leichten (*a*-Achse) und schweren (*c*-Achse) Magnetisierungsrichtung dargestellt. Der Einschub zeigt die Hystereskurven mit höherer Auflösung.

Abbildung 40, ausgezogene Linie mit Kreisen, zeigt eine SQUID-Hysteresekurve einer Anordnung von MnAs-Nanostrukturen mit einer Teilchengröße von 100 nm. Die Messung erfolgte bei einer Temperatur von 20°C und dem Magnetfeld entlang der leichten Magnetisierungsrichtung (*a*-Achse in der Filmebene). Zum Vergleich beinhaltet Abb. 40 auch die Hysteresekurven des für die Lithographie verwendeten 50 nm dicken MnAs-Films entlang der leichten (*a*-Achse) und schweren (*c*-Achse) Magnetisierungsrichtung. Man beachte die große magnetokristalline Anisotropie des MnAs-Films, die den eindomänigen Zustand gegenüber einem Vortex-Zustand stabilisiert. Interessanterweise ist die Koerzivität der Nanostrukturen vergleichbar mit der des Films, wobei die remanente Magnetisierung nur um etwa 20% kleiner ist als der Sättigungswert.

Weiterhin haben wir den Umkehrprozess der magnetischen Momente der MnAs-Nanostrukturen untersucht. Die zeitliche Relaxation lässt sich durch drei exponentielle Abfälle beschreiben (Abb. 41). Der auf der stochastischen Natur des Phasenübergangs 1. Ordnung

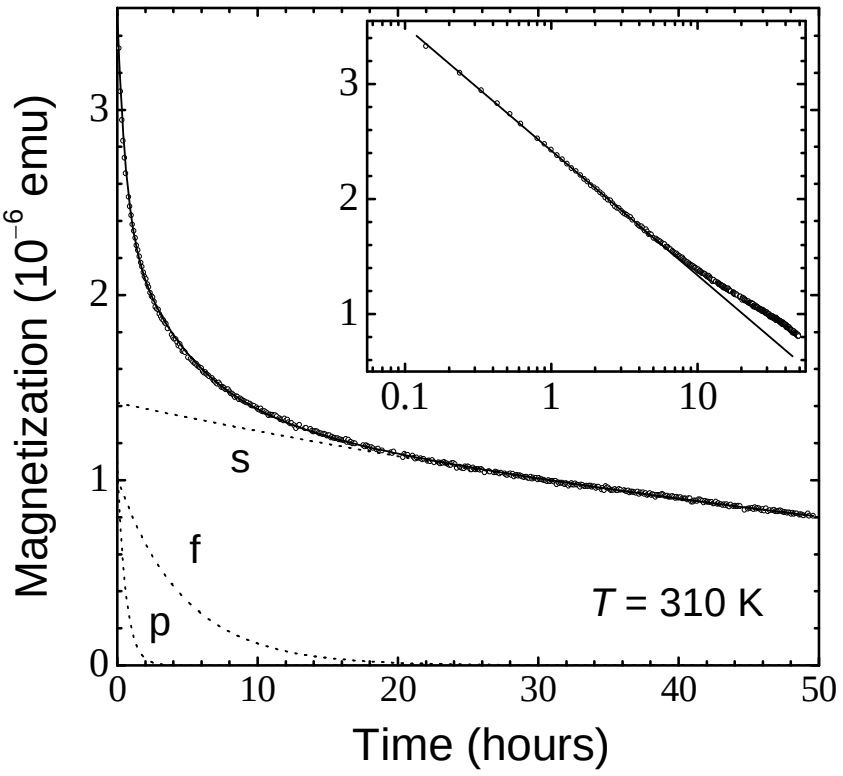

Abb. 41: Abfall der remanenten Magnetisierung in MnAs-Nanostrukturen (Durchmesser 100 nm) bei 310°C. Vor der Messung wurden die MnAs-Nanostrukturen in einem Magnetfeld von 20 kOe magnetisiert. Die Kugeln stellen die experimentellen Ergebnisse dar und die durchgezogenen Linie ist die Anpassung mit dreifach exponentiellem Abfall. Die individuellen Abfälle mit den Zeitkonstanten τ_p = 0.59 h, τ_f = 4.65 h und τ_s = 88 h sind als gestrichelte Linien dargestellt. Der Einschub zeigt die logarithmische Zeitabhängigkeit der Magnetisierung. Die Abweichung vom erwarteten logarithmischen Verhalten macht eine Analyse der Daten mit mehreren exponentiellen Abfällen notwendig.

beruhende Beitrag liefert die kürzeste charakteristische Zeitkonstante. Die mittlere Zeitkonstante ist vermutlich sehr stark an die thermische Hysterese des Phasenübergangs gekoppelt, obwohl eine direkte Verknüpfung nicht abgeleitet werden kann. Dieser Relaxationsprozess ist möglicherweise auf die Umkehr der magnetischen Momente durch virtuelle Phasenübergangsprozesse zurückzuführen. Die Relaxationseigenschaften hängen dabei stark von thermischen Zyklen als auch vom Anlegen eines Magnetfeldes (durch magnetfeldinduzierte Phasenübergänge) ab.

7. Unterprojekt mit der Johannes-Kepler-Universität Linz

Durch die Berufung des ursprünglichen Projektleiters (R. Koch) nach Linz wurde ein Teil der im Antrag formulierten Untersuchungen im August 2007 als Unterprojekt an die Johannes-Kepler-Universität vergeben, insbesondere da deren Durchführung in der nach Linz transferierten multifunktionalen MBE-Anlage geplant war. Dazu zählen insbesondere die Ermittlung der Wachstumsspannungen der Ferromagnet-Halbleiter Strukturen auf GaAs(001) kombiniert mit magnetischen Untersuchungen mit dem Biegebalkenmagnetometer, die Entwicklung eines Messverfahrens für die in situ Bestimmung des Magnetowiderstands von magnetoresistiven Elementen der entwickelten Schichtsysteme sowie die Herstellung eines Demonstrators für ein frei-programmierbares magnetologisches Element. Der experimentelle Nachweis für die Funktionsfähigkeit frei-programmierbarer magnetologischer Elemente wurde im Verlauf des Projektes durch Wang et al. [J. Appl. Phys. **97,** 10D509 (2005)] in der Literatur beschrieben. Zudem wurden durch die Markteinführung des 4 MBit MRAM-Chips Ende 2006 durch Freescale, heute Everspin Technologies [www.everspin.com] und der Weiterentwicklung zum 16 MBit MRAM-Chip im Jahr 2009 mittlerweile wesentliche Schritte des technologischen Prozesses für frei-programmierbare magnetologische Elemente gelöst, deren Aufbau der MRAM-Speicherzelle sehr ähnlich ist. Daher wurde im Rahmen dieses Projektes die Entwicklung eines Demonstrators zurückgestellt. Im Folgenden werden die Ergebnisse zu den beiden anderen Punkten vorgestellt.

7.1 Mechanische Spannungen und magnetische Eigenschaften von Fe/GaAs(001)

Die in Abschnitt 3.4 vorgestellten Untersuchungen zeigen, dass bei den bei höheren Temperaturen hergestellten Co_2FeSi Filmen eine starke Diffusion von Co und Fe in das GaAs(001)-Substrat einsetzt, welche die Spininjektion in den Halbleiter entscheidend beeinflusst. Da eine frühere Studie von Fe-/GaAs(001) gezeigt hat, dass die mechanischen Filmspannungen ein sehr empfindlicher Sensor für Interdiffusionsvorgänge sind, wurden entsprechende temperaturabhängige Experimente an den Systemen Fe/GaAs(001) und Fe_3Si/ GaAs(001) durchgeführt, um schichtdickenabhängige Information zu erhalten.

Abbildung 42 illustriert das Spannungsverhalten von zwei Fe-Schichten, die auf unterschiedlich präparierten GaAs(001)-Substraten aufgedampft wurden. Film A wurde im Rahmen dieses Projekts auf eine unter Standardbedingungen präparierte GaAs-Probe abgeschieden, wobei der Transfer in die zugehörige Metall-MBE-Kammer unter UHV-Bedingungen erfolgte. Die Filmkraftkurve von Film B stammt von der früheren Studie [Appl. Phys. Lett. **78**, 1270 (2001)]. Film B wurde auf eine GaAs-Probe abgeschieden, die zwar nach dem MBE-Standardverfahren präpariert und mit einer As-Deckschicht versehen wurde, dann aber belüftet und in eine Metall-MBE-Anlage transferiert wurde, wo dann die As-Deckschicht vor der Fe-Aufdampfung wieder desorbiert wurde. Für die Darstellung der mechanischen Spannungen ist in den folgenden Diagrammen die mit dem Biegebalkenverfahren in Echtzeit gemessene Filmkraft (= Kraft F pro Einheitsbreite w der Filme) als Funktion der mittleren Schichtdicke (t) aufgetragen. Die instantane Filmspannung (=Kraft pro Fläche, F/A) ist durch den jeweiligen Anstieg der Filmkraftkurven gegeben (= $(F/w)/t = F/A$).

Die beiden Filme auf den unterschiedlich präparierten GaAs(001)-Substraten unterscheiden sich deutlich in ihrem Spannungsverhalten. In Film A dominiert im Dickenbereich zwischen 1 – 10 nm ein Zugspannungsbeitrag, der auf Grenzflächenreaktionen und Interdiffusionsvorgänge hinweist [siehe detaillierte Diskussion in Appl. Phys. Lett. **78**, 1270 (2001)]. Erst bei Schichtdicken größer al 10 nm wird dann ein Druckspannungsbeitrag detektiert, der auf die Gitterfehlanpassung (Misfit) zwischen Fe und GaAs zurückgeführt werden kann (Gitterkonstanten: $a_{GaAs}/2 = 0.283$ nm, $a_{Fe} = 0.287$ nm). Der Betrag der mechanischen Spannun-

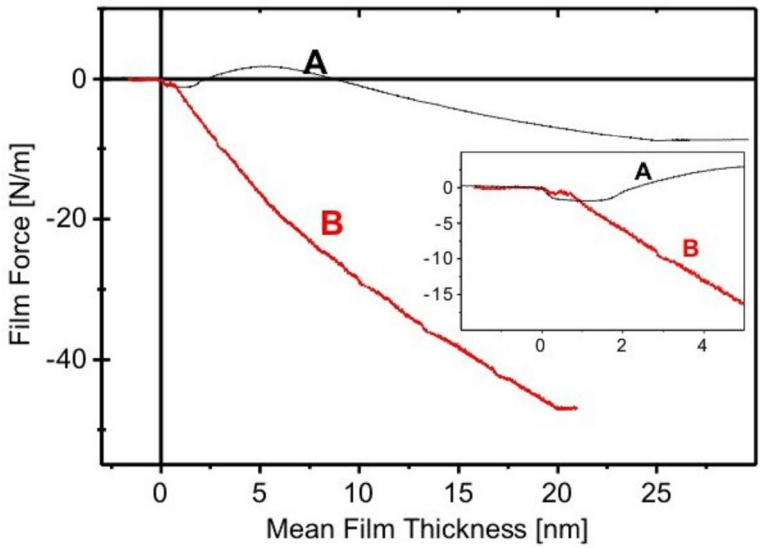

Abb. 42: Filmkraft (= Kraft F pro Einheitsbreite w der Filme) von Fe-Schichten auf unterschiedlich präparierten GaAs(001)-Substraten als Funktion der mittleren Schichtdicke, gemessen in Echtzeit während der Aufdampfung. Substrat für Film A: GaAs(001)-Probe, die unter Standardbedingungen präpariert und unter UHV-Bedingungen in die zugehörige Metall-MBE-Kammer transferiert wurde. Substrat für Film B: GaAs(001)-Probe, die nach dem MBE-Standardverfahren präpariert und mit einer As-Deckschicht versehen und nach Belüftung in eine Metall-MBE-Anlage transferiert wurde, in der die As-Deckschicht wieder desorbiert wurde [von Appl. Phys. Lett. **78**, 1270 (2001)]. Der Einschub zeigt den Anfangsbereich der beiden Filmkraftkurven mit höherer Auflösung.

gen von 0.5 GPa ist jedoch deutlich kleiner als der aus dem Misfit berechnete Spannungswert von 2.8 GPa, was auf eine teilweise Relaxation der Misfitverzerrung hinweist.

Im Gegensatz dazu zeigt Film B im Schichtdickenbereich von 0.7 – 5 nm eine Druckspannung von 2.7 ± 0.2 GPa, was sehr gut mit den maximal möglichen Misfitspannungen übereinstimmt. Der hohe Wert der Misfitspannungen kann als Kriterium für die hervorragende epitaktische Qualität der Fe Filme gewertet werden, da nur bei perfekt pseudomorphem Wachstum die Misfitspannungen vollständig übertragen werden. Bei einer Schicktdicke von ca. 5 nm nimmt der Druckspannungsbeitrag ab, was auf eine teilweise Relaxation der Misfitverzerrung durch den Einbau von Versetzungen hinweist.

Die Filmspannungen in der der Anfangsphase des Filmwachstums bis ca. 0.7 nm werden von Oberflächenstress-Effekte bestimmt (Abb. 42, Einschub). Während der Abscheidung der ersten 1.5 Monolagen (0.2 nm) von Fe in Film B treten deutlich höhere Druckspannungen von ca. 8 GPa auf, dann bleibt die Filmkraft bis 0.7 nm (~5 Monolagen) konstant. Eine genaue Auswertung dieser Daten ergibt eine Grenzflächenenergie von ca. 1.7 J/m^2 zusätzlich zur elastischen Energie aufgrund der Misfit-Verzerrung. Ein ähnliches Verhalten wird auch in Film B beobachtet.

Im Gegensatz zu der früheren Studie, in der das GaAs(001)-Substrate für den Transfer mit einer As-Deckschicht geschützt aber belüftet wurde, weisen die aktuellen Fe-Filme (Film A) keine Zugspannungen auf. Offensichtlich sind auf den in situ präparierten und unter UHV-Bedingungen transferierten Substraten Grenzflächenreaktionen und Interdiffusionseffekte stark unterdrückt. Der Vergleich von Elektronenbeugungsaufnahmen (LEED) beider Substrate zeigt eine deutlich schärfere Beugungsreflexe und damit eine verbesserte strukturelle Ordnung für das unter in situ Bedingungen präparierte Substrat. Die Spannungsuntersuchungen liefern keinen Hinweis auf eine Diffusion von Fe in das GaAs-Substrat bei einer Wachstumstemperatur von 300 K.

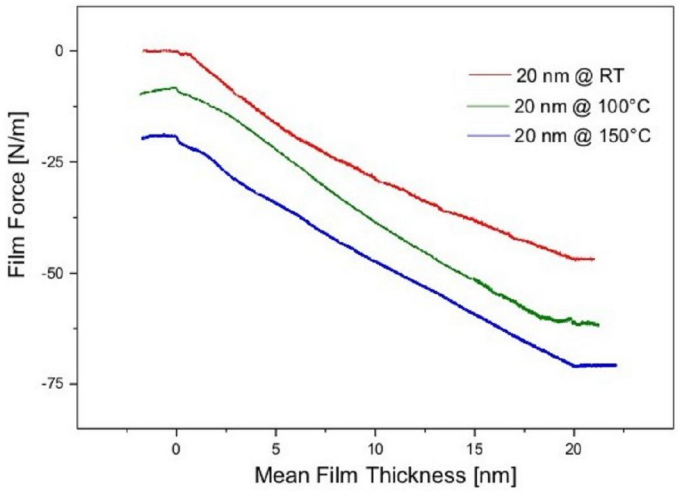

Abb. 43: Filmkraft (= Kraft F pro Einheitsbreite w der Filme) von Fe-Schichten auf GaAs(001) als Funktion der mittleren Schichtdicke, gemessen in Echtzeit während der Aufdampfung bei verschiedenen Wachstumstemperaturen.

Abbildung 43 zeigt Filmkraftkurven von Fe-Filmen, die bei unterschiedlichen Wachstumstemperaturen hergestellt wurden. Im Temperaturbereich zwischen Raumtemperatur und 150°C ist das Spannungsverhalten der Filme sehr ähnlich und von der Misfit-Verzerrung dominiert. Im Vergleich zum Raumtemperaturfilm, bei dem die teilweise Relaxation der Misfit-Verzerrung bei ca. 5 nm erfolgt, ist diese Schichtdicke beim 100°C-Film zu höheren (~10 nm), beim 150°C-Film zu tieferen (~2.5 nm) Werten verschoben. Da der Einbau von Versetzungen ein kinetisch kontrollierter Prozess ist, der durch Gitterfehler begünstigt wird, ist dies ein Hinweis für die Zunahme der Defektkonzentration bei höheren Temperaturen. Einen weitern Hinweis für einsetzende Grenzflächenreaktionen liefert die Verdopplung des Spannungsbeitrags am Beginn der Fe-Abscheidung bei einer Wachstumstemperatur von 150°C im Vergleich zum Raumtemperatur-Film.

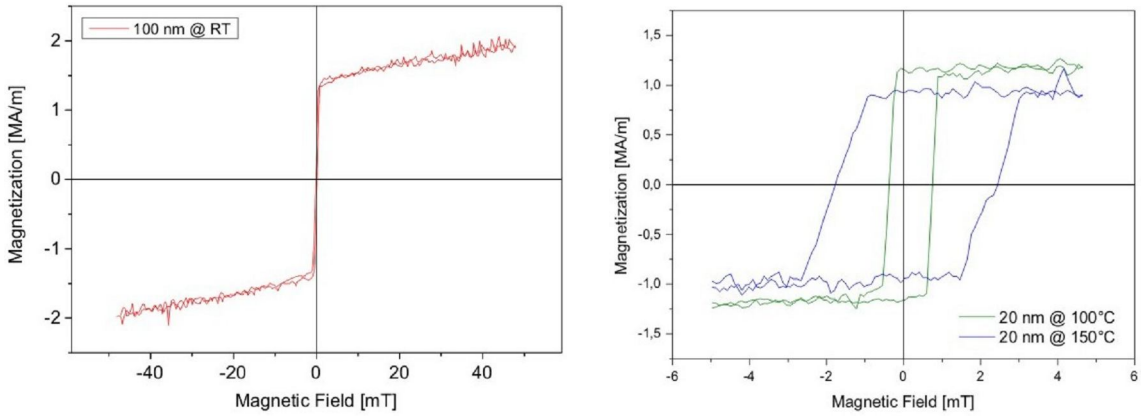

Abb. 44: Magnetische Hysteresekurven von Fe-Schichten auf GaAs(001), hergestellt bei verschiedenen Wachstumstemperaturen; das Magnetfeld wurde entlang der Fe[110]-Richtung angelegt.

Abbildung 44 zeigt magnetische Hysteresekurven der bei Raumtemperatur, 100°C und 150°C präparierten Fe-Filme, mit dem Magnetfeld entlang der (110)-Richtung von Fe. In allen Fällen liegt die leichte Magnetisierungsachse der Fe-Filme entlang der [100]-Richtung, was die Abweichung von Rechtecksverhalten der Hysteresekurven erklärt (siehe Raumtemperaturfilm in Abb. 44). Die Koerzitivfeldstärke ist beim Raumtemperaturfilm kleiner als 0.5 mT und steigt mit zunehmender Temperatur an (~2 mT beim 150°C-Film).

7.2 Mechanische Spannungen und magnetische Eigenschaften von Fe_3Si/GaAs(001)

Vor kurzem haben wir auch Untersuchungen am System Fe_3Si/GaAs(001) aufgenommen. Abbildung 45 zeigt die Filmkraftkurve eines bei einer Wachstumstemperatur von 250°C durch Ko-Verdampfung von Fe und Si mittels zweier Elektronenstrahlverdampfer hergestellten Fe_3Si-Schicht. Die Aufdampfrate beträgt ca. 0.2 nm/min und wurde für die beiden Verdampferquellen getrennt mit einem Schwingquarzmessgerät bestimmt.

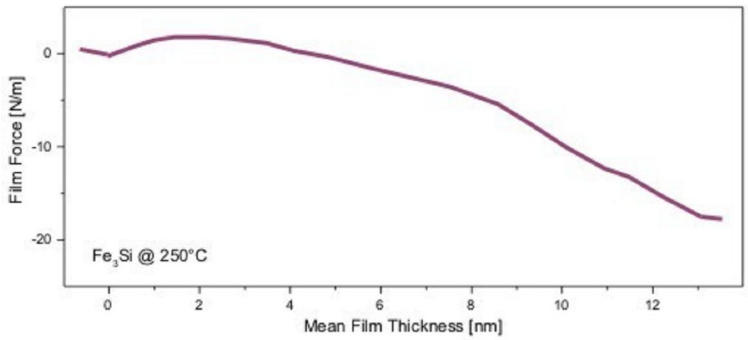

Abb. 45: Filmkraft (= Kraft F pro Einheitsbreite w der Filme) einer bei 250°C auf GaAs(001) aufgedampften Fe_3Si-Schicht als Funktion der mittleren Schichtdicke, gemessen in Echtzeit während der Aufdampfung.

Überraschenderweise entwickelt die Fe_3Si-Schicht relativ große Druckspannungen, die etwa um eine Größenordnung höher als die zu erwartenden Misfit-Spannungen sind. Dies mag ein Hinweis auf Interdiffusion, speziell von Fe in das GaAs-Substrat, sein. Umfangreichere Untersuchungen bei unterschiedlichen Substrattemperaturen sind aber erforderlich, um diese Vermutung zu erhärten.

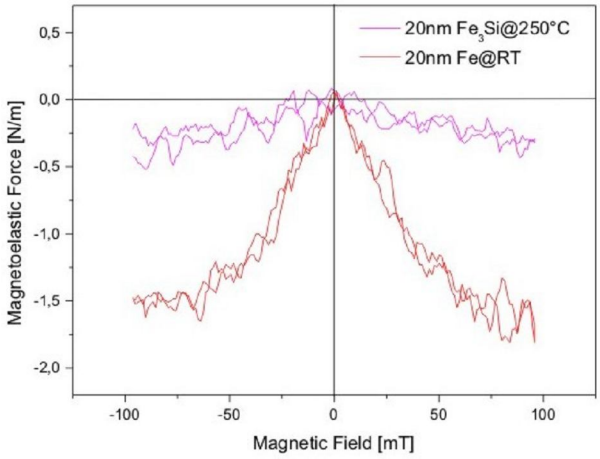

Abb. 46: Filmkraft (= Kraft F pro Einheitsbreite w der Filme) aufgrund von magnetoelastischer Kopplung in eine reiner bei Raumtemperatur auf GaAs(001) gewachsenen Fe-Schicht sowie einer Fe_3Si, die bei 250°C aufgedampft wurde; in beiden Fällen wurde das Magnetfeld entlang der [110]-Richtung von GaAs(001) angelegt.

Abbildung 46 zeigt Magnetostriktionsergebnisse der Fe_3Si-Schicht im Vergleich zu einer reinen Fe-Schicht, wobei der Wert bei hohen Feldern der magnetoelastischen Kopplungskonstanten in der Richtung des angelegten Magnetfeldes entspricht (in beiden Fällen entlang der [110]-Richtung von GaAs). Diese ersten Magnetostriktionsergebnisse lassen vermuten, dass die Magnetostriktion von Fe_3Si-Schichten deutlich kleiner als von Fe ist, was für technologische Anwendungen mit hohen Schaltraten von großem Vorteil ist.

7.3 Verfahren zur in situ Herstellung magnetoresistiver Elemente

Die Bestimmung des Magnetowiderstands eines magnetoresistiven Elements, hergestellt aus den zuvor entwickelten ferromagnetischen Schichten, stellt ein aussagekräftiges Kriterium für die Beurteilung des Erfolgs eines Optimierungsschrittes bereit. Das Ziel war es, magnetoresistive Elemente für Magnetowiderstands-Untersuchungen in situ, d.h. ohne lithographische Prozessierung herzustellen. Dadurch werden Kontakt und Wechselwirkung der Dünnschichtsysteme mit flüssigen Reagenzien vermieden, die zu einer Veränderung ihrer physikalischen Eigenschaften führen können und somit die eindeutige Zuordnung der Ursache für die geänderten Eigenschaften erschweren. Im Rahmen des Projekts wurde ein spezielles im UHV einsetzbares Maskensystem entwickelt, mit dem die unterschiedlichen Schichten eines magnetoresistiven Elements sukzessive aufgedampft werden können (2 magnetische Schichten, eine Isolierschicht und metallische Elektroden). Das Hauptproblem war die Ermittlung einer optimalen Maskengeometrie, welche einerseits das Auftreten sogenannter ‚Pinholes' vermeidet und andrerseits die unabhängige Ummagnetisierung der beiden magnetischen Schichten gewährleistet, um damit parallele und antiparallele Zustände einzustellen.

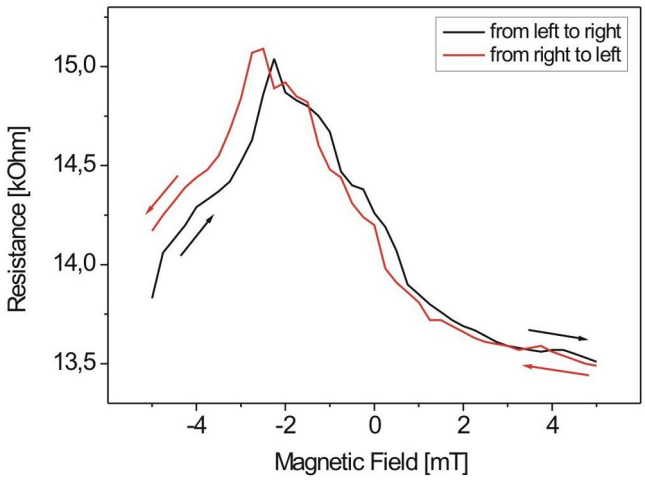

Abb. 47: Magnetowiderstandsmessung eines magnetoresistiven Elements, bestehend aus zwei bei Raumtemperatur hergestellten Fe-Schichten (siehe Kapitel 7.1), die durch eine 3 nm dicke MgO-Schicht separiert sind.

Abbildung 47 zeigt als Beispiel eine Magnetowiderstandsmessung eines magnetoresistiven Elements, das aus zwei bei Raumtemperatur hergestellten Fe-Schichten (siehe Kapitel 7.1) besteht, die durch eine 3 nm dicke MgO-Schicht separiert sind. Obwohl die Koerzitivfeldstärke der Fe-Filme kleiner als 1 mT ist, gelingt es, parallele und antiparallele Konfigurationen einzustellen. Die beiden Widerstandskurven von Abb. 47 entsprechen einem Magnetowiderstandsverhältnis von 11 Prozent, wobei die Maxima der Widerstandskurven von Hin- und Rücklauf deutlich getrennt sind. Zwar ist die Magnetowiderstandsänderung der Teststruktur noch nicht ausreichend und die Koerzitivfeldstärken der Filme viel zu klein für Anwendungen der Magnetologik. Die Messungen von Abb. 47 demonstrieren jedoch, dass mit dem entwickelten Aufbau nun ein Verfahren zur Verfügung steht, das die schnelle und zuverlässige Bewertung magnetischer Schichtsysteme für den technologischen Einsatz ermöglicht.

8. Zusammenfassung

Im Rahmen dieses Projektes wurden Ferromagnet/Halbleiter-Nanostrukturen entwickelt, die für die Umsetzung neuartiger multifunktionaler Logikkonzepte geeignet sind und eine erhöhte Effizienz der Spininjektion in den Halbleiter in Aussicht stellen. Im Einzelnen wurden umfassende Untersuchungen zur Herstellung und Nanostrukturierung von Ferromagnet-Halbleiter-Heterostrukturen durchgeführt und deren epitaktische Struktur, kristallographische Ordnung, magnetische und Magnetotransport-Eigenschaften untersucht. Für deren Eignung als potentielle Spintronik- oder Magnetologik-Bauelemente wurde die Spininjektion und Spinpolarisation ausgewählter Heusler-Legierungs-Schichten im Detail untersucht.

Der Schwerpunkt der Untersuchungen betrifft Filme aus der Materialklasse der binären und ternären Heusler-Legierungen, Fe_3Si und Co_2FeSi, die sich durch eine hohe Curie-Temperatur und eine geringe Gitterfehlanpassung auszeichnen.

Die wesentlichen Ergebnisse werden im Folgenden zusammengefasst:

- Optimiertes Wachstum einkristalliner Fe_3Si Schichten auf GaAs(113)A-Substraten von hoher epitaktischer Güte, hoher kristallographischer Ordnung und abrupter Grenzfläche zum Substrat.
- Untersuchung der Magnetotransporteigenschaften von $Fe_{3+x}Si_{1-x}$/GaAs(001)- und $Fe_{3+x}Si_{1-x}$/GaAs(113)A-Heterostrukturen unterschiedlicher Zusammensetzung, wobei die Ergebnisse durch eine Reduzierung der Kristallsymmetrie der Heusler-Legierung, beziehungsweise durch das Auftreten kohärenter Spinfluktuationen zwischen den verschiedenen Fe-Untergittern interpretiert werden können.
- Optimiertes Wachstum einkristalliner Co_2FeSi Schichten auf GaAs(001)-Substraten von hoher epitaktischer Güte, hoher kristallographischer Ordnung und abrupter Grenzfläche zum Substrat.
- Optimierung der Herstellung von Spin-LEDs mit Co_2FeSi als Spininjektor.
- Deutliche Erhöhung der Spininjektionseffizienz (Werte bis zu 51%) vom Ferromagneten in den Halbleiter gegenüber früheren Ergebnissen.
- Optimiertes Wachstum einkristalliner Co_2FeSi Schichten auf Si(111)-Substraten von guter epitaktischer Qualität, hoher kristallographischer Ordnung und abrupter Grenzfläche zum Substrat; polykristallines Wachstum auf Si(001)-Substraten.
- Bestimmung der magnetischen Domänenstruktur sowie des magnetischen Phasenübergangs von lithographisch hergestellten MnAs-Nanostrukturen mit einem Übergang von multi- zu eindomänigem Verhalten bei Strukturgrößen <100 nm.
- Untersuchung der mechanischen und magnetischen Eigenschaften von Fe- und Fe_3Si-Schichten: Nahezu vollständige Übertragung der Misfit-Spannungen bis zu hohen Schichtdicken in reinen Fe-Filmen. Hohe Druckspannungen in Fe_3Si-Filmen, die auf Interdiffusion hinweisen. Kleine Magnetostriktion für Fe_3Si-Schichten.
- Entwicklung eines in situ Verfahrens zur Herstellung magnetoresistiver Elemente, das die schnelle und zuverlässige Bewertung magnetischer Schichtsystems für den Einsatz in der Magnetologik ermöglicht.

9. Veröffentlichungen

9.1. Manuskripte in Fachzeitschriften

(1) M. Hashimoto, J. Herfort, H.-P. Schönherr, and K. H. Ploog
Epitaxial Heusler alloy Co_2FeSi/GaAs(001) hybrid structures
Appl. Phys. Lett. **87**, 102506 (2005).

(2) P. K. Muduli, J. Herfort, H.-P. Schönherr, and K. H. Ploog
Epitaxial Fe_3Si films stabilized on GaAs(113)A substrates
J. Cryst. Growth **285**, 514 (2005).

(3) P. K. Muduli, K.-J. Friedland, J. Herfort, H.-P. Schönherr, and K. H. Ploog
Antisymmetric contribution to the planar Hall effect of Fe_3Si films grown on GaAs(113)A substrates
Phys. Rev. B **72**, 104430 (2005).

(4) M. Hashimoto, J. Herfort, H.-P. Schönherr, and K. H. Ploog
Thermal stability and atomic ordering of epitaxial Heusler alloy Co_2FeSi films grown on GaAs(001)
J. Appl. Phys. **98**, 104902 (2005).

(5) R. Koch
Morphware
Scientific American **293**, 56 (2005).

(6) Y. Takagaki, C. Herrmann, E. Wiebicke, J. Herfort, L. Däweritz, and K. H. Ploog
Slow relaxation of magnetization in MnAs nanomagnets on GaAs(001)
Appl. Phys. Lett. **88**, 032504 (2006).

(7) K.-J. Friedland, M. Bowen, J. Herfort, H.-P. Schönherr, and K. H. Ploog
Intrinsic contributions to the planar Hall effect in Fe and Fe_3Si films on GaAs substrates
J. Phys. Condens. Matter **18**, 2641 (2006).

(8) R. Koch
Morphware oder Einer für Alle
Spektrum der Wissenschaft **3**, 66 (2006).

(9) M. Hashimoto, J. Herfort, H.-P. Schönherr, and K. H. Ploog
Magnetic properties of $(Co_{2/3}Fe_{1/3})_{3+x}Si_{1-x}$/GaAs(001) hybrid structures
J. Phys. Condens. Matter **18**, 6101 (2006).

(10) M. Hashimoto, J. Herfort, A. Trampert, H.-P. Schönherr, and K. H. Ploog
Growth temperature dependent evolution of the interface structure in Co_2FeSi/GaAs(001) hybrid structures
J. Vac. Sci. Technol. B **24**, 2004 (2006).

(11) P. K. Muduli, K.-J. Friedland, J. Herfort, H.-P. Schönherr, and K. H. Ploog
Investigation of magnetic anisotropy and magnetization reversal by planar Hall effect in Fe_3Si and Fe films grown on GaAs(113)A substrates
J. Phys. Condens. Matter **18**, 9453 (2006).

(12) Y. Takagaki, J. Herfort, L. Däweritz, and K. H. Ploog
Flipping of magnetic moments induced by first-order phase transition in MnAs disks on GaAs(001)
Phys. Rev. B **74**, 224417, 7 pages (2006).

(13) R. Koch
Morphware — Eine anpassungsfähige Logik
Bulletin SEV/VSE Heft **7**, 9 (2006).

(14) M. Hashimoto, J. Herfort, A. Trampert, H.-P. Schönherr, and K. H. Ploog
Growth temperature dependent interfacial reaction of Heusler alloy Co_2FeSi/GaAs(001) hybrid structures
J. Phys. D: Appl. Phys. **40**, 1631 (2007).

(15) J. Herfort, P. K. Muduli, K.-J. Friedland, H.-P. Schönherr, and K. H. Ploog
Magnetic anisotropy in Heusler alloy Fe_3Si fims on GaAs(113)A
J. Magn. Magn. Mat. **310**, 2228 (2007).

(16) M. Hashimoto, J. Herfort, A. Trampert, H.-P. Schönherr, and K. H. Ploog
Growth, interface structure and magnetic properties of Heusler alloy Co_2FeSi/GaAs(001) hybrid structures
J. Cryst. Growth **301/302**, 592 (2007).

(17) M. Hashimoto, A. Trampert , J. Herfort, and K. H. Ploog
Atomic ordering and interlayer-diffusion of Co_2FeSi films grown on GaAs(001) studied by transmission electron microscopy
J. Vac. Sci. Technol. B **25**, 1453 (2007).

(18) M. Ramsteiner, O. Brandt, T. Flissikowski, H.T. Grahn, M. Hasimoto, J. Herfort, and H. Kostial
Co_2FeSi/GaAs/(Al,Ga)As spin light-emitting diodes: Competition between spin injection and ultrafast spin alignment
Phys. Rev. B **78**, 121303(R) (2008).

(19) P. K. Muduli, K.-J. Friedland, J. Herfort, H.-P. Schönherr, and K. H. Ploog
Composition dependent properties of Fe_3Si films grown on GaAs(113)A substrates
J. Appl. Phys. **105**, 07B104 (2009).

(20) M. Zander, J. Herfort, K. Kumakura, H.-P. Schönherr, and A. Trampert
Epitaxial Heusler alloy C_2FeSi films on Si(111) substrates
Appl. Phys. Lett., submitted (2009).

9.2. Beiträge auf internationalen Konferenzen

(1) P. K. Muduli, J. Herfort, H.-P. Schönherr, and K. H. Ploog
Epitaxial growth, structural and magnetic properties of Fe and Fe_3Si films on GaAs(113)A substrates
338th Heraeus-Seminar Nanomagnetism: New Insights with Synchrotron Radiation, Bad Honnef (Germany), January 5 – 7 (2005).

(2) R. Koch **(invited)**
Reconfigurable logic with single magnetoresistive elements
GIF 24th Meeting: Novel Approaches in Magnetic Resonance: Fundamentals and Applications, Jerusalem (Israel), February 19 – 25 (2005).

(3) M. Hashimoto, J. Herfort, H.-P. Schönherr, and K. H. Ploog
MBE growth Co_2FeSi/ GaAs(001) hybrid structures
13th European Molecular Beam Epitaxy Workshop, Grindelwald (Switzerland), March 7 – 9 (2005).

(4) K.-J. Friedland, P. K. Muduli, J. Herfort, M. Bowen, H.-P. Schönherr, and K. H. Ploog (**invited)**
Intrinsic contributions to the planar Hall effect in Fe and Fe_3Si films on GaAs substrates
Intern. Workshop on Spin Phenomena in Reduced Dimensions, Regensburg (Germany), March 10 – 12 (2005).

(5) R. Koch **(invited)**
Reconfigurable logic with single magnetoresistive elements
International Symposium on Magnetism, Moscow (Russia), June 25 – 30 (2005).

(6) J. Herfort, H.-P. Schönherr, M. Hashimoto, B. Jenichen, V. Kaganer, A. Trampert, and K. H. Ploog
Epitaxial Heusler alloys on GaAs(001) substrates
12th Intern. Conf. on Modulated Semiconductor Structures (MSS-12), Albuquerque (USA), July 10 – 15 (2005).

(7) K.-J. Friedland, P. K. Muduli, J. Herfort, M. Bowen, H.-P. Schönherr, and K. H. Ploog
The planar and anomalous Hall effects in Fe and Fe_3Si films on GaAs(001) and GaAs(113) substrates
3rd Intern. Conf. on Spintronics and Quantum Information Technology (SPINTECH-III), Awaji Island (Japan), August 1 – 5 (2005).

(8) M. Hashimoto, J. Herfort; H.-P. Schönherr, and K. H. Ploog
Epitaxial Co_2FeSi/ GaAs(001) hybrid structures
3rd Intern. Conf. on Spintronics and Quantum Information Technology (SPINTECH-III), Awaji Island (Japan), August 1 – 5 (2005).

(9) J. Herfort, M. Hashimoto, A. Trampert, H.-P. Schönherr, and K. H. Ploog
Growth temperature dependent evolution of the interface structure in Co_2FeSi/GaAs(001) hybrid structures
33rd Intern. Conf. on the Physics and Chemistry of Semiconductor Interfaces (PCSI-33), Cocoa Beach (USA), January 15 – 19 (2006).

(10) J. Herfort, H.-P. Schönherr, M. Hashimoto, B. Jenichen, V. Kaganer, A. Trampert, and K. H. Ploog
Epitaxial Heusler alloys on GaAs(001) substrates
Joint Meeting of German and Polish Associations for Crystal Growth, Berlin (Germany), March 6 – 8 (2006).

(11) J. Herfort, B. Jenichen, V. M. Kaganer, K.-J. Friedland, M. Bowen, A. Trampert, H.-P. Schönherr, and K. H. Ploog
Long-range atomic ordering and its consequences in Heusler alloy Fe_3Si films on GaAs(001) substrates
4th Intern. Conf. on the Physics and Application of spin-related Phenomena in Semiconductors (PASPS-IV), Sendai (Japan), August 15 – 18 (2006).

(12) J. Herfort, P. K. Muduli, K.-J. Friedland, H.-P. Schönherr, and K. H. Ploog
Magnetic anisotropy and magnetotransport studies of Heusler alloy Fe_3Si films on GaAs(113)A substrates
17th Intern. Conf. on Magnetism (ICM-2006), Kyoto (Japan), August 20 – 25 (2006).

(13) J. Herfort, M. Hashimoto, H.-P. Schönherr, A. Trampert, and K. H. Ploog
Growth, interface structure and magnetic properties of Heusler alloy Co_2FeSi/GaAs(001) hybrid structures
14th Intern. Conf. on Molecular Beam Epitaxy (MBE2006), Tokyo (Japan), September 03 – 08 (2006).

(14) M. Hashimoto, A. Trampert, J. Herfort, and K. H. Ploog
Atomic ordering and interlayer-diffusion of Co_2FeSi films grown on GaAs(001) studied by transmission electron microscopy
34th Intern. Conf. on the Physics and Chemistry of Semiconductor Interfaces (PCSI-34), Salt Lake City (USA), January 14 – 18 (2007).

(15) M. Ramsteiner, O. Brandt, M. Hashimoto, J. Herfort, and H. Kostial
Concepts and materials for electrical spin injection into semiconductors: From metals to half-metals
Intern. Workshop on Spin- and Optoelectronics, Berlin (Germany), September 26 – 29 (2007).

(16) J. Herfort, H.-P. Schönherr, and B. Jenichen
Magnetic and structural properties of ultrathin epitaxial Fe_3Si films on GaAs(001)
52nd Intern. Conf. on Magnetism and Magentic Materials (MMM-52), Tampa (USA), November 5 – 9 (2007).

(17) J. Herfort, M. Hashimoto, K. Kumakura, A. Trampert, H. Kostial, O. Brandt, M. Ramsteiner
Epitaxial Heusler alloy Co_2FeSi films on GaAs substrates for spin injection
5th Intern. Conf. on Physics and Application of Spin-related Phenomena in semiconductors (PASPS-V), Foz do Iguacu (Brasil), August 5 – 6 (2008).

(18) P. K. Muduli, K.-J. Friedland, J. Herfort, H.-P. Schönherr, and K. H. Ploog
Composition dependent properties of Fe_3Si films grown on GaAs(113)A substrates
53rd Intern. Conf. on Magnetism and Magnetic Materials (MMM-53), Austin (USA), November 10 – 14 (2008).

(19) J. Herfort **(invited)**

Growth of Heusler alloy semiconductor heterostructures and effect of interface perfection on spin injection

15th European Molecular Beam Epitaxy Workshop, Zakopane (Poland), March 8 – 11 (2009).

9.3. Beiträge auf nationalen Konferenzen

(1) J. Herfort
Fe_3Si/GaAs(113) Heterostrukturen: Wachstum, atomare Ordnung und Magnetotransport
BMBF-Statusseminar „NanoQUIT“, Schloss Ringberg (Germany), September 25 – 27 (2005).

(2) J. Herfort, M. Hashimoto, H.-P. Schönherr, A. Trampert, and K. H. Ploog
Epitaktische Heusler-Legierung Co_2FeSi auf GaAs(001)
German Molecular Beam Epitaxy Workshop 2005, Stuttgart (Germany), October 11 – 12 (2005).

(3) R. Koch, J. Herfort, M. Hashimoto, A. Trampert, H.-P. Schönherr, Y. Tagagaki, B. Jenichen, L. Däweritz, and K. H. Ploog
Ferromagnet/Semiconductor Hetero- and Nanostructures
BMBF-Statusseminar „NanoQUIT“, Stuttgart (Germany), September 11 – 12 (2006)

(4) J. Herfort, M. Hashimoto, H.-P. Schönherr, A. Trampert, and K. H. Ploog
Epitaxial Heusler alloy cobalt iron silicide films on GaAs
Spring Meeting of the German Physical Society, Regensburg (Germany), March 26 – 30 (2007), Verhandlungen der DPG 4 (2007) Ma20.2.

(5) J. Herfort
Epitaxial Heusler alloy Co_2FeSi/GaAs(001) hybrid structures for spin injection
BMBF-Statusseminar „NanoQUIT“, Stuttgart (Germany), October 09 – 10 (2007).

(6) J. Herfort **(invited)**
Epitaxial Heusler alloy cobalt iron silicide films on GaAs substrates for spin injection
Symposium Heusler Films on Semiconductors, Hamburg (Germany), November 25 – 26 (2008).

(7) J. Herfort
Ferromagnet/Semiconductor heterostructures for magnetologics and spintronics
BMBF-Statusseminar „NanoQUIT“, Stuttgart (Germany), January 20 – 21 (2009).

(8) M. Zander, K. Kumakura, A. Trampert, and J. Herfort
Epitaxial growth of Heusler alloy cobalt iron silicide films on Si(111) and Si(001) substrates
Spring Meeting of the German Physical Society, Dresden (Germany), March 23 – 27 (2009), Verhandlungen der DPG 5 (2009) Ma32.1.

9.4. Eingeladene Seminarvorträge

(1) R. Koch
Neue Lösungsansätze für eine zukünftige nanoskalige Elektronik
Institut für Festkörperphysik, Technischen Universität Graz, Graz (Austria), June 30 (2005).

(2) J. Herfort
Epitaxial Heusler alloys on GaAs substrates
NTT Basic Research Laboratories, Atsugi (Japan), August 11 (2006).

(3) J. Herfort
Epitaxial Heusler alloys on GaAs substrates
Department of Applied Physics, University of Tokyo, Tokyo (Japan), August 14 (2006).

(4) J. Herfort
Epitaxial Heusler alloys on GaAs substrates
Institute of Scientific and Industrial Research, Osaka University, Osaka (Japan), August 28 (2006).

(5) J. Herfort
Epitaxial Heusler alloy Co_2FeSi films on GaAs substrates for spin injection
Institut für Angewandte Physik, Universität Hamburg, Hamburg (Germany), May 27 (2008).

Anhang der Publikationen

Epitaxial Heusler alloy Co_2FeSi/GaAs(001) hybrid structures

M. Hashimoto, J. Herfort, H.-P. Schönherr, and K. H. Ploog
Paul-Drude-Institut für Festkörperelektronik, Hausvogteiplatz 5-7, D-10117 Berlin, Germany

(Received 15 April 2005; accepted 19 July 2005; published online 1 September 2005)

We found that Co_2FeSi layers on GaAs(001) grown by molecular-beam epitaxy with high crystal and interface perfection as well as smooth surfaces can be obtained in the low-growth-temperature regime. The layers are thermally robust up to 250 °C. They have long-range order and crystallize in the Heusler-type $L2_1$ structure. The easy axis of magnetization is along the [110] direction caused by a dominating uniaxial in-plane magnetic anisotropy component which has an easy axis different from that of the magnetocrystalline anisotropy component. © *2005 American Institute of Physics*. [DOI: 10.1063/1.2041836]

Spintronics is a recently emerging field of new device concepts which is based on the spin degree of freedom of the electron, and is expected to lead to dramatic improvements in device performance. One of the key issues for the realization of spintronic devices is the efficient electrical injection of spin-polarized carriers into semiconductors. Electrical spin injection has been investigated mainly from Mn-doped III-V and II-VI semiconductors[1,2] and from conventional ferromagnetic metals.[3–7] Recently, Heusler alloys are of increasing interest as a candidate for a spin injection source into semiconductors, because of their high Curie temperature, their compatibility with compound and element semiconductors and half-metallicity predicted for some Heusler alloys.[8–11] There are a few reports of epitaxial Heusler alloys grown on semiconductor substrates, e.g., the full-Heusler alloys Co_2MnX,[12,13] and Ni_2MnY,[14,15] as well as the half-Heusler alloy NiMnSb.[16,17] However, no evidence of a high degree of spin-polarization as expected from theory has been observed in Heusler alloy films up to now: around 60% at maximum.[18–20]

In ferromagnet/semiconductor (FM/SC) heterostructures, mainly two obstacles with respect to their crystal structure are considered to prevent efficient electrical spin injection. One is the existence of interfacial compounds formed by diffusion of As and/or Ga into the FM layers, resulting in spin-flip scattering at the interface. The second is atomic disorder, such as vacancies, antisites and atomic swaps. This disorder introduces minority gap states and it was reported that only a few percent of antisite disorder can destroy the half-metallic nature of Heusler alloys.[21] Therefore, a highly atomically-ordered, stoichiometric and thermally stable thin film is needed for spin injection sources.

In this letter, we present our results on the fabrication and characterization of single-crystal Heusler alloy Co_2FeSi/GaAs(001) hybrid structures grown by molecular beam epitaxy (MBE). Co_2FeSi is a member of full-Heusler alloys with the cubic $L2_1$ crystal structure consisting of 4 interpenetrating fcc sublattices.[22] The lattice constant of bulk Co_2FeSi is 5.658 Å,[23] closely lattice matched to GaAs (a_{GaAs}=5.653 Å), and the lattice mismatch is as small as 0.08%. $Fe_{3-x}Co_xSi$ crystallizes in the cubic fcc structure in a wide range of x ($0<x<2.15$).[23] This phase stability allows us to control the magnetic properties, e.g., magnetic anisotropy and magnetic moment. Bulk Co_2FeSi with a large magnetic moment (5.91 μ_B at 10.2 K) is ferromagnetic up to more than 980 K,[23] which is one of the highest Curie temperature among the reported Heusler alloys. In addition, according to a band structure calculation, Co_2FeSi is located at a slightly deviated position from the Slater-Pauling curve which half-metallic Heusler alloys expected to obey. Therefore, one could expect relatively high spin-polarization degree for Co_2FeSi.[10]

In preparation of the Co_2FeSi growth, the growth conditions of the binary alloy $Co_{0.66}Fe_{0.34}$ (bcc structure) were optimized. The composition of $Co_{0.66}Fe_{0.34}$ layers was determined by comparing their lattice constant with literature data,[24] taking into account the tetragonal distortion of the layers. Then Si was added and incorporated to obtain ternary Co_2FeSi, while the Fe and Co fluxes were kept constant at the optimized amounts. Before the growth of the Co_2FeSi layers, 100 nm-thick-GaAs templates were prepared in the III-V growth chamber using standard GaAs growth conditions. As-terminated $c(4\times4)$ reconstructed GaAs (001) surfaces were prepared to prevent the formation of macroscopic defects on the surface,[25] by cooling the samples down to 420 °C under As_4 pressure. The samples were then transferred to the As-free deposition chamber under UHV of a base pressure of 5×10^{-10} Torr. The growth temperature for the Co_2FeSi layers was varied in the range 100–400 °C to find the optimum growth temperature regime. A low growth rate of about 0.1 nm/min was chosen in order to avoid the degradation of the crystal quality at these low growth temperatures. The Si cell temperature (T_{Si}) was varied from 1280 °C to 1335 °C to find the stoichiometric composition of Co_2FeSi. The thickness of the layers was determined by high-resolution x-ray diffraction (HRXRD) and x-ray reflectivity (XRR) measurements and it varies in the range from 17 nm to 23 nm in accordance with the increase of T_{Si}. The growth was *in situ* monitored using reflection high-energy electron diffraction (RHEED). The RHEED patterns of the Co_2FeSi layers show fourfold symmetric, streaky patterns with Kikuchi lines and Laue circle, indicating a two-dimensional growth mode and rather flat surfaces.

The structural properties of the films were examined *ex situ* by HRXRD with a PANalytical X'pert diffractometer using Cu K_α radiation with a Ge(220) monochrometer and an triple-bounce analyzer crystal. Figure 1 shows the results of HRXRD ω-2θ curves for Co_2FeSi(004) and $Co_{0.66}Fe_{0.34}$(002) reflections together with the simulation using the Takagi-Taupin formalism. The examined films were

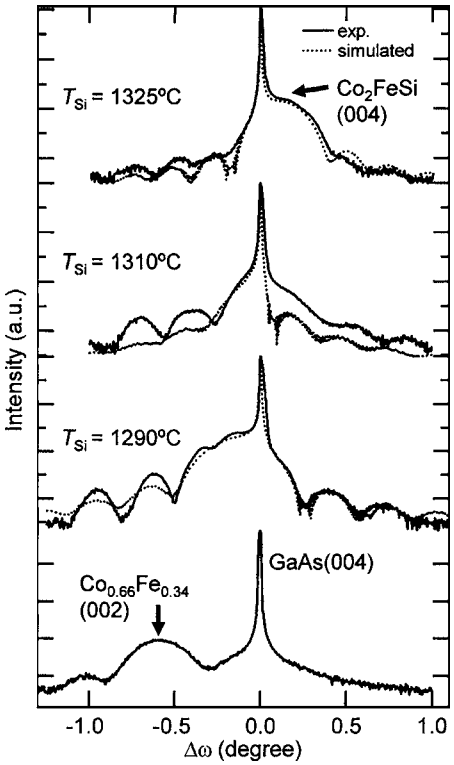

FIG. 1. Normalized ω-2θ curves for Co_2FeSi/GaAs(001) and $Co_{0.66}Fe_{0.34}$/GaAs(001) (bottom line) films grown at 100 °C with various Si cell temperatures together with the simulated curve using the Takagi-Taupin formalism (dotted lines).

grown at 100 °C with different T_{Si} (i.e., different Si composition) between 1290 °C and 1325 °C. The Co_2FeSi(004) peak systematically shifts to larger angle as T_{Si} increases up to 1325 °C, demonstrating the incorporation of Si atoms into the proper lattice sites and the formation of the ternary Co_2FeSi alloy. Distinct interference (Pendellösung) fringes are observed up to T_{Si}=1325 °C, indicating a high crystal quality, interface perfection as well as smooth surface. The smoothness of the films were further confirmed by both atomic force microscopy and XRR, and the rms surface roughness of the films turned out to be less than 1 nm for the examined films, being consistent with the results of HRXRD. To confirm the Heusler-type $L2_1$ structure, additional reflection, namely (113) reflection was recorded. Note that the (004) reflection is the principle reflection which is not influenced by disorder and the (113) is the order-dependent superlattice reflection of $L2_1$ structure.[22] The (113) reflection was clearly observed with interference fringes (not shown here), suggesting the presence of long-range atomic-ordering and the Heusler-type $L2_1$ structure.

From the perpendicular lattice mismatch $(\Delta a/a)_\perp$, the lattice constant of the layers (a_{Co_2FeSi}) was estimated and plotted as a function of T_{Si} in Fig. 2. The broken and dashed lines indicate the lattice constant of bulk Co_2FeSi and GaAs, respectively. To estimate a_{Co_2FeSi}, the tetragonal distortion of the layer, confirmed in a reciprocal space map at Co_2FeSi(113) reflections, was taken into account to obtain the unstrained parameters using the elastic constants of Fe_3Si, C_{11}=219 GPa and C_{12}=143 GPa (Ref. 26) as approximate values. The lattice constant decreases linearly with increasing T_{Si}. From a comparison with the bulk value, the stoichiometric composition of Co_2FeSi was determined.

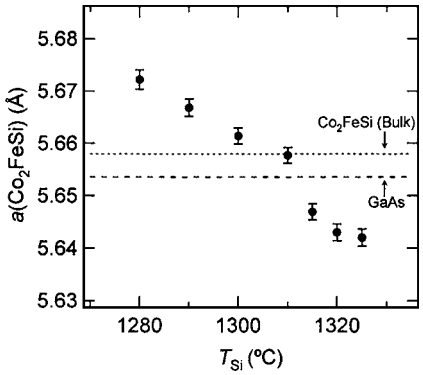

FIG. 2. Dependence of the unstrained lattice constant of Co_2FeSi layers (a_{Co_2FeSi}) on Si cell temperature. The broken line and the dashed line indicate the bulk value of Co_2FeSi and GaAs, respectively.

Figure 3 shows the results of HRXRD ω-2θ curves around (004) reflections of Co_2FeSi layers near stoichiometry grown at different temperatures between 100 °C and 350 °C. In the lower growth temperature regime, high orders of interference fringes (up to fifth order) are seen, while in T_G>250 °C the interference fringes become less pronounced, indicating the onset of crystal degradation. At T_G =350 °C, the main peak is broadened and shifted to larger angle. This peak broadening and shift with increasing T_G has also been observed in our study on Fe_3Si/GaAs(001) (Ref. 27) and is most likely due to interfacial reaction or phase separation. This is further evidenced by the wide-range ω-2θ scans with a wide-open detector for the same series of samples (not shown here). An additional peak appeared at around ω=17.3° for the sample grown at 350 °C. We ascribe this peak to either $Co_{1-x}Fe_xSi_2$(002) caused by phase separation or $(Co,Fe)_2As$(110) by interfacial reaction. Therefore, the optimum growth temperature range of Co_2FeSi at which good crystal and interface quality can be obtained is T_G <250 °C. It should be stressed that in terms of thermal stability, Co_2FeSi is much more suitable for device applications than Fe, Co and FeCo on GaAs, for which interfacial reac-

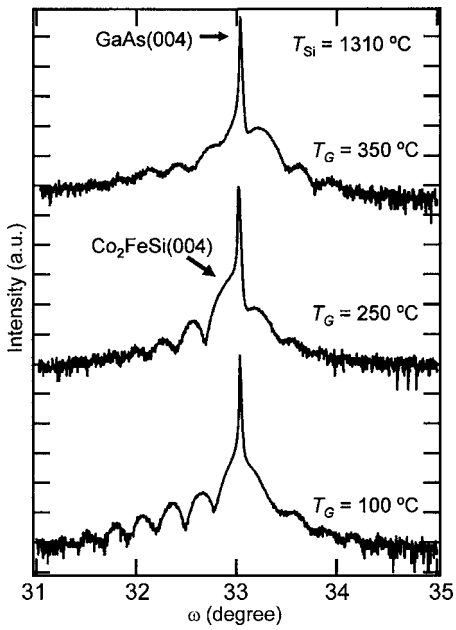

FIG. 3. Normalized ω-2θ curves for stoichiometric Co_2FeSi/GaAs(001) films grown at various growth temperature ranging from 100 °C to 350 °C.

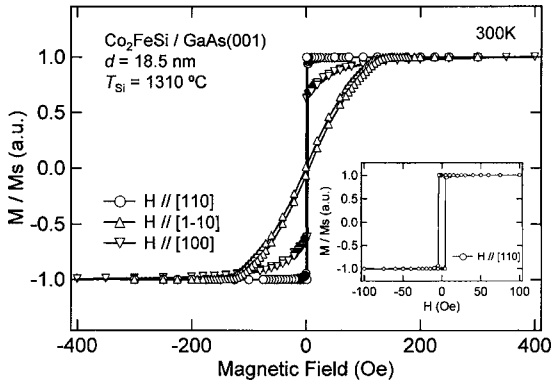

FIG. 4. Magnetization curves for 18.5 nm thick stoichiometric $Co_2FeSi/GaAs(001)$ film grown at 100 °C. The inset shows an expanded view of the magnetization curve along the [110] direction. After subtraction of the diamagnetic contribution of the GaAs substrate, the magnetizations were normalized to the saturation magnetization in each direction.

tions occur at much lower T_G.[25] However, since it is very difficult to detect nano meter-size interfacial compounds or clusters by XRD, detailed transmission electron microscopy studies are in preparation for this system.

The magnetic properties of Co_2FeSi were investigated using superconducting quantum interference device (SQUID) magnetometry at room temperature. The external magnetic field was applied along the [110], [1$\bar{1}$0], and [100] directions. All the examined $Co_{2-x}Fe_{1-y}Si_{1+x+y}$ films are ferromagnetic at room temperature and have the same easy axis of magnetization ([110] direction). Figure 4 shows the magnetization curves of the stoichiometric Co_2FeSi film grown at 100 °C and an expanded view along the [110] direction in the inset. The magnetization curves show an easy axis [110], a hard axis [1$\bar{1}$0], and an intermediate axis [100]. The magnetization curve along [110] shows a square-shaped hysteresis loop with a small coercive field of 4.5 Oe, indicating excellent crystal quality. The saturation magnetization of stoichiometric films amounts to 1250 ± 120 emu/cm^3, which is relatively close to that of bulk Co_2FeSi [1124 emu/cm^3 at 295 K (Ref. 23)], confirming the stoichiometric composition determined by HRXRD.

The easy axis of $Co_2FeSi/GaAs$ ([110] direction) is inconsistent with that expected from the magnetocrystalline anisotropy and found in other Heusler alloys like $Fe_3Si/GaAs$ ($\langle 100\rangle$ directions).[27] The discrepancy can be explained by an analysis of the in-plane magnetic anisotropy assuming two anisotropy components, the cubic magnetocrystalline anisotropy, and the uniaxial anisotropy. The effective value of the uniaxial and cubic magnetocrystalline anisotropy constants (K_u^{eff} and K_1^{eff}, respectively) for the stoichiometric Co_2FeSi film ($d=18.5$ nm) were obtained by fitting the magnetization curves along the [1$\bar{1}$0] direction using the method described by Dumm *et al.*[28] We found $K_1^{\text{eff}}=1.8\times10^4$ emu/cm^3 and $K_u^{\text{eff}}=6.3\times10^4$ erg/cm^3, respectively. These two anisotropy constants have the same sign, however they do not share the same easy axis; $\langle 100\rangle$ and [110] directions for the cubic and the uniaxial component, respectively. As a result of the dominating uniaxial component, the easy axis in total is modulated to the [110] direction. The origin of the relatively large K_u^{eff} value despite the rather large film thickness is not yet clear. We believe that K_u^{eff} is a pure interface-related term originating from an anisotropic bonding at the FM/SC interface as has been found in other FM/SC systems.[29]

In conclusion, we have grown single-crystal Heusler alloy $Co_2FeSi/GaAs(001)$ hybrid structures by molecular beam epitaxy. Co_2FeSi layers with high crystal and interface perfection as well as smooth surfaces can be obtained by carefully controlling the fluxes of Co, Fe, and Si. The high crystal and interface perfection is preserved up to growth temperature of 250 °C, being thus much more thermally stable than conventional ferromagnetic metals on GaAs.

[1] R. Fiederling, M. Keim, G. Reuscher, W. Ossau, G. Schmidt, A. Waag, and L. W. Molenkamp, Nature (London) **402**, 787 (1999).
[2] Y. Ohno, D. K. Young, B. Beschoten, F. Matsukura, H. Ohno, and D. D. Awschalom, Nature (London) **402**, 790 (1999).
[3] H. J. Zhu, M. Ramsteiner, H. Kostial, M. Wassermeier, H.-P. Schönherr, and K. H. Ploog, Phys. Rev. Lett. **87**, 016601 (2001).
[4] B. T. Jonker, A. T. Hanbicki, Y. D. Park, G. Itskos, M. Furis, G. Kioseoglou, A. Petrou, and X. Wei, Appl. Phys. Lett. **79**, 3098 (2001).
[5] X. Jiang, R. Wang, S. van Dijken, R. Shelby, R. Macfarlane, G. S. Solomon, J. Harris, and S. S. P. Parkin, Phys. Rev. Lett. **90**, 256603 (2003).
[6] T. Manago and H. Akinaga, Appl. Phys. Lett. **81**, 694 (2002).
[7] A. Kawaharazuka, M. Ramsteiner, J. Herfort, H.-P. Schönherr, H. Kostial, and K. H. Ploog, Appl. Phys. Lett. **85**, 3492 (2004).
[8] C. Palmstrøm, MRS Bull. **28**, 725 (2003).
[9] R. A. de Groot, F. M. Mueller, P. G. van Engen, and K. H. J. Buschow, Phys. Rev. Lett. **50**, 2024 (1983).
[10] I. Galanakis, P. H. Dederichs, and N. Papanikolaou, Phys. Rev. B **66**, 174429 (2002).
[11] S. Fujii, S. Sugimura, Ishida, and S. Asano, J. Phys.: Condens. Matter **2**, 8583 (1990).
[12] T. Ambrose, J. J. Krebs, and G. A. Prinz, Appl. Phys. Lett. **76**, 3280 (2000).
[13] S. N. Holmes and M. Pepper, Appl. Phys. Lett. **81**, 1651 (2002).
[14] J. Q. Xie, J. W. Dong, J. Lu, C. J. Palmstrøm, and S. Mckernan, Appl. Phys. Lett. **79**, 1003 (2001).
[15] M. S. Lund, J. W. Dong, J. Lu, X. Y. Dong, C. J. Palmstrøm, and C. Leighton, Appl. Phys. Lett. **80**, 4798 (2002).
[16] W. Van Roy, J. De Boeck, B. Brijs, and G. Borghs, Appl. Phys. Lett. **77**, 4190 (2000).
[17] P. Bach, A. S. Bader, C. Rüster, C. Gould, C. R. Becker, G. Schmidt, L. W. Molenkamp, W. Weigand, C. Kumpf, E. Umbach, R. Urban, G. Woltersdorf, and B. Heinrich, Appl. Phys. Lett. **83**, 521 (2003).
[18] S. Kämmerer, A. Thomas, A. Hütten, and G. Reiss, J. Appl. Phys. **85**, 79 (2004).
[19] L. J. Singh, Z. H. Barber, Y. Miyoshi, W. R. Branford, and L. F. Cohen, J. Appl. Phys. **95**, 7231 (2004).
[20] R. J. Soulen Jr., J. M. Byers, M. S. Osofsky, B. Nadgorny, T. Ambrose, S. F. Cheng, P. R. Broussard, C. T. Tanaka, J. Nowak, J. S. Moodera, A. Barry, and J. M. D. Coey, Science **282**, 85 (1998).
[21] S. Picozzi, A. Continenza, and A. J. Freeman, Phys. Rev. B **69**, 094423 (2004).
[22] For the details of the $L2_1$ structure, see P. J. Webster and K. R. A. Ziebeck, *Landolt-Börnstein New Series III/19c* (Springer, Berlin, 1988), p. 75.
[23] V. Niculescu, J. I. Budnick, W. A. Hines, K. Raj, S. Pickart, and S. Skalski, Phys. Rev. B **19**, 452 (1979).
[24] T. Nishizawa and K. Ishida, Bull. Alloy Phase Diagrams **5**, 250 (1984).
[25] H.-P. Schönherr, R. Nötzel, W. Ma, and K. H. Ploog, J. Appl. Phys. **89**, 169 (2001).
[26] G. Kötter, K. Nembach, F. Wallow, and E. Nembach, Mater. Sci. Eng., A **114**, 29 (1989).
[27] J. Herfort, H.-P. Schönherr, and K. H. Ploog, Appl. Phys. Lett. **83**, 3912 (2004); J. Herfort, H.-P. Schönherr, K.-J. Friedland, and K. H. Ploog, J. Vac. Sci. Technol. B **22**, 2073 (2004).
[28] M. Dumm, M. Zölfl, R. Moosbühler, M. Brockmann, T. Schmidt, and G. Bayreuther, J. Appl. Phys. **87**, 5457 (2000).
[29] E. Sjöstedt, L. Nordström, F. Gustavsson, and O. Eriksson, Phys. Rev. Lett. **89**, 267203 (2002).

Available online at www.sciencedirect.com
SCIENCE DIRECT®
ELSEVIER
Journal of Crystal Growth 285 (2005) 514–520
JOURNAL OF CRYSTAL GROWTH
www.elsevier.com/locate/jcrysgro

Epitaxial Fe_3Si films stabilized on GaAs(1 1 3)A substrates

P.K. Muduli*, J. Herfort, H.-P. Schönherr, K.H. Ploog

Paul-Drude-Institut für Festkörperelektronik, Hausvogteiplatz 5-7, D-10117 Berlin, Germany

Received 9 March 2005; received in revised form 30 August 2005; accepted 30 August 2005
Available online 20 October 2005
Communicated by C.R. Abernathy

Abstract

We report epitaxial growth of the Heusler alloy Fe_3Si on high-index GaAs(1 1 3)A substrates by molecular-beam epitaxy. The growth temperature and growth rate are optimized to 250 °C and 0.13 nm/min, respectively, for producing Fe_3Si films with structural properties comparable to that of Fe_3Si films on GaAs(0 0 1). The layers grown under these conditions exhibit high crystal quality with smoother interface/surface and maintain the [1 1 3] orientation of the GaAs substrate. The Fe–Si alloy composition is varied around the Fe_3Si stoichiometry using these optimized growth conditions. The magnetic properties of a typical Fe_3Si layer with the best structural properties exhibit a four-fold magnetic anisotropy, as expected from the magnetocrystalline anisotropy.

PACS: 81.15.Hi; 75.50.Bb; 75.70.−i

Keywords: A3. Molecular beam epitaxy; A1. High resolution X-ray diffraction; B2. Magnetic materials; B2. Fe_3Si; B2. GaAs(1 1 3)A

1. Introduction

Ferromagnet-semiconductor hybrid structures (FM/SC) are important for the field of spintronics [1]. Elemental ferromagnets like Fe, Co, Ni, or their alloys which are usually employed for such applications tend to react at the FM/SC interface. Relative low growth temperatures are required to suppress these interfacial reactions, which are considered to be detrimental to spin dependent transport across the interface. Alternative materials of better thermal stability and improved interface quality are highly desirable for such applications. In a previous work [2], we reported the growth of Fe_3Si films on GaAs(0 0 1). Fe_3Si has a cubic $D0_3$ crystal structure with a lattice constant very close to GaAs and a high Curie temperature of 840 K [3]. Fe_3Si can also be regarded as a Heusler alloy Fe_2FeSi as there are two distinct crystallographic and magnetic Fe sites. In Ref. [2], an optimum growth temperature range of $150\,^{\circ}C < T_G < 250\,^{\circ}C$ was established, where

*Corresponding author. Tel.: +00493020377364; fax: +00493020377201.
E-mail address: muduli@pdi-berlin.de (P.K. Muduli).

0022-0248/$ - see front matter © 2005 Elsevier B.V. All rights reserved.
doi:10.1016/j.jcrysgro.2005.08.049

ferromagnetic films of high crystal and interface quality were obtained [2]. This temperature is much higher than usually used for the growth of Fe films on GaAs [4–6]. Moreover, we have recently demonstrated that the Fe_3Si films are thermally stable to ex situ annealing at least up to 400 °C [7]. These properties make Fe_3Si, a very good alternative to elemental ferromagnets.

So far the growth of ferromagnets on GaAs substrates has been focused mainly on the low-index surfaces. Much less work is devoted to study ferromagnetic films on high-index semiconductor surfaces. In fact, obtaining a stable high-index surface of a ferromagnet in general is rather difficult. For instance, Fe films deposited on Cu(1 1 3) did not maintain the same orientation relationship with the substrate, which led to a highly strained and distorted bcc Fe arrangement with (1 1 2) orientation [8]. On the other hand, the thermal stability and the ordering of such surfaces with reduced symmetry and coordination number offer a variety of opportunities for inducing new phenomena and are thus promising for new device applications of the FM/SC [9]. The GaAs(1 1 3)A surface in particular is characterized by a low surface symmetry with the two major in-plane axes, namely $[3\,3\,\bar{2}]$ and $[\bar{1}\,1\,0]$ being crystallographically in-equivalent. Moreover, due to this reduced symmetry, we previously observed new features in the planar Hall effect of Fe films on GaAs(1 1 3)A, which cannot be understood in the usual picture of anisotropic magnetoresistance [10,11]. In this report we will demonstrate for the first time that a ferromagnetic Heusler alloy, namely Fe_3Si, can be stabilized even on the high-index GaAs(1 1 3)A surface with the same orientation of the substrate and with structural properties comparable to that of Fe_3Si films on GaAs(0 0 1). Our main focus here is on the growth optimization and magnetic characterization of the Fe_3Si films on GaAs(1 1 3)A.

2. Experimental procedure

The growth of Fe_3Si films was performed on well-ordered As-rich GaAs(1 1 3)A templates. First, a 70 nm thick GaAs buffer layer was prepared in a conventional III–V compound semiconductor growth chamber at a temperature of 610 °C. To get an As-rich surface, the substrate was cooled down with the As shutter open until 400 °C. The As-rich surface was chosen to avoid the formation of macroscopic defects on the surface similar to the case of Fe on GaAs(0 0 1) and GaAs(1 1 3)A substrates [6]. The growth of Fe_3Si was then performed in an As-free deposition chamber connected to the III–V growth chamber through an ultra-high vacuum interlock. Fe and Si were co-deposited from high-temperature effusion cells at a base pressure of 1×10^{-10} Torr. The following systematic approach has been adopted to optimize the growth of Fe_3Si on GaAs(1 1 3)A substrates. First, we kept the Fe to Si flux ratio constant and varied the growth temperature for Fe_3Si from 100 to 500 °C. With the obtained optimum growth temperature, we then adjusted the growth rate to obtain a smooth surface morphology. Finally, to tune the Fe–Si composition, we varied the Fe to Si flux ratio at these optimized growth conditions. The growth was monitored in situ using reflection high-energy electron diffraction (RHEED). The thickness for all layers is between 35 and 50 nm, which was determined using ex situ X-ray reflectivity (XRR) and high-resolution X-ray diffraction (HRXRD). XRR and HRXRD measurements were done using a PANalytical X'Pert diffractometer system with a Ge(2 2 0) hybrid monochromator using CuK_{α_1} radiation.

3. Results and discussion

3.1. Structural characterization

Fig. 1 shows normalized *skew-symmetric* ω–2θ scans near the GaAs(0 0 4) reflection for Fe_3Si films grown at different growth temperatures from 100 to 500 °C. The measurements were performed with an analyzer crystal in the diffracted beam optics. The sample grown at 100 °C did not show any layer peak in the ω–2θ scans nor any RHEED pattern during growth, implying that the layer is amorphous. Though the samples grown at $T_G = 200$, 250, 300, and 400 °C, show a layer

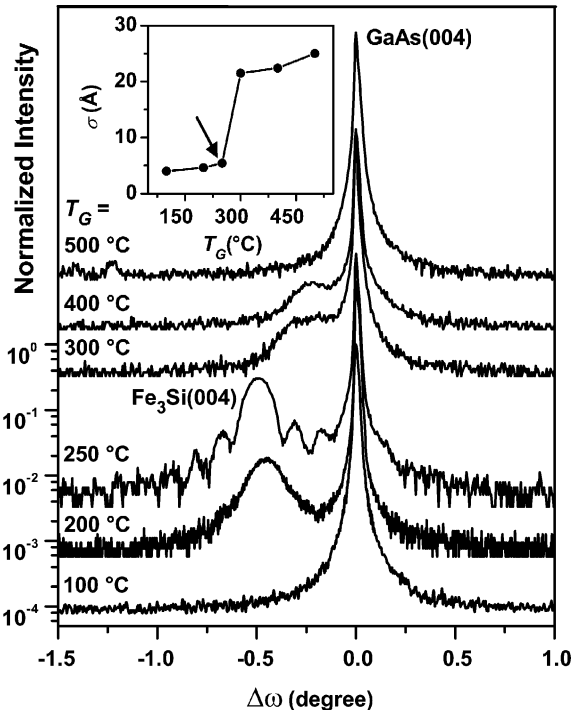

Fig. 1. Normalized *skew-symmetric* ω–2θ scans for Fe_3Si/GaAs(1 1 3)A films with different growth temperature T_G from 100 to 500 °C. The curves are normalized to the GaAs(0 0 4) reflection and are shifted with respect to each other for clarity. The inset shows a plot of the RMS roughness σ vs T_G. The arrow indicates the optimized growth temperature of 250 °C.

peak due to the Fe_3Si(0 0 4) reflection, only the sample grown at 250 °C shows distinct interference fringes, indicating a high structural ordering and an abrupt interface [2]. However, the temperature window where these fringes are observed is much narrower compared to that on GaAs(0 0 1), indicating a narrow growth temperature window for GaAs(1 1 3)A substrates. Most importantly, the epitaxial orientational relationship of the sample grown at $T_G = 250$ °C and all other samples of Fig. 3, as determined from HRXRD, is given by $Fe_3Si(1\,1\,3)[3\,3\,\bar{2}] \parallel GaAs(1\,1\,3)[3\,3\,\bar{2}]$. The same orientational relationship of Fe_3Si on GaAs(1 1 3)A is indeed consistent with our expectation on the basis of the close lattice constants of Fe_3Si and GaAs and it demonstrates the stability of these films.

For the sample grown at $T_G = 400$ °C, we found additional peaks in long range *skew-symmetric* ω–2θ scans (not shown) at $2\theta = 34.9°$ and $2\theta = 73.9°$, which are very close to Fe_2As(1 1 0) and (2 2 0) reflections, respectively [12]. Though the exact chemical composition for this layer at 400 °C is not known, the presence of the these additional peaks indicates the formation of interfacial compounds. No additional peaks were observed for $T_G \leqslant 300$ °C. Nevertheless, this implies that the growth of Fe_3Si films on GaAs(1 1 3)A can be performed at a much higher temperature compared to Fe on GaAs. Noteworthy, the optimum growth of Fe_3Si on GaAs(1 1 3)A takes place at the same T_G (though the range is much narrower) as for Fe_3Si on GaAs(0 0 1), whereas to grow Fe films on GaAs(1 1 3)A a lower T_G was required [6]. The root mean square (RMS) roughness of the films has been determined by atomic force microscopy (AFM) and is plotted vs T_G in the inset of Fig. 1. Fe_3Si films with $T_G \leqslant 250$ °C exhibit minimized RMS roughness values of about 5–6 Å (measured over a $5 \times 5\,\mu m^2$ area). A significant increase of RMS roughness occurs for $T_G > 250$ °C in agreement with the degradation of the films observed in HRXRD. For $T_G = 500$ °C, neither a layer peak nor any additional peak was observed in the *skew-symmetric* ω–2θ scans. In fact, the AFM image of this sample shows the formation of a large number of pyramidal-shaped nanocrystals indicating a three-dimensional growth mode.

The RMS roughness of the films can be reduced even further by lowering the growth rate of the Fe_3Si layer. This is demonstrated in Figs. 2(a) and (b) which show AFM images of two samples grown at 250 °C with a growth rate of 0.26 and 0.13 nm/min, respectively. It should be noted that for the experiments in Fig. 1, the Fe_3Si growth rate (as determined from thickness calibration) was maintained at about 0.26 nm/min. For the lower growth rate (Fig. 2(b)), the RMS roughness is reduced from 5 to 1.6 Å (measured over a $5 \times 5\,\mu m^2$ area). Moreover, the growth rate reduction also improves the magnetic properties. We will return to this point later. To summarize the difference in growth conditions of the Fe_3Si films on GaAs(1 1 3)A substrates, the optimized growth temperature range is narrower and the growth rate is lower compared to the growth on GaAs(0 0 1).

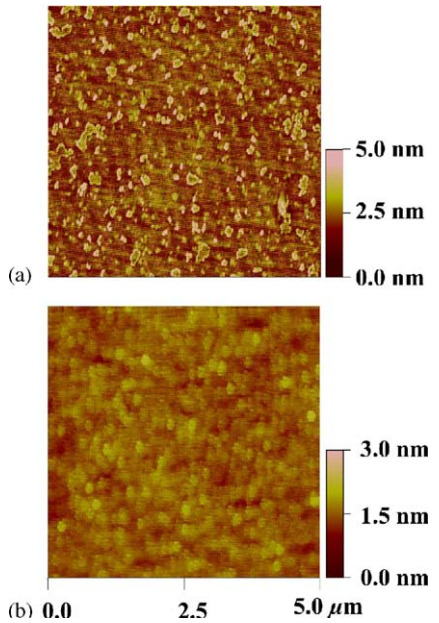

Fig. 2. AFM images of Fe_3Si films grown at 250 °C, with a growth rates of (a) 0.26 nm/min and (b) 0.13 nm/min. The RMS roughness decreases from 5 to 1.6 Å for (a) to (b), respectively.

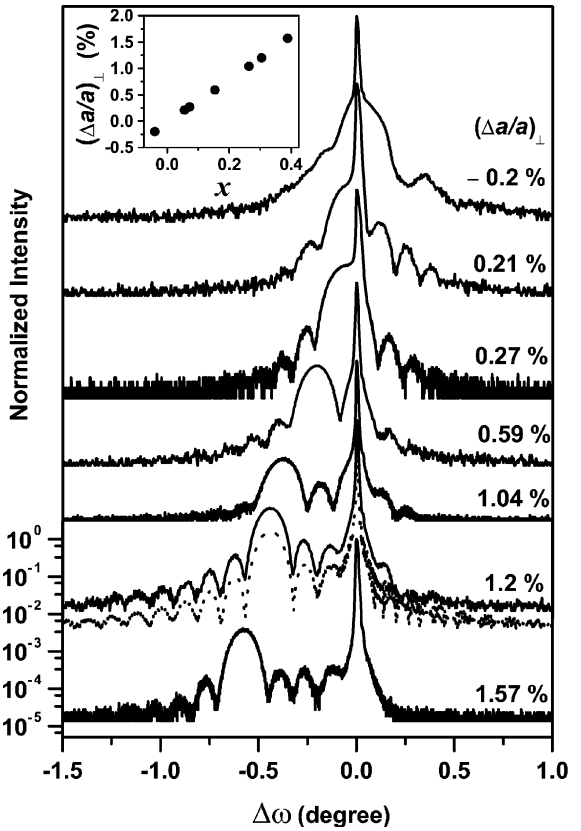

Fig. 3. Normalized *skew-symmetric* ω–2θ scans for Fe_3Si/GaAs(1 1 3)A films grown at 250 °C with different Si cell temperature. The curves are normalized to the GaAs(0 0 4) reflection and are shifted with respect to each other for clarity. The dotted line shows a simulation for a sample with $(\Delta a/a)_\perp = 1.2\%$. The inset shows a plot of x with $(\Delta a/a)_\perp$.

The phase boundary of the bulk Fe_3Si covers a range from 9 to 26.6 at% Si [13]. To examine the stability of the Fe_3Si phase in this range, the Fe–Si composition was varied using the above optimized growth conditions. For simplicity, we kept the Fe cell temperature constant and varied the Si cell temperature. Fig. 3 summarizes the results of HRXRD on these samples. The high crystal and interface quality of these films is again reflected by the presence of a large number of interference fringes for all samples. For a quantitative comparison, we have included a simulation [14] of the rocking curve using the Takagi–Taupin formalism for the Fe_3Si layer with perpendicular lattice mismatch $(\Delta a/a)_\perp = 1.2\%$. Fit parameters are $(\Delta a/a)_\perp$ and the layer thickness d, taking into account only the instrumental broadening of the diffractometer. The agreement with the experiment is excellent. The full-width-at-half-maximum along the (0 0 4) Bragg reflection of the layer is as low as 0.14° for this 40 nm thick film. In Fig. 3, the $Fe_{3+x}Si_{1-x}$ peak systematically shifts with respect to the GaAs(0 0 4) main peak indicating a different lattice constant of the layers. Here x denotes the deviation from the exact stoichiometry. As the Fe/Si flux ratio is varied around stoichiometry, any excess Fe will substitute into Si lattice sites and vice versa, leading to different lattice constants of the layers [15]. It should be mentioned that with increase of the Si content, a slight degradation of the films is observed which becomes apparent from the reduced number of interference fringes in the uppermost curves of Fig. 3. From the peak separation, $(\Delta a/a)_\perp$ of the layers was determined, which varies from 1.6% to −0.2%. All layers are found to be tetragonally distorted with a parallel lattice mismatch less than 0.05%, as evidenced by

HRXRD profiles of asymmetric (0 0 4) Bragg reflections in grazing incidence geometry (not shown here). The composition of these films was determined from $(\Delta a/a)_{\perp}$ using the method described in our previous work on the GaAs(0 0 1) system [2]. The Si content obtained from this method was found to be in the range of 15–26 at%, which lies within the phase boundary of the Fe_3Si phase covering a range from 9 to 26.6 at% Si [13]. The inset in Fig. 3 shows the correlation of x on $(\Delta a/a)_{\perp}$. Thus films with exact stoichiometry can be obtained for almost lattice-matched films.

3.2. Magnetic properties

The magnetic properties of these Fe_3Si films were studied ex situ using superconducting quantum interference device (SQUID) magnetometry. We will discuss the magnetic properties of a typical Fe_3Si layer exhibiting superior structural properties and study the effect/requirement of the low growth rate. Figs. 4(a) and (b) show room temperature (RT) magnetization curves for the corresponding samples in Fig. 2(a) and (b), respectively, representing different growth rates. The composition of the two films is comparable ($x = 0.39$ and 0.33 for Figs. 4(a) and (b)). Both the samples are ferromagnetic at RT and exhibit a dominating in-plane four-fold magnetic anisotropy, with the easy axis along the $\langle 0\,3\,\bar{1}\rangle$ directions. The two major in-plane crystallographic inequivalent directions, namely $[3\,3\,\bar{2}]$ and $[\bar{1}\,1\,0]$ are found to be magnetically equivalent and are intermediate axes. The in-plane four-fold magnetic anisotropy in these low symmetric [1 1 3] orientated samples arises from the cubic

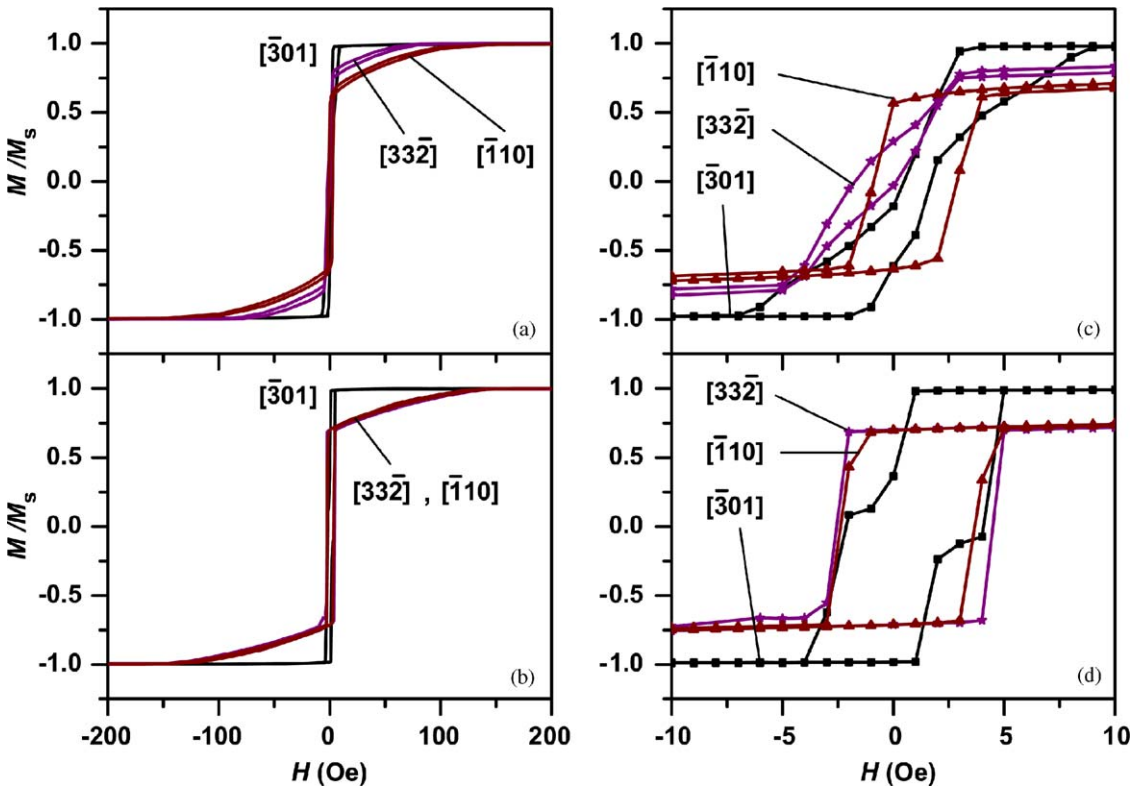

Fig. 4. Room temperature SQUID magnetization curves along different crystallographic directions for the samples shown in Fig. 2 for a growth rate of (a) 0.26 and (b) 0.13 nm/min, respectively. (c) and (d) are magnified low field region corresponding to (a) and (b), respectively.

magnetocrystalline anisotropy, and is a result of the large demagnetization energy in thin film geometry [16]. Hence, similar to the case of Fe on GaAs(1 1 3)A a reorientation of the bulk easy axis of Fe_3Si, namely $\langle 1\,0\,0\rangle$ towards $\langle 0\,3\,\bar{1}\rangle$ takes place. The coercive field for this Fe_3Si film (4–5 Oe) in general is lower compared to that of the Fe films, which also reflects the improved structural quality of the films. The saturation magnetization (M_s) of the sample in Fig. 4(b) is $(1300 \pm 200)\,\mathrm{emu/cm^3}$, which is lower compared to bulk Fe ($1740\,\mathrm{emu/cm^3}$), but comparable to the value obtained for $Fe_3Si(0\,0\,1)$ films with the same composition [17]. However, the magnetic reversal of the two samples are different and can be more clearly seen in Figs. 4(c) and (d), which are the corresponding low-field behavior of Figs. 4(a) and (b), respectively. For the sample prepared with higher growth rate, the reversal is gradual and the switching width is about 5 Oe in all directions as shown in the Fig. 4(c). On the other hand, the sample prepared with lower growth rate shows a sharp reversal, with a switching width of less than 1 Oe. We assume that the increased switching width in Fig. 4(c) is correlated with the rough surface morphology in Fig. 2(a). The interaction between the small particles (as seen in the AFM image) could be a possible reason for the increased switching width. The magnetization curve along the $[0\,3\,\bar{1}]$ direction in Fig. 4(d) shows a two-jump reversal, which is ascribed to a ''nonideal'' two-jump reversal similar to Fe films [18]. The magnetic characterization of all the other Fe_3Si films with varying composition shows ferromagnetism at RT with a dominating in-plane four-fold magnetic anisotropy. However, a small uniaxial magnetic anisotropy is also found superimposed with the four-fold magnetic anisotropy and with the easy axis lying along the $\langle \bar{1}\,1\,0\rangle$ axes for samples with higher Si content. The low coercive field is maintained in the studied composition range around the stoichiometry. A significant decrease of M_s (compared to the bulk value) is found for the sample with the highest Si content of 26 at%. More detailed studies of the effect of different compositions and the growth temperature on the magnetic properties will be discussed elsewhere.

4. Conclusions

Our studies shows that high quality Fe_3Si films can be grown on GaAs(1 1 3)A maintaining the [1 1 3] orientation of the substrate. The growth conditions are optimized at a growth temperature of 250 °C and a low growth rate of 0.13 nm/min at which the layer quality is comparable to the Fe_3Si films on GaAs(0 0 1) substrates. We have demonstrated the importance of a low growth rate, which is more specific to the [1 1 3] orientation, to obtain a smooth surface morphology and superior magnetic properties. The optimized growth of Fe_3Si with varying Fe–Si alloy composition is also demonstrated around the Fe_3Si stoichiometry. All the layers are shown to be ferromagnetic at RT. The layers exhibit a dominating four-fold magnetic anisotropy, which arises from the magnetocrystalline anisotropy and large demagnetization energy of the Fe_3Si films. These studies show the stability of the high-index surface of a thermally stable ferromagnet, Fe_3Si on a semiconductor substrate. This might be useful for future device applications.

Acknowledgements

Part of this work has been supported by the German BMBF under the research program *NanoQUIT* (contract no. 01BM463). The authors would like to thank O. Brandt, L. Däweritz, and M. Hashimoto for useful discussions and B. Jenichen for critical reading of the manuscript.

References

[1] G.A. Prinz, Science 282 (1998) 1660.
[2] J. Herfort, H.-P. Schönherr, K.H. Ploog, Appl. Phys. Lett. 83 (2003) 3912.
[3] G. Schlatte, G. Inden, W. Pitch, Z. Metallk. 65 (1974) 94; H. Wever, G. Frohberg, Z. Metallk. 65 (1974) 747.
[4] M. Zölfl, M. Brockmann, M. Köhler, S. Kreuzer, T. Schweinbck, S. Miethaner, F. Bensch, G. Bayreuther, J. Magn. Magn. Mater. 175 (1997) 16.
[5] Y.B. Xu, E.T.M. Kernohan, D.J. Freeland, A. Ercole, M. Tselepi, J.A.C. Bland, Phys. Rev. B 58 (1998) 890.
[6] H.-P. Schönherr, R. Nötzel, W. Ma, K.H. Ploog, J. Appl. Phys. 89 (2001) 169.

[7] J. Herfort, H.-P. Schönherr, A. Kawaharazuka, M. Ramsteiner, K.H. Ploog, J. Crystal. Growth 278 (2005) 666.
[8] S. Fölsch, B.-C. Choi, K.-H. Rieder, Phys. Rev. B 54 (1996) 10855.
[9] A.J. Freeman, Ru-quian Wu, J. Magn. Magn. Mater. 100 (1991) 497 (and references therein).
[10] K.-J. Friedland, R. Nötzel, H.-P. Schönherr, A. Riedel, H. Kostial, K.H. Ploog, Physica E 10 (2001) 442.
[11] K.J. Friedland, P.K. Muduli, J. Herfort, H.-P. Schönherr, K.H. Ploog, J. Supercond. 18 (2005) in press, doi: 10.1007/s10948-005-0002-5.
[12] B. Lépine, S. Ababou, A. Guivarc'h, G. Jezéquél, S. Députier, R. Guérin, A. Filipe, A. Schuhl, F. Abel, C. Cohen, A. Rocher, J. Crestou, J. Appl Phys. 83 (1998) 3077.
[13] M. Hansen, Constitution of Binary Alloys, McGraw-Hill, New York, 1958
R.P. Elliot, Constitution of Binary Alloys, Suppl. 1, McGraw-Hill, New York, 1965 (see Fe-Si phase diagram).
[14] For the simulation in the *skew geometry*, the (0 0 4) reflection of GaAs(1 1 3) was approximated by the symmetric (0 0 4) reflection of GaAs(0 0 1). For the dynamical X-ray diffraction formalism used in this simulation see, O. Brandt, P. Waltereit, K.H. Ploog, J. Phys. D 35 (2002) 577.
[15] W.A. Hines, A.H. Menotti, J.I. Budnick, T. Litrenta, V. Niculescu, K. Raj, Phys. Rev. B 13 (1976) 4060.
[16] P.K. Muduli, J. Herfort, H.-P. Schönherr, K.H. Ploog, J. Appl. Phys. 97 (2005) 123904;
P.K. Muduli, J. Herfort, H.-P. Schönherr, L. Däweritz, K.H. Ploog, Appl. Phys. A 81 (2005) 901.
[17] J. Herfort, H.-P. Schönherr, K.-J. Friedland, K.H. Ploog, J. Vac. Sci. Technol. B 22 (2004) 2073.
[18] C. Daboo, R.J. Hicken, E. Gu, M. Gester, S.J. Gray, D.E.P. Eley, E. Ahmad, J.A.C. Bland, R. Ploessl, J.N. Chapman, Phys. Rev. B 51 (1995) 15964.

Antisymmetric contribution to the planar Hall effect of Fe_3Si films grown on GaAs(113)*A* substrates

P. K. Muduli,* K.-J. Friedland, J. Herfort, H.-P. Schönherr, and K. H. Ploog
Paul-Drude-Institut für Festkörperelektronik, Hausvogteiplatz 5-7, D-10117 Berlin, Germany
(Received 19 May 2005; revised manuscript received 1 August 2005; published 22 September 2005)

The planar Hall effect (PHE) in ferromagnets is believed to result from the anisotropic magnetoresistance (AMR) and hence does not change the sign by reversing the direction of the applied in-plane magnetic field. Our studies of the ferromagnetic Heusler alloy Fe_3Si films grown on low-symmetric GaAs(113)A substrates however show a change in the sign of the PHE by reversing the direction of the applied field, indicating the existence of an additional antisymmetric component superimposed with the usual symmetric AMR term. This antisymmetric component shows a maximum along the major in-plane $\langle 33\bar{2}\rangle$ axes and vanishes along the other major in-plane $\langle \bar{1}10\rangle$ axes. A phenomenological model based on the symmetry of the crystal provides a good explanation of the observed antisymmetric contribution to the PHE. The model shows that this component arises from the antisymmetric part of the magnetoresistivity tensor and is basically a second order Hall effect. It is shown that the observed effect can be ascribed to the Umkehr effect, which refers to the coexistence of even and odd terms in the component of magnetoresistivity tensor. A sign reversal of this antisymmetric component is also found for a Si content above 21 at. % and at temperatures below a certain critical temperature which increases with increasing Si content.

DOI: 10.1103/PhysRevB.72.104430 PACS number(s): 75.47.−m, 73.50.Jt, 73.43.Qt, 72.15.Gd

I. INTRODUCTION

Ferromagnet-semiconductor hybrid structures (FM/SC) have received significant attention for their possible application in spintronics.[1–3] Most of the previous studies of FM/SC were concentrated on low-index film orientation. Much less work has been devoted to study ferromagnetic films on high-index semiconductor substrates. In fact, obtaining a stable high-index surface of a ferromagnet in general is rather difficult. For instance, Fe films deposited on Cu(113) did not maintain the same orientational relationship with the substrate, which led to a highly strained and distorted bcc Fe arrangement with (112) orientation.[4] On the other hand, the thermal stability and ordering of such surfaces with reduced symmetry and coordination number offer the opportunities to manipulate the magnetic properties in FM/SC.[5] In a previous work,[6] we have reported on the successful growth of the Heusler alloy Fe_3Si on GaAs(113)A substrates. Fe_3Si has the cubic $D0_3$ crystal structure with a lattice constant very close to GaAs. This fact allows us to stabilize the [113] orientation of the Fe_3Si films on GaAs(113)A with structural properties comparable to those of Fe_3Si films on GaAs(001).[7] In this paper we will show that the magnetotransport properties, especially the planar Hall effect of these films are significantly affected by the reduced symmetry of the [113] orientation.

The so-called planar Hall effect (PHE) refers to the transverse voltage developed perpendicular to the current for a magnetic field applied in the film plane. It is believed to originate from a purely anisotropic magnetoresistance (AMR) effect[8] and depends on the angle between the magnetization and the direction of the sensing current. Suppose that a saturating external magnetic field, applied in the plane of the film, varies so that the angle θ_M of the magnetization **M** varies, then the resistivities ρ_{xx} and ρ_{xy} measured parallel and perpendicular to the current **J** for a single domain and polycrystalline film are given by[9,10]

$$\rho_{xx} = \rho_\perp + (\rho_\parallel - \rho_\perp)\cos^2\theta_M, \tag{1}$$

$$\rho_{xy} = \frac{1}{2}(\rho_\parallel - \rho_\perp)\sin 2\theta_M, \tag{2}$$

where $\rho_\perp$ and $\rho_\parallel$ are the resitivities at $\mathbf{J}\perp\mathbf{M}$, and $\mathbf{J}\parallel\mathbf{M}$, respectively. Equations (1) and (2) are conventionally used to describe the AMR and PHE, respectively. According to Eq. (2) we have $\rho_{xy}(H>+H_{sat})=\rho_{xy}(H<-H_{sat})$, where H is the applied magnetic field and H_{sat} denotes the in-plane saturation field. This is understood from the fact that both AMR and PHE are believed to arise from the symmetric part of the magnetoresistivity tensor, which does not change sign when the direction of the magnetic field is reversed.[9] In this paper we will show that for single crystalline Fe_3Si films grown on low-symmetric GaAs(113)A substrates, Eq. (2) for the PHE is not strictly followed. In contrast, the PHE shows a combination of even (symmetric) and odd (antisymmetric) terms when a saturating magnetic field is applied in any direction other than the symmetric $\langle \bar{1}10\rangle$ axes, indicating an observation of Umkehr effect.[11] The situation is similar to our previous experiments of Fe on GaAs(113)A substrates,[12,13] where we had reported an experimental observation of the effect. In this paper, we will develop a phenomenological model by taking into account the symmetry of the crystal to explain this effect. We will show how the observed antisymmetric component arises from a second order term of the antisymmetric part of the magnetorestivity tensor, as a result of the lower symmetry of the [113] orientation. The dependence of this antisymmetric component on the Si content of the Fe_3Si films and the measurement temperature will also be discussed. Possible reasons for the change in sign of this

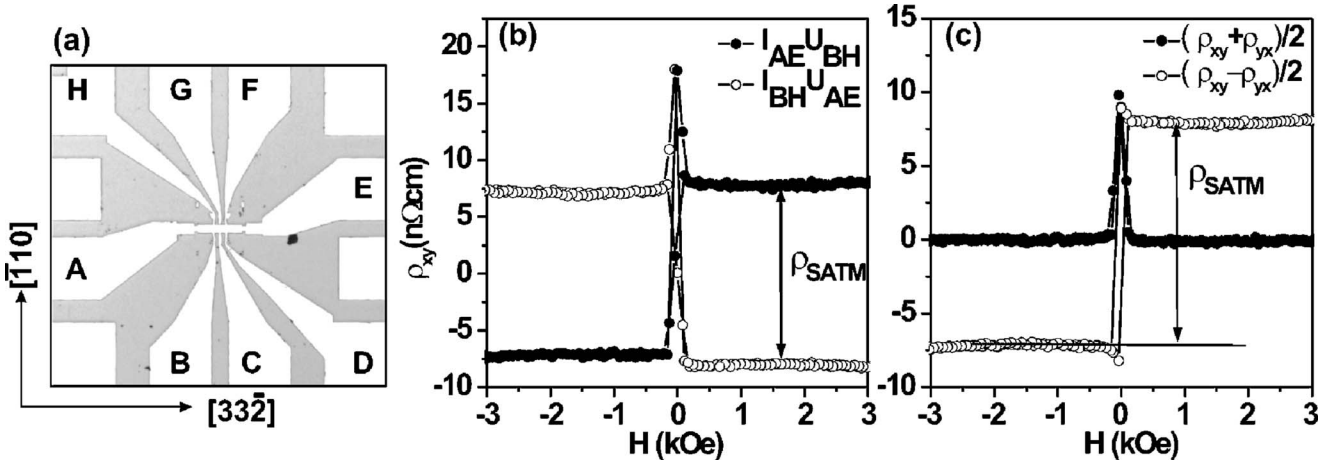

FIG. 1. (a) Optical microscopy image of the Hall bar structure employed for the magnetotransport studies. The contacts are labeled and the crystallographic directions of the (113) plane are shown. (b) Planar Hall effect response from $Fe_{3+x}Si_{1-x}$ films grown on GaAs(113)A at 300 K for a sample with $x=0.07$ and magnetic field applied along $[33\bar{2}]$. (c) Separation of the symmetric and antisymmetric contribution of PHE.

antisymmetric component with composition and temperature will also be discussed.

II. EXPERIMENT

$Fe_{3+x}Si_{1-x}$ films with thicknesses in the range of 35–50 nm were grown on well-ordered As-rich GaAs(113)A templates by molecular-beam epitaxy. Here x describes the deviation from the exact stoichiometry. The details of the growth can be found elsewhere.[6] It is important to note that the [113] orientation of $Fe_{3+x}Si_{1-x}$ has been stabilized on GaAs(113)A, which is in fact a result of the rather small lattice mismatch between Fe_3Si and GaAs. The Si content was carefully varied in the range of 15–26.6 at. % Si, i.e., $0.4>x>-0.06$ which lies within the phase boundary of the stable Fe_3Si phase covering a range from 9 to 26.6 at. %Si.[14,15]

For the magnetotransport measurements Hall bar structures as shown in Fig. 1(a) were prepared by standard lithography techniques. The Hall bars were aligned along the $[33\bar{2}]$ direction by a combination of photolithography and ion-beam sputtering. A perfect alignment of the Hall bar structures ensures a homogenous current flow. Both AMR (ρ_{xx}) and PHE (ρ_{xy}) were measured simultaneously with a current of 3 mA along the Hall bar. A programmable stepper motor was used for the rotation of the sample in the magnetic field. Two different kinds of measurements were performed. First, we studied the angular dependence of the PHE response when a fixed in-plane magnetic field was applied. Second, the in-plane field orientation was kept fixed along a specific direction with respect to the longitudinal axis of the Hall bars, while the field magnitude was swept linearly between ±3 kOe. As the low transverse Hall resistivity, ρ_{xy} is smaller than the longitudinal resistivity, ρ_{xx}, some crossover from ρ_{xx} to ρ_{xy} may appear. In this case, we have corrected ρ_{xy} by $\rho_{xy}^{\mathrm{corr}}(H,\theta_H)=\rho_{xy}(H,\theta_H)-\gamma\,\rho_{xx}(H,\theta_H)$, where the factor γ was kept constant for a particular contact configuration.

III. RESULTS AND DISCUSSION

A. Experimental results

1. Antisymmetric component in PHE

In Fig. 1, we show the room temperature (300 K) PHE response from a nearly stoichiometric $Fe_{3+x}Si_{1-x}$ sample with $x=0.07$. An optical microscopy image of the Hall bar structure employed is shown in Fig. 1(a) with the contacts labeled as A, B,….,H in a counterclockwise sense. The PHE response is depicted in Fig. 1(b) for two cases with the current along AE and BH, which correspond to the $[33\bar{2}]$ and $[\bar{1}10]$ directions, respectively. The magnetic field was kept fixed along the $[33\bar{2}]$ direction. The planar Hall voltage was measured along the contacts BH and AE for the current along AE and BH, respectively. We denote the two cases $I_{AE}U_{BH}$ and $I_{BH}U_{AE}$ by ρ_{xy} and ρ_{yx}, respectively. Here, the positive x axis is taken along the $[33\bar{2}]$ direction. As can be seen, the PHE is completely saturated at a rather low field of less than 0.2 kOe (Ref. 16) but the PHE shows a sign change with reversal of the magnetic field direction, irrespective of the current direction. This was never observed in Fe and $Fe_{3+x}Si_{1-x}$ films grown on GaAs(001) substrates[13,17] and is completely unexpected from Eq. (2), which predicts only a symmetric contribution.[8,9] Also ρ_{xy} and ρ_{yx} have opposite signs just like the conventional Hall effect. This implies the presence of an antisymmetric component in PHE for the $Fe_{3+x}Si_{1-x}$ films on GaAs(113)A. In fact, the symmetric and the antisymmetric contribution can be separated by adding and subtracting the signals ρ_{xy} and ρ_{yx}, which is shown in Fig. 1(c). We clearly have an additional antisymmetric contribution to the PHE superimposed to the usual symmetric contribution of Eq. (2). Since the sample is completely saturated, we can rule out any contribution of domains to this effect. We define the difference, $\rho_{xy}(H>+H_{sat})-\rho_{xy}(H<-H_{sat})$ as a saturated antisymmetric transverse resistivity ρ_{SATM}, which is a measure of the antisymmetric component. When the sample is rotated slightly out-of-plane, the contribution from the anomalous

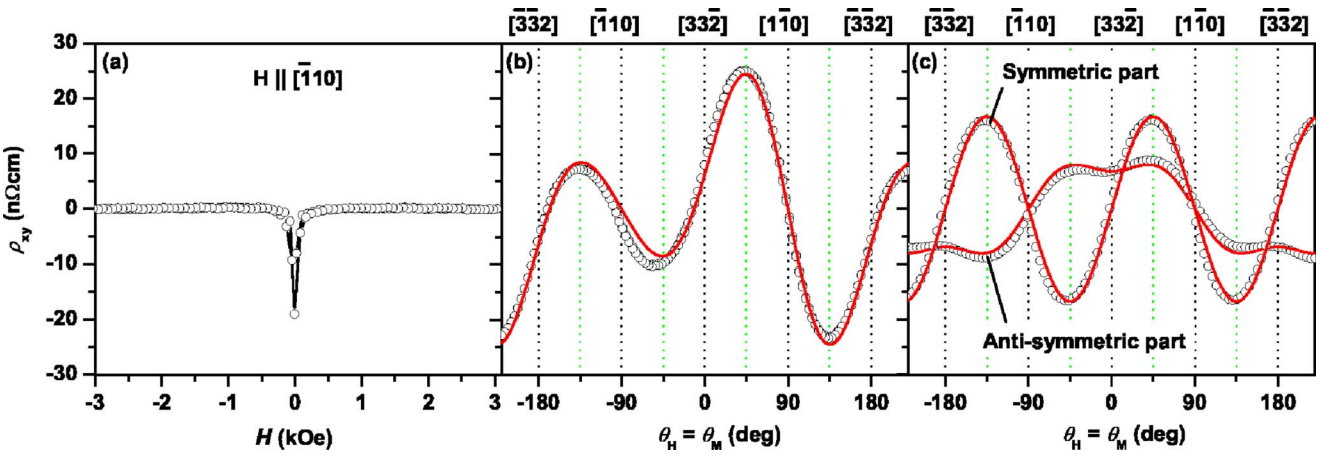

FIG. 2. (Color online) (a) Planar Hall effect response from the $Fe_{3+x}Si_{1-x}$ (x=0.07) film grown on GaAs(113)A with magnetic field applied in-plane along $[\bar{1}10]$ at 300 K showing the vanishing antisymmetric component. (b) Angular dependence of ρ_{xy} at 300 K with a saturating in-plane magnetic field so that $\theta_H=\theta_M$. Open circles represent experimental data and solid line (in red color) is a fit using Eq. (3) (see text). (b) Separation of the symmetric and antisymmetric part of the PHE. Open circles represent experimental data and solid lines (in red color) are fitted curves using a $\sin 2\theta_M$ behavior for symmetric part and $\rho^0_{SATM}\cos\theta_M+\rho^1_{SATM}\cos^3\theta_M$ type behavior for antisymmetric part. The major in-plane crystallographic directions for the (113) plane are also shown with 0° along $[33\bar{2}]$.

Hall effect (AHE) starts to appear as a slope in the high field region which is similar to that observed in Fe films on GaAs(113)A substrates.[12] But ρ_{SATM} does not vanish when a magnetic field is applied slightly out-of-plane in different directions. Since we are dealing with an antisymmetric contribution, the direction of the applied field relative to the current and the orientation of transverse resistivity determine the sign of ρ_{SATM}. To define the sign of ρ_{SATM}, from now on we will stick to the convention that the current is applied along AE and the PHE is measured along BH. For this configuration we found a positive sign of ρ_{SATM} (in the sample with x=0.07) at 300 K with a magnetic field applied along the $[33\bar{2}]$ direction. Of course the sign of ρ_{xy} changes when the direction of the field is reversed by 180°, i.e., toward $[\bar{3}\bar{3}2]$. But, fortunately these two directions can be identified unambiguously from x-ray diffraction (XRD) by measuring an asymmetric reflection such as (004). We can thus keep the field direction fixed along $[33\bar{2}]$ which has been confirmed for all samples by XRD. The positive direction of the magnetic field was defined in such a way that the Hall voltage in this configuration is negative for a n-type semiconductor sample.

When the magnetic field is aligned along the $\langle\bar{1}10\rangle$ axes, the antisymmetric component vanishes (ρ_{SATM}=0) as shown in Fig. 2(a). Since this is a common in-plane axis with the (001) plane, ρ_{SATM} must be related to the symmetry of the [113] orientation. The dependence of ρ_{xy} on the field orientation angle θ_H (defined with respect to the $[33\bar{2}]$ direction) can be more clearly seen in Fig. 2(b), which shows the angular dependence of PHE measured at 300 K with a fixed positive saturating magnetic field (H=+1 kOe). The field orientation angle θ_H is varied from −220° to +220° in the plane of the sample. The high field ensures a complete saturation of the sample so that $\theta_H=\theta_M$. The angular dependence is completely reversible and does not follow the $\sin 2\theta_H$ dependence of Eq. (2). A separation of the symmetric and antisymmetric component can be achieved by taking the sum and difference of the angular dependence of the PHE for positive and negative fields above saturation. The result is shown in Fig. 2(c). The symmetric part follows the well-known $\sin 2\theta_H$ dependence of Eq. (2). The antisymmetric part, on the other hand, can be fitted by an equation of the form $\rho^0_{SATM}\cos\theta_H+\rho^1_{SATM}\cos^3\theta_H$, shown by the solid line, where ρ^0_{SATM} and ρ^1_{SATM} are arbitrary constants to be interpreted. Using this functional form, the PHE response from $Fe_{3+x}Si_{1-x}$(113) films can be modified to

$$\rho_{xy}=\rho_s^{PHE}\sin 2\theta_H+\rho^0_{SATM}\cos\theta_H+\rho^1_{SATM}\cos^3\theta_H, \quad (3)$$

where we have introduced a constant ρ_s^{PHE} to take into account the experimental observation that $(\rho_\parallel-\rho_\perp)$ derived from the PHE response [by using Eq. (2)] is smaller than that derived from the ρ_{xx} response. In this particular sample, both quantities differ by one order of magnitude (see Fig. 5). Here $\theta_H=0^\circ$ is defined with respect to the current direction, which is along the $[33\bar{2}]$ direction. Using this modified equation for the PHE, we fit the angular dependence of Figs. 2(b) and 2(c) which are shown as solid lines. The best fitting is obtained for ρ_s^{PHE}=16.5 nΩ cm, ρ^0_{SATM}=16 nΩ cm, and ρ^1_{SATM} =−10 nΩ cm.

2. Composition and temperature dependence of the antisymmetric component in PHE

In Fig. 3 we show the field and angular dependence of ρ_{xy} for the same $Fe_{3+x}Si_{1-x}$(113) film (x=0.07) at 77 K. Figure 3(a) shows the field dependence of ρ_{xy} with magnetic field applied parallel to $[33\bar{2}]$. As can be seen, the sign of the antisymmetric component is reversed, i.e, ρ_{SATM} is negative in contrast to the positive value of ρ_{SATM} at 300 K [see Fig. 1(a) for the configuration $I_{AE}U_{BH}$]. Figures 3(b) and 3(c) show the corresponding dependencies of ρ_{xy} on the field ori-

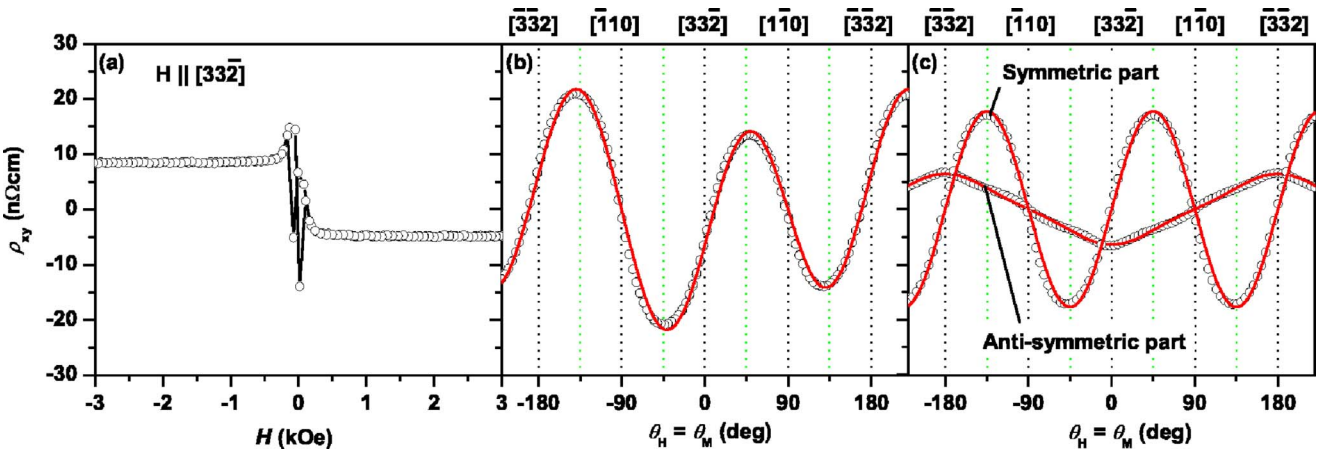

FIG. 3. (Color online) (a) Planar Hall effect response from $Fe_{3+x}Si_{1-x}$(113) (x=0.07) film at 77 K with magnetic field applied in-plane along [33$\bar{2}$]. (b) Corresponding angular dependence of ρ_{xy} at 77 K with a saturating in-plane magnetic field so that $\theta_H = \theta_M$. (c) Separation of the symmetric and antisymmetric part of the PHE. Open circles represent experimental data and solid lines (in red color) are fitted curves as explained in Fig. 2.

entation angle θ_H at a saturating field ($\theta_H = \theta_M$). The open circles represent experimental data and the solid lines are the fitted curves using Eq. (3) similar to Figs. 3(b) and 3(c). The best fitting is obtained for $\rho_s^{PHE} = 17.8$ nΩ cm, $\rho_{SATM}^0 = -4.4$ nΩ cm, and $\rho_{SATM}^1 = -2$ nΩ cm. The change in sign of ρ_{SATM} is clearly seen. To study the temperature and composition dependence of the antisymmetric component in more detail, we have measured the difference: $\rho_{SATM} = \rho_{xy}(H > +H_{sat}) - \rho_{xy}(H < -H_{sat})$ for a series of samples with x varying from +0.39 to −0.04 and temperatures varying from 300 to 4 K. The saturating magnetic field was applied along [33$\bar{2}$], so that $\rho_{SATM} = 2(\rho_{SATM}^0 + \rho_{SATM}^1)$ [see Eq. (3)]. The results are summarized in Fig. 4(a), which shows several important results. First, ρ_{SATM} decreases with decreasing x and temperature (except the sample with $x = -0.04$). Second, ρ_{SATM} changes sign below a certain critical temperature which increases with decreasing x (increase of Si content). Interestingly, the sign of ρ_{SATM} for samples very close to stoichiometry ($x \sim 0$) is negative at RT, which is the same as in Fe films grown on GaAs(113)A substrates.[13] However, for Fe films on GaAs(113)A no change in sign of ρ_{SATM} has been observed in the measurement temperature range of 4 to 300 K.

3. Anisotropic magnetoresistance

Before concluding this section of experimental results, we will show that the AMR response from these $Fe_{3+x}Si_{1-x}$(113) samples can be well-described by Eq. (1). The results of AMR (ρ_{xx}) measurements are summarized in Fig. 5 for the sample with x=0.07. Clearly, ρ_{xx} is a symmetric function of the applied field direction [see Fig. 5(a)] and the angular dependence of ρ_{xx} for a saturating field shows a perfect $\cos^2\theta_M$ dependence [see Figs. 5(b) and 5(c)]. Surprisingly, the ρ_{xx} amplitude, $(\rho_\parallel - \rho_\perp)$, which is the difference of ρ_{xx} for 0° and 90°, is negative but is similar to our previous findings on $Fe_{3+x}Si_{1-x}$ films on GaAs(001).[17] For this sample with x =0.07, a clear change in sign of ρ_{SATM} was observed at about 150 K [see Fig. 4(a)], however, no change in sign of $(\rho_\parallel - \rho_\perp)$ is observed even at 77 K [see Fig. 5(c)]. This implies that the change in sign of ρ_{SATM} is uncorrelated to any AMR based mechanism such as the different electron mean free path as suggested by Granberg *et al.*[18] in AMR studies of Fe films. The negative value of $(\rho_\parallel - \rho_\perp)$, which is just opposite to that of the Fe, indicates a different spin-dependent scattering mechanism.[9]

From our superconducting quantum interference device (SQUID) magnetometry studies, the magnetic anisotropy of these [113] oriented samples are well known to exhibit a dominant in-plane fourfold magnetic anisotropy, with the easy axes along the in-plane $\langle\bar{3}01\rangle$ axes.[6] The saturation magnetization M_s of these Fe_3Si films as measured by

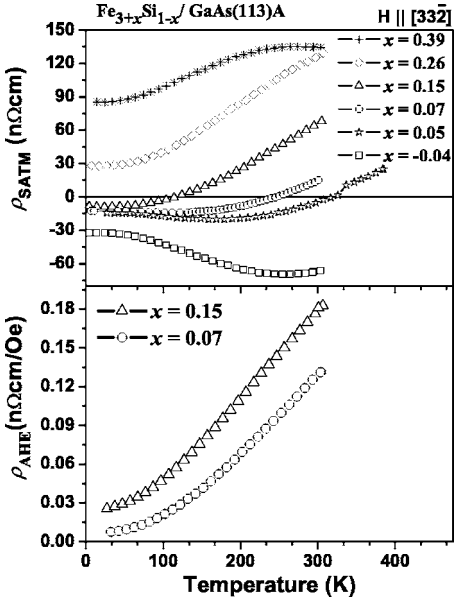

FIG. 4. (a) Temperature and composition dependence of the $\rho_{SATM} = \rho_{xy}(H > +H_{sat}) - \rho_{xy}(H < -H_{sat})$ measured with a saturating field applied near to the [33$\bar{2}$] direction. (b) Temperature dependence of ρ_{AHE} for two typical samples with x=0.07 and 0.15.

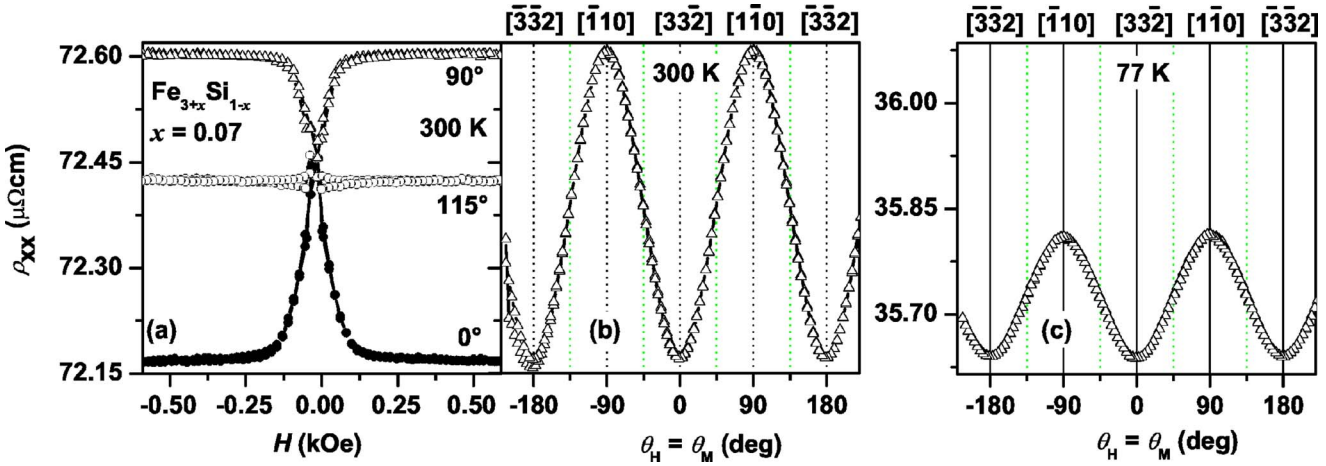

FIG. 5. (Color online) (a) Field dependence of the AMR (ρ_{xx}) from the $Fe_{3+x}Si_{1-x}$(113) film with x=0.07 at 300 K for different in-plane orientations. The open circles represent the easy axis of magnetization, for which the AMR signal does not change. Angular dependence of ρ_{xx} at a fixed saturating field of H=1 kOe obtained at (b) 300 K and (c) 77 K. For comparison, the amplitude of AMR is kept fixed for the three figures.

SQUID magnetometry is between 500 and 1450 emu/cm^3 at 300 K, where M_s decreases with increasing Si content.[6] This corresponds to a demagnetization field ($=4\pi M_s$) of about 6.2–18.2 kOe which is much larger than the measured low in-plane saturation field ($\simeq 2K_1/M_s$) of $<$200 Oe. The large demagnetization energy does not allow the moment to rotate out-of-plane. Hence, in all the samples reported here, the magnetization lies in-plane. In fact, the in-plane four-fold magnetic anisotropy is a consequence of the magnetocrystalline anisotropy similar to that of Fe films on GaAs(113)A substrates.[19] Because of the high Curie temperature of these samples, the temperature dependence of the magnetic properties is weak and did not show any significant differences. The magnetic anisotropy is also obvious from the field dependent behavior of ρ_{xx} in Fig. 5(a). However, a detailed discussion of the magnetic anisotropy is not relevant in the present discussion, since our main focus here is about a true saturating property.

B. Phenomenological model

In this section we will present a phenomenological model,[9,20] based on the symmetry of the crystal to understand the origin of the antisymmetric component in the PHE of single crystalline $Fe_{3+x}Si_{1-x}$ films grown on low-symmetric GaAs(113)A substrates. When a saturating field **H** with components $H_i = H\alpha_i$, is applied to a crystal, the relationship between the electric field **E** and current density **J** is defined through the relation

$$E_i = \rho_{ij}(\alpha) J_j, \tag{4}$$

where, $\rho_{ij}(\alpha)$ is the second rank magnetoresistivity tensor and E_i and J_j are components of the electric field **E** and current density **J**, respectively. The tensor $\rho_{ij}(\alpha)$ depends on the direction cosines, α_i, of the magnetization vector and hence can be expressed as a series expansion in ascending powers of the α_i[9,20]

$$\rho_{ij}(\alpha) = a_{ij} + a_{kij}\alpha_k + a_{klij}\alpha_k\alpha_l + a_{klmij}\alpha_k\alpha_l\alpha_m + \cdots, \tag{5}$$

where the Einstein summation convention is understood. The tensors with elements $a_{ij}, a_{kij}, a_{klij}\cdots$, simplify due to the crystal symmetry.[20] The tensor $\rho_{ij}(\alpha)$ being of second rank can be divided into its symmetrical and antisymmetrical parts,

$$\rho^s_{ij}(\alpha) = \frac{1}{2}[\rho_{ij}(\alpha) + \rho_{ji}(\alpha)] \tag{6}$$

and

$$\rho^a_{ij}(\alpha) = \frac{1}{2}[\rho_{ij}(\alpha) - \rho_{ji}(\alpha)]. \tag{7}$$

Onsager's theorem[20] applied to a magnetically saturated crystal gives

$$\rho_{ij}(\alpha) = \rho_{ji}(-\alpha), \tag{8}$$

so that that ρ^s_{ij} is an even function of the α_i and ρ^a_{ij} is an odd function of the α_i.

For both contributions, we have the power series

$$\rho^s_{ij}(\alpha) = a_{ij} + a_{klij}\alpha_k\alpha_l + \cdots \tag{9}$$

and

$$\rho^a_{ij}(\alpha) = a_{kij}\alpha_k + a_{klmij}\alpha_k\alpha_l\alpha_m + \cdots. \tag{10}$$

Traditionally, if one considers the leading terms (up to second order in α_i) in above equations and neglect the higher order terms, the associated electric fields $\mathbf{E}_s$ and $\mathbf{E}_a$ represent the generalized magnetoresistance and Hall effects, respectively.[9,20,21] With this consideration, PHE for which the magnetic field is applied in-plane, should arise from ρ^s_{ij} and should also be an even function of the applied field direction. However, in our PHE experiments on the Fe_3Si(113) films [also on Fe(113) films], we see an addi-

tional component, which is an odd function of the magnetic field direction. Consequently, this component must involve an antisymmetrical part ρ_{ij}^{a}.

Before proceeding further we will need to derive all the components of the magnetoresistivity tensor ρ_{ij} for the classical crystal class **m3m**, to which both Fe_3Si (F**m3m**) and Fe (I**m3m**) belong. The $D0_3$ crystal structure of Fe_3Si belongs to the space group F**m3m**. Details can be found in Appendix A. Let us first consider the simple case of an (001) oriented thin-film, with current $J=(J_1,0,0)$ along the [100] direction. We assume that the magnetization **M** lies in the (001) plane, making an angle θ_M to the current. In this case the measured Hall voltage is given by

$$E_2 = \rho_{21} J_1, \tag{11}$$

where the indexes 1, 2, and 3 refer to the x, y, and z axes, respectively. The α_is are given by $\alpha_1=\cos\theta_M$, $\alpha_2=\sin\theta_M$, and $\alpha_3=0$. The planar Hall resistivity can be found by substituting the α_is in Eq. (A2)

$$\rho_{21} = \frac{C_4}{2}\sin 2\theta_M, \tag{12}$$

which is similar to the well-known $\sin 2\theta_M$ relation of Eq. (2). However, the prefactor of $\sin 2\theta_M$ in the above equation, i.e., C_4 is no longer equal to the AMR amplitude, $\rho_{\parallel}-\rho_{\perp}$ for the single crystalline samples.[22] It may be mentioned that the prefactor $\rho_{\parallel}-\rho_{\perp}$ in Eq. (2) for the polycrystalline films result from the averaging over a large number of randomly oriented crystallites.[8,22] Nevertheless, the coefficient C_4 as introduced in Appendix A is a coefficient from the symmetric part of the tensor ρ_{ij}^{s}, and hence traditionally PHE is attributed to an AMR effect.[8,21] Now we consider the case of the low-symmetric [113] oriented films. The measurements were performed with a current in the $[33\bar{2}]$ direction and the Hall voltage was measured along the $[\bar{1}10]$ direction. Thus, to find the measured planar Hall resistivity, we must perform a coordinate transformation[20,23] of ρ_{21}. This transformation is performed in Appendix B. The final equation for the measured planar Hall resistivity in (113) films is given in Eq. (B4) of Appendix B. If we consider terms up to third order of α_i, we can write the measured Hall resistivity for the (113) films in the following way:

$$\rho_{21}^{(113)} = \frac{(9C_1+2C_4)}{22}\sin 2\theta_M + \frac{9(a_{12223}-a_{11123})}{11\sqrt{2}}\cos\theta_M - \frac{42\sqrt{2}(a_{12223}-a_{11123})}{121}\cos^3\theta_M, \tag{13}$$

which agrees with Eq. (3) for $\rho_s^{PHE}=(9C_1+2C_4)/22$, $\rho_{SATM}^{0}=9(a_{12223}-a_{11123})/(11\sqrt{2})$, and $\rho_{SATM}^{1}=-42\sqrt{2}(a_{12223}-a_{11123})/121$. The coefficient C_1 is also introduced in Appendix A. Here, for the symmetric part, we have considered terms up to the second order of α_i as described in the first term with the well-known $\sin 2\theta_M$ dependence. However, as the most exciting result of this calculation, there are two additional terms which arise from the antisymmetric part of the tensor ρ_{ij}^{a}. *These are third-order contributions of* α_i *and arise from the lower symmetry of the (113) plane, where the magnetization* **M** *rotates due to the large demagnetization energy of the* Fe_3Si *films*. It is easy to show that these additional antisymmetric terms vanishe for magnetic fields applied along the $\langle\bar{1}10\rangle$ axes ($\theta_M=90^\circ$) and change sign with the change in the direction of the applied magnetic field along all other in-plane directions. Hence, this equation provides a perfect explanation of the antisymmetric contribution observed in the PHE (Sec. III A 1). Both ρ_{SATM}^{0} and ρ_{SATM}^{1} contain the difference $(a_{12223}-a_{11123})$, which could be of either sign from the viewpoint of symmetry. Thus $\rho_{SATM}=2(\rho_{SATM}^{0}+\rho_{SATM}^{1})$ can be both positive and negative in agreement with the experimental results (Sec. III A 2). It should be mentioned that this additional antisymmetric component could not be obtained on the high-symmetric (001) plane in agreement with experiments on [001] oriented ferromagnetic thin films.[13,17] The appearance of third-order contributions of α_i is not surprising, since to describe the magnetoresistivity anisotropy effects terms up to a fourth-order contribution of α_i has been shown to be necessary.[24,25] These third-order terms in α_i can be termed as a second order Hall effect [see Eq. (10)]. The fourth-order terms contribute additional $\sin 2\theta_M$ and $\sin 4\theta_M$ terms which are symmetric and are neglected for simplicity. This is justified, since to describe the experimental data, terms up to third orders, as considered in the above Eq. (13) are found sufficient.

The coexistence of even and odd terms in the component of magnetoresistivity tensor in the above Eq. (13) has been called the Umkehr effect[11] in literature. This effect was discussed theoretically in 1975 by Akgöz and Saunders[26] based on the symmetry restrictions on the form of galvanomagnetic/thermomagnetic tensors. Experimentally, the Umkehr effect was observed in thermomagnetic effects[11,26] and magnetotransport[27] measurements in Bismuth. As pointed out by Akgöz and Saunders,[26] the effect is not restricted to the trigonal crystal structure of Antimony and Bismuth and the Umkehr effect can also be observed in cubic crystals depending on the measurement geometry as considered in the present case.

It is also possible to show within this phenomenological approach that the AMR Eq. (1) is valid even for this low-symmetric orientation, in agreement with the experimental observations. The longitudinal resistivity, $\rho_{xx}^{(113)}$ can be derived in the same manner

$$\rho_{xx}^{(113)} = \rho_{11}^{(113)} \approx C_0 + \frac{9}{22}(C_1-C_4) + \frac{126C_4-5C_1}{121}\cos^2\theta_M, \tag{14}$$

which reproduces Eq. (1) for $\rho_{\perp}=C_0+9(C_1-C_4)/22$ and $(\rho_{\parallel}-\rho_{\perp})=(126C_4-5C_1)/121$. This equation also provides a good explanation for the experimental observation $\rho_s^{PHE} \neq (\rho_{\parallel}-\rho_{\perp})$, which in fact is a result of the single crystalline nature of the sample.

Now we will discuss the sign change of ρ_{SATM} with composition and temperature. For Fe_3Si films on GaAs(001) substrates we previously observed a sign change in the PHE due to the ordering toward the stoichiometric Fe_3Si

composition.[17] However, in that case the PHE was a symmetric function of the applied field direction. But ρ_{SATM} is an antisymmetric contribution (in fact a second-order Hall effect) and hence a similar origin, like the AHE is most likely responsible. In fact, the change in sign of the AHE in binary alloys with composition and temperature is rather well known.[28–32] The anomalous Hall resistivity ρ_{AHE} for a saturating magnetic field and for the (113) symmetry also involves the tensor elements a_{12223} and a_{11123}

$$\rho_{AHE}^{(113)} = \frac{1}{121}(121a_{123} + 83a_{11123} + 38a_{12223}). \qquad (15)$$

This can be found easily by using Eqs. (11) and (A2) for a saturating magnetic field applied along the normal [113]. In this equation, the first term containing the usual tensor element a_{123}, represents a first-order contribution of α_i, whereas the other two terms are third-order contributions just like in the PHE. The presence of the same tensor elements a_{11123} and a_{12223} in PHE and AHE may imply a similar physical origin of ρ_{SATM} and ρ_{AHE}. To see whether ρ_{AHE} also changes sign with temperature, we measured AHE for samples with $x=0.07$ and $x=0.15$, in which a clear change in sign of ρ_{SATM} was observed at about 150 and 250 K, respectively. In Fig. 4(b), we show the behavior of ρ_{AHE} with temperature for these two samples. As can be seen, no change in sign of ρ_{AHE} is observed for both samples. However, this may be understood from the fact that ρ_{SATM} is a higher-order contribution, and in AHE this contribution is not the most significant ones. [See Eqs. (13) and (15).]

At the end, we will discuss the possible origin of the observed sign change of the antisymmetric component. First we will like to mention yet another observation from the results of high-resolution x-ray diffraction (HRXRD) measurements which was performed using a PANalytical X'Pert diffractometer. In HRXRD a study of the crystal or atomic ordering of these Fe_3Si films was performed by analyzing different superlattice reflections similar to our recent studies of long-range ordering of Fe_3Si films on GaAs(001).[33] For the $D0_3$ crystal structure of Fe_3Si, Bragg reflections are produced by either all odd or all even Miller indices (h,k,l). The reflections for which h,k,l are all even with $\frac{1}{2}(h+k+l) = 2n$, n being an integer, are fundamental reflections and are unaffected by the state of ordering. The reflections for which h,k,l are all even with $\frac{1}{2}(h+k+l)=2n+1$ is sensitive to a $(A,C) \rightarrow D$ disorder whereas the reflections for which all the h,k,l odd are sensitive to both $B \rightarrow D$ and $(A,C) \rightarrow D$ disorder, where the notations A,C, and D refer to different sublattice of Fe_3Si as described in the literature.[34–36] The sublattices A,B, and C are occupied by Fe atoms whereas the sublattice D is occupied by Si atoms. The relative intensity of these two classes of reflections depends on the state of ordering, but for a prefect ordered lattice the intensities should be equal.[33,36,37] For example, the (002) reflection and the (113) reflections should have the same intensity for a perfectly ordered Fe_3Si lattice. We found an increase in the intensity of the (002) reflection with increasing Si content. The superlattice and symmetric (113) reflection with h,k,l being all odd was detectable only for samples with a Si content of 26 at. % ($x=-0.04$). Hence, a good long-range atomic order is found in the nearly stoichiometric as-grown films which also establish the formation of a $D0_3$ crystal structure. As discussed before in the context of Fig. 4(a), the stoichiometric samples have a negative sign of ρ_{SATM} (for a magnetic field applied along $[33\bar{2}]$) at 300 K. Fe samples on GaAs(113)A also have a negative sign of ρ_{SATM} at 300 K. Since both Fe and Fe_3Si belong to the same crystal class, there seems to have some correlation between the two phenomena (the negative sign of the ρ_{SATM} and the improvement of atomic ordering). A microscopic theory of electron transport may provide further understanding of this possible correlation. In principle, when all the restrictions imposed by the band structure symmetry are included in such a calculation, the form obtained for PHE should be identical to that found from the phenomenological model.

IV. CONCLUSION

We have performed an extensive study of the magnetotransport properties of Fe_3Si films grown on GaAs(113)A substrates by molecular-beam epitaxy. The PHE of these films show an additional antisymmetric contribution, which arises from the lower symmetry of the [113] orientation and large demagnetization energy of the Fe_3Si films. A phenomenological model developed to understand the observed experimental data provides good explanation of the antisymmetric component and shows that this additional component comes from the antisymmetric part of the magnetoresistivity tensor like for the conventional Hall effect. It is shown that the observed effect can be ascribed to the Umkehr effect, which refers to the coexistence of even and odd terms in the component of magnetoresistivity tensor. This additional antisymmetric component is found to change the sign by varying the Si content in $Fe_{3+x}Si_{1-x}$ films and the measurement temperature. In fact the sign reversal occurs for a Si content above 21 at. % and at temperatures above a certain critical temperature which increases with increasing Si content. The microscopic origin of this additional contribution is not yet understood.

ACKNOWLEDGMENTS

Part of this work has been supported by the German BMBF under the resesarch program NanoQUIT (contract no. 01BM463). The authors would like to thank E. Wiebicke and A. Riedel for Hall bar sample preparation. We also like to thank O. Brandt, M. Bowen, L. Däweritz, M. Hashimoto, R. Hey, B. Jenichen, and P. Kleinert for useful discussions.

APPENDIX A: DETERMINATION OF COMPLETE MAGNETORESISTIVITY TENSOR ELEMENTS FOR THE CRYSTAL CLASS M3M

In matrix notation the magnetoresitivity tensor ρ_{ij} can be written as

$$\rho = \begin{pmatrix} \rho_{11} & \rho_{12} & \rho_{13} \\ \rho_{21} & \rho_{22} & \rho_{23} \\ \rho_{31} & \rho_{32} & \rho_{33} \end{pmatrix}. \qquad (A1)$$

The elements ρ_{ij} can be expressed in terms of the tensors $a_{ij}, a_{kij}, a_{klij}$, etc.. As already mentioned, the elements of these tensors simplify due to the crystal symmetry. For the crystal class **m3m**, the nonzero elements are tabulated by Birss.[20] Mcguire and Potter[9] derived the elements of the symmetric magnetoresistivity tensor ρ_{ij}^{s} through fifth order for the crystal class **m3m**. The antisymmetric magnetoresistivity tensor ρ_{ij}^{a} can be derived using the nonzero coefficients of the tensors $a_{ij}, a_{kij}, a_{klij}, \ldots$, etc. listed by Birss.[20] The resulting elements ρ_{ij} of Eq. (A1) can be written as follows

$$\rho_{11} = C_0 + C_1\alpha_1^2 + C_2\alpha_1^4 + C_3\alpha_2^2\alpha_3^2$$

$$\rho_{12} = C_4\alpha_1\alpha_2 + C_5\alpha_1\alpha_2\alpha_3^2 + (a_{123}\alpha_3 + a_{12223}\alpha_1^2\alpha_3 + a_{12223}\alpha_2^2\alpha_3 + a_{11123}\alpha_3^3)$$

$$\rho_{13} = C_4\alpha_1\alpha_3 + C_5\alpha_1\alpha_3\alpha_2^2 - (a_{123}\alpha_2 + a_{12223}\alpha_1^2\alpha_2 + a_{11123}\alpha_2^3 + a_{12223}\alpha_2\alpha_3^2)$$

$$\rho_{21} = C_4\alpha_1\alpha_2 + C_5\alpha_1\alpha_2\alpha_3^2 - (a_{123}\alpha_3 + a_{12223}\alpha_1^2\alpha_3 + a_{12223}\alpha_2^2\alpha_3 + a_{11123}\alpha_3^3)$$

$$\rho_{22} = C_0 + C_1\alpha_2^2 + C_2\alpha_2^4 + C_3\alpha_3^2\alpha_1^2$$

$$\rho_{23} = C_4\alpha_2\alpha_3 + C_5\alpha_2\alpha_3\alpha_1^2 + (a_{123}\alpha_1 + a_{11123}\alpha_1^3 + a_{12223}\alpha_1\alpha_2^2 + a_{12223}\alpha_1\alpha_3^2)$$

$$\rho_{31} = C_4\alpha_1\alpha_3 + C_5\alpha_1\alpha_3\alpha_2^2 + (a_{123}\alpha_2 + a_{12223}\alpha_1^2\alpha_2 + a_{11123}\alpha_2^3 + a_{12223}\alpha_2\alpha_3^2)$$

$$\rho_{32} = C_4\alpha_2\alpha_3 + C_5\alpha_2\alpha_3\alpha_1^2 - (a_{123}\alpha_1 + a_{11123}\alpha_1^3 + a_{12223}\alpha_1\alpha_2^2 + a_{12223}\alpha_1\alpha_3^2)$$

$$\rho_{33} = C_0 + C_1\alpha_3^2 + C_2\alpha_3^4 + C_3\alpha_1^2\alpha_2^2, \tag{A2}$$

where the C_0, C_1, C_2, C_3, etc. are short-hand notations of Mcguire and Potter[9] for the coefficients in the symmetric part of magnetoresistivity tensor ρ_{ij}^{s} given by the following equations:

$$C_0 = a_{11} + a_{1122} + a_{111122}$$

$$C_1 = a_{1111} - a_{1122} - 2a_{111122} + a_{112211}$$

$$C_2 = a_{111111} + a_{111122} - a_{112211}$$

$$C_3 = a_{112233} - 2a_{111122}$$

$$C_4 = a_{2323} + a_{111212}$$

$$C_5 = a_{112323} - a_{111212}. \tag{A3}$$

The factors in the brackets of Eq. (A2) arise from the antisymmetric part of the tensor ρ_{ij}^{a}. For the diagonal elements, the antisymmetric part is zero, whereas the off-diagonal elements satisfy the following relation:

$$\rho_{ij}^{a} = -\rho_{ji}^{a}, \text{ when } i \neq j. \tag{A4}$$

APPENDIX B: TRANSFORMATION INTO THE (113) SYSTEM

We use the following matrix l which transforms the (001) basis vector system to the basis vector system of (113):

$$l = \begin{pmatrix} \frac{3}{\sqrt{22}} & \frac{3}{\sqrt{22}} & -\sqrt{\frac{2}{11}} \\ -\frac{1}{\sqrt{2}} & \frac{1}{\sqrt{2}} & 0 \\ \frac{1}{\sqrt{11}} & \frac{1}{\sqrt{11}} & \frac{3}{\sqrt{11}} \end{pmatrix}. \tag{B1}$$

The elements of this matrix l_{ij} are determined by the relative orientation of the old and new sets of axes, e.g., $l_{12} = \cos \widehat{x_2 O x_1'}$, where Ox_2 and Ox_1' are the old y axis and the new x axis, respectively (see Birss[20] for details). In our case l_{12} presents the cosine of the angle between the [010] and the $[33\bar{2}]$ axis. According to the measurements, we choose the new x axis along $[33\bar{2}]$, y axis along $[\bar{1}10]$, and z axis along [113]. To find the measured planar Hall resistivity in the new co-ordinate system we need to use the transformation properties of a second rank tensor (Neumann's principle),[20] which is given by

$$\rho_{ij}' = l_{ip} l_{jq} \rho_{pq}. \tag{B2}$$

Using the last two Eqs. (B1) and (B2) the measured planar Hall resistivity in the (113) system, $\rho_{21}^{(113)}$, can now be derived

$$\rho_{21}^{(113)} = \frac{3}{2\sqrt{11}}(\rho_{21} + \rho_{22} - \rho_{11} - \rho_{12}) + \frac{1}{\sqrt{11}}(\rho_{13} - \rho_{23}). \tag{B3}$$

Since the demagnetization energy of these Fe_3Si films are rather large, the magnetization **M** is restricted to the (113) plane. In this case the direction cosines of **M** as used in our previous studies of Fe(113) films[19] can be shown to be $\alpha_1 = (3/\sqrt{22})\cos\theta_M - (1/\sqrt{2})\sin\theta_M$, $\alpha_2 = (3/\sqrt{22})\cos\theta_M + (1/\sqrt{2})\sin\theta_M$, $\alpha_3 = -(\sqrt{2/11})\cos\theta_M$, where θ_M is measured with respect to the $[33\bar{2}]$ axis. Using these direction cosines in Eqs. (A2), we can derive the measured planar Hall resistivity for the case of [113] oriented films in terms of θ_M

$$\begin{aligned}\rho_{21}^{(113)} = {} & \frac{9C_1}{11}\cos\theta_M\sin\theta_M + \frac{81C_2}{121}\cos^3\theta_M\sin\theta_M \\ & + \frac{9C_2}{11}\cos\theta_M\sin^3\theta_M - \frac{18C_3}{121}\cos^3\theta_M\sin\theta_M \\ & + \frac{2C_4}{11}\cos\theta_M\sin\theta_M - \frac{9C_5}{121}\cos^3\theta_M\sin\theta_M \\ & + \frac{C_5}{11}\cos\theta_M\sin^3\theta_M + \frac{15(a_{12223} - a_{11123})}{121\sqrt{2}}\cos^3\theta_M \\ & + \frac{9(a_{12223} - a_{11123})}{11\sqrt{2}}\cos\theta_M\sin^2\theta_M. \end{aligned} \tag{B4}$$

This equation is valid up to the fourth-order contribution of α_i and contains both symmetric and antisymmetric contributions. The symmetric part contains the coefficients C_i's. Note that terms containing the coefficients C_2, C_3, and C_5 are fourth-order contributions of α_i [see Eq. (A2)]. Other symmetric terms containing the coefficients C_1 and C_4 are second-order contributions of α_i. The antisymmetric part which contains the tensor elements a_{12223} and a_{11123} are third-order contributions of α_i. Thus, if we consider terms up to third order in α_i we can write the above equation in the following form:

$$\rho_{21}^{(113)} = \frac{(9C_1 + 2C_4)}{22}\sin 2\theta_M + \frac{15(a_{12223} - a_{11123})}{121\sqrt{2}}\cos^3\theta_M + \frac{9(a_{12223} - a_{11123})}{11\sqrt{2}}\cos\theta_M \sin^2\theta_M, \quad \text{(B5)}$$

which can also be expressed in the following form:

$$\rho_{21}^{(113)} = \frac{(9C_1 + 2C_4)}{22}\sin 2\theta_M + \frac{9(a_{12223} - a_{11123})}{11\sqrt{2}}\cos\theta_M - \frac{42\sqrt{2}(a_{12223} - a_{11123})}{121}\cos^3\theta_M. \quad \text{(B6)}$$

*Electronic address: muduli@pdi-berlin.de

[1] G. A. Prinz, Science **282**, 1660 (1998).
[2] S. A. Wolf, D. D. Awschalom, R. A. Buhrman, J. M. Daughton, S. von Molnár, M. L. Roukes, A. Y. Chtchelkanova, and D. M. Treger, Science **294**, 1488 (2001).
[3] J. D. Boeck, W. V. Roy, V. Motsnyi, Z. Liu, K. Dessein, and G. Borghs, Thin Solid Films **412**, 3 (2002).
[4] S. Fölsch, B.-C. Choi, and K. H. Rieder, Phys. Rev. B **54**, 10855 (1996).
[5] A. J. Freeman and R. Wu, J. Magn. Magn. Mater. **100**, 497 (1991).
[6] P. K. Muduli, J. Herfort, H.-P. Schönherr, and K. H. Ploog (to be published).
[7] J. Herfort, H.-P. Schönherr, and K. H. Ploog, Appl. Phys. Lett. **83**, 3912 (2003).
[8] D. A. Thompson, L. T. Romankiw, and A. F. Mayadas, IEEE Trans. Magn. **11**, 1039 (1975).
[9] T. McGuire and R. Potter, IEEE Trans. Magn. **11**, 1018 (1975).
[10] J. P. Jan, in *Solid State Physics*, edited by F. Seitz and D. Turnbull (Academic Press, New York, 1957), Vol. 5, pp. 1–96.
[11] This term was introduced by E. Gruneisen and J. Gielessen, Ann. Phys. **27**, 243 (1936).
[12] K.-J. Friedland, R. Nötzel, H.-P. Schönherr, A. Riedel, H. Kostial, and K. Ploog, Physica E (Amsterdam) **10**, 442 (2001).
[13] K. J. Friedland, J. Herfort, P. K. Muduli, H.-P. Schönherr, and K. H. Ploog, J. Supercond. (to be published).
[14] M. Hansen, *Constitution of Binary Alloys* (McGraw-Hill, New York, 1958).
[15] R. P. Elliot, *Constitution of Binary Alloys*, Suppl. 1 (McGraw-Hill, New York, 1965).
[16] The saturation field is rather low and is about 0.11 kOe, as is also evidenced from SQUID magnetometry.
[17] M. Bowen, K.-J. Friedland, J. Herfort, H.-P. Schönherr, and K. H. Ploog, Phys. Rev. B **71**, 172401 (2005).
[18] P. Granberg, P. Isberg, T. Baier, B. Hjörvarsson, and P. Nordblad, J. Magn. Magn. Mater. **195**, 1 (1999).
[19] P. K. Muduli, J. Herfort, H.-P. Schönherr, and K. H. Ploog, J. Appl. Phys. **97**, 123904 (2005).
[20] R. R. Birss, *Symmetry and Magnetism* (North-Holland, Amsterdam, 1964).
[21] I. A. Campbell and A. Fert, in *Ferromagnetic Materials*, edited by E. P. Wohlfarth (North-Holland, Amsterdam, 1982), Vol. 3, p. 747.
[22] T. T. Chen and V. A. Marsocci, Solid State Commun. **10**, 783 (1972); Physica (Amsterdam) **59**, 498 (1972).
[23] J. F. Nye, *Physical Properties of Crystals: Their Representation by Tensors and Matrices* (Oxford University Press, London, 1985), p. 9, reprint ed.
[24] W. Döring, Ann. Phys. **32**, 259 (1938).
[25] E. Fawcett and W. A. Reed, Phys. Rev. Lett. **9**, 336 (1962).
[26] Y. C. Akgöz and G. A. Saunders, J. Phys. C **8**, 1387 (1975).
[27] B. Lenoir, F. Brochin, and J.-P. Michenaud, Europhys. Lett. **58**, 93 (2002).
[28] F. P. Beitel and J. E. M. Pugh, Phys. Rev. **112**, 1516 (1958).
[29] E. R. Sanford, A. C. Ehrlich, and E. M. Pugh, Phys. Rev. **123**, 1947 (1961).
[30] H. Ashworth, D. Sengupta, G. Schnakenberg, L. Shapiro, and L. Berger, Phys. Rev. **185**, 792 (1969).
[31] S. Foner, F. E. Allison, and E. M. Pugh, Phys. Rev. **109**, 1129 (1958).
[32] A. Sinha and A. K. Majumdar, J. Appl. Phys. **50**, 7533 (1979).
[33] B. Jenichen, V. M. Kaganer, J. Herfort, D. K. Satapathy, H.-P. Schönherr, W. Braun, and K. H. Ploog, Phys. Rev. B72, 075329 (2005).
[34] V. Niculescu, K. Raj, J. I. Budnick, T. J. Burch, W. A. Hines, and A. H. Menotti, Phys. Rev. B **14**, 4160 (1976).
[35] W. A. Hines, A. H. Menotti, J. I. Budnick, T. J. Burch, T. Litrenta, V. Niculescu, and K. Raj, Phys. Rev. B **13**, 4060 (1976).
[36] V. Niculescu, J. I. Budnick, W. A. Hines, K. Raj, S. Pickart, and S. Skalski, Phys. Rev. B **19**, 452 (1979).
[37] P. J. Webster and K. R. A. Ziebeck, in *Landolt-Börnstein-Group III Condensed Matter*, edited by P. J. Webster and K. R. A. Ziebeck (Springer-Verlag, Berlin, 1988), Vol. 19, pp. 75–79.

Thermal stability and atomic ordering of epitaxial Heusler alloy Co_2FeSi films grown on GaAs(001)

M. Hashimoto, J. Herfort, H.-P. Schönherr, and K. H. Ploog
Paul-Drude-Institut für Festkörperelektronik, Hausvogteiplatz 5-7, D-10117 Berlin, Germany

(Received 11 July 2005; accepted 17 October 2005; published online 28 November 2005)

The thermal stability and the atomic ordering of single-crystal Heusler alloy Co_2FeSi layers grown by molecular beam epitaxy on GaAs(001) have been studied. We found that the Co_2FeSi layers have a long-range atomic order and crystallize in a partly disordered $L2_1$ structure in the low growth temperature (T_G) regime. The long-range atomic order of the layers is further improved with increasing T_G up to 350 °C. However, the increase of T_G induces an interfacial reaction between the Co_2FeSi layer and the GaAs substrate. The analysis of the in-plane magnetic anisotropy reveals that the interface perfection is improved up to T_G=200 °C and deteriorated due to an interfacial reaction above 200 °C. © *2005 American Institute of Physics*. [DOI: 10.1063/1.2136213]

I. INTRODUCTION

Spintronics (or spin electronics) is a recently emerging field of device concepts which is based on the spin degree of freedom of the electron, and is expected to lead to dramatic improvements in device performance. One of the key issues for the realization of spintronic devices is the efficient electrical injection of spin-polarized carriers into semiconductors. Electrical spin injection has been investigated mainly with Mn-doped III-V and II-VI semiconductors[1,2] and with conventional ferromagnetic metals.[3–6] Recently, Heusler alloys are of increasing interest as a candidate for a spin injection source into semiconductors, because of their high Curie temperature (from 200 to 1100 K), their compatibility with compound and element semiconductors, and half-metallicity predicted for some Heusler alloys.[7–10] There are a few reports of epitaxial Heusler alloys grown on semiconductor substrates, e.g., the full-Heusler alloys Co_2MnX (X=Ge, Ga),[11,12] and Ni_2MnY (Y=In, Ga),[13,14] as well as the half-Heusler alloy NiMnSb.[15,16] In addition, the growth of the binary Heusler alloy Fe_3Si on GaAs was reported[17,18] and a high crystal and interface perfection in the Fe_3Si layers was demonstrated in the proper growth temperature range.[17] More recently, electrical spin injection from Fe_3Si (Ref. 19) and Co_2MnGe (Ref. 20) was demonstrated. However, no evidence of a high degree of spin polarization as expected from theory has been observed in Heusler alloy films, up to now around 60% at maximum.[21–23]

In ferromagnet/semiconductor (FM/SC) heterostructures, mainly two obstacles with respect to their crystal structure are considered to prevent efficient electrical spin injection. One is the existence of interfacial compounds formed by diffusion of As and/or Ga into the FM layers, resulting in spin-flip scattering at the interface. The second is atomic disorder, such as vacancies and antisites. This disorder introduces minority gap states, and it was reported that only a few percent of antisite disorder can destroy the half-metallic nature of Heusler alloys.[24] Therefore, a highly atomically ordered, stoichiometric, and thermally stable thin film is needed for spin injection sources.

Co_2FeSi is a member of full-Heusler alloys with the cubic $L2_1$ crystal structure consisting of four interpenetrating fcc sublattices.[25] The lattice constant of bulk Co_2FeSi is 5.658 Å,[26] closely lattice matched to GaAs (a_{GaAs}=5.653 Å), and the lattice mismatch is as small as 0.08%. $Fe_{3-x}Co_xSi$ crystallizes in the cubic fcc structure in a wide range of x ($0<x<2.15$).[26] This phase stability allows control of the magnetic properties; e.g., magnetic anisotropy and magnetic moment. Bulk Co_2FeSi with a large magnetic moment (5.91 μ_B at 10.2 K) is ferromagnetic up to more than 980 K,[26] which is one of the highest Curie temperatures among the reported Heusler alloys. Here, we present a detailed study of the thermal stability and atomic ordering of single-crystal Heusler alloy Co_2FeSi films grown on GaAs (001) substrates by molecular beam epitaxy (MBE). The structural, electrical, and magnetic properties of Co_2FeSi films with various Si compositions and grown at different temperatures were systematically investigated.

II. SAMPLE PREPARATION

Before the growth of the Co_2FeSi layers, 100 nm thick GaAs templates were prepared in the III-V growth chamber using standard GaAs growth conditions. As-terminated $c(4\times4)$ reconstructed GaAs (001) surfaces were prepared by cooling the samples down to 420 °C under As_4 pressure to prevent the formation of macroscopic defects on the surface.[27] The samples were then transferred to the As-free deposition chamber under UHV at a base pressure of 5×10^{-10} Torr. The growth temperature T_G for the Co_2FeSi layers was varied in the range 100-400 °C to find the optimum growth temperature regime. A low growth rate of about 0.1 nm/min was chosen in order to avoid the degradation of the crystal quality at these low growth temperatures. The thickness of the layers d was determined by high-resolution x-ray diffraction (HRXRD) and x-ray reflectivity (XRR) measurements, and it varies in the range from 17 to 23 nm in accordance with the increase of T_{Si}. The growth was *in situ* monitored using reflection high-energy electron diffraction (RHEED). The RHEED pattern of the Co_2FeSi layer shows a rather spotty pattern at low T_G. The pattern gradually changes to sharp streaks with Kikuchi lines and a Laue circle

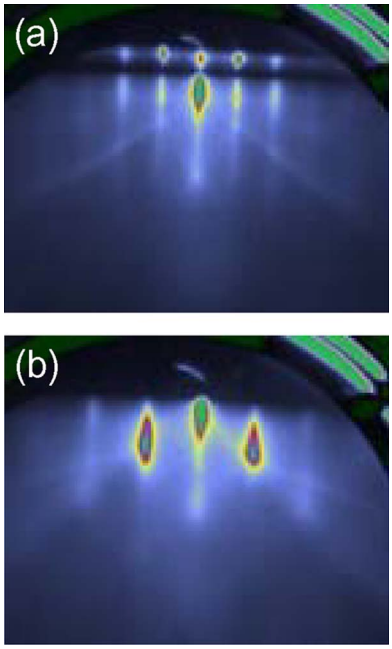

FIG. 1. (Color online) RHEED patterns of the Co_2FeSi layer grown at 250 °C along the (a) [110] and (b) [100] crystallographic directions during growth.

with increasing T_G, indicating a two-dimensional growth mode and a well-ordered single-crystal surface. Figure 1 shows typical RHEED patterns of Co_2FeSi film grown at 250 °C along the [110] and [100] crystallographic directions. After deposition of about 1–2 ML of the Co_2FeSi layer, an elongated streak pattern emerges. The pattern subsequently changes to sharp streaks and the streaky pattern is established during the deposition of about 3–6 ML of the Co_2FeSi layer. Then, the situation is maintained throughout the further growth.

The stoichiometric composition of Co_2FeSi was determined in the following way. First, the growth conditions of the binary alloy $Co_{0.66}Fe_{0.34}$ (bcc structure) were optimized. The composition of $Fe_{0.66}Co_{0.34}$ layers was determined by comparing the lattice constant with literature data,[28] taking into account the tetragonal distortion of the layers. Then, Si was added and incorporated to obtain ternary $Co_{2-x}Fe_ySi_{1+x+y}$ films, while the Fe and Co fluxes were kept constant at the optimized amounts. The Si cell temperature T_{Si} was varied from 1280 to 1335 °C to find the stoichiometric composition of Co_2FeSi. The perpendicular lattice mismatch $(\Delta a/a)_\perp$ of these $Co_{2-x}Fe_ySi_{1+x+y}$ films were subsequently examined by HRXRD using the $Co_2FeSi(004)$ reflection. From the value of $(\Delta a/a)_\perp$, the lattice constants of $Co_{2-x}Fe_ySi_{1+x+y}$ films were obtained, taking into account the tetragonal distortion of the layer, as confirmed in a reciprocal space map around $Co_2FeSi(113)$ reflections. Finally, from a comparison with the lattice constant of bulk Co_2FeSi from the literature,[26] the stoichiometric composition of Co_2FeSi was determined. More details of the determination are described elsewhere.[29]

III. RESULTS AND DISCUSSION

A. Structural properties

The structural properties of the films were examined *ex situ* by HRXRD with a PANalytical X'pert diffractometer

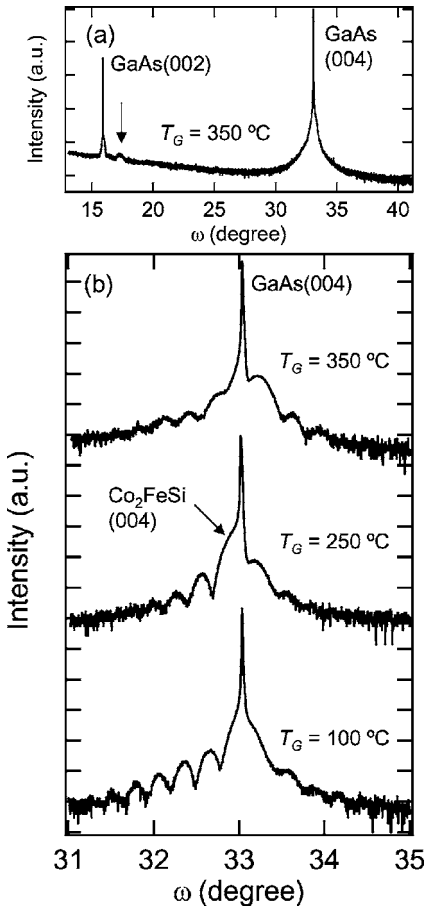

FIG. 2. HRXRD ω-θ curves around the $Co_2FeSi(004)$ reflection for stoichiometric Co_2FeSi/GaAs(001) films grown at substrate temperature ranging from 100 to 350 °C. For the growth temperature of 350 °C, a wide-ranged ω-2θ curve with a wide-open detector is shown in the upper panel.

using Cu K_α radiation with a Ge(220) monochrometer and a triple-bounce analyzer crystal. Figure 2 shows the results of HRXRD ω-2θ curves of the $Co_2FeSi(004)$ reflection of stoichiometric Co_2FeSi films grown at different growth temperatures between 100 °C and 350 °C. In the lower growth temperature regime, high orders of interference fringes (up to fifth order) are seen, indicating a high crystal quality and interface perfection as well as a smooth surface. At T_G=250 °C, the interference fringes become less pronounced, indicating the onset of crystal degradation. At T_G=350 °C, the main peak is broadened and shifted to a larger angle, most likely due to an interfacial reaction. This was further evidenced by wide-range ω-2θ scans with a wide-open detector for the same series of films. An additional peak appears at around ω=17.3° for films grown above 350 °C, as is seen in the upper panel of Fig. 2 (arrows). We ascribe this peak to the $(Co,Fe)_2As(110)$ reflection caused by interfacial reaction between the Co_2FeSi layer and the GaAs substrate. Note that, based on these HRXRD results, the growth temperature at which an interfacial compound is formed is much higher than that of Fe, Co, and FeCo on GaAs.[27] This fact makes Co_2FeSi much more suitable for device applications than those ferromagnetic metals. However, since it is very difficult to detect nanometer-size interfacial compounds or clusters by XRD, further investiga-

tions of the interface perfection by an analysis of the in-plane magnetic anisotropy will be described later.

To confirm the atomic ordering of the films, additional reflections, namely the (002) and (113) reflections, were recorded. For the $L2_1$ structure, three types of reflections are allowed: (i) h, k, l are all odd [e.g., (113) reflection]; (ii) h, k, l are all even and $h+k+l=4n+2$ [e.g., (002) reflection]; and (iii) h, k, l are all even and $h+k+l=4n$ [e.g., (004) reflection], where n is an integer and h, k, l are the Miller indices of the diffracting plane. Type (iii) are the fundamental reflections which are not influenced by disorder, and the other two are the order-dependent superlattice reflections.[25] Type (i) reflections are reduced to zero in the limit of a complete disorder between Si and Fe sublattices, which leads to the reduction of the crystal symmetry to the $B2$ (CsCl) structure. Type (ii) reflections, on the other hand, are reduced to zero in the limit of complete disorder between all three sublattices, resulting in a further reduction of the crystal symmetry to the $A2$ (bcc) structure. Figure 3 depicts (a) the ω-2θ curve around the $Co_2FeSi(002)$ reflection, and (b) the reciprocal space map around the $Co_2FeSi(113)$ reflection of a stoichiometric Co_2FeSi film ($d=18.5$ nm) grown at 100 °C, and (c) the line profile along the dotted line shown in Fig. 3(b). Two main results can be derived from the figures. First, the two superlattice reflections of the $L2_1$ structure, namely the (002) and (113) reflections, are clearly seen with interference fringes, indicating the presence of a long-range atomic ordering and the Heusler-type $L2_1$ structure even for low T_G. The superlattice reflections were observed for Co_2FeSi films grown at different T_{Si} (namely different Si composition) and T_G as well. For the determination of the precise ordering parameters, further analyses of the superlattice reflections are underway. However, since the (113) reflections were taken in a reciprocal space mapping, it is difficult to quantitatively analyze the development of atomic ordering depending on T_{Si} and T_G from the intensity of superlattice reflections with respect to that of the fundamental one. Therefore, we performed electrical resistivity measurements instead on the films grown at different T_{Si} and T_G, as described in the following paragraphs. Second, the perfectly oriented vertical fringes indicate that the epitaxially grown Co_2FeSi layers are fully strained. This situation is preserved at least up to $d=38$ nm as far as we have studied.

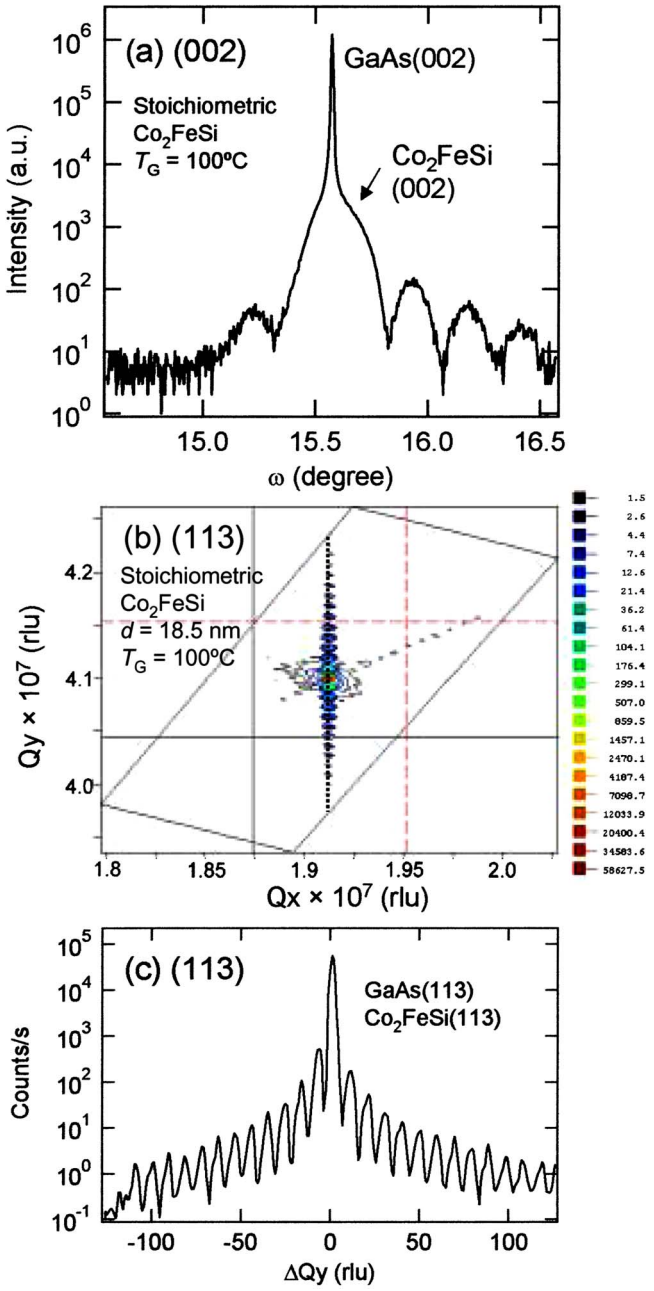

FIG. 3. (Color online) (a) HRXRD ω-2θ curve around $Co_2FeSi(002)$ reflection; (b) reciprocal space map around $Co_2FeSi(113)$ reflection; and (c) the line profile along the dotted line shown in (b) of a stoichiometric Co_2FeSi film grown at 100 °C.

B. Electrical properties

In order to obtain further information about atomic ordering of the Co_2FeSi films, we performed resistivity measurements on films with different Si compositions and T_G. Since the residual resistivity generally depends on the concentration of defects and impurities in the film, it can be used as a benchmark for evaluating the quality of alloy films. The resistivity of the Co_2FeSi films was measured using van der Pauw and Hall bar structures at two temperatures (77 and 300 K). The results are displayed in Fig. 4(a) together with that for $Co_{0.66}Fe_{0.34}$ (Si=0%). The broken line indicates the stoichiometric composition of Co_2FeSi determined by the lattice constant. The resistivity of the films monotonically increases with the Si composition. This is in contrast to the behavior expected for a perfectly ordered system, where the resistivity has a minimum at the stoichiometric composition due to the reduction of alloy scattering. This suggests that part of the Si atoms occupy inappropriate sublattice sites, namely the Co(A,C) and/or Fe(B) sites, resulting in Si antisite defects, although the majority of Si atoms occupies the Si(D) sites. Therefore, we conclude that the long-range atomic order and the $L2_1$ structure evidenced from the HRXRD results are not perfect due to the low growth temperature.

The long-range atomic order, however, is enhanced by elevating the growth temperature, as can be seen in Fig. 4(b). The figure shows the growth temperature dependence of the

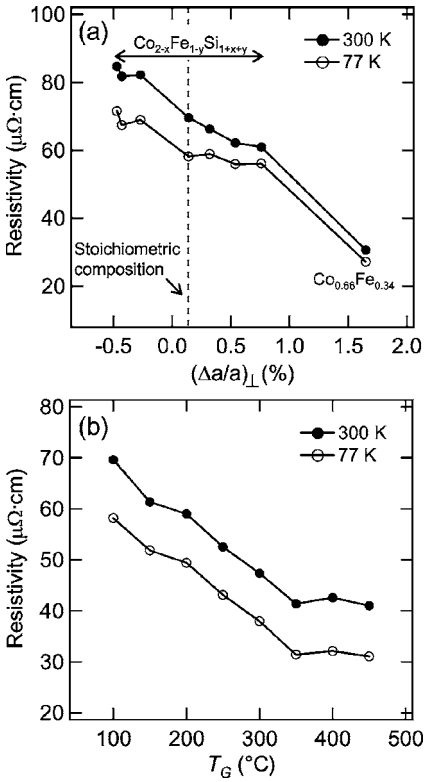

FIG. 4. Resistivity of Co_2FeSi films with (a) different Si compositions together with that of $Co_{0.66}Fe_{0.34}$ film and (b) different growth temperature measured on van der Pauw and Hall bar structures at 77 and 300 K. The broken line indicates the stoichiometric composition of Co_2FeSi determined by the lattice constant.

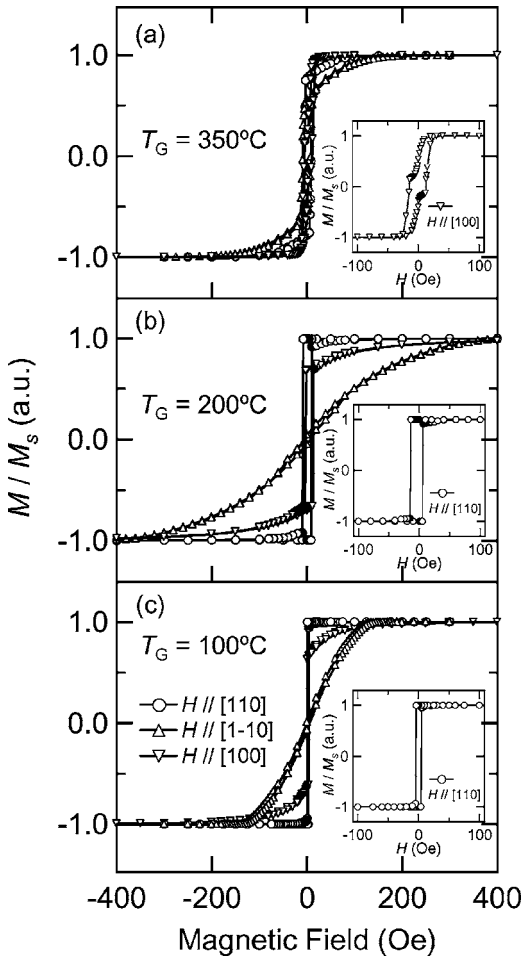

FIG. 5. Normalized magnetization curves of 18.5 nm thick stoichiometric $Co_2FeSi/GaAs(001)$ films grown at (a) 350 °C; (b) 200 °C; and (c) 100 °C. All the measurements were performed at room temperature. The external magnetic field was applied along three crystallographic axes ([110], [1$\bar{1}$0], and [100] directions). The insets show expanded views of the magnetization curves along the easy axis. After subtraction of the diamagnetic contribution from the GaAs substrate, the magnetizations were normalized to the saturation magnetization of each direction.

resistivity for stoichiometric Co_2FeSi films. The decrease of the resistivity with increasing T_G up to 350 °C demonstrates the improvement of the atomic ordering of crystal structure. The crystalline quality of the bulk structure, therefore, is better at higher T_G, in clear contrast to that of the interface structure where higher T_G results in interfacial reactions, as we have seen in the HRXRD results. Therefore, the optimum growth temperature for $Co_2FeSi/GaAs$ lies in the regime where the crystalline quality of the interface and the bulk structure are compromised.

C. Magnetic properties

The in-plane magnetic anisotropy of $Co_2FeSi/GaAs$ heterostructures was investigated using superconducting quantum interference device (SQUID) magnetometry. All measurements were performed at room temperature. The external magnetic field was applied along three crystallographic axes, namely the [110], [1$\bar{1}$0], and [100] directions. After subtraction of the diamagnetic contribution of the GaAs substrate, the magnetizations were normalized to the saturation magnetization of each direction. All examined Co_2FeSi films are ferromagnetic at room temperature. In Fig. 5, we show the normalized magnetization curves of the stoichiometric Co_2FeSi films grown at (a) 350 °C, (b) 200 °C, and (c) 100 °C and the expanded views along the easy axis in the inset. Two main results can be derived from the measurements.

First, the shape of the magnetization curves and the angle dependence of the magnetization dramatically change at T_G=350 °C. The magnetization curves of T_G<200 °C show square-shaped hysteresis loops and strongly anisotropic angle dependences. The magnetization curves of T_G<200 °C exhibit an easy axis [110], a hard axis [1$\bar{1}$0], and an intermediate axis [100]. The easy axis along the [110] direction is caused by a dominating uniaxial in-plane magnetic anisotropy component which has an easy axis different from that of the cubic magnetocrystalline anisotropy component (⟨100⟩ directions). The well-defined square-shaped hysteresis loop along the [110] direction with a small coercive field of 4.5 Oe confirms the excellent crystal quality of the films. The saturation magnetization M_s of stoichiometric films amounts to 1250±120 emu/cm^3, which is relatively close to that of bulk Co_2FeSi [1124 emu/cm^3 at 295 K (Ref. 26)], confirming the stoichiometric composition determined from the lattice constant. The M_s value decreases with increasing T_G, most likely due to the formation of a magnetically modified layer at the interface. The magnetiza-

tion curve of the T_G=350 °C sample, on the other hand, changes to a nearly isotropic angle dependence. The uniaxial anisotropy component almost disappears and the cubic term remains. The easy axis in total is consequently converted to the easy axis of the cubic component: the ⟨100⟩ direction. Note that the double steplike loop of the easy axis of the T_G=350 °C sample seen in the inset of Fig. 5(a) originates from a slight deviation of the easy axis from the ⟨100⟩ directions due to the remaining slight uniaxial component.

Second, the in-plane magnetic anisotropy significantly increases with elevating T_G from 100 to 200 °C. The in-plane magnetic anisotropy of Co_2FeSi films was analyzed, assuming that a free-energy density consists of a cubic magnetocrystalline anisotropy term K_1^{eff} and a uniaxial anisotropy term K_u^{eff} (Ref. 30)

$$\varepsilon(\phi) = -\frac{1}{4}K_1^{\text{eff}}\sin^2(2\phi) + K_u^{\text{eff}}\sin^2(\phi) - HM_s\cos(\phi-\alpha), \quad (1)$$

where α is the angle between external field H and the [110] direction, and ϕ is the angle between magnetization and the [110] direction. Assuming a coherent rotation as a magnetization reversal process, the relation between magnetic field and magnetization is given by minimizing $\varepsilon(\phi)$ (Ref. 30)

$$H(m) = 2K_1^{\text{eff}}(2m^3-m)/M_s + 2K_u^{\text{eff}}m/M_s, \quad (2)$$

where $m=\sin(\phi)$ is the normalized magnetization component. By fitting the magnetization curves along the $[1\bar{1}0]$ direction with this expression, two effective magnetic anisotropy constants, K_1^{eff} and K_u^{eff}, were obtained. K_u^{eff} is plotted as a function of T_G in Fig. 6(a). As can be seen from the figure, K_u^{eff} reaches a maximum at around T_G=200 °C and decreases with the further increase of T_G. The value of K_u^{eff} finally becomes almost negligible at T_G=350 °C. Note that the value of K_u^{eff} at T_G=350 °C is not plotted in Fig. 6(a), since it cannot be obtained analytically due to the absence of a reversible hard axis.

In general, K_u^{eff} and K_1^{eff} can be decomposed assuming a superposition of a volume term $K_{u,1}^{\text{vol}}$ and an interface contribution $K_{u,1}^{\text{int}}$,

$$K_{u,1}^{\text{eff}} = K_{u,1}^{\text{vol}} + K_{u,1}^{\text{int}}/d, \quad (3)$$

where d is the thickness of the film.[30] We plot K_u^{eff} and K_1^{eff} vs inverse d of Co_2FeSi films grown at 100 °C in Fig. 6(b). K_1^{eff} is independent of d, indicating that K_1^{eff} is a volume-related term, whereas K_u^{eff} is linearly dependent on inverse d. As obtained from the fit, K_u^{vol} is nearly zero and $K_u^{\text{int}}=(7.3\pm0.9)\times10^{-2}$ erg/cm^2, demonstrating that K_u^{eff} is a pure interface-related term, as is observed in other FM/SC systems. The value of K_u^{int} is in between those of Fe (Ref. 31) and $Fe_{0.34}Co_{0.66}$ (Ref. 30) on GaAs: 1.2×10^{-1} and 2.6×10^{-2} erg/cm^2, respectively. Since the value of K_u^{int} has been estimated from a series of films grown at 100 °C, namely at the lowest end of the low T_G regime in Fig. 5(a), K_u^{int} can be expected to be larger at higher T_G. In general, the uniaxial in-plane magnetic anisotropy observed in FM/SC systems is anticipated to originate from an anisotropic bonding at the interface.[32] Therefore, the T_G dependence of K_u^{eff} reflects the interface perfection including atomic ordering and abruptness. Hence, the quality of the interface is improved with the increase of T_G up to 200 °C, and then it deteriorates due to the interfacial reaction for $T_G>200$ °C. Thus, we conclude from the analysis of the in-plane magnetic anisotropy that the optimum T_G to obtain a perfect interface structure is around 200 °C.

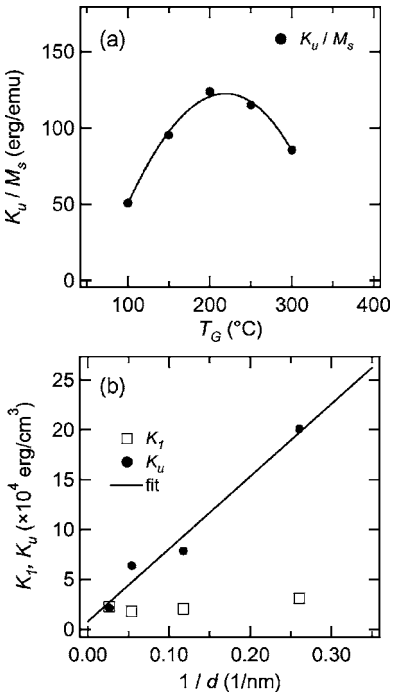

FIG. 6. (a) Uniaxial magnetocrystalline anisotropy constant (K_u^{eff}/M_s) of stoichiometric Co_2FeSi films as a function of growth temperature. (b) Uniaxial and cubic magnetocrystalline anisotropy constants (K_u^{eff} and K_1^{eff}, respectively) as a function of inverse film thickness d. The solid line shows the linear fit for K_u^{eff}.

IV. CONCLUSIONS

In conclusion, we have grown single-crystal full-Heusler alloy Co_2FeSi films on GaAs (001) by molecular beam epitaxy. Co_2FeSi layers with high crystal and interface perfection as well as smooth surfaces can be obtained by carefully controlling the fluxes of Co, Fe, and Si. The HRXRD and resistivity studies revealed that the layers have a long-range order and crystallize in a partly disordered Heusler-type $L2_1$ structure in the low growth temperature regime. The long-range atomic order of the layers is improved by elevating the growth temperature up to 350 °C. The increase of the growth temperature, however, results in an interfacial reaction between the Co_2FeSi layer and the GaAs substrate. The analysis of the in-plane magnetic anisotropy revealed that the interface perfection improves up to T_G=200 °C and deteriorates due to interfacial reactions above 200 °C. The optimum growth temperature for Co_2FeSi/GaAs heterostructures with high interface and crystal perfection, as well as high degree of atomic ordering, is thus around 200 °C. Hence, Co_2FeSi films are much more thermally stable than conventional ferromagnetic metals on GaAs. These results

indicate that Heusler alloys are promising candidates as a source for efficient electrical spin injection into semiconductors.

ACKNOWLEDGMENTS

This work was partly supported by the German BMBF under the research program NanoQUIT (Contract No. 01BM463). The authors would like to thank P. K. Muduli for useful discussions, A. Riedel for technical assistance, and R. Koch for a careful reading of the manuscript.

[1]R. Fiederling, M. Keim, G. Reuscher, W. Ossau, G. Schmidt, A. Waag, and L. W. Molenkamp, Nature (London) **402**, 787 (1999).
[2]Y. Ohno, D. K. Young, B. Beschoten, F. Matsukura, H. Ohno, and D. D. Awschalom, Nature (London) **402**, 790 (1999).
[3]H. J. Zhu, M. Ramsteiner, H. Kostial, M. Wassermeier, H.-P. Schönherr, and K. H. Ploog, Phys. Rev. Lett. **87**, 016601 (2001).
[4]B. T. Jonker, A. T. Hanbicki, Y. D. Park, G. Itskos, M. Furis, G. Kioseoglou, A. Petrou, and X. Wei, Appl. Phys. Lett. **79**, 3098 (2001).
[5]X. Jiang, R. Wang, S. van Dijken, R. Shelby, R. Macfarlane, G. S. Solomon, J. Harris, and S. S. P. Parkin, Phys. Rev. Lett. **90**, 256603 (2003).
[6]T. Manago and H. Akinaga, Appl. Phys. Lett. **81**, 694 (2002).
[7]C. Palmstrøm, MRS Bull. **28**, 725 (2003).
[8]R. A. de Groot, F. M. Mueller, P. G. van Engen, and K. H. J. Buschow, Phys. Rev. Lett. **50**, 2024 (1983).
[9]I. Galanakis, P. H. Dederichs, and N. Papanikolaou, Phys. Rev. B **66**, 174429 (2002).
[10]S. Fujii, S. Sugimura, J. Ishida, and S. Asano, J. Phys.: Condens. Matter **2**, 8583 (1990).
[11]T. Ambrose, J. J. Krebs, and G. A. Prinz, Appl. Phys. Lett. **76**, 3280 (2000).
[12]S. N. Holmes and M. Pepper, Appl. Phys. Lett. **81**, 1651 (2002).
[13]J. Q. Xie, J. W. Dong, J. Lu, C. J. Palmstrøm, and S. Mckernan, Appl. Phys. Lett. **79**, 1003 (2001).
[14]M. S. Lund, J. W. Dong, J. Lu, X. Y. Dong, C. J. Palmstrøm, and C. Leighton, Appl. Phys. Lett. **80**, 4798 (2002).
[15]W. Van Roy, J. De Boeck, B. Brijs, and G. Borghs, Appl. Phys. Lett. **77**, 4190 (2000).
[16]P. Bach, A. S. Bader, C. Rüster, C. Gould, C. R. Becker, G. Schmidt, L. W. Molenkamp, W. Weigand, C. Kumpf, E. Umbach, R. Urban, G. Woltersdorf, and B. Heinrich, Appl. Phys. Lett. **83**, 521 (2003).
[17]J. Herfort, H.-P. Schönherr, and K. H. Ploog, Appl. Phys. Lett. **83**, 3912 (2003); J. Herfort, H.-P. Schönherr, K.-J. Friedland, and K. H. Ploog, J. Vac. Sci. Technol. B **22**, 2073 (2004).
[18]A. Ionescu, C. A. F. Vaz, T. Trypiniotis, C. M. Gürtler, H. García-Miquel, J. A. C. Bland, M. E. Vickers, R. M. Dalgliesh, S. Langridge, Y. Bugoslavsky, Y. Miyoshi, L. F. Cohen, and K. R. A. Ziebeck, Phys. Rev. B **71**, 094401 (2005).
[19]A. Kawaharazuka, M. Ramsteiner, J. Herfort, H.-P. Schönherr, H. Kostial, and K. H. Ploog, Appl. Phys. Lett. **85**, 3492 (2004).
[20]X. Y. Dong, C. Adelmann, J. Q. Xie, C. J. Palmstrøm, X. Lou, J. Strand, P. A. Crowell, J.-P. Barnes, and A. K. Petford-Long, Appl. Phys. Lett. **86**, 102107 (2005).
[21]S. Kämmerer, A. Thomas, A. Hütten, and G. Reiss, J. Appl. Phys. **85**, 79 (2004).
[22]L. J. Singh, Z. H. Barber, Y. Miyoshi, W. R. Branford, and L. F. Cohen, J. Appl. Phys. **95**, 7231 (2004).
[23]R. J. Soulen Jr., J. M. Byers, M. S. Osofsky, B. Nadgorny, T. Ambrose, S. F. Cheng, P. R. Broussard, C. T. Tanaka, J. Nowak, J. S. Moodera, A. Barry, and J. M. D. Coey, Science **282**, 85 (1998).
[24]S. Picozzi, A. Continenza, and A. J. Freeman, Phys. Rev. B **69**, 094423 (2004).
[25]For the details of $L2_1$ structure, see P. J. Webster and K. R. A. Ziebeck, *Landolt-Börnstein New Series III/19c* (Springer, Berlin, 1988), p. 75.
[26]V. Niculescu, T. J. Burch, K. Raj, and J. I. Budnick, J. Magn. Magn. Mater. **5**, 60 (1977); V. Niculescu, J. I. Budnick, W. A. Hines, K. Raj, S. Pickart, and S. Skalski, Phys. Rev. B **19**, 452 (1979).
[27]H.-P. Schönherr, R. Nötzel, W. Ma, and K. H. Ploog, J. Appl. Phys. **89**, 169 (2001).
[28]T. Nishizawa and K. Ishida, Bull. Alloy Phase Diagrams **5**, 250 (1984).
[29]M. Hashimoto, J. Herfort, H.-P. Schönherr, and K. H. Ploog, Appl. Phys. Lett. **87**, 102506 (2005).
[30]M. Dumm, M. Zölfl, R. Moosbühler, M. Brockmann, T. Schmidt, and G. Bayreuther, J. Appl. Phys. **87**, 5457 (2000).
[31]M. Brockmann, M. Zölfl, S. Miethaner, and G. Bayreuther, J. Magn. Magn. Mater. **198–199**, 184 (1999).
[32]E. Sjöstedt, L. Nordström, F. Gustavsson, and O. Eriksson, Phys. Rev. Lett. **89**, 267203 (2002).

MORPHWARE

Magnetic logic may usher in an era in which computing devices can change instantly from one type of hardware to another

BY REINHOLD KOCH

Flexibility or performance?

That choice is a constant trade-off for microprocessor designers. General-purpose processors in personal computers execute a broad set of software commands that can cope with any task from graphics to complex calculations. But their flexibility comes at the expense of speed. In contrast, application-specific integrated circuits (ASICs), optimized for a given task, such as the computing required in graphics or sound cards, are very fast but lack adaptability.

Some processors fit a niche between these two types of hardware. Called morphware, they can be reconfigured and optimized for any task. One example—the commercially available field-programmable gate array (FPGA)—consists of large blocks of transistors that perform logic operations and that can be "rewired" by the software. Customization enables FPGAs to accelerate data encryption, automatic military target recognition or data compression by a factor of 10 to 100—enabling, for instance, dramatically enhanced security or faster target acquisition times as compared with a general-purpose CPU (central processing unit).

FPGAs rely on the ubiquitous transistor-based technology called complementary metal oxide semiconductor (CMOS). They have limitations, however. Changing operations on the fly—converting, say, a calculation of a matrix of numbers to a parallel-processing computation—requires the relatively slow rewiring of connections between large blocks of transistors, not the individual elements (gates) that perform a processor's logic operations. FPGAs generally take up a large amount of space, resulting in a very low density of circuitry and limiting the number and speed of processing operations.

In the past few years, a number of groups have begun to explore a new type of morphware processor that uses layers of magnetic materials to create reconfigurable logic elements. The advantages of these magnetologic elements are that the information stored does not disappear when external power is shut off and that they do not have to be refreshed while the device is in operation. Unlike CMOS-based systems, the logic is nonvolatile. This stability of magnetic bits explains the key role of magnetic materials in data storage, such as hard disks. In a magnetologic device, nonvolatility of information would also reduce power consumption, and a single element

Overview/*Chameleon Chip*

- The brains of most contemporary computers—the central processing units—are either built to execute a broad set of commands or are optimized for speed.
- A class of processor, known as morphware, offers the best of both worlds. It executes one application quickly and then, based on software commands, changes the processor's wiring to optimize itself for a new application.
- A new type of morphware, called magnetologic, is built from layered metallic materials, each layer of which is magnetized to represent a digital bit. This chameleon of processors can alter its functionality by changing wiring, or gates, many times per second, allowing it to switch rapidly from, say, a cell phone to an MP3 player.
- Because magnetologic stores the results of each processing operation, it can function as both a processor and a memory device.

BRYAN CHRISTIE DESIGN (*preceding pages*)

HOW A BASIC MAGNETOLOGIC GATE WORKS

Two ferromagnetic layers, separated by a nonmagnetic spacer, can switch polarity (*arrows*) to output a digital "1" or "0." Electric currents applied through slablike input lines produce the magnetic field needed for changing magnetization. A current through the two top lines switches the magnetization of the top layer. A current through three input lines shifts both layers. A positive magnetization (*right-pointing arrow*) represents a digital "1," and a negative magnetization (*left-pointing arrow*) a digital "0." After the input currents switch the two layers' parallel or antiparallel states, the result can be read as a bit through the output line.

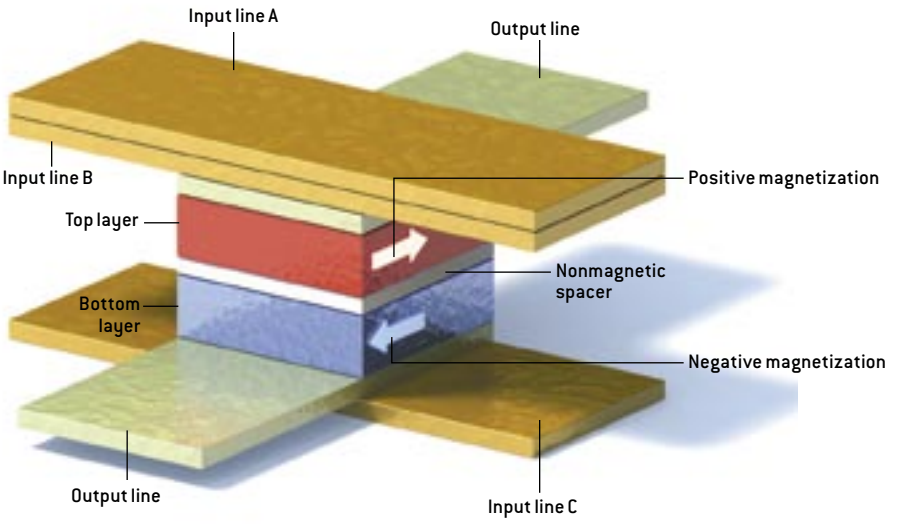

would be capable of performing different logic functions that typically require multiple transistors.

From Cell Phone to MP3 Player

MAGNETOLOGIC COULD BRING electronic multitasking to a new level, letting a designer create a cell phone that could later morph into a music player, thereby reducing the need for separate microprocessors in electronic equipment. Because the switching speed of magnetologic gates is fast, switching at billions of cycles per second (gigahertz), this chameleon of processors can alter its functionality many times within the space of even one second.

The operation of magnetologic builds on a technology for storing digital bits known as magnetic random-access memory (MRAM), which is now nearing commercialization. Each unit of MRAM consists of two ferromagnetic metallic alloys separated by a nonmagnetic spacer that ensures that the magnetization of one layer does not affect the other and that the polarity (direction of magnetization) can be shifted independently [*see box above*]. The memory element represents the value of a digital bit, which depends on whether the magnetization of the upper and lower layers are aligned in parallel or oppose each other. Lower resistance to the flow of electric current occurs when the magnetization of both layers is in parallel—a state that represents, say, a digital "1." When the polarity of both layers is opposite, the so-called magnetoresistance increases (a "0" state).

To switch the resistance of the MRAM element from low (1) to high (0), or vice versa, an electric current must flow through inputs connected to the memory element. Besides the simple 0 or 1 that it stores in memory, a single MRAM element can be used to represent basic logic functions, such as AND or OR.

Elementary magnetologic gates date back to the early 1960s but were quickly supplanted by silicon microchips. In 2000 William C. Black, Jr., and Bodhisattva Das of Iowa State University published a seminal report on magnetologic based on magnetoresistance. Two years later Siemens Research in Erlangen, Germany, demonstrated experimentally a reconfigurable magnetologic element. Then, in 2003, our group at the Paul Drude Institute in Berlin published a paper that proposed using a simpler implementation for changing the logic states of the various computational elements.

Making a Logic Gate

A MAGNETOLOGIC GATE is very similar to an MRAM cell. It also consists of two magnetic layers separated by a nonmagnetic spacer in which the parallel and antiparallel magnetizations exhibit low and high resistance and provide the logic outputs "1" and "0," respectively. In general, the magnetoresistance of layered systems is significantly higher than that of systems not built in layers, easing the reading and writing of bits. This property is known as giant magnetoresistance or tunneling magnetoresistance, depending on which type of spacer

THE AUTHOR

REINHOLD KOCH is the leader of the nanoacoustics group at the Paul Drude Institute for Solid State Electronics in Berlin. Born in Tirol, Austria, he received his doctorate in chemistry at the University of Innsbruck in 1981. He was granted a Max Kade Fellowship during 1985 and 1986 at the Stanford-NASA Joint Institute for Surface and Microstructure Research in California. From 1988 to 1998 he was assistant teacher in the physics department of the Free University in Berlin and received the Karl Scheel Award in 1994 for his contributions on the evolution of stress in thin films and structural investigations with a scanning tunneling microscope.

BRYAN CHRISTIE DESIGN

Magnetologic stores a digital bit without the need for continuous refreshing by an external current.

material is used. Both effects depend on the electrons' spins (their angular momenta), which are all aligned in the same direction, almost as if the electrons were tiny balls spinning on their axes. These effects are used to "read" the value of a bit.

Changing the orientation of spin is used to "write" a bit—in other words, to change the magnetization from one direction to another. The direction of magnetization of either layer can be reversed by the magnetic field of a current flowing through the input lines. But a number of investigators are examining another method, in which spin exerts a torque that can switch a layer's magnetization from one direction to another [see "Spintronics," by David D. Awschalom, Michael E. Flatté and Nitin Samarth; SCIENTIFIC AMERICAN, June 2002].

In the design we put forward at Paul Drude, the magnetologic gate contains three inputs—A, B and C—each of which is addressed by a current of equal magnitude. Our concept makes use of the fact that a magnetoresistive element, though providing only two output values (a 0 and a 1), can be in four different initial states, two of them parallel and two of them antiparallel, allowing the configuration of distinct logic states. Previous magnetologic designs required more complex circuitry that would employ, for example, input currents of different intensity.

In our design, a logic operation begins by setting the gate polarity in one of these four states by addressing two or three of the input lines. Then, in a second step, the logic operation is performed by activating only the upper two input lines, A and B. A chosen initial state can only be reversed when two or three of the input lines are addressed with the same polarity magnetic field, changing the output value from 1 to 0, or the converse [*see box below*]. This process has the advantage that the logic state can be reprogrammed with each new operation.

CHANGING BITS

Logic operations are performed in a magnetologic gate in two steps. An AND gate, for instance, can be created by first setting the device to a 0 state (*left*): the top layer holds a negative magnetization (*left-pointing arrow*); the bottom assumes a positive magnetization (*right-pointing arrow*). Currents that emit a positive magnetic field (*red*) then flow through the two upper input lines, labeled A and B. Magnetization of the top layer becomes positive (*right*). By so doing, the bit changes from a 0 to a 1 and is stored in its new state. The output line is used only to read whether the bit is in a 0 or 1 state.

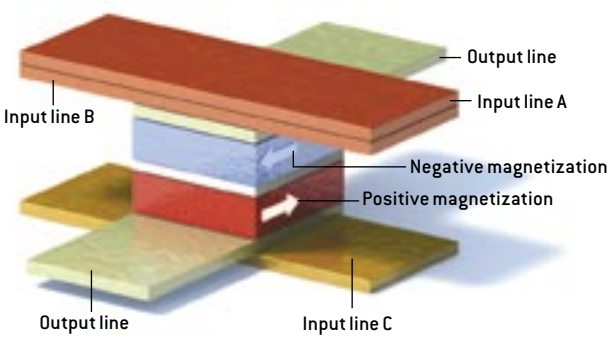

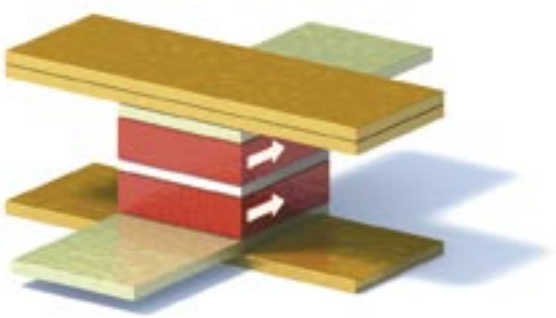

AND GATE

CURRENT	A	B	OUTPUT
⇇	0	0	0
⇆	0	1	0
⇄	1	0	0
⇉	1	1	1

BRYAN CHRISTIE DESIGN

CHANGING GATES

Addressing all three input lines—A, B and C—changes an AND gate to its opposite, a NOT AND, or NAND, gate. Currents that emit a negative magnetic field (*blue*) are applied to all three input lines (*left*). The bottom layer, which exhibits a positive magnetization, then switches to a negative magnetization (*right*). The output of a NAND gate (*purple*) is the opposite of an AND gate (*green*). The C line does not bear on the logic operations shown in the truth tables.

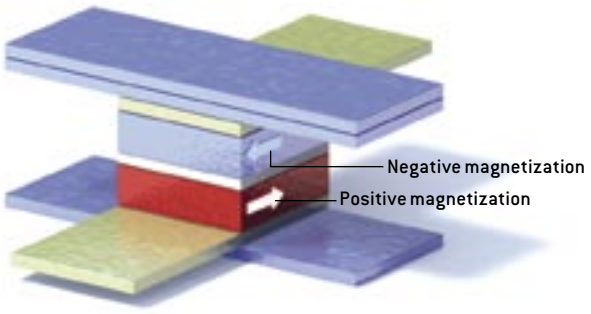

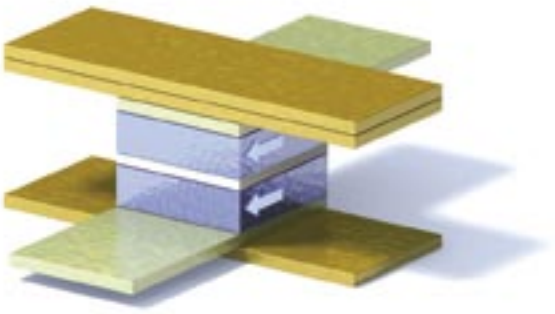

AND GATE

CURRENT	A	B	OUTPUT
⇇	0	0	0
⇆	0	1	0
⇄	1	0	0
⇉	1	1	1

NAND GATE

CURRENT	A	B	OUTPUT
⇇	0	0	1
⇆	0	1	1
⇄	1	0	1
⇉	1	1	0

Because the magnetologic gate maintains its assigned polarity in the absence of an external current, a bit is stored without continuous refreshing and can be read out without deleting the information. Thus, the combined logic and storage capability saves not only energy but also time, compared with information processed by conventional CMOS circuitry.

For the AND function, for example, we start from an antiparallel state with an output of 0. Viewed in cross section, the polarity of the top layer points to the left, whereas the bottom layer points right. Only positive currents that are applied to both inputs A and B—currents that generate a positive magnetic field—can switch the direction of magnetization of the top layer from left to right. The OR gate operates using an analogous method, but the magnetizations of both layers point to the right at the beginning of the procedure. The other two basic logic functions are obtained by switching the bottom layer. All three inputs—A, B and C—are applied to switch the lower layer. The magnetic field needed to switch the polarity of the top layer is less than that for the bottom layer, so the two can be addressed independently. Switching the bottom layer transmutes the output of an AND and OR function into its opposite: NOT AND (NAND) or NOT OR (NOR) [*see box above*].

The OR and AND functions correspond to Boolean addition and multiplication, respectively. Together with NAND and NOR, they represent a powerful basis for describing even the most complex circuits. By changing the procedure of addressing the inputs, magnetoresistive logic gates can produce even more advanced logic functions. For instance, the XOR gate—key to a critical logic unit called a full adder—differentiates between the same and opposite inputs, yielding an output 1 for any two of the same inputs (0/0 or 1/1) and 0 for opposite inputs (0/1 or 1/0). Two magnetoresistive elements can create the XOR gate as compared with eight to 14 transistors in CMOS technology.

The magnetologic gates can also be employed to construct an entire full adder—the most widely used logic unit in a processor. A full adder sums binary inputs A and B plus a carry digit brought forward from a previous calculation. The addition of the three digits produces a new sum as well as a new carry digit. The nonvolatility and the programmability of the magnetologic gates mean that a full adder can be fashioned with only three gates, rather than the 16 transistors with CMOS. The magnetic full adder might become competitive in speed even with the fastest CMOS full adders and boasts superior power efficiency.

Looking Ahead

THE FATE OF MORPHWARE could closely resemble that of commercially announced MRAM cells. The input lines A and B would be arranged in the form of a rectangular grid, a so-called crossbar geometry, similar to that in an MRAM. The magnetoresistive gate elements would sit in the crossing points and be switched only when both input lines are addressed simultaneously. The gates would have to be stacked on top of a template of CMOS transistors that would relay signals indicating when each gate element should begin and stop processing. The transistors in this configuration would also be used to amplify the small currents needed to read a magnetoresistive bit [*see box on page 63*].

The chameleonlike nature of a morphware processor re-

BRYAN CHRISTIE DESIGN

A magnetic chameleon processor constitutes an array of logic gates, each of which is programmable individually by the software.

tains many advantages. Because of the programmability of the logic gates, hardware no longer determines processor capabilities. In CMOS, the logic of a conventional transistor gate is defined by the wiring and is therefore fixed. A magnetic processor constitutes an array of logic gates, each of them programmable individually by the software.

A magnetic chameleon processor therefore needs far fewer logic gates than a conventional processor, in which only a few percent of the hardwired gates are useful for any given task. The programmability also means that newer and better software can easily be implemented, even on older magnetologic processors. Because the switching speed of magnetologic gates is fast, billions of cycles per second, a chameleon processor can alter its functions many times within the course of that second. The nonvolatility of a logic element—the fact that it stores the output of its last operation—also gives the device a benefit in speed. Although magnetologic is fast, its gigahertz switching time is comparable to that of CMOS processors. But nonvolatility means that a clock is not needed to synchronize the extraction of digital bit values from the storage cells in a computer's memory, which simplifies and speeds processing. The bits themselves are stored where they are processed. Unlike CMOS, magnetologic does not necessarily have to reduce component size to increase performance—in other words, it bypasses miniaturization. This advantage may appear increasingly attractive as chip manufacturers struggle to make components ever smaller.

Design of a future chameleon processor is still an academic proposition—for now, no one is considering its development outside of the few laboratories that have published technical

PICK YOUR PROCESSOR

	Programmable	Speed of Reprogramming	Number of Components for Basic Logic	Timing
Magnetologic	Yes	~ 0.1 nanosecond	One magnetologic gate	Executed in parallel without need for a clock to synchronize data transfer
Conventional processor	No	Not applicable	Four transistors	Executed serially; needs a clock, which makes it slower and more complex
Field-programmable gate array	Yes	> 10 nanoseconds	Unable to address individual logic elements	Executed serially; needs a clock

Four transistors are needed (*left*) to perform the functions of a basic AND logic gate, whereas just one magnetologic element can accomplish the same task (*right*).

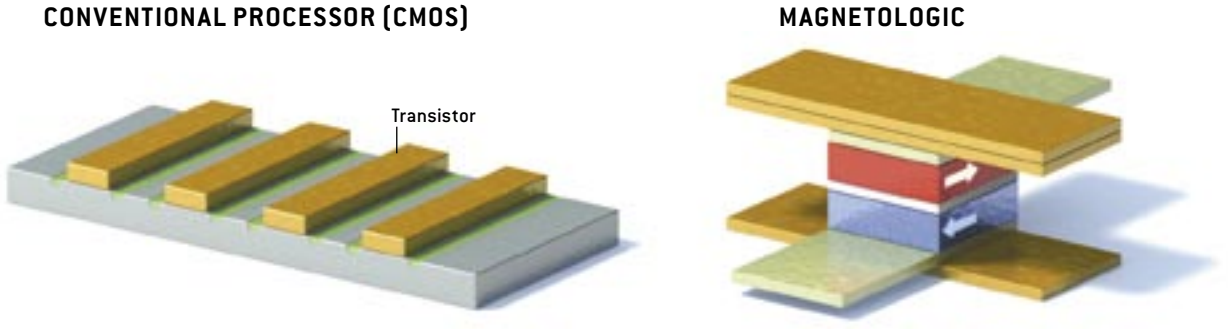

BRYAN CHRISTIE DESIGN

MAGNETOLOGIC PROCESSOR

Arrays of magnetologic gates form the building blocks of a magnetologic processor, which is displayed in an artist's conception of a simplified design. Such a processor would require fewer gates than a conventional one. Transistors (*not shown*) would still be needed to address the various elements—to turn them on and off—and to amplify their small output currents. Software defines the functions that the processor performs at any given time.

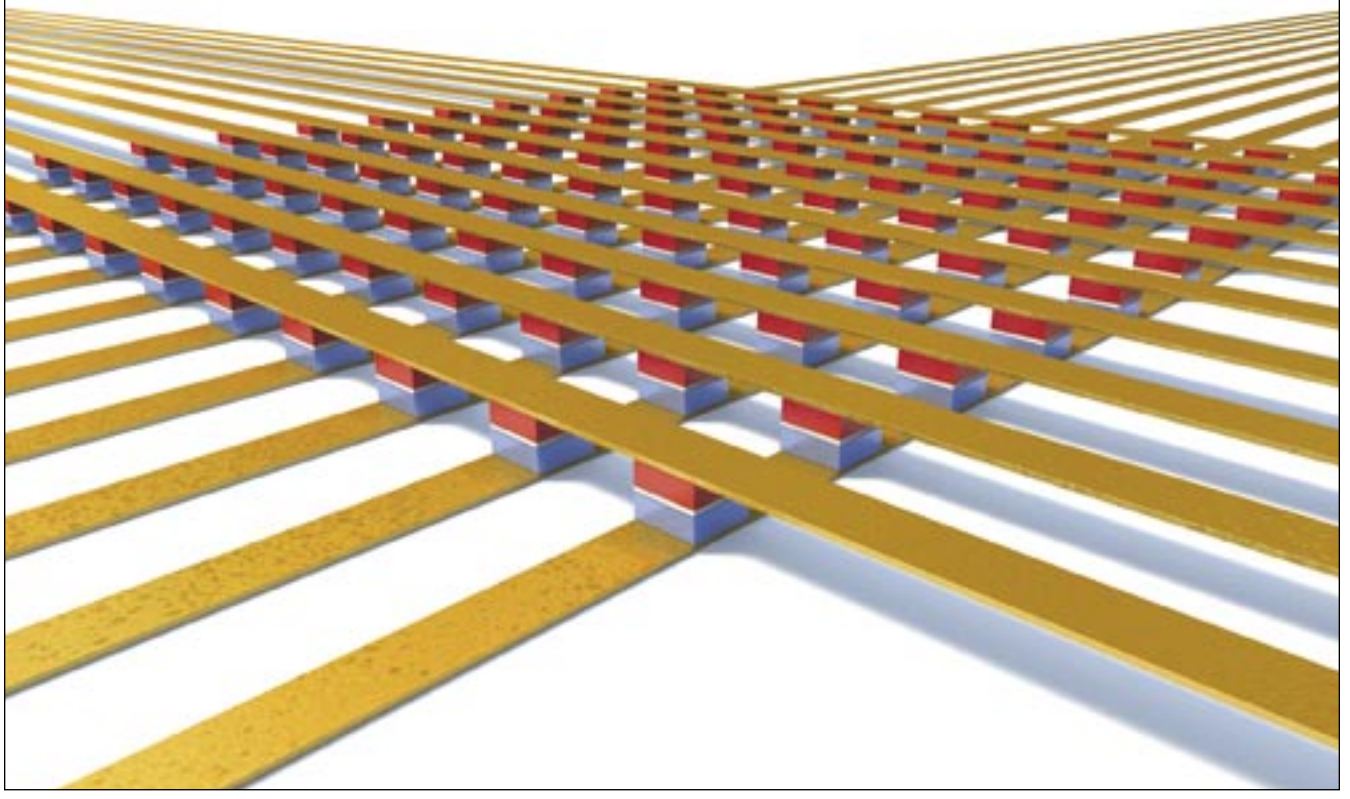

papers. Because of its close similarity to MRAM, magnetologic may benefit from engineering work that is addressing problems such as the coupling of magnetic fields between layers in the memories. Similarly, it could suffer if the industry slows development of the technology. Already some companies have hesitated to move ahead with MRAM, estimating that yet another version of random-access memory is unlikely to pull in large revenues. In magnetologic's early implementation, MRAM itself might function as an elementary processor that could be used in early products. But because only one magnetic layer is switched in MRAM, only two programmable functions could be accessed, either AND/OR or NAND/NOR.

To achieve the full potential of a magnetic chameleon processor, many challenging, but ultimately solvable, problems must be surmounted: First, both magnetic layers need to be switched independently, which is still difficult to do in a real working gate. Also, because the processor is working to full capacity most of the time, it generates pockets of heat locally that could compromise the integrity of the data. So reliability requirements for reading and writing operations are much higher. Engineers must show that magnetologic gates can achieve a lifetime as high as 10^{16} to 10^{17} operations, requiring longevity improvements of two or three orders of magnitude. In the meantime, one mitigating factor is that defective gates can be detected and bypassed when a computer boots up. To optimize magnetologic, new magnetic compounds are needed that are compatible with semiconductors and exhibit a giant magnetoresistance [see "Magnetic Field Nanosensors," by Stuart A. Solin; Scientific American, July 2004].

Perhaps one of the most imposing hurdles is to develop a compiler language and new algorithms that take full advantage of the real-time reprogrammability of the logic gates. To bring a magnetic chameleon processor to market will require an interdisciplinary research effort that uses the combined skills of specialists in materials science and technology, hardware design and electronics, computer sciences, and mathematics. SA

MORE TO EXPLORE

Programmable Logic Using Giant-Magnetoresistance and Spin-Dependent Tunneling Devices. W. C. Black, Jr., and B. J. Das in *Journal of Applied Physics,* Vol. 87, No. 9; pages 6674–6679; May 1, 2000.

Reconfigurable Computing: A Survey of Systems and Software. Katherine Compton and Scott Hauck in *ACM Computing Surveys,* Vol. 34, No. 2, pages 171–210; 2002.

The Future of Universal Memory. Russell P. Cowburn in *Materials Today,* Vol. 6, No. 7–8, pages 32–38; July–August 2003.

Programmable Computing with a Single Magnetoresistive Element. A. Ney et al. in *Nature,* Vol. 425, pages 485–487; October 2, 2003.

BRYAN CHRISTIE DESIGN

Slow relaxation of magnetization in MnAs nanomagnets on GaAs(001)

Y. Takagaki,[a] C. Herrmann, E. Wiebicke, J. Herfort, L. Däweritz, and K. H. Ploog
Paul-Drude-Institut für Festkörperelektronik, Hausvogteiplatz 5-7, 10117 Berlin, Germany

(Received 24 August 2005; accepted 23 November 2005; published online 17 January 2006)

We demonstrate slow relaxation of the magnetization in MnAs nanoparticles fabricated from epitaxially grown films on GaAs(001). In disks having a diameter as small as 100 nm and a thickness of 50 nm, the decay of the magnetization at 27 °C, which is merely ~10 °C below the Curie temperature T_C, is less than 1% over a period of one day. The large uniaxial magnetocrystalline anisotropy and the abrupt loss of the ferromagnetism at T_C of MnAs are responsible for the slow relaxation. © *2006 American Institute of Physics*.
[DOI: 10.1063/1.2166196]

In the course of miniaturizing a unit cell of magnetic storages, the associated magnetic energies eventually become smaller than the thermal energy k_BT. The magnetization of a particle having a uniaxial magnetic anisotropy can thus flip to the opposite direction by thermally surmounting an energy barrier. This instability imposes a limit to the data storage density, which has increased steadily since the 1950s at a rate of tenfold in 6 years.[1,2] There is a number of proposals to extend the limit. One intriguing example is the use of the exchange biasing effect to suppress the superparamagnetism.[3] Even within a conventional approach, one can, in principle, avoid the thermal instability by choosing materials having a large anisotropy constant K, as thermal agitation is a function of a quantity KV/k_BT, where V is the particle volume.[2] However, K cannot be too large in practice as the external magnetic field required to record magnetic data scales in proportion to K. Thermally assisted magnetic recording, for instance, is a compromising technique, in which the recording is carried out at an elevated temperature to reduce the coercivity.[4]

In this letter, we demonstrate a markedly slow relaxation of the magnetization in MnAs nanoparticles resulting from the large K value ($=7\times10^5$ J/m^3 at room temperature[5]) of the material. (Note for comparison that $K=4.8\times10^4$ J/m^3 in bcc Fe.) MnAs is attractive also from the viewpoint of the thermally assisted magnetic recording as the Curie temperature T_C of bulk MnAs is only about 40 °C. In spite of the long-term stability of the magnetization at room temperature, the coercivity is diminished by increasing the temperature by a mere several tens of a degree.

We investigate the magnetization in MnAs disks fabricated from two 50-nm-thick films. The MnAs layers were grown on GaAs(001) substrates using molecular beam epitaxy.[6] The growth conditions were optimized to have the surface of the epitaxial MnAs layers being oriented as $(1\bar{1}00)$.[7] The [0001] and $[11\bar{2}0]$ directions of MnAs were aligned along the $[1\bar{1}0]$ and [110] directions of GaAs, respectively. The MnAs/GaAs heterostructures were processed to the arrays of MnAs disks using microfabrication technologies. A NiCr etch mask was prepared on the MnAs surface using electron beam lithography and the lift-off technique. The MnAs layers were transformed into disks depicted by the mask using Ar ion milling at an acceleration voltage of 150 V. We examine two samples, of which the scanning electron micrographs are shown in Fig. 1. The magnetization of the samples was measured using a superconducting-quantum-interference-device magnetometer (Quantum Design MPMS XL). The metal mask was left on top of the MnAs disks during the measurements. We have confirmed that the deposited NiCr is paramagnetic, and so it does not affect the relaxation of the magnetization in the MnAs disks.

In Fig. 2, we show the magnetization curve of the MnAs disks shown in Fig. 1(a) at a temperature $T=20$ °C. The diameter of the disks is $d=100$ nm. The external magnetic field H is applied along the magnetic easy axis, which is along the $[11\bar{2}0]$ direction of MnAs. The magnetization M is normalized by the saturation magnetization M_s. For comparison, the magnetization curves of the MnAs film from which the sample was fabricated are also plotted. Here, H is applied along the MnAs$[11\bar{2}0]$ direction (easy axis) for the dotted line and along the MnAs[0001] direction (hard axis) for the dashed line. Notice that the uniaxial magnetocrystalline anisotropy in MnAs films is remarkably large. As we show later, the large anisotropy leads to unique magnetic properties of MnAs disks. The coercivity of the disks (0.73 kOe) is similar to that of the film. In the disks, the remanence M_r is only 20% smaller than M_s. The similarity of the magnetization curve of the disks to that of the film suggests that the thermal effects on the magnetic moments are considerably small in the MnAs disks.

Before we analyze the magnetic properties of the disks further, let us describe the behavior of the magnetic domains

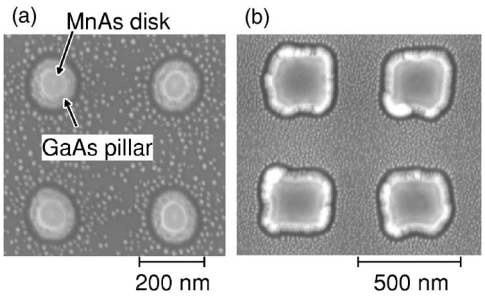

FIG. 1. Scanning electron micrographs of MnAs disks fabricated from 50-nm-thick films grown on GaAs(001). The size of the disks is (a) 100 and (b) 200 nm. The two samples were processed from separate films. The MnAs disks sit on top of GaAs pillars as the Ar ion milling proceeded about 100 nm deep into the substrates. The square arrays of the disks were defined along the cleavage directions of GaAs.

[a]Electronic mail: takagaki@pdi-berlin.de

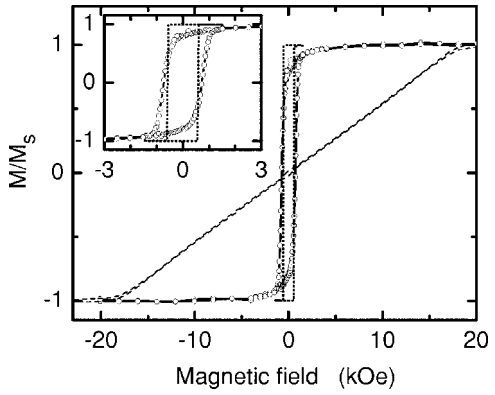

FIG. 2. Magnetization curves of MnAs film and disks fabricated from the film. The magnetization M is normalized to the saturation magnetization M_s. The in-plane external magnetic field is applied for the film along the uniaxial easy axis, MnAs[$11\bar{2}0$] (dotted line), or the hard axis, MnAs[0001] (dashed line). For the disks having the size of 100 nm, Fig. 1(a), the magnetic field is applied along the easy axis (solid line with circles). The hysteresis loops are shown with an expanded scale in the inset.

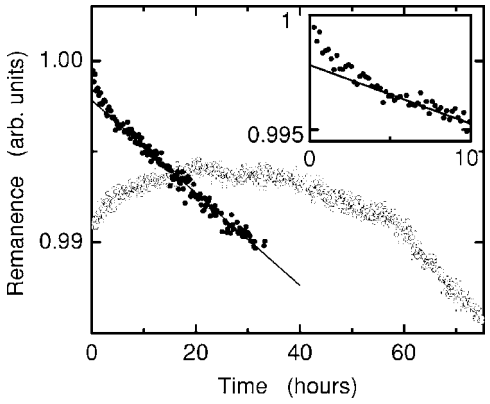

FIG. 3. Time dependence of the remanence, normalized by a common value, in disks having a diameter of 100 nm, Fig. 1(a). The disks were magnetized prior to the measurements in a magnetic field of 20 kOe. The temperature is 27 and 20 °C for the filled and open circles, respectively. The sample was at a lower (higher) temperature than the measurement temperature for the filled (open) circles immediately before the measurements. The solid line is a fit assuming an exponential decay, Eq. (1). The inset is an expanded plot to show a rapidly decaying component.

in submicrometer disks. The magnetic domain structure undergoes a fundamental change when the dimensions of ferromagnetic elements are reduced to nanometer scales. That is, a transition between a vortex state and a single-domain state occurs.[8] In the disks larger than a critical size, the magnetic structure is a vortex (closure-flux-type multidomain) state,[9] unless the magnetic properties of the ferromagnetic material are highly anisotropic. When the disk size is below the critical value, however, the domain-wall energy exceeds the magnetostatic energy arising from stray fields. The reversal in the energy relationship originates from the nonzero width of the domain walls. A single magnetic domain thus occupies the entire disk in the latter regime even after demagnetization. We have established using magnetic force microscopy that the critical size to reach the single domain regime is about 100 nm for the present MnAs layer thickness.[10]

We now turn our attention back to the relaxation of the magnetization in the disks. In the sample with $d=100$ nm, most of the disks are single domain particles.[10] The relaxation of the magnetization in these so-called nanomagnets arises from the probabilistic process of the thermally induced reversal of their magnetic moments. The decay of the magnetization with time t is hence given as

$$M_r(t) = M_r(0)\exp(-2t/\tau), \tag{1}$$

where τ^{-1} is the flipping rate of the magnetic moments. We show in Fig. 3 the time dependence of the magnetization at $H=0$ after the MnAs disks were magnetized at $H=20$ kOe. One finds that the experimental results are not as simple as predicted by Eq. (1).

The sample temperature was 27 and 20 °C for the filled and open circles, respectively. However, the qualitatively different time dependence in the two measurements is a consequence of the contrasting temperature at which the sample dwelled prior to the measurements. The sample was warmed to the measurement temperature for the filled circles, whereas the sample temperature was 32 °C before the measurement for the open circles. The magnetization initially increased in the measurement run shown by the open circles. In contrast, a rapid decay (the deviation from the extrapolation of the long-time behavior indicated by the solid line in the inset of Fig. 3) was observed in the measurement run shown by the filled circles. Through measurements under various thermal histories, we have established that the increase and the rapid decrease in the magnetization take place when the samples are cooled and warmed to the measurement temperature, respectively. We, therefore, attribute these rapidly quenching contributions to the temperature hysteresis of the first-order phase transition between the ferromagnetic α phase and the nonmagnetic β phase of MnAs at T_C ($\approx$40 °C).

In a wide temperature range around T_C, which includes room temperature, both of the disks consisting of α-MnAs and of β-MnAs exist when the material is grown on GaAs.[10] This type of coexistence is a manifestation that a first-order phase transition does not occur immediately when the temperature is varied from a value favoring one phase to another value favoring the other phase. An abrupt phase transition takes place in each disk probabilistically by surmounting the potential barrier separating the phases. The thermal hysteresis thus gives rise to a relaxation behavior. We note, however, that some characteristics of the rapid decay are not clearly understood at present by the interpretation based on the thermal hysteresis. (i) The increase of the magnetization implies that the newly converted α-MnAs disks are, at least predominantly, magnetized in the direction of the magnetic moments of the surrounding disks. Dipole-dipole interaction might be responsible for the magnetic ordering. (ii) The initial increase ($\beta \rightarrow \alpha$ transition) takes place on a time scale which is much longer than that when the counterpart ($\alpha \rightarrow \beta$ transition) leads to a decay of the magnetization. The asymmetry may be intimately related to (i), i.e., the $\alpha \rightarrow \beta$ transition always results in a decrease of the magnetization, whereas the $\beta \rightarrow \alpha$ transition does not have to increase the magnetization.

Once the fast-relaxation contributions diminish, the magnetization decays at a comparable rate for both of the measurement runs in Fig. 3. We attribute this slow decay to the thermal switching of the magnetic moments. If we assume a relaxation given by Eq. (1) (the solid line in Fig. 3), the relaxation time is estimated to be $\tau \sim 300$ days. The switching events of the magnetization are hence indicated to

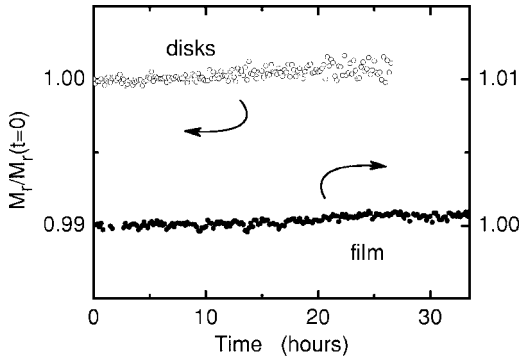

FIG. 4. Time dependence of the remanence M_r normalized to the value at time $t=0$ at 20 °C. The open and filled circles correspond to disks having a size of 200 nm, Fig. 1(b), and the MnAs film from which the disks were fabricated, respectively. The samples were magnetized at 5 kOe prior to the measurements.

be scarce in MnAs disks owing to the gigantic uniaxial magnetocrystalline anisotropy.

In general, magnetic moments thermally fluctuate around the easy axis. The extremely slow relaxation suggests that the deviation angles are restricted to be fairly small in MnAs disks and the thermal effects provide no appreciable contribution for lowering M_r below M_s. The difference between M_r and M_s in Fig. 2 is hence ascribed to a distortion of atomic magnetic moments by magnetic interactions, i.e., a "spin texture" that develops near the edges of the disks.[11]

Figure 4 shows the time dependence of the magnetization in disks having $d=200$ nm, see Fig. 1(b). For this disk size, the two phases of MnAs coexist within a single disk, presumably in the form of a core-shell-type phase segregation.[10] With respect to the magnetic properties, on the one hand, the magnetic energy is estimated to be several times larger in this sample than in the sample in Fig. 3, thereby stabilizing the magnetization. On the other hand, as the disks are in the multidomain regime, the magnetization can relax not only by flipping the total magnetic moment but also by creating a domain wall, i.e., reversing a part of the magnetization. The disks are expected to contain no more than two domains, as the large magnetocrystalline anisotropy in MnAs$(1\bar{1}00)$ films disfavors a tilt of the magnetization away from the easy axis caused by the shape anisotropy.[10] The relaxation would not be enhanced by a domain-wall movement. The experimental result demonstrates that the relaxation is, at least, comparably slow in the multidomain disks.

To overcome the recording magnetic field limit which is encountered when a high-K material is used, thermally assisted magnetic recording has been proposed.[4] MnAs-based devices are prospective for such applications as, despite the thermal stability of the magnetization at room temperature, T_C of the material can be exceeded by increasing the temperature by several tens of a degree. We also emphasize a unique magnetic property of MnAs, i.e., the loss of the ferromagnetism at T_C is discontinuous.[12] The magnetic moment remains unusually large even for temperatures slightly below T_C, and the magnetic anisotropy can be substantial to prevent the thermal randomization, as we demonstrated in the present work. Although T_C of bulk MnAs may be too low for some applications, we point out that the phase transition temperature in epitaxial films grown on substrates can be manipulated by strain control. The transition temperature in disks can be raised by enhancing the tensile strain due to the thermal expansion mismatch between MnAs and the substrate material. In addition, the thermal hysteresis could be suppressed by optimizing the growth conditions.[13]

In conclusion, we have evaluated the relaxation time of the magnetization in 100- and 200-nm-large MnAs disks on GaAs(001). The uniaxial magnetocrystalline anisotropy in MnAs is found to be large enough to stabilize the magnetization even at room temperature. The thermal stability is maintained even though the temperature is merely 15–20 °C below the Curie temperature of MnAs.

Part of this work was supported by the Federal Ministry of Education and Research (nanoQUIT program).

[1] S. H. Charap, P.-L. Lu, and Y. He, IEEE Trans. Magn. **33**, 978 (1997).
[2] D. Weller and A. Moser, IEEE Trans. Magn. **35**, 4423 (1999).
[3] V. Skumryev, S. Stoyanov, Y. Zhang, G. Hadjipanayis, D. Givord, and J. Nogués, Nature (London) **423**, 850 (2003).
[4] T. W. McDaniel, J. Phys.: Condens. Matter **17**, R315 (2005).
[5] F. Schippan, G. Behme, L. Däweritz, K. H. Ploog, B. Dennis, K.-U. Neumann, and K. R. A. Ziebeck, J. Appl. Phys. **88**, 2766 (2000).
[6] L. Däweritz, L. Wan, B. Jenichen, C. Herrmann, J. Mohanty, A. Trampert, and K. H. Ploog, J. Appl. Phys. **96**, 5056 (2004).
[7] M. Tanaka, J. P. Harbison, M. C. Park, Y. S. Park, T. Shin, and G. M. Rothberg, Appl. Phys. Lett. **65**, 1964 (1994).
[8] C. Kittel, Rev. Mod. Phys. **21**, 541 (1949).
[9] M. Hanson, C. Johansson, B. Nilsson, P. Isberg, and R. Wäppling, J. Appl. Phys. **85**, 2793 (1999).
[10] Y. Takagaki, B. Jenichen, C. Herrmann, E. Wiebicke, L. Däweritz, and K. H. Ploog (unpublished).
[11] D. Schaadt and T. Hesjedal (private communication).
[12] J. B. Goodenough and J. A. Kafalas, Phys. Rev. **157**, 389 (1967).
[13] A. M. Grishin, S. I. Khartsev, and K. V. Rao, Appl. Phys. Lett. **68**, 2008 (1996).

INSTITUTE OF PHYSICS PUBLISHING JOURNAL OF PHYSICS: CONDENSED MATTER

J. Phys.: Condens. Matter **18** (2006) 2641–2653 doi:10.1088/0953-8984/18/9/004

Intrinsic contributions to the planar Hall effect in Fe and Fe_3Si films on GaAs substrates

K-J Friedland, M Bowen, J Herfort, H P Schönherr and K H Ploog

Paul-Drude-Institute for Solid State Electronics, Hausvogteiplatz 5-7, 10117 Berlin, Germany

E-mail: kjf@pdi-berlin.de

Received 18 October 2005
Published 17 February 2006
Online at stacks.iop.org/JPhysCM/18/2641

Abstract

We show that the antisymmetric planar Hall effect in Fe and Fe_3Si layers grown on GaAs(113)A substrates and the symmetric intrinsic planar Hall effect in Fe_3Si on GaAs(001) are closely related to each other. These effects appear in conjunction with additional contributions to the anomalous Hall effect, which reflect the magnetic field-induced crystalline anisotropy upon atomic ordering of the crystal. In the context of recent theoretical studies based on the Berry phase and the spin chirality, we explain the behaviour of the planar Hall effect with a microscopic model that takes into account dynamic non-coplanar spin configurations. We analyse such non-coplanar spin configurations, which are in accordance with the symmetry of the investigated systems, and find a good correspondence with experimental results.

(Some figures in this article are in colour only in the electronic version)

1. Introduction

Magnetotransport phenomena in ferromagnetic layers with in-plane external magnetic fields, including the anisotropic magnetoresistance (AMR) [1] and its twin the planar Hall effect (PHE) [2–4], are widely used to study the magnetization and its reversal as a function of the external magnetic field. In contrast to other methods such as superconducting quantum interference device (SQUID) magnetometry, magnetotransport measurements provide information on the magnetic behaviour of small volumes such as low-dimensional structures and are therefore of importance for spintronics.

The anomalous Hall effect (AHE), with magnetic fields perpendicular to the ferromagnetic layers, probes spin-dependent electron states and scattering by spontaneous magnetization. Presently, the theoretical understanding of the AHE has progressed considerably in the framework of Berry phase effects caused by the electron motion along non-coplanar spin configurations in systems such as manganites [5], spin-frustrated pyrochlore molybdates [6], and (III, Mn)V compounds [7]. A theoretical relation between the AHE and the k-space

Berry phase of occupied Bloch states has also been proposed for conventional ferromagnets such as bcc Fe [8]. In addition, a chirality-driven anomalous Hall effect due to non-trivial spin configurations was already studied for ferromagnets in the weak coupling regime [9], as realized in conventional transition metal ferromagnets. Thus, these new concepts generally relate magnetotransport to spin texture and magnetic ordering. Yet there is only little understanding of such Berry phase and spin chirality effects with respect to the AMR and the PHE.

Conventionally, the PHE in ferromagnetic layers is understood as originating from AMR, i.e., from the difference in resistivities between $\rho_{\parallel}$ and $\rho_{\perp}$ for orientations of the current along and perpendicular to the in-plane magnetization **M**, respectively. This difference gives rise to off-diagonal components in the magnetoresistivity tensor ρ_{xy}, which is conventionally called the planar Hall effect. The AMR-related origin of the PHE contrasts the ordinary and anomalous Hall effects which result from separation of charge by the Lorentz force or spins by the spin–orbit interaction.

Up to second order of magnetization contributions in the magnetoresistivity tensor, ρ_{xx} and ρ_{xy} exhibit the following dependence on the angle between the current and the magnetization θ_{M} upon rotating a single-domain magnetization in the plane of a ferromagnetic and isotropic thin film [10, 11]:

$$\rho_{xx} = \rho_{\perp} + (\rho_{\parallel} - \rho_{\perp}) \cos^2(\theta_{\mathrm{M}}), \tag{1a}$$

$$\rho_{xy} = \rho^{s}_{xy} \cos(\theta_{\mathrm{M}}) \sin(\theta_{\mathrm{M}}). \tag{1b}$$

Both ρ_{xx} and ρ_{xy} are symmetric with respect to the direction of the magnetization. Conventionally, the quantities $\rho_{\parallel} - \rho_{\perp}$ and ρ^{s}_{xy} are ascribed to the AMR and the symmetric PHE, respectively. Recent experiments have revealed additional contributions to the PHE in ferromagnetic systems with reduced symmetry. An additional symmetric contribution to the PHE was observed for stoichiometric Fe_3Si when grown on GaAs(001) substrates [12]. Fe_3Si with the $D0_3$ crystal symmetry can be regarded as a Heusler alloy with non-equivalent Fe sites. For two of the Fe sites, the nearest-neighbour environment is reduced to a tetragonal one. It was then argued [12] that different configurations of coherent spin fluctuations between the Fe sublattices are responsible for the additional PHE. Fe and Fe_3Si layers grown on GaAs(113)A exhibit an antisymmetric contribution to the PHE [13–15] with respect to the direction of the magnetization. This reflects the so-called 'Umkehr' effect [16] when even and odd terms coexist in the off-diagonal components of the magnetoresistivity tensor due to crystal symmetry.

In this paper, we summarize experimental results that indicate that the antisymmetric PHE in Fe and Fe_3Si layers grown on GaAs(113)A and the symmetric PHE in Fe_3Si layers grown on GaAs(001)PHE are closely linked to the AHE. We systematically observe a sign change and large values of the PHE upon lowering the temperature when approaching the atomically well-ordered crystalline structure. As such we designate this PHE as intrinsic (IPHE) to the crystal lattice and its intersublattice interactions. In the context of recent studies of the Berry phase and spin chirality effects, we propose a microscopic model that takes into account dynamic non-coplanar spin configurations and that may explain the behaviour of the IPHE in (113)A oriented films. Our model relies only on symmetry arguments with respect to particular spin states as a result of intersublattice interactions for a given magnetic field-induced anisotropy.

2. Experimental details

Fe and Fe_3Si layers with thicknesses between 9 and 89 nm were grown in an As-free molecular beam epitaxy (MBE) chamber connected to a III–V semiconductor MBE chamber via an

interlock. The growth of the GaAs buffer layers was performed on semi-insulating GaAs(001) and GaAs(113)A substrates at properly optimized conditions before transferring the samples through ultrahigh vacuum ($<1 \times 10^{-10}$ Torr) for subsequent Fe and Fe_3Si growth. The growth temperature was 50 and 0 °C for Fe films on GaAs(001) and GaAs(113)A, respectively, and 250 °C for Fe_3Si. More details about the growth as well as the structural and morphological properties of the films can be found in [17, 18] for Fe and [19, 20] for Fe_3Si.

Magnetotransport measurements were carried out at stabilized temperatures. A programmable stepper motor was used to rotate the sample relative to the magnetic field direction. In most cases, we used Hall bar structures prepared by standard lithography techniques. The structures were carefully aligned to create a current flow along the $[33\bar{2}]$ and $[\bar{1}10]$ directions for films on GaAs(113)A substrates and along the $[\bar{1}10]$ and [110] directions for films on GaAs(001) substrates. These directions are all in-plane hard axes of magnetization, as a dominant fourfold magnetic anisotropy is observed in all investigated samples [19–21]. Ohmic contacts were obtained by bonding Au wires directly onto the Hall bar terminals, which results in sufficiently low contact resistances. In some cases, we used rectangular samples with an approximate size of 3×4 mm^2, for which we carefully aligned the terminals to achieve uniform current and equal potential lines at zero magnetic field. Nevertheless, because of the small transverse (planar Hall) resistivity ρ_{xy} compared to the longitudinal resistivity ρ_{xx}, a crossover from ρ_{xx} to ρ_{xy} may occur due to non-perfect alignment of the Hall terminals as the field strength H or the angle θ_H between the current and the external magnetic field is changed. We therefore corrected ρ_{xy} to $\rho_{xy}^{\mathrm{corr}}(H, \theta_H) = \rho_{xy}(H, \theta_H) - t\rho_{xx}(H, \theta_H)$, while keeping the weight t fixed for all measurements of a particular contact configuration at a fixed temperature. Here t is of the order $1\text{–}10 \times 10^{-5}$. No significant differences in the magnetoresistivities as a function of the magnetic field strength were found for lithographically processed Hall bar structures and rectangular samples. To measure the transverse magnetoresistance, we chose a contact configuration that results in a negative Hall voltage for an n-type semiconductor sample in the conventional Hall geometry. We define the corresponding magnetic field direction as being positive.

3. Results and discussion

3.1. Intrinsic PHE in Fe and Fe_3Si grown on GaAs(113)A and GaAs(001) substrates

An unusual Hall effect was observed in Fe and $Fe_{3+x}Si_{1-x}$ layers grown on GaAs(113)A substrates. This is a saturated antisymmetric planar Hall effect (SAPHE), $\rho_{xy}^{\mathrm{SAPHE}}$, which reflects a transverse electric field, when the magnetic field is aligned along the $[33\bar{2}]$ direction [13–15], and which can be regarded as manifestation of the 'Umkehr effect' [16] due to the crystal symmetry. The SAPHE exists even for a current that is aligned along the same $[33\bar{2}]$ direction, i.e., even when the current and magnetic field are parallel. In the following we briefly summarize the previous major experimental results on which the unified model relies. We present in figure 1(a) the magnetic field dependences of ρ_{xy} at $T = 300$ K for a 10 nm thick Fe film grown on a GaAs(113)A substrate. For magnetic fields above $H_{\mathrm{sat}} \approx 0.2$ kOe, ρ_{xy} becomes completely saturated. Upon sweeping the magnetic field to the opposite direction, ρ_{xy} changes sign, which is never observed for Fe and Fe_3Si layers grown on GaAs(001) [14, 15].

To prove the real antisymmetry of the transverse magnetoresistivity with respect to Onsager's relation $\rho_{xy}(\boldsymbol{\alpha}) = \rho_{yx}(-\boldsymbol{\alpha})$, where the vector $\boldsymbol{\alpha}$ represents the direction of the magnetization, we measured ρ_{xy} and ρ_{yx} by interchanging the current and voltage terminals and examined the symmetric $(\rho_{xy} + \rho_{yx})/2$ and antisymmetric $(\rho_{xy} - \rho_{yx})/2$ contributions to the planar Hall effect (see figures 1(a) and (b)). This analysis reveals the antisymmetry, which

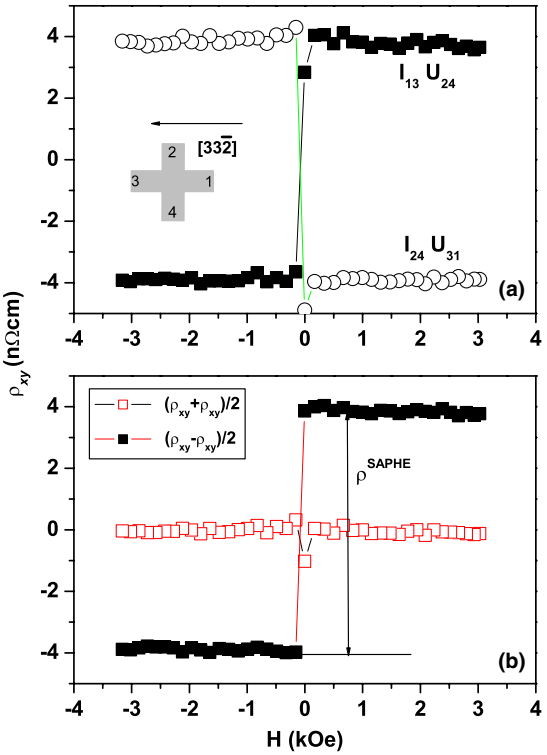

Figure 1. (a) Planar Hall effect response at $T = 300$ K of a 10 nm thick Fe film grown on GaAs(113)A for a magnetic field applied along [33$\bar{2}$]. The inset depicts the sample and contact geometry. (b) The separation of the symmetric and antisymmetric contributions to the PHE data of panel (a).

is defined as $\rho_{xy}^{\mathrm{SAPHE}} = \rho_{xy}^{a}(H > +H_{\mathrm{sat}}) - \rho_{xy}^{a}(H < -H_{\mathrm{sat}})$. No $\rho_{xy}^{\mathrm{SAPHE}}$ was observed for magnetic fields along the [$\bar{1}$10] direction. A similar $\rho_{xy}^{\mathrm{SAPHE}}$ was found in $Fe_{3+x}Si_{1-x}$ layers grown on GaAs(113) substrates [13]. It is important to note that the observed $\rho_{xy}^{\mathrm{SAPHE}}$ does not arise from an AHE component due to a slight but unavoidable out-of-plane sample misalignment, since such a contribution from the AHE would appear as a slope in the high-field region. Furthermore, the antisymmetry of $\rho_{xy}^{\mathrm{SAPHE}}$ is clearly in contrast to other phenomena such as the 'giant planar Hall effect' in (Ga, Mn)As [3], for which an apparent antisymmetry arises from carrier scattering at domain walls and which can in fact be attributed to a symmetric PHE.

In the case of thin films grown epitaxially on GaAs(113)A substrates, rotating the magnetic field in the film plane leads to a rotation of the magnetization in the low-symmetry (113) plane of the crystal lattice. As a consequence, we no longer observe a four-fold symmetry in ρ_{xy}, as evidenced in figure 2 by the dependence of ρ_{xy} on θ_{M} for a $Fe_{3+x}Si_{1-x}$ layer near the Fe_3Si stoichiometric composition with $x = 0.07$ at (a) $T = 300$ K and (b) $T = 77$ K. Here θ_{M} is the angle between the direction of magnetization and the current direction along the [33$\bar{2}$] axis.

We calculate θ_{M} from the ρ_{xx} data using (1*a*) as described in [14]. This symmetry reduction in the transport related magnetocrystalline anisotropy is not supported by SQUID magnetization measurements, which are in accordance with a four-fold magnetocrystalline anisotropy [20]. Recently, we have shown how $\rho_{xy}^{\mathrm{SAPHE}}$ is phenomenologically related to a third-order contribution of the magnetoresistivity tensor. For the classical crystal class $m3m$, to

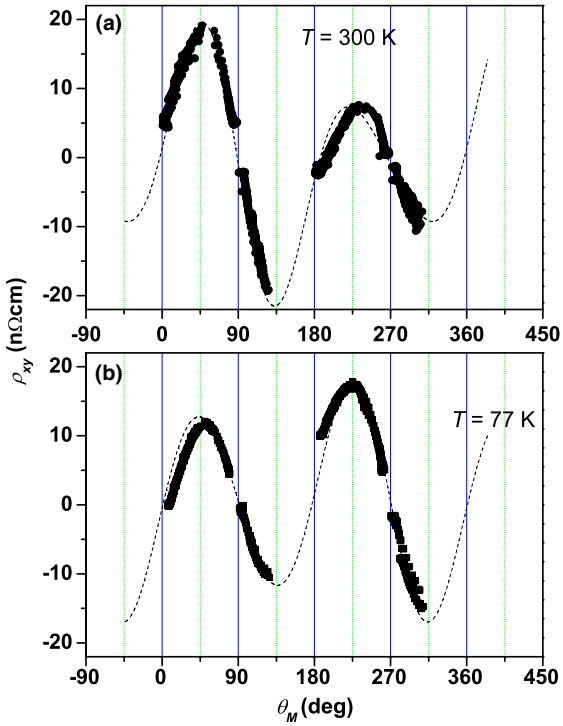

Figure 2. Planar Hall effect response of a 40 nm thick $Fe_{3+x}Si_{1-x}$ ($x = 0.07$) film grown on GaAs(113)A with a current along $[33\bar{2}]$ as a function of the angle θ_M between magnetization and current at saturated magnetic field and at (a) $T = 300$ K, (b) $T = 77$ K. The dotted lines are fits to (2) with $\rho_{xy}^{s(113)} = 40$ nΩ cm, $\rho_{xy}^{\mathrm{SAPHE}} = 3.6$ nΩ cm at $T = 300$ K and $\rho_{xy}^{s(113)} = 36$ nΩ cm, $\rho_{xy}^{\mathrm{SAPHE}} = -1.2$ nΩ cm at $T = 77$ K.

which both Fe_3Si ($Fm3m$) and Fe ($Im3m$) belong, one can find for $\rho_{xy}^{(113)}$, which corresponds to a current applied along $[33\bar{2}]$ and a voltage measured along $[\bar{1}10]$, an expression valid up to the third order of magnetization [15]:

$$\rho_{xy}^{(113)} = \rho_{xy}^{s(113)} \sin(\theta_M)\cos(\theta_M) + \rho_{xy}^{a(113)}[(33/5)\cos(\theta_M) - (84/15)\cos^3(\theta_M)]. \quad (2)$$

In addition to the conventional symmetric second-order contribution $\rho_{xy}^{s(113)} \sin(\theta_M)\cos(\theta_M)$, $\rho_{xy}^{(113)}$ exhibits an additional antisymmetric term of third order with an amplitude of $\rho_{xy}^{a(113)}$. This term can directly be related to $\rho_{xy}^{\mathrm{SAPHE}}$. This result is qualitatively different from the PHE observed for GaAs(001) substrates which, given the symmetry conditions of this phenomenological approach, can only contain even-order terms. (2) is in line with the experimental observation on (113)A-oriented films of an additional contribution to the planar Hall effect (second term in (2)) that changes sign upon reversing the direction of the magnetic field. This antisymmetric term is also called the second-order Hall effect.

It is an interesting novel result of the present sample that $\rho_{xy}^{\mathrm{SAPHE}}$ changes sign with decreasing temperature from $T = 300$ K down to $T = 77$ K, which manifests itself in figures 2(a) and (b) as an interchange of the maximum values at $\theta_M = 45°$ and 225°, respectively. However, the AMR signal ($\rho_\perp - \rho_\parallel$) does not change its sign. In addition, we do not observe a sign change of $\rho_{xy}^{\mathrm{SAPHE}}$ with temperature for $Fe_{3+x}Si_{1-x}$ films away from the Fe_3Si stoichiometric composition with $|x| > 0.1$. The sign of $\rho_{xy}^{\mathrm{SAPHE}}$ is negative for layers

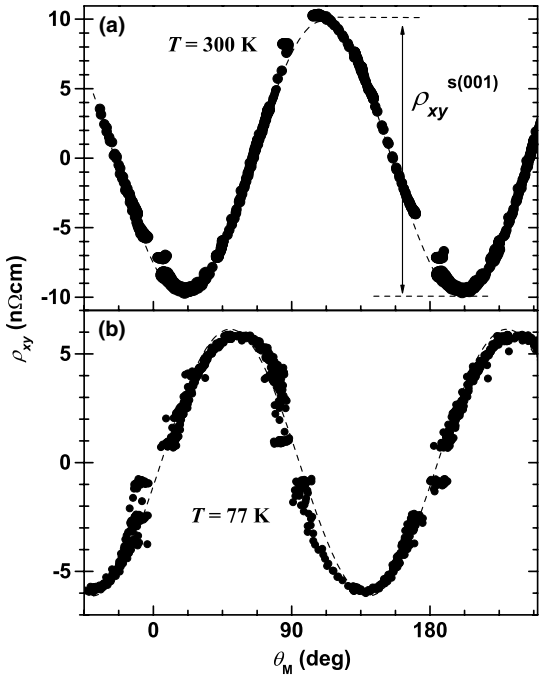

Figure 3. Planar Hall effect response of a 40 nm thick $Fe_{3+x}Si_{1-x}$ ($x = 0.01$) film grown on GaAs(001) with a current along [$\bar{1}$10] as a function of the angle θ_M between magnetization and current at saturated magnetic field and at (a) $T = 300$ K, (b) $T = 77$ K. The dotted lines are fits to (1*b*) with $\rho_{xy}^{s(001)} = 19$ nΩ cm, at $T = 300$ K and $\rho_{xy}^{s(001)} = -12$ nΩ cm at $T = 77$ K.

near the Fe_3Si stoichiometric composition at low temperatures and of the same sign as the one for Fe layers on GaAs(113)A substrates, even though the sign of $\rho_\perp - \rho_\parallel$ is opposite in Fe and $Fe_{3+x}Si_{1-x}$ layers.

$Fe_{3+x}Si_{1-x}$ layers grown on GaAs(001) show a symmetric PHE with an amplitude $\rho_{xy}^{s(001)}$ according to (1*b*). Compared to $\rho_{xy}^{\mathrm{SAPHE}}$, $\rho_{xy}^{s(001)}$ also changes sign upon lowering the temperature from $T = 300$ to 77 K in nearly stoichiometric Fe_3Si grown on GaAs(001) [12]. Figures 3(a) and (b) present the dependences of ρ_{xy} on θ_M at (a) $T = 300$ K and (b) at $T = 77$ K for a (001)-oriented sample with $x = +0.01$ with a current along [110].

We interpret the sign change as resulting from an additional symmetric IPHE contribution $\rho_{xy}^{\mathrm{symmIPHE}}$ of opposite sign that is present in addition to the conventional AMR term $\rho_{xy}^{\mathrm{AMR}} = \rho_\parallel - \rho_\perp$ [12].

$\rho_{xy}^{\mathrm{symmIPHE}}$ is negative and in fact represents the anisotropic contribution to the PHE due to crystalline symmetry. With decreasing temperature, $|\rho_{xy}^{\mathrm{symmIPHE}}|$ increases and eventually compensates ρ_{xy}^{AMR} at T_{ord}. We note that T_{ord} reaches the maximum value of $T_{\mathrm{ord}}^{\mathrm{max}} \approx 251$ K for a nearly stoichiometric sample ($x = +0.01$). In contrast to this behaviour, non-stoichiometric $Fe_{3+x}Si_{1-x}$ layers with $|x| > 0.1$ show no sign change in the PHE down to $T = 4.2$ K.

3.2. Composition and temperature dependence of the symmetric and antisymmetric PHE in Fe_3Si

We have previously shown that a significant degree of atomic ordering of the $Fe_{3+x}Si_{1-x}$ crystals occurs around $|x| < 0.1$ [12, 22, 23]. In this case, the sheet resistivity ρ_{xx} exhibits

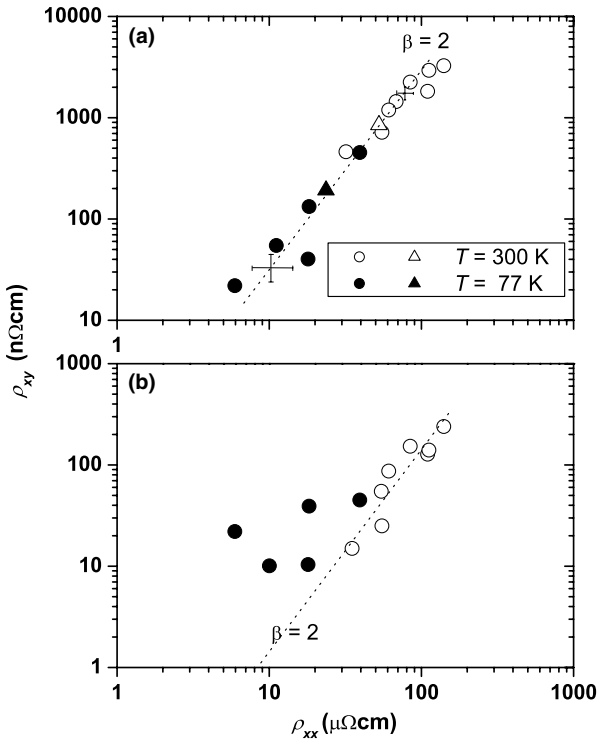

Figure 4. (a) Anomalous Hall effect and (b) planar Hall effect in $Fe_{3+x}Si_{1-x}$ films as a function of the resistivity. The dotted lines represent the power law $\rho_{xy} \propto \rho_{xx}^{\beta}$ with $\beta = 2$, $T = 300$ K. A common legend describes both panels: circles and triangles for (001) and (113)A substrates, respectively.

a deep minimum around $x = 0$, while the conductivity ratio $\rho^{300\ \mathrm{K}}/\rho^{77\ \mathrm{K}}$ for resistivities ρ_{xx} at $T = 300$ and 77 K increases to a value of five, indicating the suppression of alloy scattering and the dominance of phonon scattering at high temperatures at nearly stoichiometric composition.

At the same time, ordered Fe_3Si layers grown on GaAs(001) and GaAs(113)A substrates respectively give rise at low temperature to additional, negative contributions $\rho_{xy}^{\mathrm{symmIPHE}}$ and $\rho_{xy}^{\mathrm{SAPHE}}$ to the planar Hall effect (PHE), which we therefore ascribe as intrinsic to a more ordered Fe_3Si Heusler alloy lattice. To find the relationship of different contributions in the PHE, we examine the composition and temperature dependences of $\rho_{xy}^{\mathrm{SAPHE}}$ and $\rho_{xy}^{s(001)}$ as compared to the anomalous Hall effect ρ_{xy}^{AHE} measured in the conventional Hall geometry with the magnetic field perpendicular to the film plane.

Figure 4(a) shows the anomalous Hall effect in ρ_{xy}^{AHE} for $Fe_{3+x}Si_{1-x}$/GaAs(001) layers as a function of sheet resistivity ρ_{xx}. Changes to ρ_{xx} encompass varying the measurement temperature either to $T = 77$ or 300 K, film thickness between 9 and 87 nm, as well as composition x. We find a general scaling dependence $\rho_{xy}^{\mathrm{AHE}} \propto \rho_{xx}^{\beta}$ with $\beta \cong 2$, similar to the one found for Fe layers grown on GaAs [13]. This scaling spans over ordered and disordered samples for both high and low temperatures, indicating that the physical origin of ρ_{xy}^{AHE} does not depend on whether the scattering is related to phonons or impurities. A scaling with $\beta = 2$ is ascribed to an extrinsic side-jump scattering [24] or to intrinsic scattering processes [25]. As shown in figure 4(b), the same scaling behaviour with $\beta \cong 2$ is also found for the symmetric planar Hall effect $\rho_{xy}^{s(001)} \propto \rho_{xx}^{\beta}$ in disordered $Fe_{3+x}Si_{1-x}$ samples with $x > 0.1$ or in ordered

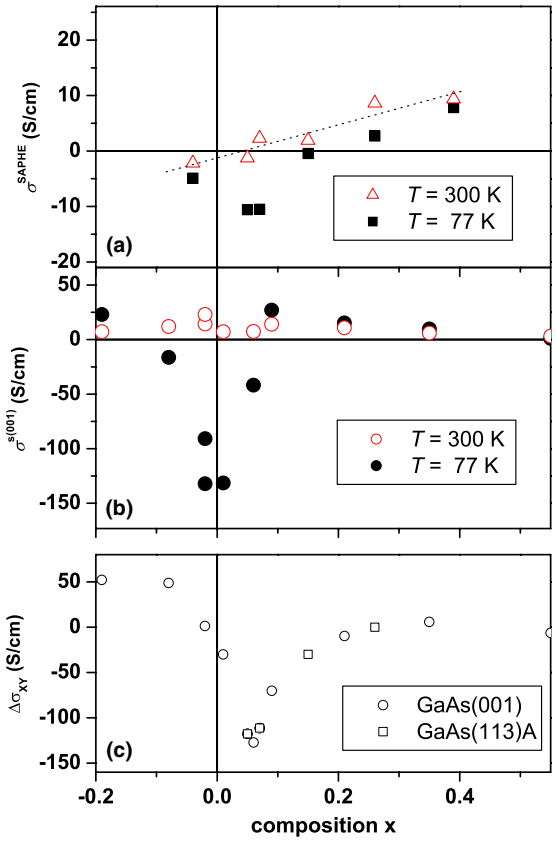

Figure 5. The saturated antisymmetric PHE, (b) the symmetric planar Hall effect and (c) the anomalous Hall effect in $Fe_{3+x}Si_{1-x}$ films as a function of composition x for $T = 300$ and $T = 77$ K.

samples at high temperatures. In contrast, $\rho_{xy}^{s(001)}$ in well-ordered samples at low temperatures is significantly larger than one would expect from the extrapolated scaling dependence $\rho_{xy}^{s(001)} \propto \rho_{xx}^2$ (i.e., for low ρ_{xx}). This reflects the additional contribution $\rho_{xy}^{\text{symmIPHE}}$ in this case and indicates a different physical origin of $\rho_{xy}^{\text{symmIPHE}}$ as compared to the conventional symmetric planar Hall effect in disordered samples or at high temperatures. Unfortunately, a similar analysis is not possible for the present set of $Fe_{3+x}Si_{1-x}$/GaAs (113)A samples due to a much too narrow range of resistivities. Therefore, we calculate the corresponding Hall conductivities $\sigma^{s(001)}$, σ^{SAPHE} and σ^{AHE} according to $\sigma = \rho_{xy}/\rho_{xx}^2$ in order to demonstrate the relationship between these quantities around $x = 0$.

We present in figures 5(a) and (b) the compositional dependences of the SAPHE and the symmetrical PHE at $T = 300$ and 77 K. At high temperatures, σ^{SAPHE} and $\sigma^{s(001)}$ vary slowly with x, which one could expect from the $\rho_{xy}^{s(001)} \propto \rho_{xx}^2$ scaling [see figure 4(b)]. However, at low temperatures, σ^{SAPHE} and $\sigma^{s(001)}$ change rapidly with a minimum around $x = 0$. In addition, figure 5(c) shows the compositional dependence of the AHE conductivity difference $\Delta\sigma^{\text{AHE}} = \sigma_{\text{min}}^{\text{AHE}} - \sigma^{\text{AHE}}(300\text{ K})$ between the value found at $T = 300$ K and the minimum value $\sigma_{\text{min}}^{\text{AHE}}$ (for most of the samples σ^{AHE} decreases by lowering the temperature to a minimum value around $T = 100$ K (not shown here); the temperature dependence of σ^{AHE} will be discussed elsewhere). We thus observe a minimum near $x = 0$. From the phenomenological

point of view, the negative contributions in σ^{SAPHE} and $\sigma^{s(001)}$ are higher-order contributions in the magnetoresistivity tensor in the presence of the magnetic field and due to crystalline anisotropy with ordering of the crystal that are third-order contributions for $Fe_{3+x}Si_{1-x}$/GaAs (113)A (see (2)) and fourth-order contributions for $Fe_{3+x}Si_{1-x}$/GaAs (001). For the case of $Fe_{3+x}Si_{1-x}$/GaAs (113)A, it was shown that these higher-order contributions also appear in the AHE [15] and may result in a negative $\Delta\sigma^{\mathrm{AHE}}$ around $x = 0$.

4. Discussion of the PHE for nearly stoichiometric Fe_3Si

Note that in nearly stoichiometric Fe_3Si the absolute values of σ^{SAPHE}, $\sigma^{s(001)}$ and $\Delta\sigma^{\mathrm{AHE}}$ are large and reach more than 100 S m^{-1}. Recently, large anomalous Hall conductivities were attributed to Berry phase effects. It was shown by experimental and theoretical studies that a finite AHE may exist in systems with more than two non-coplanar spin sublattices [26, 27]. An anomalous Hall effect contribution that is related to the k-space Berry phase of occupied Bloch states was even predicted for ferromagnetic bcc Fe [8]. According to this explanation, the AHE arises due to the conduction of carriers from a very narrow portion of the Fermi surface that is split by the spin–orbit interaction. The near degeneracy of spin-up and spin-down states at such points in the band structure may thus give rise to a non-trivial spin topology throughout the ferromagnet's lattice. The anomalous Hall conductivity will then be proportional to this Berry phase and results in large anomalous Hall conductivities, as observed in the AHE and the IPHE in Fe and Fe_3Si layers.

Fe and Fe_3Si are systems with a clear band magnetism [28]; therefore, static non-coplanar spin configurations like the ones in frustrated spin systems do not exist. Nevertheless, non-coplanar spin configurations may arise statically around defects or dynamically due to spin fluctuations, spin waves, and magnons [29]. As a result, carriers are moving in a magnetic field that varies in space and time due to the background of fluctuating local moments. As a result, a Berry phase arises that contributes to the conductivity. Due to the high symmetry of Fe_3Si, multiply degenerate contributions to the AHE or PHE from the ensemble of possible spin configurations will cancel out, while the Berry phase remains intact. Extended theoretical calculations of the band structure are needed in order to find out which parts in k-space of Fe_3Si may result in an intrinsic AHE and therefore also in the IPHE.

The strong temperature dependence of the IPHE, and the good agreement between T_{ord} and the exchange energy $J_{\mathrm{ex}}[(\mathrm{B} \leftrightarrow (\mathrm{A}, \mathrm{C})] = 145$ K between the Fe_3Si B and (A, C) sublattices calculated by Stearns [28] from Mössbauer spectroscopy on a Fe_3Si powder, led us to propose a microscopic description for the appearance of $\rho_{xy}^{\mathrm{symmIPHE}}$ [12]. This model considers spin interactions between the non-equivalent sublattices in the Fe_3Si Heusler alloy. Coherent spin fluctuations between sublattices resulting from such interactions were argued to give rise to the formation of non-coplanar spin configurations.

Tatara *et al* [9] studied theoretically the relationship between the anomalous Hall effect and non-trivial spin configurations in ferromagnets in the weak coupling regime, which is the case for all transition metal ferromagnets including Fe and Fe_3Si. The interaction of the carrier spins with the slowly varying background of localized spins S_X leads to an anomalous Hall conductivity

$$\sigma_{xy}^{(3)} = (4\pi)^2 \sigma_0 J^3 \nu^2 \tau \chi_0, \tag{3}$$

where $\chi_0 = \frac{1}{6N} \sum_{\boldsymbol{X}_i} S_{\boldsymbol{X}_1} \cdot (S_{\boldsymbol{X}_2} \times S_{\boldsymbol{X}_3})[f(\boldsymbol{X}_1, \boldsymbol{X}_2, \boldsymbol{X}_3)]$ is the uniform (or net) chirality, σ_0 is the Drude conductivity, J the exchange coupling coefficient, τ the scattering time and ν is the density of states. $f(\boldsymbol{X}_1, \boldsymbol{X}_2, \boldsymbol{X}_3)$ is a numerical factor that depends on the spatial position of the different spins. This Hall contribution is of second order and encompasses also a third-order

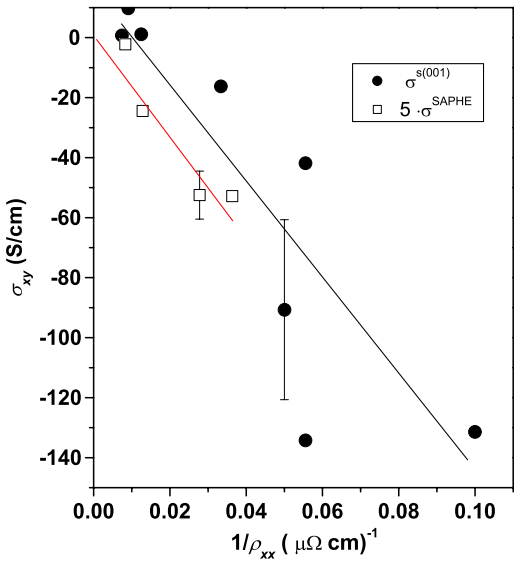

Figure 6. Dependence of the conductivities $\sigma^{s(001)}$ and σ^{SAPHE} on the inverse film resistivity $1/\rho_{xx}$ for different composition at $T = 77$ K for $Fe_{3+x}Si_{1-x}$ on GaAs(001) and GaAs(113)A substrates. The error bars correspond to statistical variation in the $\rho_{xy}^{s(001)} \propto \rho_{xx}^2$ law in figure 4(a).

term with respect to the exchange interaction. It is dominant in the clean, well-ordered regime and at low temperatures, as it is the case here near the Fe_3Si stoichiometric composition.

We have already shown [15], that at least the ρ^{SAPHE} for the (331)A case is a second-order Hall effect

$$\rho^{\mathrm{SAPHE}} = \rho_{xy}^{a(113)} = 9(a_{32221} + a_{31121} - 2a_{33321})/(22\sqrt{2}), \tag{4}$$

which phenomenologically is described by the third-order components a_{32221}, a_{31121} and a_{33321} in the magnetoresistivity tensor, expanded in ascending powers of magnetization. For the crystal class $m3m$, to which both Fe_3Si ($Fm3m$) and Fe ($Im3m$) belong, $a_{32221}+a_{31121}-2a_{33321}$ simplifies to $2(a_{12223}-a_{11123})$ [30]. In fact the quantities a_{ijklm} are the i, j, k partial derivatives with respect to the magnetization directions of the l, m components of the magnetoresistivity tensor, and reflect the longitudinal and transverse resistivities by a simultaneous change of three magnetization components along the i, j, k directions. In addition, (4) shows that the magnetization components of all directions contribute to ρ^{SAPHE}. For our microscopic model we reverse this conclusion by stressing that any non-coplanar spin or moment configuration with a non-zero chirality will contribute to higher-order contributions in the magnetoresistivity tensor. In Fe_3Si, for example, a_{ijklm} would describe a coherent three-spin interaction between three non-equivalent Fe sites. However, the possible mechanisms to achieve a finite net chirality are still the subject of debate [31]. As discussed by Tatara [9], in regular lattices with simple nearest-neighbour exchange interactions, chiralities on adjacent plaquettes tend to cancel out each other due to symmetry.

The chirality-driven anomalous Hall conductivity described by (3) is proportional to the scattering time τ, which implies a different mechanism for this AHE as compared to the resistivity $\rho_{xy}^{\mathrm{AHE}} \propto \rho_{xx}^2$ for the disordered case [see figure 4(a)]. The behaviour of σ^{SAPHE} and $\sigma^{s(001)}$ for $Fe_{3+x}Si_{1-x}$ around $x = 0$ and at low temperatures suggests that the IPHE can be described by an equation similar to (3) as the resistivity decreases significantly for atomically ordered samples. To demonstrate this hypothesis, we plot in the figure 6 σ^{SAPHE} and $\sigma^{s(001)}$

as a function of the inverse resistivity. This shows that the absolute value of both conductivities increases with τ, although with a large scatter in the values, which should be expected, given that these data are extracted from samples with different composition.

Finally, in the context of (3), we use the spin chirality of on-site spins given the Fe_3Si crystal symmetry to demonstrate qualitatively the sign change of the SAPHE with atomic ordering of the lattice. The unit cell of Fe_3Si consists of four sublattices. The D sublattice consists of Si sites, while the other three labelled A, B, and C contain the magnetically non-equivalent Fe sites. The Fe on the A, C sublattices with only four nearest-neighbour Fe sites carry a magnetic moment of 1.06 μ_B, while the Fe in the B sublattice with eight nearest-neighbour Fe sites carries a moment of 2.23 μ_B.

We consider particular triads of spins $\mathbf{S}_A$, $\mathbf{S}_B$ and $\mathbf{S}_C$ on the A, B, C sites of the lattice with a dominant component along the macroscopic magnetization direction $\mathbf{m}$. Within the unit cell, an on-site spin $\mathbf{S}$ may deviate from $\mathbf{m}$, whereby the deviation $\boldsymbol{\Delta}\mathbf{S}$ orients along preferential directions due to an inner cell anisotropy of the spin density distribution (SDD). The SDD of Fe_3Si has been inferred by Moss and Brown from neutron diffraction experiments [32]. The SDD for all Fe sites is extended along the $\langle 100\rangle$ directions, which define the easy axes of magnetization. In addition, the SDD around the Fe (A, C) sites exhibits lobes that point towards the Si D sites along the $\langle 111\rangle$ directions. We will use these directions in order to define preferential orientations of spin fluctuations $\boldsymbol{\Delta}\mathbf{S}_A$ and $\boldsymbol{\Delta}\mathbf{S}_C$ on the Fe_3Si A and C sublattices in the ordered case. We will contrast this to the disordered case, which encompasses both structural and thermal disorder. Structurally, the substitution of Si on Fe sites leads to a chemical environment around A and C sites with a greater chemical symmetry than the tetragonal one in the ordered case. Thermally, the disruption of intersublattice exchange interactions also increases the symmetry of fluctuations on such sites. Thus, both forms of disorder lead to additional configurations of spin fluctuations. Regarding the B sublattice sites, the surrounding SDD is nearly isotropic, so that we assume that the spin fluctuation $\boldsymbol{\Delta}\mathbf{S}_B$ can rotate freely in accordance with the constriction that the magnetization $\mathbf{M} = 2\mathbf{S}_B + \mathbf{S}_A + \mathbf{S}_C$ oriented along $\mathbf{m}$.

We now show that the spin chirality $\chi = \mathbf{S}_B \cdot (\mathbf{S}_C \times \mathbf{S}_A)$ that determines the intrinsic magnetotransport may become non-zero for certain directions of the magnetization $\mathbf{M}$ and may become positive or negative in both the ordered and the disordered cases for a given $\mathbf{M}$. It is straightforward to show that $\chi = \mathbf{M} \cdot (\boldsymbol{\Delta}\mathbf{S}_C \times \boldsymbol{\Delta}\mathbf{S}_A)$ so that we may consider the influence of spin chirality directly on spin fluctuation triads (SFTs). As an example, we present in figure 7(a) the sketch in the disordered case of an SFT $\boldsymbol{\Delta}\mathbf{S}_A$, $\boldsymbol{\Delta}\mathbf{S}_B$, and $\boldsymbol{\Delta}\mathbf{S}_C$ for (113)A-oriented Fe_3Si that is used to compose a magnetization $\mathbf{M}$ along $[33\bar{2}]$. $\boldsymbol{\Delta}\mathbf{S}_A$ and $\boldsymbol{\Delta}\mathbf{S}_C$ are oriented along $[1\bar{1}1]$ and $[\bar{1}11]$, respectively. Such an SFT yields a positive spin chirality. Upon reversing the direction of $\mathbf{M}$, this SFT may transform such that $\boldsymbol{\Delta}\mathbf{S}_A$ is along $[\bar{1}1\bar{1}]$ and $\boldsymbol{\Delta}\mathbf{S}_C$ is along $[1\bar{1}\bar{1}]$, leading to a sign change in χ. We emphasize that, for this configuration, the spin fluctuation $\boldsymbol{\Delta}\mathbf{S}_A$ points towards a nearest-neighbour D site, while $\boldsymbol{\Delta}\mathbf{S}_C$ points towards a nearest-neighbour Fe site, i.e., describing the disordered case. As an example in the ordered case, figure 7(b) shows the sketch of an SFT for $\mathbf{M}$ along $[33\bar{2}]$ with $\boldsymbol{\Delta}\mathbf{S}_A$ along $[1\bar{1}1]$ and $\boldsymbol{\Delta}\mathbf{S}_C$ along $[1\bar{1}\bar{1}]$ that leads to $\chi < 0$, i.e., opposite to the one of the SFT in figure 7(a). This implies that the sign change in χ upon ordering could reflect the switching in one of the A or C on-site fluctuations from a B to a D site. Thus, this sketch can describe the SAPHE in (113)A-oriented well-ordered Fe_3Si when intersublattice interactions control the orientations of spin fluctuations. In the case of the Fe lattice, no such temperature-induced sign change of χ can occur for a possible spin chirality-driven SAPHE in agreement with the constant sign of ρ^{SAPHE} at low and high temperatures.

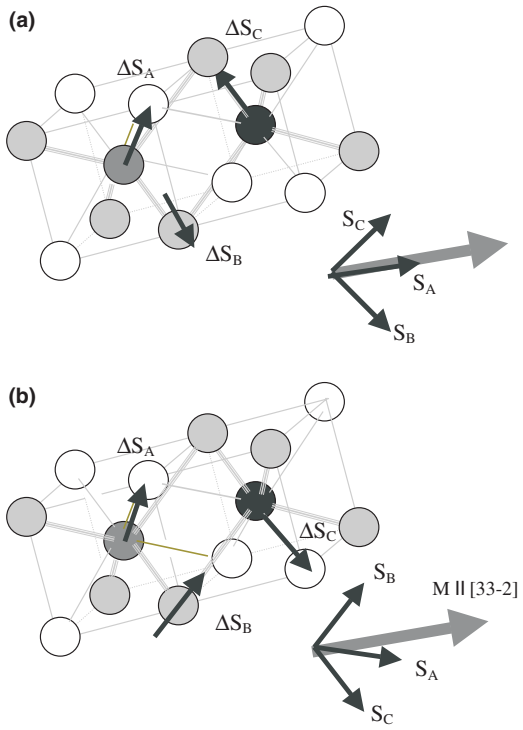

Figure 7. A spin fluctuation triad in (113)A-oriented Fe_3Si with (a) $\mathbf{\Delta S}_A$ along $[1\bar{1}1]$ and $\mathbf{\Delta S}_C$ along $[\bar{1}11]$ describing the atomically disordered lattice and (b) $\Delta\mathbf{S}_A$ along $[1\bar{1}1]$ and $\mathbf{\Delta S}_C$ along $[1\bar{1}\bar{1}]$ describing the atomically ordered lattice. In both panels, the spin $\mathbf{S}_B$ can orient freely to form a triad corresponding to a magnetization along $[33\bar{2}]$.

5. Conclusion

The intrinsic planar Hall effect in ferromagnetic Fe and Fe_3Si layers grown on GaAs(001) and GaAs(113)A substrates appears in conjunction with additional contributions to the anomalous Hall effect (AHE) and reflects the magnetic field-induced crystalline anisotropy upon atomic ordering of the crystal. We have shown that the IPHE follows a different scaling behaviour as compared to the disordered case. We describe this difference using a microscopic model that takes into account collective spin fluctuations and the non-trivial spin topology of the Fe_3Si lattice given the symmetry of the investigated systems, and we find a good correlation between the results of the model and the experiment.

Acknowledgments

We thank A Riedel for technical assistance and H Kostial, P K Muduli, P Kleinert, Y Takagaki and G Tatara for stimulating discussions.

References

[1] McGuire T R and Potter R I 1975 *IEEE Trans. Magn.* **11** 1018
[2] Mitze C, Osthöver C, Voges F, Hasenkox U, Waser R and Arons R R 1999 *Solid State Commun.* **109** 189

[3] Tang H X, Kawakami R K, Awschalom D D and Roukes M L 2003 *Phys. Rev. Lett.* **90** 107201
[4] Friedland K-J, Kästner M and Däweritz L 2003 *J. Supercond.* **16** 261
[5] Lyanda-Geller Y, Chun S H, Salamon M B, Goldbart P M, Han P D, Tomioka Y, Asamitsu A and Tokura Y 2001 *Phys. Rev.* B **63** 184426
[6] Taguchi Y, Oohara Y, Yoshizawa H, Nagaosa N and Tokura Y 2001 *Science* **291** 2573
[7] Jungwirth T, Qian N and MacDonald A H 2002 *Phys. Rev. Lett.* **88** 207208
[8] Yao Y, Kleinmann L, MacDonald A H, Sinova J, Jungwirth T, Wang D-S, Wang E and Niu Q 2004 *Phys. Rev. Lett.* **92** 037204
[9] Tatara G and Kawamura H 2002 *J. Phys. Soc. Japan* **71** 2613
[10] Campbell I A and Fert A 1982 *Ferromagnetic Materials* vol 3, ed E P Wohlfarth (Amsterdam: North-Holland) p 797
[11] Chen T T and Marsocci V A 1972 *Physica* **59** 498
Chen T T and Marsocci V A 1972 *Solid State Commun.* **10** 783
[12] Bowen M, Friedland K-J, Herfort J, Schönherr H-P and Ploog K H 2005 *Phys. Rev.* B **71** 172401
[13] Friedland K-J, Nötzel R, Schönherr H-P, Riedel A, Kostial H and Ploog K H 2001 *Physica* E **10** 442
[14] Friedland K-J, Muduli P K, Herfort J, Schönherr H-P and Ploog K H 2005 *J. Supercond.* **18** (Published online: 12 July)
[15] Muduli P K, Friedland K-J, Herfort J, Schönherr H-P and Ploog K H 2005 *Phys. Rev.* B **72** 104430
[16] Akgöz Y C and Saunders G A J 1975 *Phys. C: Solid State Phys.* **8** 1387
[17] Schönherr H-P, Nötzel R, Ma W and Ploog K H 2001 *J. Appl. Phys.* **89** 169
[18] Herfort J, Braun W, Trampert A, Schönherr H-P and Ploog K H 2004 *Appl. Surf. Sci.* **237** 181
[19] Herfort J, Schönherr H-P and Ploog K H 2003 *Appl. Phys. Lett.* **83** 3912
[20] Muduli P K, Herfort J, Schönherr H-P and Ploog K H 2005 *J. Cryst. Growth* **285** 514
[21] Muduli P K, Herfort J, Schönherr H-P and Ploog K H 2005 *J. Appl. Phys.* **97** 123904
[22] Herfort J, Schönherr H-P, Friedland K-J and Ploog K H 2004 *J. Vac. Sci. Technol.* B **22** 2073
[23] Jenichen B, Kaganer V M, Herfort J, Satapathy D K, Schönherr H-P, Braun W and Ploog K H 2005 *Phys. Rev.* B **72** 075329
[24] Berger L 1970 *Phys. Rev.* B **2** 4559
[25] Karplus R and Luttinger J 1954 *Phys. Rev.* **95** 1154
[26] Shindou R and Nagaosa N 2001 *Phys. Rev. Lett.* **87** 116801
[27] Fang Z, Nagaosa N, Takahashi K S, Asamitsu A, Mathieu R, Ogasawara T, Yamada H, Kawasaki M, Tokura Y and Terakura K 2003 *Science* **302** 92
[28] Stearns M B 1968 *Phys. Rev.* **168** 588
[29] Szymański M, Jankowski M, Dobrzyński L, Wiśniewski A and Bednarski S 1991 *J. Phys.: Condens. Matter* **3** 4005
[30] Birss R R 1964 *Symmetry and Magnetism* (Amsterdam: North-Holland) chapter 5, section 4
[31] Ye J, Kim Y B, Millis A J, Shraiman B I, Majumdar P and Tesanovic Z 1999 *Phys. Rev. Lett.* **83** 3737
[32] Moss J and Brown P J 1972 *J. Phys. F: Met. Phys.* **2** 358

Morphware oder einer für alles

Diesen Artikel können Sie als Audiodatei beziehen, siehe: www.spektrum.de/audio

Wie ein Chamäleon die Farbe, soll ein Morphwarechip seine Funktion verändern. Damit das auch noch in Echtzeit vonstatten geht, setzen Berliner Forscher auf magnetische Schaltkreise.

Von Reinhold Koch

Vielseitig oder schnell, diese Frage stellt sich den Entwicklern von Mikroprozessoren immer wieder. Am einen Ende der Skala rangiert das Herz jedes Computers, der zentrale Prozessor (CPU). Als echte Universalmaschine berechnet er räumliche Bilder, unterstützt Textverarbeitung, löst komplizierte Gleichungssysteme, übernimmt Steuerfunktionen. Diese Vielseitigkeit geht aber auf Kosten der Geschwindigkeit, beruht sie doch auf einem komplizierten System von Befehlsebenen: ganz oben die für den jeweiligen Einsatz nötigen Anweisungen der Software, ganz unten die Steuerbefehle für die Prozessorhardware. Anwendungsspezifische Integrierte Schaltungen, kurz ASICs, sind einfacher strukturiert und deshalb schneller. Sie verstehen nur wenige Steuerbefehle und diese sind »maschinennah«, das heißt auf die konkrete Schaltung zugeschnitten. Auf Sound- oder Grafikkarten verrichten solche Chips ihren Dienst und nehmen der CPU einen Teil der anfallenden Arbeit ab.

Mittlerweile gibt es Hardware, deren logischer Aufbau nicht ein für allemal festliegt, sondern rekonfigurierbar ist. Ein Beispiel solcher »Morphware« sind die bereits kommerziell erhältlichen FPGAs (Field-Programmable Gate Arrays). Sie bestehen aus Modulen, in denen eine Vielzahl von Transistoren so zusammengefasst sind, dass sie gemeinsam bestimmte logische Operationen durchführen können. Die »Verdrahtung« der Module lässt sich programmieren, mithin ihr Zusammenspiel und damit die Schaltungslogik umbauen. In der Praxis haben sich solche FPGAs bereits bewährt: Sie verschlüsseln oder komprimieren Daten und erkennen Objekte in Videoaufnahmen zehn- bis hundertmal schneller als eine herkömmliche CPU.

Solche Morphware basiert aber noch auf der etablierten Siliziumtechnologie CMOS (Complementary Metal Oxide Semiconductor), das bringt Nachteile mit sich. Vor allem benötigt die Neuverschaltung der logischen Blöcke mehr als zehn Nanosekunden, während der daraus resultierende Prozessor etwa hundertmal schneller arbeitet. Eine Rekonfigurierung innerhalb eines Computertakts ist deshalb nicht möglich. Derselbe Prozessor könnte also nicht ohne Zwischenstopps Satellitenbilder verarbeiten, komprimieren und senden. Zudem sind FPGAs sehr groß, was ihre Anzahl in einem System und damit die Zahl und Geschwindigkeit gleichzeitig ausführbarer logischer Operationen limitiert.

Deshalb entwickeln einige Forschungsgruppen neuerdings Morphware, deren logische Elemente (Gatter, englisch *gates*) aus dünnen magnetischen Schichten bestehen. Da sie nicht einmal eine zehntel Nanosekunde brauchen, um eine andere logische Struktur anzunehmen, ist die Neukonfiguration innerhalb des Prozessortakts kein Traum mehr. Derartige Elemente haben obendrein den Vorteil, dass die berechnete Information gespeichert bleibt, selbst wenn der Rechner ausgeschaltet wird. Im Gegensatz dazu muss sie bei CMOS-Bauteilen während des Betriebs permanent aufgefrischt werden. Magnetologische Komponenten benötigen also weniger Strom. Mehr noch: Weil die berechnete Information erhalten bleibt, steht sie für einen folgenden Verarbeitungsschritt zur Verfügung und muss nicht intern aus einem Speicher erneut geladen werden.

Grundlage dieser famosen Eigenschaften ist die Technologie neuer Datenspeicher, die als MRAM (Magnetic Random-Access Memory) demnächst auf

IN KÜRZE

Magnetlogische Morphware

So genannte Morphwareprozessoren lassen sich mittels einer programmierbaren inneren Verdrahtung für neue Aufgaben optimieren. Alternativ zur Siliziumtechnologie könnten diese Elemente auf einer Magnetologik basieren: **Ausrichten magnetischer Schichten durch Steuerströme** ändert ihren elektrischen Widerstand von niedrig nach hoch und umgekehrt. Dieses Prinzip wird bereits genutzt, um in so genannten MRAMs binäre Daten zu speichern. Mit einer leichten Variation lassen sich aber auch logische Operationen realisieren, wie sie allen Computerberechnungen zu Grunde liegen.

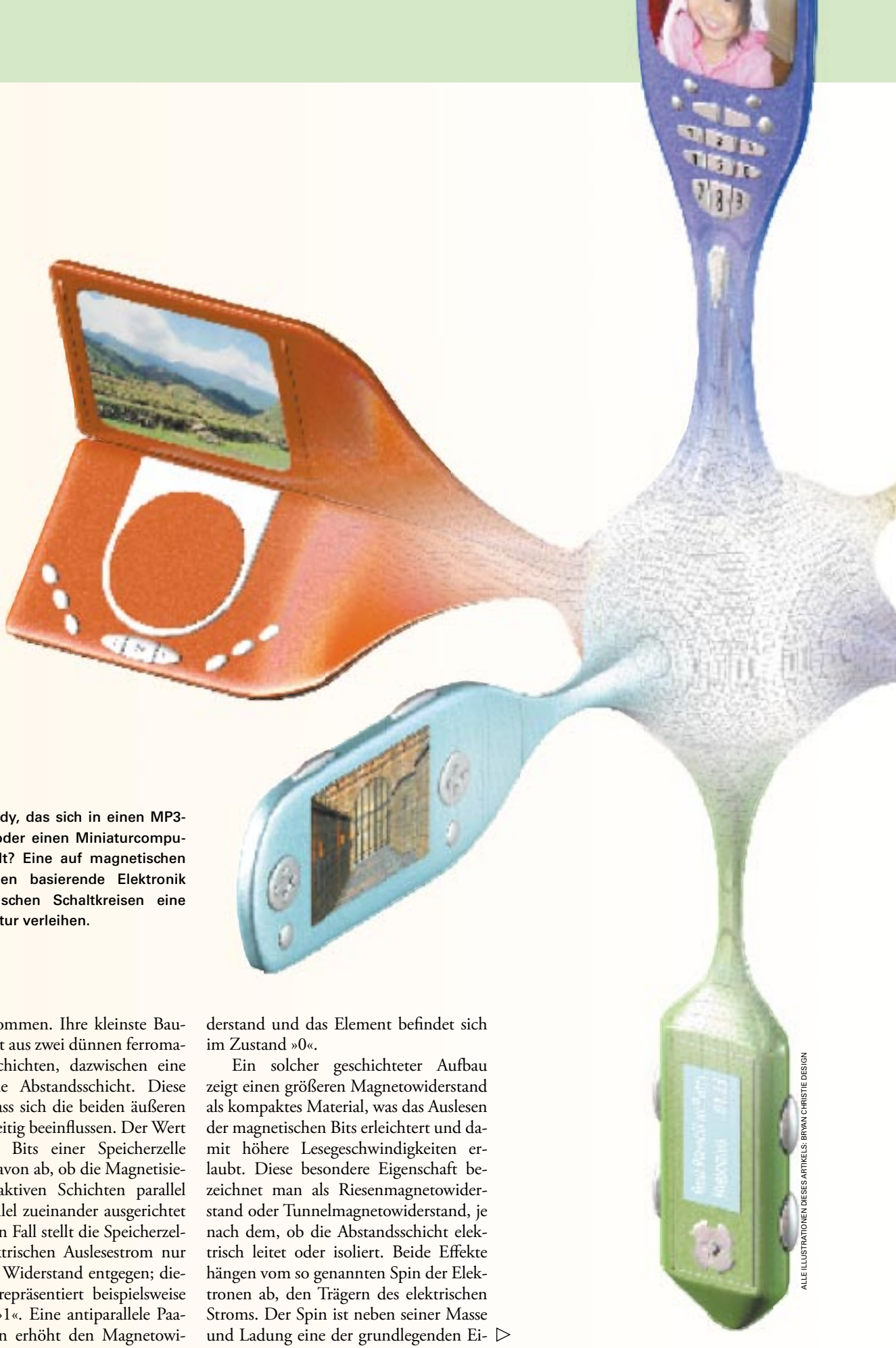

Ein Handy, das sich in einen MP3-Player oder einen Miniaturcomputer verwandelt? Eine auf magnetischen Logikbausteinen basierende Elektronik soll elektronischen Schaltkreisen eine Chamäleonnatur verleihen.

ALLE ILLUSTRATIONEN DIESES ARTIKELS: BRYAN CHRISTIE DESIGN

den Markt kommen. Ihre kleinste Baueinheit besteht aus zwei dünnen ferromagnetischen Schichten, dazwischen eine unmagnetische Abstandsschicht. Diese verhindert, dass sich die beiden äußeren Lagen gegenseitig beeinflussen. Der Wert des digitalen Bits einer Speicherzelle hängt dann davon ab, ob die Magnetisierungen der aktiven Schichten parallel oder antiparallel zueinander ausgerichtet sind. Im ersten Fall stellt die Speicherzelle einem elektrischen Auslesestrom nur einen kleinen Widerstand entgegen; dieser Zustand repräsentiert beispielsweise eine digitale »1«. Eine antiparallele Paarung hingegen erhöht den Magnetowiderstand und das Element befindet sich im Zustand »0«.

Ein solcher geschichteter Aufbau zeigt einen größeren Magnetowiderstand als kompaktes Material, was das Auslesen der magnetischen Bits erleichtert und damit höhere Lesegeschwindigkeiten erlaubt. Diese besondere Eigenschaft bezeichnet man als Riesenmagnetowiderstand oder Tunnelmagnetowiderstand, je nach dem, ob die Abstandsschicht elektrisch leitet oder isoliert. Beide Effekte hängen vom so genannten Spin der Elektronen ab, den Trägern des elektrischen Stroms. Der Spin ist neben seiner Masse und Ladung eine der grundlegenden Ei- ▷

genschaften des Elektrons, vereinfacht gesprochen kann er als eine Rotation um die eigene Achse und damit als Drehmoment verstanden werden. Weil bewegte elektrische Ladungen aber stets ein Magnetfeld erzeugen, geht mit der Rotation auch eine Magnetisierung einher – das Elektron wirkt sozusagen wie ein winziger Stabmagnet. Von der jeweiligen Ausrichtung dieses Stabmagneten (parallel oder antiparallel zur Magnetisierung der zweiten Lage) hängt es nun ab, ob die Strom führenden Elektronen einen kleinen oder großen Widerstand beim Übergang von einer zur anderen magnetischen Schicht verspüren.

Auch beim Schreiben eines Bits spielt der Eigendrehimpuls der Elektronen eine Rolle. Derzeit erfolgt das Ummagnetisieren der Schichten noch über das Magnetfeld eines äußeren Stroms, doch an einer Alternative wird bereits geforscht: Der Spin der Leitungselektronen, die durch das Element fließen, soll zukünftig die Magnetisierung schalten (Spektrum der Wissenschaft, 8/2002, S. 28).

Zusätzlich zu seiner Speicherfunktion lassen sich mit einer MRAM-Zelle auch die elementaren logischen Funktionen realisieren, auf denen alle Rechenschritte in Prozessoren beruhen: Die AND-Operation verknüpft zwei Eingangsdaten so, dass das Resultat nur dann eine »1« ergibt, wenn an beiden Eingängen eine »1« anliegt, das OR hingegen erfordert dazu lediglich eine »1« an einem der beiden Eingänge.

Magnetologische Gatter gab es schon in den frühen 1960er Jahren, sie wurden aber schnell von den aufstrebenden Siliziummikrochips verdrängt. Erst im Jahr 2000 griffen William C. Black, Jr. und Bodhisattva Das von der Iowa State University das Thema in einem wegweisenden Artikel wieder auf. Bereits zwei Jahre später demonstrierte ein Siemens-Forscherteam in Erlangen die Machbarkeit eines rekonfigurierbaren magnetischen Logikelements. Und 2003 veröffentlichte meine Gruppe am Paul-Drude-Institut für Festkörperelektronik in Berlin ein neues und einfacheres Konzept, um verschiedene logische Funktionen mit nur einem solchen Baustein zu realisieren.

Der Aufbau eines magnetologischen Gatters ähnelt dem einer MRAM-Zelle: Zwei magnetische Schichten, getrennt durch eine unmagnetische, haben eine parallele oder antiparallele Magnetisierung und das Ensemble zeigt demgemäß einen niedrigen beziehungsweise hohen Magnetowiderstand. Ein Lesestrom ermittelt dann das Ausgangssignal »1« oder »0«.

Das an unserem Institut entwickelte Design verwendet drei Eingänge – A, B und C – von denen jeder mit einem Strom derselben Größe angesteuert wird. Unser Konzept macht sich zu Nutze, dass am Ausgang eines Magnetowiderstandselements zwar nur zwei verschiedene Werte ausgelesen werden können, nämlich »1« und »0«, das Element bezüglich seiner Magnetisierung aber insgesamt vier verschiedene Anfangszustände einnehmen kann: Weil der Gesamtspin in jeder ferromagnetischen Schicht nach links oder rechts weist, gibt es sowohl zwei parallele als auch zwei antiparallele Kombinationen. Wir haben erkannt, dass jede davon eine andere logische Funktion ermöglicht.

Bei unserem Aufbau beginnt eine logische Operation damit, die Polarität des Gatters in einen dieser vier Anfangzustände zu setzen (siehe Kasten rechts). Zur Ummagnetisierung der oberen Schicht werden die Eingänge A und B mit Strom in derselben Richtung, also positiv oder negativ, beschickt. Kommt Eingang C noch hinzu, wird auch noch die untere Schicht polarisiert.

Diesem Setzschritt schließt sich die eigentliche logische Operation an, für die nur die obere Schicht angesteuert werden muss. Der Zwei-Stufen-Prozess hat den Vorteil, dass die logische Funktion des Gatters nach jeder Berechnung neu eingestellt werden kann. Da die zugewiesene Polarität des Ausgangs und damit das aus der Operation resultierende Bit auch nach dem Abschalten des Lesestroms erst einmal erhalten bleibt, entfällt wie erwähnt das periodische Auffrischen; auch das Auslesen kann ohne Löschen und Neuschreiben des Bits erfolgen. Die kombinierte Logik- und Speicherfähigkeit spart daher Energie und Zeit.

Der Vorgang lässt sich besonders gut am Beispiel der AND-Funktion erläutern. Man startet mit einem der beiden antiparallelen Zustände, das heißt dem Ausgangswert »0«. Im Querschnitt betrachtet, zeigt die Magnetisierung der oberen Schicht nach links und die der unteren Schicht nach rechts. Damit der Ausgangswert des Gatters von »0« nach »1« springt, muss die Magnetisierung der oberen Schicht nach rechts gedreht werden. Dazu beschickt man die beiden Eingänge A und B mit einem als »positiv« definierten Strom. Nun sind beide Schichten parallel orientiert und gemäß der Logiktabelle resultiert der Ausgangswert »1«.

Der Programmablauf für ein OR-Gatter verläuft analog, jedoch ist der Anfangszustand beider Schichten nach

Wie funktioniert ein magnetologisches Gatter?

Zwei ferromagnetische Lagen, die durch eine nichtmagnetische Schicht getrennt sind, können ihre Magnetisierungsrichtung verändern, um eine digitale »1« (Pfeil nach rechts) oder »0« (Pfeil nach links) zu repräsentieren. Elektrischer Strom in den Eingangsleitungen erzeugt ein Magnetfeld, das die gewünschte Umschaltung vornimmt. Die beiden oberen Zuleitungen (A und B) – die den Informationseingängen entsprechen – sind dabei für die obere Schicht zuständig. Strom durch alle drei Steuerleitungen kann zudem die Magnetisierung beider Lagen umkehren. Ist diese parallel, wird am Ausgang eine »1« gelesen, bei antiparalleler Ausrichtung eine »0«.

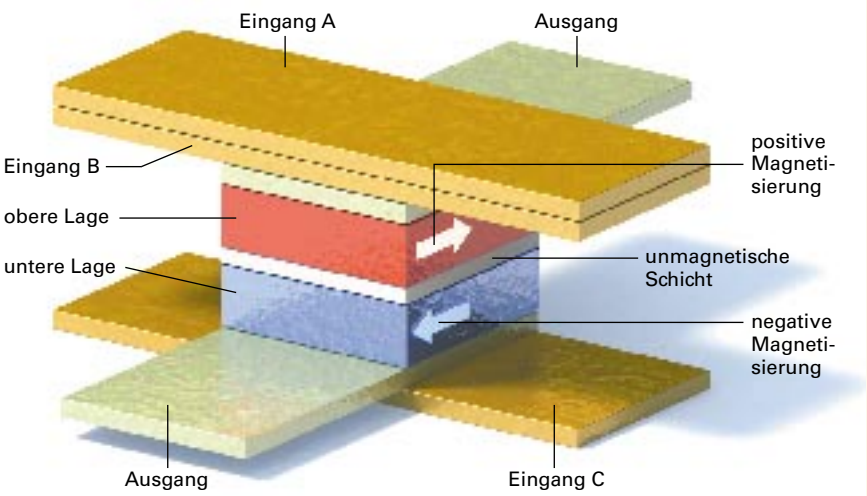

Logische Operationen

Mit einem magnetologischen Gatter erfolgt eine logische Operation in zwei Stufen. Zum Beispiel wird ein AND-Gatter gebildet, indem man das Element zuerst in einen »0«-Zustand setzt, also für eine antiparallele Ausrichtung der Magnetisierungen sorgt (linke Grafik): Die obere Schicht repräsentiert eine »0« (Pfeil nach links), die untere Schicht eine »1« (Pfeil nach rechts). Am Ausgang liegt ein »0« an, wie es die AND-Operation erfordert. Durch die Stromrichtung lassen sich nun weitere logische Verknüpfungen durchführen, doch nur dann, wenn die Ströme in den Eingangsleitungen A und B (rot) die obere Schicht ummagnetisieren, repräsentieren beide ferromagnetischen Schichten eine »1« und das Ausgabebit wechselt gemäß der AND-Verknüpfung von »0« auf »1« (Grafik Mitte).

Durch Ansteuerung der drei Eingangleitungen verwandelt sich ein solches AND-Gatter in sein Gegenstück, das NOT AND- oder kürzer NAND-Element. Dazu werden Ströme, die ein negativ gerichtetes Magnetfeld (blau) erzeugen, an die Eingangsleitungen A, B und C angelegt. Die Magnetisierung der unteren Schicht kehrt sich dabei um (rechtes Gatter). Nun lassen sich NAND-Operationen über die Leitungen A und B ansteuern (C wird nur für den Anfangszustand benötigt und taucht deshalb in der Tabelle nicht auf).

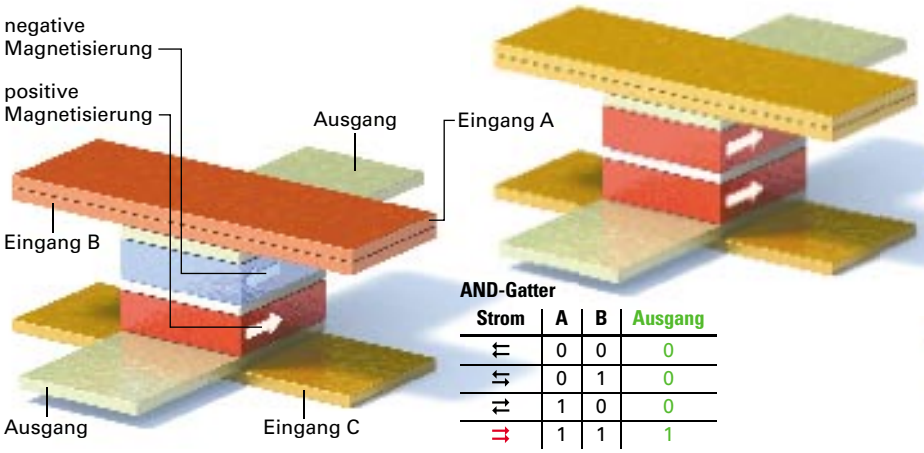

AND-Gatter

Strom	A	B	Ausgang
⇆	0	0	0
⇅	0	1	0
⇄	1	0	0
⇉	1	1	1

NAND-Gatter

Strom	A	B	Ausgang
⇆	0	0	1
⇅	0	1	1
⇄	1	0	1
⇉	1	1	0

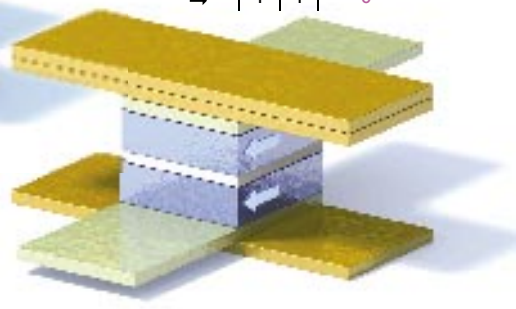

rechts magnetisiert; der Output ist also zunächst »1«. Nur ein »negativer« Strom an beiden Eingängen würde die Orientierung der oberen Lage umkehren, also einen insgesamt antiparallelen Zustand mit Ausgangswert »0« erzeugen, ein »positiver« Strom am Eingang A oder B oder an beiden hingegen ließe den Ausgabewert unverändert.

Zwei weitere logische Funktionen ergeben sich, wenn man die Magnetisierung der unteren Schicht auf »links« setzt. Dazu werden alle drei Eingänge – A, B und C – mit einem »negativen« Strom angesteuert. Das Umschalten der unteren Schicht macht aus dem Output »1« eine »0« und umgekehrt. Die AND-Funktion verwandelt sich damit zu ihrem Gegenstück, dem NOT AND (NAND), und das OR zu einem NOT OR (NOR).

OR- und AND-Funktionen entsprechen der Boole'schen Addition beziehungsweise Multiplikation. Zusammen mit NAND und NOR bilden sie eine starke Basis, um selbst die komplexesten Schaltkreise aufzubauen. Durch eine modifizierte Ansteuerung lassen sich überdies noch höherwertigere logische Funktionen realisieren wie das XOR, das zwischen gleichen und entgegengesetzten Eingängen unterscheidet: XOR gibt eine »1« bei gleichen Eingängen (»0«/«0« oder »1«/«1«) aus, eine »0« bei komplementären (»1«/«0« oder »0«/«1«) . Zwei MRAM-Gatter reichen dazu aus, in der CMOS-Technologie sind 14 Transistoren nötig.

XOR ist die wichtigste Komponente eines so genannten Volladdierers und der wiederum ist die am häufigsten benötigte Einheit in einem Prozessor: Er summiert zwei binäre Eingänge sowie den Übertrag einer vorhergehenden Berechnung, das liefert eine neue Summe und einen neuen Übertrag. Ein solches Element lässt sich komplett magnetologisch aufbauen. Dank der Nichtflüchtigkeit und Programmierbarkeit reichen dafür drei Gatter, in CMOS-Technologie sind es mindestens 16 Transistoren. Wir schätzen, dass die magnetische Variante es mit den schnellsten Silizium-Volladdierern aufnehmen kann und dabei deutlich weniger Energie verbraucht.

Die Eingangsleitungen A und B könnten wie bei den MRAMs als Gitter aufgebaut werden, mit den magnetologischen Elementen in den Kreuzungspunkten: Erhalten beide Zuführungen gleichzeitig ein Steuersignal, schaltet das jeweilige Element. Eine Matrix von CMOS-Transistoren würde als Interface fungieren und die Nachverstärkung der für die Weiterverarbeitung zu kleinen Leseströme übernehmen.

Die Chamäleonnatur eines Morphwareprozessors verspricht viele Vorteile. Auf Grund der Reprogrammierbarkeit seiner Gatter wäre der Einsatzbereich nicht länger durch die Hardware vorherbestimmt. In CMOS wird die Logik eines normalen Transistorgatters durch die Verdrahtung definiert und fixiert. Ein magnetologischer Prozessor hingegen stellt nur einen quasi universellen Block aus logischen Gattern bereit, von denen jedes individuell für die gewünschte Anwendung programmiert werden kann.

Ein solcher Prozessor kommt mit viel weniger logischen Gattern aus als sein CMOS-Kollege, weil dieser immer nur wenige Prozent davon für eine Aufgabe einsetzen kann. Erfordert eine Berechnung etwa besonders oft die Funktion eines Volladdierers, kann sich die Magne- ▷

Wählen Sie Ihren Prozessor

	programmierbar	Geschwindigkeit der Reprogrammierbarkeit	Anzahl der Komponenten für elementare Logikfunktionen	Timing
Magnetologik	ja	~0.1 Nanosekunden	ein Gatter	paralleler Betrieb, gegebenenfalls auch ohne Uhr zur Synchronisation des Datentransfers
Herkömmlicher Prozessor	nein	nicht zutreffend	vier Transistoren	serieller, getakteter Betrieb
FPGAs	ja	>10 Nanosekunden	individuelle Adressierung der Logikelemente nicht möglich	serieller, getakteter Betrieb

Zum Aufbau eines AND-Schaltkreises werden vier Transistoren benötigt (links), während bereits ein magnetologisches Element für die Darstellung derselben Logikfunktion ausreicht.

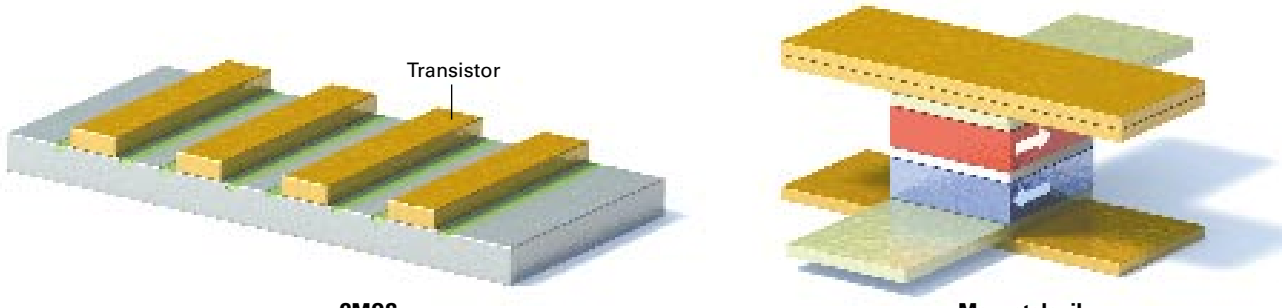

CMOS **Magnetologik**

▷ tomorphware immer wieder entsprechend neu konfigurieren, während die Kalkulation in der herkömmlichen Maschine stockt. Die Flexibilität der Gatter bedeutet auch, dass neue Software leicht implementierbar ist.

Da die Schaltgeschwindigkeit wie bei CMOS-Chips Milliarden Zyklen pro Sekunde beträgt, vermag ein Chamäleonprozessor seine Funktion viele Male innerhalb einer Sekunde zu wechseln. Dank der Nichtflüchtigkeit der berechneten Bits müssen sie nicht zeit- und energieaufwändig vom Prozessor in den Speicher und zurück befördert werden. Das ermöglicht effizientere Algorithmen und Arbeitsprozesse – die Leistungsfähigkeit der Prozessoren wächst auch ohne die in der Siliziumtechnologie dazu nötige Miniaturisierung.

Dank der großen Ähnlichkeit zum MRAM kann die Magnetologik vorerst von dessen Entwicklung profitieren. So muss in beiden Bauelementen das magnetische Übersprechen zwischen den Ferromagnetika unterbunden werden. Zunächst könnte also ein MRAM-Chip als Prozessor fungieren, der – weil nur eine seiner beiden Schichten schaltbar ist – AND und OR beziehungsweise NAND und NOR realisieren kann. Deshalb hoffen wir, dass die Industrie die Entwicklung dieser Speicherzellen vorantreibt. Leider geht sie dies eher zögerlich an – mit neuen Speichertechnologien lässt sich derzeit wenig verdienen.

Um jedoch das volle Potenzial eines magnetischen Prozessors auszuschöpfen, müssen diverse Probleme gelöst werden. Derzeit gelingt es weder uns noch Kollegen in anderen Einrichtungen, die beiden magnetischen Lagen unabhängig voneinander zu schalten. Da ein magnetischer Prozessor auf Grund seiner Flexibilität wohl die meiste Zeit unter Volllast arbeiten wird, entwickelt er zudem sehr viel mehr Wärme als sein Siliziumpendant, was die Haltbarkeit beeinträchtigt. Den Ingenieuren muss es gelingen, für magnetologische Gatter eine Lebensdauer von 10^{16} bis 10^{17} Schaltzyklen zu erreichen – das Hundert- bis Tausendfache der bislang erreichten Werte. Bis dahin mag es helfen, dass defekte Gatter während des Hochfahrens eines Computers entdeckt und überbrückt werden. Zur Optimierung einer Magnetologik suchen wir noch Materialien mit höherem Magnetowiderstand, die sich zudem mit Halbleitern kombinieren lassen (Spektrum der Wissenschaft 11/2004, S. 76). Die größte Hürde aber dürfte es sein, eine geeignete Compilersprache zu entwickeln und neue Algorithmen zu finden, die alle Vorteile der in Echtzeit reprogrammierbaren logischen Gatter ausnutzen. ◀

Der Chemiker **Reinhold Koch** leitet die Forschergruppe Nanoakustik am Paul-Drude-Institut für Festkörperelektronik in Berlin. Dort habilitierte er 1993 an der Freien Universität. 1994 erhielt er den Karl-Scheel-Preis für seine Arbeiten auf dem Gebiet der mechanischen Spannungen in dünnen Schichten sowie Strukturuntersuchungen mit einem Rastertunnelmikroskop.

AUTOR UND LITERATURHINWEISE

Programmable computing with a single magnetoresistive element. Von A. Ney, C. Pampuch, R. Koch und K. H. Ploog in: Nature, Bd. 425, S. 485, 2. Oktober 2003

The future of universal memory. Von Russel Cowburn in: Materials Today, Bd. 1, Heft 7–8, S. 32, Juli–August 2003

Reconfigurable computing: a survey of systems and software. Von Katherine Compton und Scott Hauck in: ACM Computing Surveys, Bd. 34, Heft 2, S. 171, 2002

Programmable logic using giant-magnetoresistance and spin-dependent tunneling devices. Von W. C. Black, Jr. und B. J. Das in: Journal of Applied Physics, Bd. 87, Heft 90, S. 6674, 1. Mai 2000

INSTITUTE OF PHYSICS PUBLISHING JOURNAL OF PHYSICS: CONDENSED MATTER

J. Phys.: Condens. Matter **18** (2006) 6101–6108 doi:10.1088/0953-8984/18/26/028

Magnetic properties of epitaxial Heusler alloy $(Co_{2/3}Fe_{1/3})_{3+x}Si_{1-x}$/GaAs(001) hybrid structures

M Hashimoto, J Herfort, H-P Schönherr and K H Ploog

Paul-Drude-Institut für Festkörperelektronik, Hausvogteiplatz 5–7, 10117 Berlin, Germany

E-mail: hashimoto@pdi-berlin.de

Received 24 March 2006, in final form 28 April 2006
Published 19 June 2006
Online at stacks.iop.org/JPhysCM/18/6101

Abstract

The magnetic properties of full Heusler alloy $(Co_{2/3}Fe_{1/3})_{3+x}Si_{1-x}$/GaAs(001) hybrid structures grown by molecular beam epitaxy have been investigated. The magnetic moment, the coercive field and the in-plane magnetic anisotropy of $(Co_{2/3}Fe_{1/3})_{3+x}Si_{1-x}$ films with various Si compositions ($-0.46 \leqslant x \leqslant 1$) are discussed. The increase in amount of Si results in a significant reduction in the cubic magnetocrystalline anisotropy constant $|K_1^{\mathrm{eff}}|$. K_1^{eff} changes sign and saturates near the stoichiometric composition of Co_2FeSi and the easy axis of the cubic component changes from the $\langle 110 \rangle$ direction to the $\langle 100 \rangle$ direction accordingly. However, due to the presence of a dominating uniaxial magnetic anisotropy component, the easy axis of magnetization in total is shifted to the [110] direction. The saturation magnetization of stoichiometric Co_2FeSi films turned out to be 1250 ± 120 emu cm^{-3}, being equivalent to 6.1 ± 0.57 (μ_B/formula unit (fu)). The relatively close value of magnetic moment to the theoretically expected integer value (6 μ_B) suggests that Co_2FeSi films could be half-metallic ferromagnets.

(Some figures in this article are in colour only in the electronic version)

1. Introduction

Half-metallic ferromagnets (HMFs), which have 100% spin-polarized carriers at the Fermi level, are promising candidates for spintronics devices, e.g. magnetic tunnelling junction and spin injection device. Potential HMFs include some diluted magnetic semiconductors, oxides and Heusler alloys. Heusler alloys are especially attractive because of their high Curie temperature, close lattice matching with semiconductors and theoretically predicted half-metallicity [1]. Some Heusler alloys, e.g. NiMnSb, Co_2MnSi, and Co_2MnGe, are predicted to be half-metallic by theoretical studies [2–5]. Moreover, recently we have clarified that Heusler alloy/semiconductor (SC) hybrid structures have a more thermally stable interface

than conventional elemental ferromagnets (FM)/SC [6, 7]. Therefore, Heusler alloy/SC hybrid structures are much more suitable for device-processing steps after epitaxial growth.

Co_2FeSi is a full Heusler alloy with a cubic $L2_1$ crystal structure consisting of four interpenetrating fcc sublattices [8]. The lattice constant of bulk Co_2FeSi is 5.658 Å [9], being closely lattice matched to GaAs ($a_{GaAs} = 5.653$ Å). The lattice mismatch is as small as 0.08%. Bulk Co_2FeSi with a large magnetic moment (5.91 μ_B at 10.2 K) is ferromagnetic up to more than 980 K [9]; these are among the highest Curie temperatures and magnetic moments of the reported Heusler alloys. According to electronic band structure calculations based on the local density approximation (LDA), Co_2FeSi is located at a position slightly deviating from the Slater–Pauling curve which half-metallic Heusler alloys are expected to obey [5]. On the other hand, recent calculations based on LDA + U, which take into account the electron correlation effect, have revealed that Co_2FeSi can have an integer magnetic moment (6 μ_B/formula unit (fu)), suggesting that it should be a HMF [10]. These characteristics make this material promising for applications in spintronic devices.

The $L2_1$ structure can also be considered as a combination of two binary B2 alloys, i.e. CoFe and CoSi in the case of Co_2FeSi [8]. Since binary CoFe does crystallize in the B2 structure when it is ordered, it is possible to tune the composition continuously from the binary CoFe to the Heusler alloy Co_2FeSi by changing the Si composition. This enables a systematic study of the transition of its magnetic properties between the two different classes of alloys in the present system. In this report, we study the magnetic properties of full Heusler alloy $(Co_{2/3}Fe_{1/3})_{3+x}Si_{1-x}$ films ($-0.46 \leqslant x \leqslant 1$) having various Si compositions including binary $Co_{0.66}Fe_{0.34}$ grown by molecular beam epitaxy (MBE) on GaAs(001) substrates. The impact of Si incorporation on the magnetic moment, coercive field and in-plane magnetic anisotropy of $(Co_{2/3}Fe_{1/3})_{3+x}Si_{1-x}$ is described.

2. Sample preparation

In preparation of the Co_2FeSi, the growth conditions of the binary alloy $Co_{0.66}Fe_{0.34}$ (bcc structure) were optimized. The composition of $Co_{0.66}Fe_{0.34}$ layers was determined by comparing their lattice constant with literature data [11], taking into account the tetragonal distortion of the layers as confirmed by reciprocal space mappings around the (113) and (224) reflections (not shown here). To estimate the unstrained lattice constant of the films the elastic constants of CoFe [12] have been used. Then Si was added and incorporated to obtain ternary $(Co_{2/3}Fe_{1/3})_{3+x}Si_{1-x}$, while the Fe and Co fluxes were kept constant at the determined amounts.

Before the growth of the $(Co_{2/3}Fe_{1/3})_{3+x}Si_{1-x}$ layers, 100 nm-thick GaAs buffer layers were grown in the III–V growth chamber using standard GaAs growth conditions. As-terminated c(4 × 4) reconstructed GaAs(001) surfaces were prepared by cooling the samples down to 420 °C under As_4 pressure to prevent the formation of macroscopic defects on the surface similar to our studies on Fe/GaAs(001) [13]. The samples were then transferred to the As-free metal deposition chamber under UHV at a base pressure of 5×10^{-10} Torr. The growth temperature T_G for the $Co_{0.66}Fe_{0.34}$ and $(Co_{2/3}Fe_{1/3})_{3+x}Si_{1-x}$ layers was kept at 100 °C due to the requirement of low T_G to avoid the interfacial reaction in CoFe/GaAs growth. We confirmed that the Co_2FeSi/GaAs interface is thermally robust up to $T_G = 200$ °C [7]. A low growth rate of about 0.1 nm min^{-1} was chosen in order to avoid the degradation of the crystal quality at this low growth temperature. The Si cell temperature T_{Si}, and hence the composition of the films, was varied from 1280 to 1335 °C. Correspondingly the perpendicular lattice mismatch between the layer and the substrate $(\Delta a/a)_\perp$ varied linearly from 0.76% ($T_{Si} = 1280$ °C) to −0.47% ($T_{Si} = 1325$ °C) [14]. Further elevation of T_{Si} resulted in a

substantial reduction of the $Co_2FeSi(004)$ reflection peak in the ω–2θ curve at $T_{Si} = 1335\,^{\circ}C$ due to crystal degradation. From a comparison of a_{Co_2FeSi} with that of the bulk value, the stoichiometric film was determined to have a tetragonal distortion of $(\Delta a/a)_{\perp} = 0.14\%$ [14]. Then the Si composition x of $(Co_{2/3}Fe_{1/3})_{3+x}Si_{1-x}$ was estimated, by interpolation from the lattice constants, to be in the range $-0.46 \leqslant x \leqslant 1$. In this notation, $x = -3$, 0 and 1 correspond to pure Si, stoichiometric Co_2FeSi and $Co_{0.66}Fe_{0.34}$, respectively. The thickness of the layers determined by high-resolution x-ray diffraction (HRXRD) and x-ray reflectivity (XRR) measurements varies in the range from 17 to 23 nm in accordance with the constant growth time of 180 min and the increase of T_{Si}. An atomically abrupt interface was confirmed from the observation of interference fringes in the HRXRD ω–2θ curves and by transmission electron microscopy for the film grown at 100 °C [7]. The long-range atomic ordering, namely the formation of the Heusler-type $L2_1$ structure even at this low T_G for samples around stoichiometric Co_2FeSi, is confirmed by the presence of the (113) and (002) superlattice reflection [15]. More details of the growth and structural characterizations are described elsewhere [14, 15].

3. Results and discussions

The magnetic properties of the $(Co_{2/3}Fe_{1/3})_{3+x}Si_{1-x}$ films were investigated using superconducting quantum interference device (SQUID) magnetometry. All the measurements were performed at room temperature and the external magnetic field was applied along three different in-plane crystallographic axes, [110], [1$\bar{1}$0] and [100]. After subtracting the diamagnetic contribution of the GaAs substrate, the magnetization was normalized to the saturation magnetization M_s. The films were not capped. However, we consider its influence on the magnetic moment to be much smaller than that from the uncertainty of volume estimation. All the examined $(Co_{2/3}Fe_{1/3})_{3+x}Si_{1-x}$ films are ferromagnetic at room temperature with the easy axis along the [110] direction. The obtained magnetization curves of the $(Co_{2/3}Fe_{1/3})_{3+x}Si_{1-x}$ films were categorized into three types: (i) $Co_{0.66}Fe_{0.34}$ ($x = 1$) where a so-called split loop was observed along the [1$\bar{1}$0] direction; (ii) $(Co_{2/3}Fe_{1/3})_{3+x}Si_{1-x}$ with $-0.46 \leqslant x \leqslant 0.46$, where an uniaxial magnetic anisotropy (UMA) dominates; and (iii) $(Co_{2/3}Fe_{1/3})_{3+x}Si_{1-x}$ with $x < -0.46$, where a degradation of the crystalline quality occurred. The normalized magnetization curves of each type are displayed in figure 1 together with the magnetization curves along the easy axis direction in an expanded scale in the right panel.

The magnetization curves of $Co_{0.66}Fe_{0.34}$ show a square-shaped hysteresis loop with a relatively large H_c of 20 Oe along the easy axis, a split loop along the [1$\bar{1}$0] direction, and a strong hard axis with a saturation field H_{sat} of about 1000 Oe along the [100] direction (figures 1(d) and (h)). The incorporation of Si into $Co_{0.66}Fe_{0.34}$ induces several changes in the magnetization curves. We see a disappearance of the split loop, reductions of H_c and H_{sat} along the [100] direction as the composition approaches stoichiometry in figures 1(c), (g), (b) and (f). The magnetization curves of stoichiometric Co_2FeSi shows an easy axis [110], a reversible hard axis [1$\bar{1}$0] and an intermediate axis [100] as can be seen in figures 1(b) and (f). The magnetization curve along the [110] direction shows a square-shaped hysteresis loop with a significantly reduced coercive field H_c of 4.5 Oe, indicating an excellent crystalline quality. The reversible hard axis along the [1$\bar{1}$0] direction indicates the presence of an in-plane UMA component. This is typical in cubic FM grown on zinc-blende SC systems [16–19] and is attributed to an anisotropic bonding at the FM/SC interface [20]. The saturation field H_{sat} along the $\langle 100 \rangle$ direction is significantly reduced to $H_{sat} \approx 200$ Oe, which can be associated with a reduction of the cubic magnetic anisotropy component, such that UMA becomes the

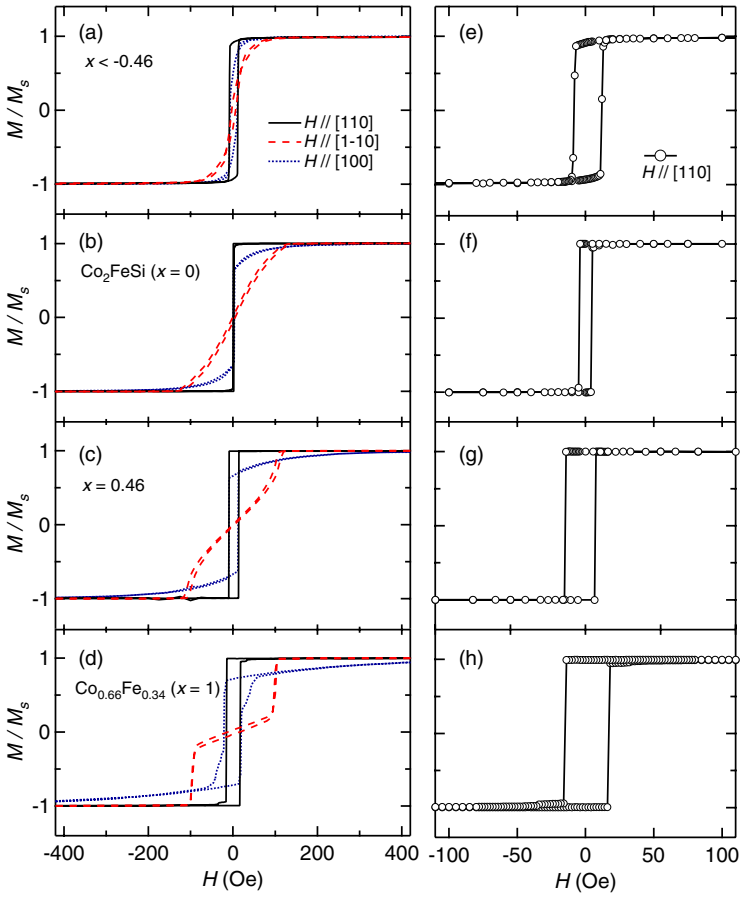

Figure 1. Normalized magnetization curves of: (a), (e) $(Co_{2/3}Fe_{1/3})_{3+x}Si_{1-x}$ with $x < -0.46$; (b), (f) stoichiometric Co_2FeSi ($x = 0$); (c), (g) $(Co_{2/3}Fe_{1/3})_{3+x}Si_{1-x}$ with $x = 0.46$; and (d), (h) $Co_{0.66}Fe_{0.34}$ ($x = 1$). All curves were taken at room temperature. The external magnetic field was applied along three different crystallographic axes, [110], [1$\bar{1}$0] and [100]. The right panel (e)–(g) shows the magnetization curves along the easy axis in an expanded scale. The diamagnetic contribution of the substrate has been subtracted.

dominating component in its in-plane magnetic anisotropy. The excessive incorporation of Si results in a further modification of the magnetization curves, as can be seen in figures 1(a) and (e). The magnetization curve becomes a rounder-shaped square with an increased H_c due to the crystal degradation. In addition, the in-plane UMA is further reduced.

M_s and H_c of the $(Co_{2/3}Fe_{1/3})_{3+x}Si_{1-x}$ films are plotted as a function of Si composition x in figure 2. H_c is along the [110] direction. M_s decreases almost linearly with increasing Si composition. The rather large scatter of the data is due to the uncertainty in determining the exact volume of the $(Co_{2/3}Fe_{1/3})_{3+x}Si_{1-x}$ layers. M_s of $Co_{0.66}Fe_{0.34}$ (1800 ± 74 emu cm^{-3} $\simeq$ 210 ± 9 emu g^{-1}) is comparable to the literature data of 1710 emu cm^{-3} [19] and 219.94 and 209.96 emu g^{-1} for bulk $Co_{0.6}Fe_{0.4}$ and $Co_{0.7}Fe_{0.3}$, respectively, in [21]. The M_s of the stoichiometric Co_2FeSi film amounts to 1250 ± 120 emu cm^{-3}, being equivalent to 6.1 ± 0.57 (μ_B/fu). Although the error is rather large, the value is relatively close to the theoretically expected integer value of 6 (μ_B/fu), suggesting that thin Co_2FeSi films could be

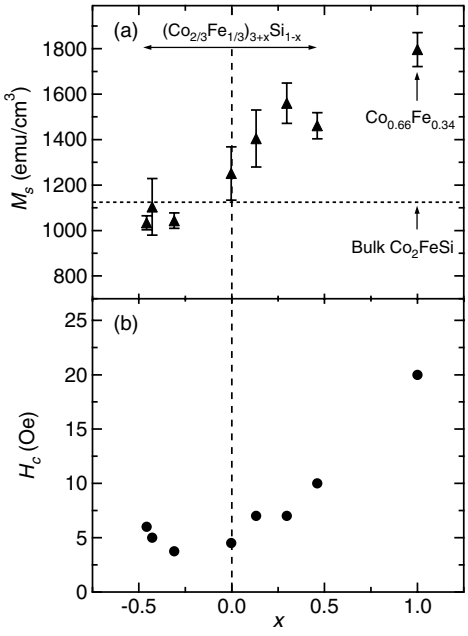

Figure 2. (a) Saturation magnetization M_s and (b) coercive field H_c along the [110] direction as a function of the Si content x for $Co_{0.66}Fe_{0.34}$ and $(Co_{2/3}Fe_{1/3})_{3+x}Si_{1-x}$. The dotted and dashed lines are M_s of bulk Co_2FeSi [9] and the stoichiometric composition of Co_2FeSi determined by HRXRD, respectively.

a HMF. The relatively large M_s of the stoichiometric film compared to that of bulk Co_2FeSi (1124 emu cm^{-3} at 295 K) may be due to a rather high degree of disorder (10–16%) in the bulk Co_2FeSi [9]. However, although the $L2_1$ structure was revealed for the films studied, the determination of the degree of ordering is currently under way. M_s remains nearly constant upon elevation of T_G up to 250 °C and gradually decreases above 250 °C, most likely due to the formation of a magnetically modified layer at the interface [7]. H_c decreases from the value of $Co_{0.66}Fe_{0.34}$ with increasing Si composition as shown in figure 2(b). H_c shows a minimum region in $-0.31 \leqslant x \leqslant 0$. Note that generally structural degradation of the layer and interface will increase H_c. Hence the minimum region corresponds to the region where an excellent crystal quality is maintained around the stoichiometric composition.

In order to explain the changes in the magnetization curves, the in-plane magnetic anisotropy of $(Co_{2/3}Fe_{1/3})_{3+x}Si_{1-x}$ was investigated by assuming a free energy density consisting of a cubic magnetocrystalline anisotropy term and an UMA term:

$$\varepsilon(\phi) = -\tfrac{1}{4}K_1^{\text{eff}}\sin^2(2\phi) + K_u^{\text{eff}}\sin^2(\phi) - HM_s\cos(\phi - \alpha), \tag{1}$$

where α is the angle between the external field and the [110] direction and ϕ is the angle between magnetization and the [110] direction [19]. Assuming a coherent rotation as a magnetization reversal process, by minimizing $\varepsilon(\phi)$, we obtain the relation between magnetic field H and magnetization M:

$$H(m) = 2K_1^{\text{eff}}(2m^3 - m)/M_s + 2K_u^{\text{eff}}m/M_s \tag{2}$$

where $m = \sin(\phi)$ is the normalized magnetization component [19]. Fitting the magnetization curves along the $[1\bar{1}0]$ direction with this expression, two effective anisotropy constants, K_1^{eff} and K_u^{eff}, were obtained. For the magnetization curves which show a discontinuous split loop,

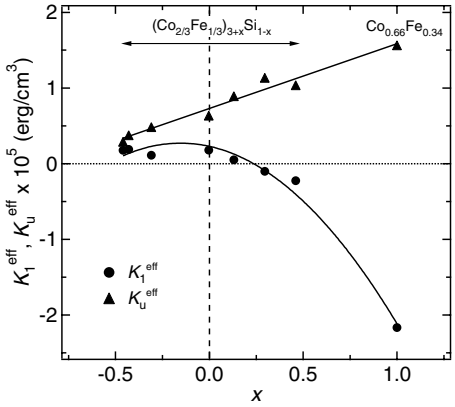

Figure 3. K_1^{eff} and K_u^{eff} of $Co_{0.66}Fe_{0.34}$ and $(Co_{2/3}Fe_{1/3})_{3+x}Si_{1-x}$ as a function of the Si content x. The dashed line is the stoichiometric composition determined by HRXRD and the solid lines are guides for the eye.

as in the case of $Co_{0.66}Fe_{0.34}$ with $H \parallel [1\bar{1}0]$, the anisotropy constants can be obtained using the following expressions derived from the same model (equation (1)),

$$K_1^{\mathrm{eff}} = \frac{1}{2}\frac{M_s(-1 + H_s s)}{(H_s^3 s^3 + H_s^2 s^2 + H_s s + 1)s}, \tag{3}$$

$$K_u^{\mathrm{eff}} = \frac{1}{2}\frac{M_s H_s (H_s^2 s^2 + H_s s + 2)}{H_s^3 s^3 + H_s^2 s^2 + H_s s + 1} \tag{4}$$

where s and H_s are the slope near $H = 0$ and the split field where the discontinuity takes place, respectively [19]. All the experimental magnetization curves were fitted well with this model, indicating that the magnetization reversal process takes place by a coherent rotation of magnetization as a single domain. In order to check the validity of the fitting, we performed simulations of the magnetization curves along the other two directions with the Stoner–Wohlfarth model using the obtained magnetic anisotropy constants, K_1^{eff} and K_u^{eff}. We obtained an excellent agreement between the simulated and experimental results for the reversible parts of the magnetization curves, suggesting the validity of the single-domain coherent-rotation model as well as the obtained magnetic anisotropy constants. On the other hand, the irreversible parts, i.e. H_c, were not reproduced since the Stoner–Wohlfarth model does not take into account the micro-magnetic structure of the layer [22].

K_1^{eff} and K_u^{eff} of the $(Co_{2/3}Fe_{1/3})_{3+x}Si_{1-x}$ films are plotted as a function of x in figure 3. As can be seen in the figure, K_u^{eff} linearly decreases with increasing Si content. This is partly due to the fact that K_u^{eff} is inversely proportional to the film thickness since K_u^{eff} is a pure interface-related term [15]. However, as far as the proportion of the interface contribution only is concerned, the expected decrease of K_u^{eff} corresponding to the thickness ranging from 17 to 23 nm is only $\Delta K_u^{\mathrm{eff}} = (-1.1 \pm 0.1) \times 10^4$ erg cm^{-3}. The value was estimated using the interface contribution constant of UMA, $K_u^{\mathrm{int}} = (7.2 \pm 0.9) \times 10^{-2}$ erg cm^{-2} [15]. This is almost one order of magnitude smaller than the actual decrease of $\Delta K_u^{\mathrm{eff}} = -7.4 \times 10^4$ erg cm^{-3}. Therefore, the reduction of K_u^{eff} cannot be attributed to the decrease of the interface contribution with increasing d but to a modification of the Co_2FeSi/GaAs interface itself. Most likely it reflects the modification of the bonding configuration at the interface by the incorporation of Si. On the other hand, $|K_1^{\mathrm{eff}}|$ decreases with increasing Si content. K_1^{eff} changes the sign and subsequently saturates near the stoichiometric composition of Co_2FeSi. The change of the

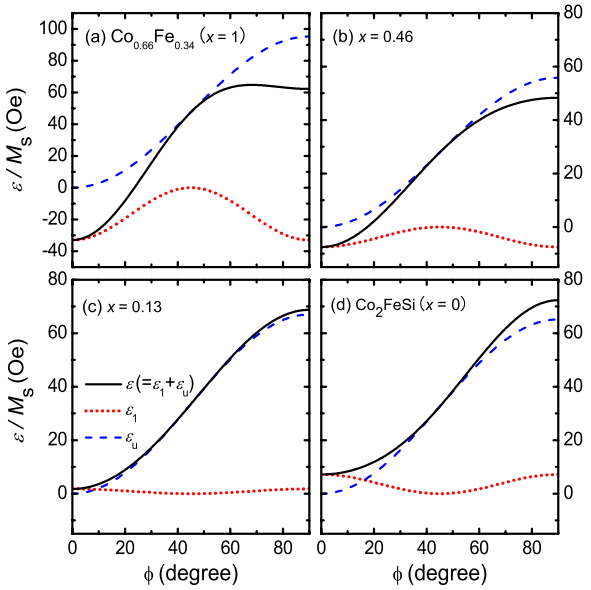

Figure 4. Free energy density $\varepsilon(\phi)$ calculated by using the fitted anisotropy constants K_1^{eff} and K_u^{eff} for (a) $Co_{0.66}Fe_{0.34}$ and ((b)–(d)) $(Co_{2/3}Fe_{1/3})_{3+x}Si_{1-x}$ having different Si contents. Total free energy density (black line), contribution from the magnetocrystalline anisotropy ε_1 (red dotted line) and from the uniaxial anisotropy ε_u (blue dashed line) is shown.

sign and the saturation of K_1^{eff} most likely corresponds to the change of the crystal structure from the bcc structure of $Co_{0.66}Fe_{0.34}$ into the $L2_1$ structure as evidenced by the appearance of the superlattice reflections (002) and (113) in the Co_2FeSi films [15]. As a result, the UMA is dominant near the stoichiometric composition, as already shown in the magnetization curves (figure 1(b)). The anisotropy constants of the Co_2FeSi ($d = 18.5$ nm) and $Co_{0.66}Fe_{0.34}$ (17.4 nm) films turned out to be $K_1^{\text{eff}} = 1.8 \times 10^4$ erg cm^{-3}, $K_u^{\text{eff}} = 6.3 \times 10^4$ erg cm^{-3} and $K_1^{\text{eff}} = -2.2 \times 10^5$ erg cm^{-3}, $K_u^{\text{eff}} = 1.6 \times 10^5$ erg cm^{-3}, respectively. The K_1^{eff} of $Co_{0.66}Fe_{0.34}$ is comparable to the literature value (-2.85×10^5 erg cm^{-3} [19]), while K_u^{eff} is one order of magnitude larger than that of the literature (1.5×10^4 erg cm^{-3} [19]). We assume that the comparatively large K_u^{eff} value, despite the rather large thickness of the $(Co_{2/3}Fe_{1/3})_{3+x}Si_{1-x}$ films, can be ascribed to the excellent interface perfection of the hybrid structure caused by the low growth temperature as well as the low growth rate.

In order to obtain further insights into the in-plane magnetic anisotropy depending on the Si composition and its relevance to the magnetization reversal process, we calculated the angle dependence of the free energy density $\varepsilon(\phi)$ with equation (1) using the obtained anisotropy constants. Figure 4 shows the angle dependence of the free energy density together with the UMA and cubic magnetocrystalline anisotropy components of (a) the $Co_{0.66}Fe_{0.34}$ film and (b)–(d) several $(Co_{2/3}Fe_{1/3})_{3+x}Si_{1-x}$ films having different Si contents. In the case of $Co_{0.66}Fe_{0.34}$, a relatively large K_u^{eff} component shares the common easy axis with the cubic magnetocrystalline anisotropy component at $\phi = 0°$, in the [110] direction. As a result, the total $\varepsilon(\phi)$ has a local minimum at $\phi = 90°$, in the $[1\bar{1}0]$ direction. This condition allows the magnetization to jump from near the [110] direction to the $[1\bar{1}0]$ direction and vice versa at H_s, resulting in the split loop [23]. As the formation of the $L2_1$ structure develops, the cubic magnetocrystalline anisotropy becomes weakened. It changes the sign at $x = 0.13$ (figure 4(c)), and accordingly the position of the minima of the cubic magnetocrystalline component rotates

by 45°. Therefore, the inherent easy axis of Co_2FeSi is along the ⟨100⟩ direction, although it appears to be along the [110] direction. Namely, due to the presence of the relatively strong UMA, which has a conflicting easy axis with the cubic magnetocrystalline one, the easy axis is in total shifted to the [110] direction.

4. Conclusion

We have studied the magnetic properties of epitaxial Heusler alloy $(Co_{2/3}Fe_{1/3})_{3+x}Si_{1-x}$/GaAs(001) hybrid structures. The magnetic moment, coercive field and in-plane magnetic anisotropy of $(Co_{2/3}Fe_{1/3})_{3+x}Si_{1-x}$ with various Si contents ($-0.46 \leqslant x \leqslant 1$) were described. Incorporation of Si into $Co_{0.66}Fe_{0.34}$ results in a significant reduction of the cubic magnetocrystalline anisotropy constant $|K_1^{\mathrm{eff}}|$. K_1^{eff} changes its sign and saturates near the stoichiometric composition. Due to the dominating uniaxial magnetic anisotropy component, the easy axis of magnetization in total is shifted to the [110] direction. The magnetic moment of the stoichiometric Co_2FeSi films is relatively close to the theoretically expected integer value of 6 (μ_B/fu), suggesting that Co_2FeSi could be a half-metallic ferromagnet. These results make this material promising for spintronics applications.

Acknowledgments

This work was partly supported by the German BMBF under the research programme NanoQUIT (contract no 01BM463). The authors would like to thank L Pérez for useful discussions and for a careful reading of the manuscript.

References

[1] Palmstrøm C 2003 *Mater. Res. Soc. Bull.* **28** 725
[2] de Groot R, Mueller F, van Engen P and Buschow K 1983 *Phys. Rev. Lett.* **50** 2024
[3] Fujii S, Sugimura S, Ishida S and Asano S 1990 *J. Phys.: Condens. Matter* **2** 8583
[4] Ishida S, Fujii S, Kashiwagi S and Asano S 1995 *J. Phys. Soc. Japan* **654** 2152
[5] Galanakis I, Dederichs P H and Papanikolau N 2002 *Phys. Rev.* B **66** 174429
[6] Herfort J, Schönherr H-P and Ploog K H 2003 *Appl. Phys. Lett.* **83** 3912
Herfort J, Jenichen B, Kaganer V, Trampert A, Schönherr H-P and Ploog K H 2006 *Physica* E **32** 371
[7] Hashimoto M, Herfort J, Trampert A, Schönherr H-P and Ploog K H 2006 *J. Vac. Sci. Technol.* B at press
[8] Webster P J and Ziebeck K R A 1988 *Landolt–Börnstein New Series III/19c* (Berlin: Springer) p 75
[9] Niculescu V, Budnick J I, Hines W A, Raj K, Pickart S and Skalski S 1979 *Phys. Rev.* B **19** 452
[10] Wurmehl S, Fecher G H, Kandpal H C, Ksenofontov V, Felser C, Lin H-J and Morais J 2005 *Phys. Rev.* B **72** 184434
[11] Nishizawa T and Ishida K 1984 *Bull. Alloy Phase Diagrams* **5** 250
[12] Hearmon R F S 1979 *Landolt–Börnstein New Series III/11* (Berlin: Springer) p 12
[13] Schönherr H-P, Nötzel R, Ma W and Ploog K H 2001 *J. Appl. Phys.* **89** 169
[14] Hashimoto M, Herfort J, Schönherr H-P and Ploog K H 2005 *Appl. Phys. Lett.* **87** 102506
[15] Hashimoto M, Herfort J, Schönherr H-P and Ploog K H 2005 *J. Appl. Phys.* **98** 104902
[16] Krebs J J, Jonker B T and Prinz G A 1987 *J. Appl. Phys.* **61** 2596
[17] Kneedler E M, Jonker B T, Thibado P M, Wagner R J, Shanabrook B V and Whitman L J 1997 *Phys. Rev.* B **56** 8163
[18] Reiger E, Reinwald E, Garreau G, Ernst M, Zölfl M, Bensch F, Bauer S, Preis H and Bayreuther G 2000 *J. Appl. Phys.* **87** 5923
[19] Dumm M, Zölfl M, Moosbühler R, Brockmann M, Schmidt T and Bayreuther G 2000 *J. Appl. Phys.* **87** 5457
[20] Sjöstedt E, Nordström L, Gustavsson F and Eriksson O 2002 *Phys. Rev. Lett.* **89** 267203
[21] Bardos D I 1969 *J. Appl. Phys.* **40** 1371
[22] Daboo C, Hicken R J, Gu E, Gester M, Gray S J, Eley D E P, Ahmad E, Bland J A C, Ploessl R and Chapman J N 1995 *Phys. Rev.* B **51** 15964
[23] Yang F, Shang C H, Chien C L, Ambrose T, Krebs J J, Prinz G A, Nikitenko V I, Gornakov V S, Shapiro A J and Shull R D 2002 *Phys. Rev.* B **65** 174410

Growth temperature dependent evolution of the interface structure in Co_2FeSi/GaAs(001) hybrid structures

M. Hashimoto,[a] J. Herfort,[b] A. Trampert, H.-P. Schönherr, and K. H. Ploog
Paul-Drude-Institut für Festkörperelektronik, Hausvogteiplatz 5-7, 10117 Berlin, Germany

(Received 26 January 2006; accepted 20 April 2006; published 25 July 2006)

The growth temperature dependence of the interface perfection of full Heusler alloy Co_2FeSi/GaAs(001) hybrid structures have been examined using transmission electron microscopy (TEM) and high-resolution x-ray diffraction (HRXRD). The film grown at 100 °C shows an atomically abrupt interface without interfacial reaction. In the high-resolution transmission electron microscope (HRTEM) image from the 200 °C film, however, a 1–2 ML (monolayer) interlayer having a contrast different from both Co_2FeSi and GaAs was observed at the interface, indicating that interfacial reaction starts at this growth temperature. The layer grown at 350 °C shows a further reacted interface in the HRTEM image, i.e., undulations and large steps at the interface. The interface perfection strongly correlates with the in-plane uniaxial magnetic anisotropy (UMA) as the UMA constant rapidly decreases above 200 °C in accordance with the progress of the interfacial reaction. © *2006 American Vacuum Society.* [DOI: 10.1116/1.2218863]

I. INTRODUCTION

Heusler alloys are promising candidates as a source for electrical spin injection into semiconductors at room temperature, because of their high Curie temperature and close lattice matching with semiconductors.[1] In addition, a number of Heusler alloys are predicted to be half-metallic by theoretical studies, i.e., they are expected to be 100% spin polarized at the Fermi level.[2–5] It is believed that the spin injection efficiency depends on the interface perfection of the ferromagnet/semiconductor (FM/SC) hybrid structures. The growth of a FM layer on SC substrates at high growth temperature generally leads to the formation of magnetically modified interfacial compounds which could reduce the spin polarization of injected carriers. Therefore, a thermally stable FM/SC interface is highly desirable for efficient electrical spin injection. Besides, it was suggested for Heusler alloys that half-metallicity is guaranteed only for certain combinations of atomic termination at the Heusler/SC interface.[6,7] Therefore, a comprehensive understanding of Heusler alloy/SC interface structures is of crucial importance for the realization of effective electrical spin injection. However, little information is available so far regarding the detailed microstructure of the interface depending on the growth temperature and the thermal stability of Heuser/SC hybrid structures.

Co_2FeSi is a member of full-Heusler alloys with the cubic $L2_1$ crystal structure consisting of four interpenetrating fcc sublattices.[8] The lattice constant of bulk Co_2FeSi is 5.658 Å,[9] closely lattice matched to GaAs (a_{GaAs}=5.653 Å). The lattice mismatch is as small as 0.08%. Bulk Co_2FeSi with a large magnetic moment ($5.91\mu_B$ at 10.2 K) is ferromagnetic up to more than 980 K,[9] which is one of the highest Curie temperatures among the reported Heusler alloys. According to electronic structure calculations based on the local density approximation (LDA), Co_2FeSi is located at a position slightly deviating from the Slater-Pauling curve which half-metallic Heusler alloys are expected to obey.[5] On the other hand, recent calculations based on LDA+U, which take into account the electron correlation effect, have revealed that Co_2FeSi can have an integer magnetic moment ($6\mu_B$/f.u.), suggesting that it should be a half-metallic ferromagnet.[10] In our previous studies, we have shown that Co_2FeSi/GaAs(001) hybrid structures with $L2_1$ atomic ordering and interface perfection can be achieved in the growth temperature range around 200 °C by molecular beam epitaxy (MBE).[11,12] In this report, we examine in detail the interface perfection of Co_2FeSi/GaAs(001) hybrid structures depending on the growth temperature.

II. EXPERIMENT

The Co_2FeSi layers were grown on GaAs(001) substrates by MBE. Before the growth of the Co_2FeSi layers, 100-nm-thick GaAs templates were prepared in the III-V growth chamber using standard GaAs growth conditions. As-terminated $c(4\times4)$ reconstructed GaAs(001) surfaces were prepared by cooling the samples down to 420 °C under As_4 pressure to prevent the formation of macroscopic defects on the surface similar to our studies on Fe/GaAs(001).[13] The samples were then transferred to the As-free deposition chamber under UHV at a base pressure of 5×10^{-10} Torr. The growth temperature T_G for the Co_2FeSi layers was varied in the range of 100–400 °C. A low growth rate of about 0.1 nm/min was chosen in order to avoid the degradation of the crystal quality at these low growth temperatures. The thickness of the layers d was determined by high-resolution x-ray diffraction (HRXRD) and x-ray reflectivity (XRR) measurements to be 18.5 nm. The growth was *in situ* monitored using reflection high-energy electron diffraction (RHEED). The RHEED pattern of the Co_2FeSi layer is rather

[a]Electronic mail: hashimoto@pdi-berlin.de
[b]Electronic mail: herfort@pdi-berlin.de

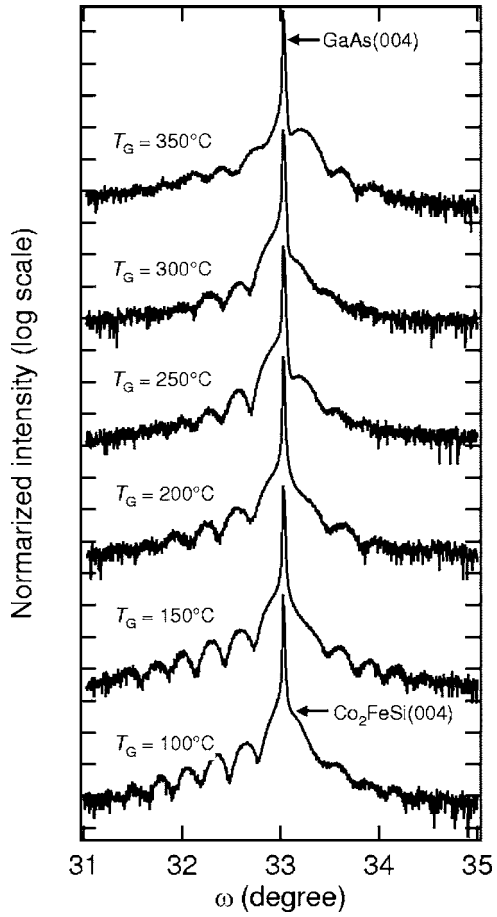

FIG. 1. HRXRD ω-2θ curves of the $Co_2FeSi(004)$ reflection of stoichiometric Co_2FeSi grown at different growth temperatures between 100 and 350 °C. The curves are shifted for clarity.

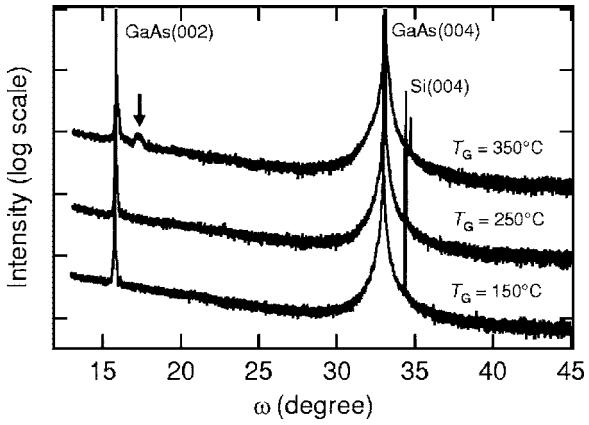

FIG. 2. Wide-range XRD ω-2θ curves taken with a wide-open detector of the films grown at T_G=150, 250, and 350 °C. The sharp peaks at ω =34.56° are originated from the Si(004) reflection from the sample holder. An additional peak appeared in the curve of 350 °C film as indicated by an arrow.

spotty at low T_G. The pattern gradually changes to sharp streaks with Kikuchi lines and a Laue circle with increasing T_G, indicating a two-dimensional growth mode and a well-ordered single-crystal surface. After deposition of about 1–2 ML (monolayer) of the Co_2FeSi layer, a pattern with elongated streak emerges. The pattern subsequently changes to sharp streaks during the deposition of about 3–6 ML of the Co_2FeSi layer. This pattern is then maintained throughout the further growth. Details of the growth and structural characterizations including the determination of the stoichiometric composition are described elsewhere.[11,12]

The structural characterization of the Co_2FeSi/GaAs(001) interface was performed by HRXRD and cross-sectional transmission electron microscopy (TEM). The HRXRD ω-2θ curves were taken after growth with a Panalytical X'pert diffractometer using Cu $K\alpha$ radiation with a Ge(220) monochrometer and a triple-bounce analyzer crystal. Thin specimens for TEM were prepared in cross-sectional configuration along both the [110] and the orthogonal [1$\bar{1}$0] direction. After mechanical grinding, Ar-ion milling was applied to achieve electron transparency with thinning conditions of 2.5–2.7 keV beam energy and a beam incident angle of 2.5°–3° in order to minimize surface damage. A JEM-3010 microscope was used for the conventional TEM as well as the high-resolution (HR) TEM analysis (point resolution: 0.17 nm). The images were acquired in real time with a TV rate or a 1000×1000 slow-scan charge-coupled device (CCD) camera and transferred into a computer for storage and further image processing.

The magnetic properties of the Co_2FeSi films were investigated using a Quantum Design superconducting quantum interference device (SQUID) magnetometer. All the measurements were performed at room temperature and the external magnetic field was applied along three different in-plane crystallographic axes, [110], [1$\bar{1}$0], and [100]. After subtracting the diamagnetic contribution of the GaAs substrate, the magnetizations were normalized to the saturation magnetization (M_s) of each direction.

III. RESULTS AND DISCUSSION

Figure 1 shows the results of HRXRD ω-2θ scans around the $Co_2FeSi(004)$ reflection of stoichiometric Co_2FeSi films grown at different growth temperatures between 100 and 350 °C. The large numbers of interference (Pendellösung) fringes up to the fifth order in the low growth temperature films are an indication of a high crystal quality and interface perfection as well as a smooth surface. The interference fringes become gradually less pronounced with increasing growth temperature as seen in Fig. 1. This is due to a degradation of the well-defined interface of the Co_2FeSi/GaAs structure caused by interfacial reaction. The reduction of the interference fringes can be observed around T_G=200 −250 °C. This suggests that the reaction temperature of Co_2FeSi/GaAs hybrid structures is around 200−250 °C. A further interface degradation is seen at T_G=350 °C, where the main $Co_2FeSi(004)$ peak is broadened and shifted to larger angle.

The interfacial reaction was clearly evidenced by wide-range ω-2θ scans with a wide-open detector for the same series of films. Figure 2 shows wide-range ω-2θ curves of the films grown at several T_G. The sharp peaks at ω

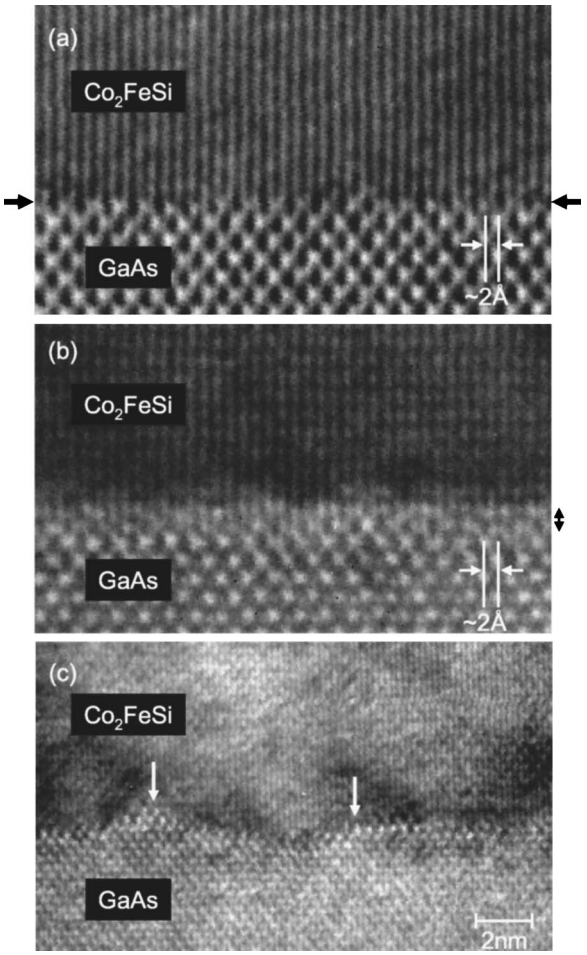

FIG. 3. Cross-sectional HRTEM images along the [110] zone axis of Co_2FeSi/GaAs films grown at (a) 100 °C, (b) 200 °C, and (c) 350 °C. A lower magnification image is shown for the 350 °C film for a better perspective of the reacted regions. The lattice spacing of GaAs $d\{220\} \approx 2$ Å is indicated for scaling.

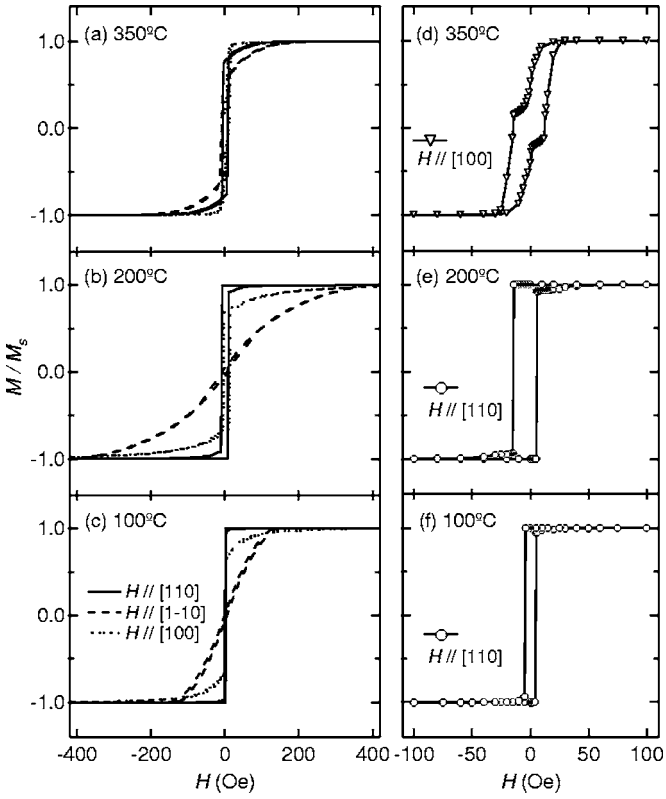

FIG. 4. Normalized magnetization curves of the Co_2FeSi grown at [(a) and (d)] 350 °C, [(b) and (e)] 200 °C, and [(c) and (f)] 100 °C taken at room temperature. The external magnetic field was applied along three different crystallographic axes, [110], [1$\bar{1}$0], and [100]. The right panel [(d)–(f)] shows the magnetization curves along the easy axis, [110] for $T_G < 200$ °C and [100] for $T_G = 350$ °C, in an expanded scale. The diamagnetic contribution of the substrate has been subtracted.

$= 34.56°$ originate from the Si(004) reflection of the sample holder. No peaks were detected for the films with $T_G \leqslant 300$ °C other than the GaAs(002) and (004) substrate peaks which overlap with the Co_2FeSi(002) and (004) peaks, respectively. On the other hand, an additional peak was observed for the films grown at 350 °C at $\omega = 17.3°$ as indicated by an arrow in Fig. 2. This peak can be attributed to either CoAs(111) or tetragonal $(Fe_{1-x}Co_x)_2As(110)$ $(0 < x < 0.3)$ reflections[14,15] formed at the Co_2FeSi/GaAs interface. Note that $(Fe_{1-x}Co_x)_2As$ crystallizes in the tetragonal Cu_2Sb-type structure in the limited composition regime $0 < x < 0.3$.[16] The crystal structure changes to hexagonal in the intermediate-to-high Co composition regime $0.38 < x < 0.99$.[15]

Since XRD characterizations generally have the disadvantage of being not sensitive to detect nanometer-size interfacial compounds or grains, more careful examinations of the interface perfection were performed using TEM. Figure 3 shows cross-sectional HRTEM (phase contrast) images along the [110] zone axis of the Co_2FeSi films grown at (a) 100, (b) 200, and (c) 350 °C. We show a lower magnification image for the 350 °C film to give a better perspective of the reacted regions. As can be seen in Fig. 3, the interface of the 100 °C film is atomically abrupt as expected from the HRXRD results. The distinct difference in the interference pattern between Co_2FeSi and GaAs allows us to determine accurately the position of the interface. We observe a perfect matching of the Co_2FeSi(220) and GaAs(220) atomic planes across the interface, i.e., the layer is coherently strained. However, for the 200 °C film we observe a modified layer of 1–2 ML which has similar lattice fringes to that of Co_2FeSi but a different contrast from either GaAs or Co_2FeSi. This can be attributed to a modification of the interface structure, indicating that an interfacial reaction starts around 200 °C. However, a simulation of the Co_2FeSi/GaAs interface contrast is required to get further insight into the real interface structure at this T_G. The HRTEM image of the 350 °C film reveals a further progress of the interfacial reaction. The interface structure of the 350 °C film shows undulations and large steps at the interface as indicated by white arrows due to the enhanced mobility of the diffusing atoms. We consider from the interference fringes in the HRXRD curves that the 150 °C film has a comparable interface perfection to that of the 100 °C film. Therefore, the reaction temperature of the Co_2FeSi/GaAs(001) interface is estimated to be around

200 °C. This is significantly higher than that of Fe and Co grown on GaAs, for which reaction temperatures of 95 and −10 °C, respectively, were reported.[17,18] Our results, therefore, suggest that Co_2FeSi has an advantage over these conventional ferromagnets as a FM contact with respect to the thermal stability of the interface.

In the following paragraph, we discuss the influence of the interfacial reaction on the magnetic properties. The details of the analysis were described elsewhere.[12] The normalized magnetization curves of Co_2FeSi films grown at different temperatures are shown in Fig. 4(a) T_G=350 °C, (b) 200 °C, and (c) 100 °C. The magnetization curves along the easy axis direction are also shown in an expanded scale in the right panel. All the examined Co_2FeSi films are ferromagnetic at room temperature.

We observed a drastic change of the magnetization curves at T_G=350 °C. The magnetization curves for $T_G \leqslant 300$ °C show square-shaped hysteresis loops and a strongly anisotropic angle dependence. The magnetization curves of $T_G \leqslant 300$ °C consist of an easy axis [110], a hard axis $[1\bar{1}0]$, and an intermediate axis [100]. The easy axis along the [110] direction is caused by the dominating in-plane uniaxial magnetic anisotropy (UMA) component which has an easy axis different from that of the cubic magnetocrystalline anisotropy component (⟨100⟩ directions). The well-defined square-shaped hysteresis loop along the [110] direction with a small coercive field of 4.5 Oe (T_G=100 °C) confirms the excellent crystalline quality of the films.

The magnetization curve of the T_G=350 °C film, on the other hand, shows a much smaller anisotropic angle dependence. This is due to the disappearance of the dominating in-plane UMA component. As a result, the in-plane magnetic anisotropy consists of only a weak cubic magnetocrystalline component. The easy axis in total is consequently converted to the easy axis of the cubic magnetocrystalline component: the ⟨100⟩ directions. Note that the double steplike loop of the easy axis of the T_G=350 °C sample seen in Fig. 4(d) originates from a slight deviation of the easy axis from the ⟨100⟩ directions due to the remaining slight uniaxial component.

The in-plane magnetic anisotropy of Co_2FeSi was analyzed further by assuming two in-plane magnetic anisotropy components, an UMA term and a cubic magnetocrystalline anisotropy term as in the case of other *c*-FM/zinc-blende (Z.B.)-SC systems.[19,20] The two effective magnetic anisotropy constants K_1^{eff} and K_u^{eff} for the cubic magnetocrystalline and UMA components, respectively, were obtained by fitting the reversible magnetization curves along the $[1\bar{1}0]$ direction with the following expression:

$$H(m) = 2K_1^{\text{eff}}(2m^3 - m)/M_s + 2K_u^{\text{eff}}m/M_s, \quad (1)$$

where m is the normalized magnetization component.[20] The in-plane UMA constant K_u^{eff} of Co_2FeSi is plotted as a function of T_G in Fig. 5(a). The UMA component is a pure-interface related term as it shows the linear dependence on the inverse film thickness.[12] Moreover, the UMA in *c*-FM/Z.B.-SC systems is attributed to an anisotropic bonding at the FM/SC interface.[21] Therefore, one can presume

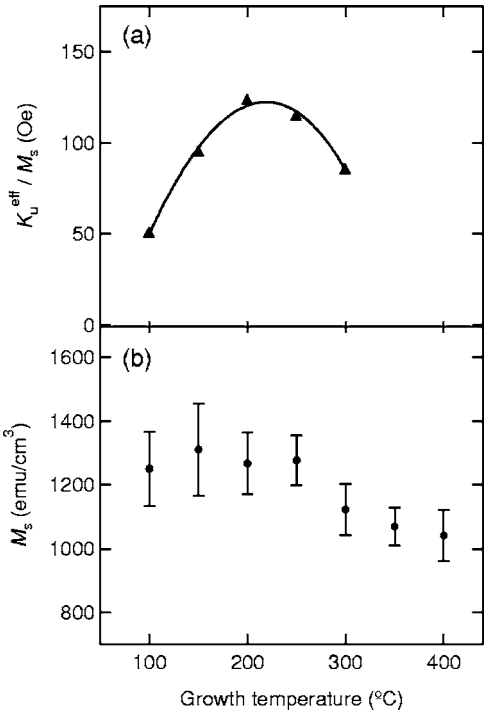

FIG. 5. Growth temperature dependence of (a) uniaxial magnetic anisotropy constant K_u^{eff} normalized to M_s and (b) saturation magnetization M_s of Co_2FeSi/GaAs(001). The solid line is a guide for the eye. K_u^{eff} almost disappears at 350 °C.

that the formation of interface compounds and/or a modification of the interface structure results in a reduction of UMA. As can be seen in Fig. 5(a), the in-plane magnetic anisotropy significantly increases with elevating T_G from 100 to 200 °C as the atomic ordering of the Co_2FeSi layer develops. The K_u^{eff} has a maximum around T_G=200 °C, indicating that the Co_2FeSi/GaAs interface grown at 200 °C is expected to be the most abrupt and atomically ordered. This is almost consistent with the TEM observation where only subtle change was detected at this T_G. The reduction of K_u^{eff} above T_G=200 °C is in agreement with the presence of interfacial reactions as clearly evidenced by both HRXRD and TEM. The K_u^{eff} component finally almost disappears at 350 °C as seen in the magnetization curves [Fig. 4(a)], in accordance with the further degraded interface occurring at this T_G, i.e., the formation of an interfacial compound confirmed in the wide-range ω-2θ curves as well as in the interface undulations observed in HRTEM studies. These results clearly demonstrate a strong correlation between in-plane UMA and interface perfection.

The saturation magnetization of Co_2FeSi decreases for $T_G > 250$ °C as can be seen in Fig. 5(b). Both of the interface compounds expected from the HRXRD results are not ferromagnetic, namely, CoAs is paramagnetic[22] and $(Fe_{1-x}Co_x)_2As$ (x=0) is antiferromagnetic with a Néel temperature T_N of 353 K (Ref. 16) with T_N decreasing when the Co composition increases in the range of $0 < x < 0.3$.[15] Note that the hexagonal $(Fe_{1-x}Co_x)_2As$ ($0.38 < x < 0.99$) is ferromagnetic with Curie temperatures of 320 K (x=0.4) and

260 K ($x=0.6$), but with much smaller magnetic moments ($2.4\mu_B$/f.u. and $1.7\mu_B$/f.u. for $x=0.4$ and 0.6, respectively).[23] It is, therefore, very likely that the formation of this compound at the Co_2FeSi/GaAs interface causes a gradual reduction of M_s with increasing T_G. The formation of magnetically modified compounds at the interface can be detrimental to electrical spin injection into SC layer. Note that M_s for the films grown below 250 °C is relatively close to that of bulk Co_2FeSi [1124 emu/cm^3 at 295 K (Ref. 9)].

IV. CONCLUSIONS

We have studied the growth temperature dependence of the interface perfection of Co_2FeSi/GaAs(001) hybrid structures and its influences on the in-plane uniaxial magnetic anisotropy (UMA). The low growth temperature film has an atomically abrupt interface as evidenced by HRTEM and HRXRD. A modified layer of 1–2 ML was detected for the 200 °C film in the HRTEM image, indicating that the interfacial reaction starts around $T_G=200$ °C. The 350 °C film shows an undulation and large steps at the interface in the HRTEM images as well as an additional peak [probably from CoAs or $(Fe_{1-x}Co_x)_2As$] in the HRXRD ω-2θ curve. The in-plane UMA is strongly correlated with the interface perfection. It has a maximum around 200 °C and decreases in accordance with the progress of the interfacial reaction. Our results suggest that the Heusler-alloy Co_2FeSi has a considerable advantage as a ferromagnetic contact over conventional elemental ferromagnets in its thermal stability of the interface.

ACKNOWLEDGMENTS

This work was partly supported by the German BMBF under the research program NanoQUIT (Contract No. 01BM463). The authors would like to thank P. K. Muduli for useful discussions and L. Däweritz for a careful reading of the manuscript.

[1]C. Palmstrøm, MRS Bull. **28**, 725 (2003).
[2]R. de Groot, F. Mueller, P. van Engen, and K. Buschow, Phys. Rev. Lett. **50**, 2024 (1983).
[3]S. Fujii, S. Sugimura, S. Ishida, and S. Asano, J. Phys.: Condens. Matter **2**, 8583 (1990).
[4]S. Ishida, S. Fujii, S. Kashiwagi, and S. Asano, J. Phys. Soc. Jpn. **64**, 2152 (1995).
[5]I. Galanakis, P. H. Dederichs, and N. Papanikolau, Phys. Rev. B **66**, 174429 (2002).
[6]S. Picozzi, A. Continenza, and A. J. Freeman, J. Phys. Chem. Solids **64**, 1697 (2003).
[7]I. Galanakis, J. Phys.: Condens. Matter **16**, 8007 (2004).
[8]P. J. Webster and K. R. A. Ziebeck, Landolt-Börnstein, New Series, Vol. III, Pt. 19c (Springer, Berlin, 1988), p. 75.
[9]V. Niculescu, J. I. Budnick, W. A. Hines, K. Raj, S. Pickart, and S. Skalski, Phys. Rev. B **19**, 452 (1979).
[10]S. Wurmehl, G. H. Fecher, H. C. Kandpal, V. Ksenofontov, C. Felser, H.-J. Lin, and J. Morais, Phys. Rev. B **72**, 184434 (2005).
[11]M. Hashimoto, J. Herfort, H.-P. Schönherr, and K. H. Ploog, Appl. Phys. Lett. **87**, 102506 (2005).
[12]M. Hashimoto, J. Herfort, H.-P. Schönherr, and K. H. Ploog, J. Appl. Phys. **98**, 104902 (2005).
[13]H.-P. Schönherr, R. Nötzel, W. Ma, and K. H. Ploog, J. Appl. Phys. **89**, 169 (2001).
[14]For the crystal structure of CoAs, see R. W. G. Wyckoff, *Crystal Structures* (Wiley, New York, 1963), Vol. 1.
[15]P. Önnerud, Y. Andersson, R. Tellgren, T. Ericsson, P. Nordblad, A. Krishnamurthy, and B. K. Srivastava, J. Magn. Magn. Mater. **147**, 346 (1995).
[16]H. Katsuraki and N. Achiwa, J. Phys. Soc. Jpn. **21**, 2238 (1966).
[17]B. D. Schultz, H. H. Farrell, M. M. R. Evans, K. Lüdge, and C. J. Palmstrøm, J. Vac. Sci. Technol. B **20**, 1600 (2002).
[18]K. Lüdge, B. D. Schultz, P. Vogt, M. M. R. Evans, W. Braun, C. J. Palmstrøm, W. Richter, and N. Esser, J. Vac. Sci. Technol. B **20**, 1591 (2002).
[19]E. Reiger *et al.*, J. Appl. Phys. **87**, 5923 (2000).
[20]M. Dumm, M. Zölfl, R. Moosbühler, M. Brockmann, T. Schmidt, and G. Bayreuther, J. Appl. Phys. **87**, 5457 (2000).
[21]E. Sjöstedt, L. Nordström, F. Gustavsson, and O. Eriksson, Phys. Rev. Lett. **89**, 267203 (2002).
[22]K. Adachi and S. Ogawa, Landolt-Börnstein, New Series, Vol. III, Pt. 27a (Springer-Verlag, Berlin, 1988).
[23]P. Önnerud, Y. Andersson, R. Tellgren, and P. Nordblad, Solid State Commun. **101**, 271 (1997).

INSTITUTE OF PHYSICS PUBLISHING JOURNAL OF PHYSICS: CONDENSED MATTER

J. Phys.: Condens. Matter **18** (2006) 9453–9462 doi:10.1088/0953-8984/18/41/012

Investigation of magnetic anisotropy and magnetization reversal by planar Hall effect in Fe_3Si and Fe films grown on GaAs(113)A substrates

P K Muduli[1], K-J Friedland, J Herfort, H-P Schönherr and K H Ploog

Paul-Drude-Institut für Festkörperelektronik, Hausvogteiplatz 5-7, D-10117 Berlin, Germany

E-mail: pranabmuduli@gmail.com

Received 1 August 2006, in final form 12 September 2006
Published 29 September 2006
Online at stacks.iop.org/JPhysCM/18/9453

Abstract

Magnetic anisotropy and magnetization reversal in Fe_3Si and Fe films grown on GaAs(113)A substrates are studied using the planar Hall effect (PHE). The PHE in this orientation exhibits an antisymmetric component in addition to the usual symmetric component. The relative magnitude of symmetric and antisymmetric components in the PHE is affected by the composition of the Fe_3Si films and the thickness of the Fe films, which lead to a complex behaviour of the planar Hall resistivity in the low magnetic field region below saturation. However, irrespective of the composition/thickness of the films, magnetization reversal can be described qualitatively within a single domain by the simple Stoner–Wolfarth model of magnetization reversal. This allows us to determine the magnetic anisotropy properties of these films in good agreement with the experimental results of anisotropic magnetoresistance and superconducting quantum interference device magnetometry.

(Some figures in this article are in colour only in the electronic version)

1. Introduction

An understanding of the magnetic anisotropy in epitaxial films is crucial to engineer the magnetic properties. Recently, the planar Hall effect (PHE) has emerged as a popular tool for studying magnetic anisotropy and magnetization reversal in ferromagnetic thin films grown on semiconducting substrates [1–4], which are promising for spintronics applications. PHE refers to the resulting electric field developed perpendicular to the current direction and which lies in the plane of the current and magnetic field. In fact, PHE and other magnetotransport effects, such as anisotropic magnetoresistance and the anomalous Hall effect, are very sensitive tools for studying magnetic anisotropy and magnetization reversal in these low-dimensional magnetic

[1] Present address: Department of Physics and Astronomy, University of North Carolina, Chapel Hill, NC 27599-3255, USA.

structures, particularly because of their relative insensitivity to the semiconducting or insulating substrate. For thin films, it is difficult to subtract the magnetic contribution of the substrate in traditional magnetometry techniques like vibrating sample magnetometry or superconducting quantum interference device (SQUID) magnetometry. In magnetotransport measurements, only the metallic portion (or the film portion) of the sample is measured. In our previous works, we reported these magnetotransport effects from epitaxial Fe [5, 3] and Fe_3Si [6] films on a high-index substrate, namely GaAs(113)A. The unique orientation used in these studies has a low surface symmetry and results in an additional antisymmetric component in the PHE [6]. The antisymmetric component manifests itself as a change in sign of the PHE when the direction of the in-plane applied saturated magnetic field is reversed, and is a unique observation of a second-order Hall effect. In [6], the behaviour of PHE for Fe_3Si on GaAs(113)A was discussed as a function of composition and temperature. However, the discussion was restricted to high magnetic fields above saturation. In this paper we will concentrate on the low magnetic field behaviour of PHE below saturation and use it to determine the magnetic anisotropy of these high-index orientation films. We will discuss the magnetization reversal in the Fe_3Si films over a range of compositions and also extend the study to Fe films of different thicknesses. The room-temperature values of the phenomenological coefficients of the PHE and their behaviour with composition of Fe_3Si and thickness of Fe films will also be discussed. It should be mentioned that both Fe and Fe_3Si are ferromagnetic at room temperature and have a close lattice match with GaAs. Thus, these are highly promising material systems for spintronics applications.

2. Experiment

The high-quality Fe_3Si and Fe films used in this work were grown on GaAs(113)A substrates by molecular-beam epitaxy [7, 8]. Fe_3Si films were grown at a growth temperature of 250 °C, whereas the Fe films were grown at a relatively low growth temperature of 0 °C. Films grown under these conditions exhibit a high crystal quality and a smooth interface/surface, keeping the same orientation of the substrate. The phase boundary of the stable Fe_3Si phase covers a range from 9 to 26.6 at.% Si [9, 10]. This offers the advantage of varying the composition, and hence the magnetic properties in these films, while maintaining the cubic crystal structure. In [7], we demonstrated the growth and stability of $Fe_{3+x}Si_{1-x}$ films on GaAs(113)A substrates over a range of compositions of $0.4 > x > -0.06$, where x denotes the deviation from stoichiometry. These high-quality films are used in the present study of the PHE. For the PHE measurements, the layers were lithographically patterned into Hall bars 30 μm in width and with a 22.5 μm separation between the voltage leads for electrical transport measurements. The behaviour of the PHE for two different kinds of measurements will be discussed. First, the in-plane field orientation is kept fixed along a specific direction with respect to the longitudinal axis of the Hall bars, while the field magnitude is swept linearly. Second, we studied the angular dependence of the PHE response when a fixed in-plane magnetic field was applied. As the low transverse Hall resistivity, ρ_{xy}, is smaller than the longitudinal resistivity, ρ_{xx}, some crossover from ρ_{xx} to ρ_{xy} may appear. In this case, we have corrected ρ_{xy} by $\rho_{xy}^{\mathrm{corr}}(H, \theta_{\mathrm{H}}) = \rho_{xy}(H, \theta_{\mathrm{H}}) - \gamma\, \rho_{xx}(H, \theta_{\mathrm{H}})$, where the factor γ was kept constant for a particular contact configuration. All measurements shown in this work will be restricted to room temperature for simplicity.

3. Results

In figure 1, we show the magnetic field dependence of planar Hall resistivity ρ_{xy} in $Fe_{3+x}Si_{1-x}$ films grown on GaAs(113)A substrates for two different compositions, $x = 0.15$ and 0.07. The

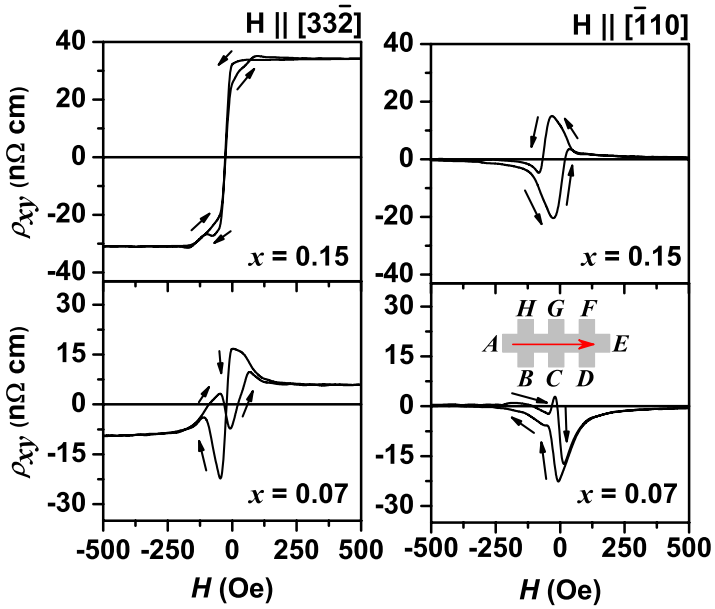

Figure 1. Field dependence of the PHE (ρ_{xy}) from $Fe_{3+x}Si_{1-x}$(113) films at 300 K. The first (second) column is for a magnetic field applied parallel to the major in-plane [33$\bar{2}$] ([$\bar{1}$10]) axis, whereas the first (second) row is for a $Fe_{3+x}Si_{1-x}$ layer with $x = 0.15$ ($x = 0.07$). The inset on the lower right plot shows a schematic of the contacts and geometry of the PHE measurements, with the arrow showing the current direction along [33$\bar{2}$].

planar Hall resistivities are shown for a magnetic field parallel to the two major in-plane [33$\bar{2}$] and [$\bar{1}$10] axes, which are perpendicular to each other. The measurement geometry is similar to [6]. The current was applied along the contacts AE and the PHE (ρ_{xy}) was measured along the contacts such as BH in a counterclockwise sense, as shown in the inset of figure 1. The current direction was made parallel to the [33$\bar{2}$] direction so that the PHE is measured along the [$\bar{1}$10] direction. The characteristic properties of ρ_{xy} in this figure can be understood from the following equation developed in [6] for [113]-oriented films:

$$\rho_{xy} = \rho_s^{\mathrm{PHE}} \sin 2\theta_M + \rho_{\mathrm{SATM}}^0 \cos\theta_M + \rho_{\mathrm{SATM}}^1 \cos^3\theta_M, \tag{1}$$

where $\rho_s^{\mathrm{PHE}} = (9C_1 + 2C_4)/22$, $\rho_{\mathrm{SATM}}^0 = 9(a_{12223} - a_{11123})/(11\sqrt{2})$, and $\rho_{\mathrm{SATM}}^1 = -42\sqrt{2}(a_{12223} - a_{11123})/121$. Here, the coefficients C_1 and C_4 relate to the symmetric component of the magnetoresistivity tensor, whereas the coefficients a_{12223} and a_{11123} relate to the antisymmetric component of the magnetoresistivity tensor. θ_M represents the direction of magnetization **M** with respect to the [33$\bar{2}$] direction. Let θ_H represents the applied magnetic field **H** with respect to the [33$\bar{2}$] direction. When a saturating field is applied along [33$\bar{2}$] (which represents a low-symmetry axis), $\theta_H = \theta_M = 0$, and the PHE in figure 1 exhibits a sign change when the direction of the applied field is reversed. Clearly, this is associated with the last two terms in equation (1), which originate from the antisymmetric component of the magnetorestivity tensors and are non-zero along this axis. When the saturating magnetic field is applied along [$\bar{1}$10], $\theta_H = \theta_M = 90^\circ$ and hence the antisymmetric components involving cosine terms vanish. In this case, the PHE is an even function of the applied magnetic field. In other words, only the first term in equation (1), which arises from the symmetric component of the magnetoresistivity tensor, contributes.

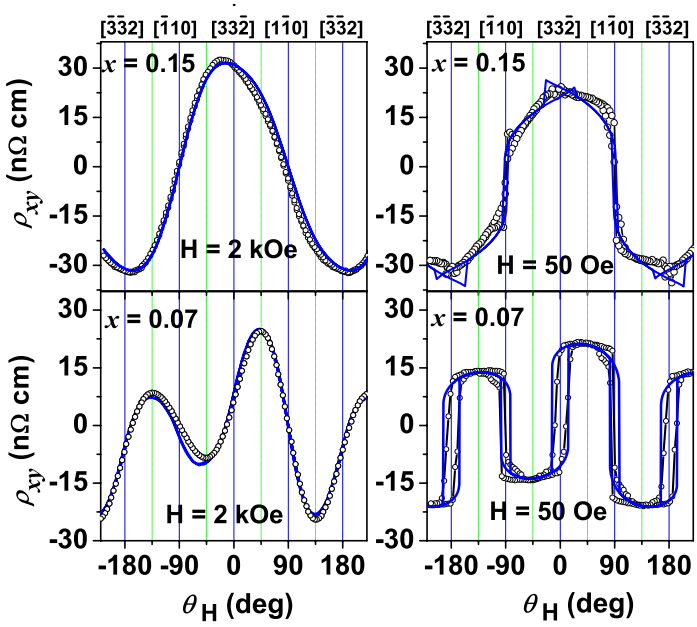

Figure 2. Experimental (symbols) and calculated (thick solid line) angular dependences of PHE (ρ_{xy}) for two $Fe_{3+x}Si_{1-x}$ samples with $x = 0.15$ (first row) and $x = 0.07$ (second row) at applied field strengths of $H = +2$ kOe (first column) and $H = +50$ Oe (second column). Here, $\theta_H = 0°$ corresponds to the $[33\bar{2}]$ direction, which is also the direction of the current.

At low magnetic field below saturation, the behaviour of the planar Hall resistivity for the two samples along the two directions differ significantly. In fact, at low magnetic field the magnetization is not saturated and hence $\theta_H \neq \theta_M$. Thus, the behaviour of the PHE is sensitive to the manner in which the magnetization rotates in-plane, which in turn is sensitive to the magnetic anisotropy and the mechanism of magnetization reversal. This is the focus of this paper. In figure 1, the arrows in the low magnetic field show the behaviour of the PHE as the direction of the field is reversed. Clearly, the behaviour is very different in both directions as well as for both samples. This seems to indicate a very different mechanism of magnetization reversal in all these cases. However, we will show that the resulting different behaviour is a consequence of the presence of an antisymmetric component which changes with the direction of the applied magnetic field and the composition of the films, and that the mechanism of the rotation of magnetization is similar in all these cases.

In order to completely understand the behaviour of the PHE in figure 1, first we calculate the amplitudes of the PHE in equation (1), namely ρ_s^{PHE}, ρ_{SATM}^0, and ρ_{SATM}^1 by using the high-field angular dependence of the PHE. The angular dependence of ρ_{xy} is shown in figure 2 at different applied magnetic fields. At high magnetic field, e.g. for $H = +2$ kOe, the magnetization is completely saturated and the PHE is completely reversible. From the fitting of this high-field behaviour (shown as a solid line) with equation (1), we determine the PHE amplitudes ρ_s^{PHE}, ρ_{SATM}^0, and ρ_{SATM}^1. By lowering the magnetic field, the magnetization deviates from the one imposed by the external magnetic field and ρ_{xy} exhibit jumps with hysteresis behaviour. The four-jumps in the low-field behaviour from 0° to 360° are interpreted as four hard axes, in other words the presence of a four-fold magnetic anisotropy [3]. However, the amplitude of the jumps as well as the width of the jumps along 0° (180°) is very different

compared to that along 90° (−90°). To understand these rather unusual PHE response curves in detail, we model the magnetic anisotropy of these films. It is known that the Fe films grown on GaAs(113)A substrates exhibit a combination of four-fold and a uniaxial magnetic anisotropy (UMA) [8, 11]. Since Fe_3Si also has a cubic structure, we consider a similar magnetic anisotropy for both systems. The in-plane magnetic anisotropy energy density, E_{IPMA}, for (113) surface symmetry can be obtained by using the symmetry of the (113) surface and taking into account the large demagnetization energy of these films, similarly to Fe/GaAs(113)A films [8]:

$$E_{\mathrm{IPMA}} = (K_1/484)[89 + 16\cos 2\theta_{\mathrm{M}} + 48\cos 4\theta_{\mathrm{M}}] + K_{\mathrm{u}}\sin^2(\theta_{\mathrm{M}}) - MH\cos\theta_{\mathrm{H}} \tag{2}$$

where K_1 and K_{u} are the cubic four-fold and uniaxial anisotropy constants, respectively. The magnetization **M** is assumed to lie in-plane, which is justified given the large demagnetization energy of these films. The first two terms in the above equation involving K_1 and K_{u} represent the four-fold and uniaxial magnetic anisotropy, respectively, whereas the last term represents the Zeeman energy. Using this anisotropy energy, we calculate the low-field PHE response of figures 1 and 2. The hysteresis behaviour of the sample is modelled using a single-domain model [12–15], where the magnetization is assumed to rotate coherently according to the Stoner–Wohlfarth (SW) model [16]. In this model, the magnetic anisotropy energy E_{IPMA} and the history of the applied field **H** determine the orientation of **M**, which changes the angle θ_{M} while maintaining the saturation magnitude M_{s}. At high field, **M** lies in a global minimum of E_{IPMA} at χ (H, θ_{H}). As the direction/magnitude of **H** is changed, **M** rotates to follow the locus of this energy minimum χ (H, θ_{H}). Magnetic switching occurs at the point where this minimum vanishes, when **M** jumps to the new neighbouring minimum. It is possible to determine wether the jumps observed in the data of figures 1 and 2 are determined by the SW model or not. In order to do this, we calculate the PHE response using the SW model. First, the angle of magnetization was derived by numerically tracking the evolution of the local minimum of the free energy in equation (2), and then equation (1) is used to find the PHE response. The final calculated PHE response curves are shown in the low-field behaviour of figure 2 as solid lines. We use K_1/M_{s} and the uniaxial ratio, $r = K_{\mathrm{u}}/K_1$, as fitting parameters. As can be seen, there is a very good qualitative agreement between the calculated and experimental curves. The amplitude and the width of the jumps in the PHE at 0° (180°) and 90° (−90°) are correctly reproduced. In fact, the larger width of the jumps in PHE at 0° compared to 90° imply that the $[33\bar{2}]$ axis, which represents 0°, is harder compared to the $[\bar{1}10]$ axis, indicating the presence of a UMA with an easy axis along $[\bar{1}10]$. At very low field, the calculated planar Hall resistivity deviates slightly from the experimental curve, since at such low field the rotation of magnetization is solely determined by the microscopic magnetic structure of the sample. This is the reason why the irreversible part does not agree with the SW model.

The field dependence of the PHE can also be calculated in a similar manner. In this case, we numerically track the minima in anisotropy energy as the field is swept and then use equation (1) to calculate the planar Hall resistivity. The calculations are shown in figure 3, which correspond to figure 1 and also show a very good qualitative agreement. The behaviour of the PHE as the direction of the field is reversed is also indicated by the arrows. They agree perfectly with the experimental data in figure 1. A small possible misalignment is also taken into account in the calculation. The result shows that the magnetization reversal in these films can be completely described within a single-domain picture in the light of the SW model. We found this agreement in all the $Fe_{3+x}Si_{1-x}(113)$ films that were studied for composition x between 0.39 and −0.04. The results are summarized in table 1, which shows a summary of different parameters found from the fitting of the PHE data. We also found the same agreement in Fe films of different thicknesses. In figure 4, we show an example of two Fe films with

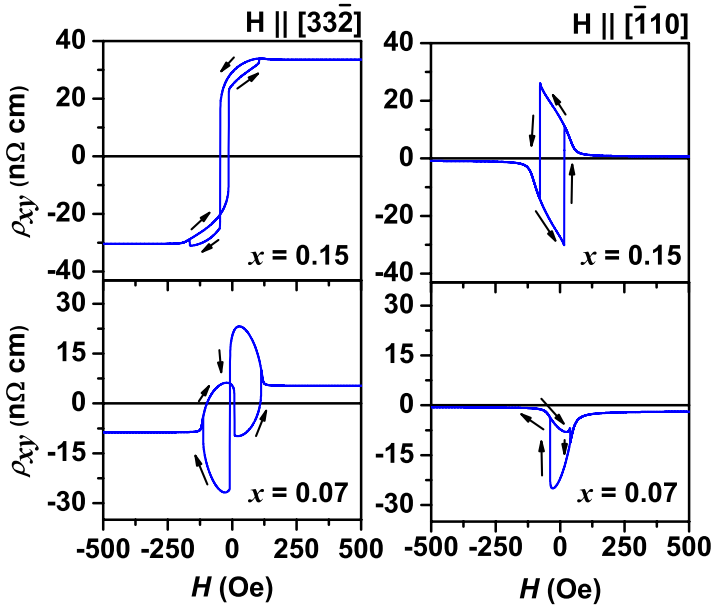

Figure 3. Calculated field dependence of the PHE (ρ_{xy}) from the $Fe_{3+x}Si_{1-x}$ (113) film. The first (second) column is for a magnetic field applied parallel to the major in-plane [33$\bar{2}$] ([$\bar{1}$10]) axis, whereas the first (second) row is for an $Fe_{3+x}Si_{1-x}$ layer with $x = 0.15$ ($x = 0.07$).

Table 1. Summary of data derived by the fitting of planar Hall resistivity of $Fe_{3+x}Si_{1-x}$ and Fe films on GaAs(113)A at 300 K. The magnetic properties such as K_1/M_s and $r = K_u/K_1$ are determined by fitting the low-field behaviour of the PHE. The PHE coefficients ρ^s_{PHE}, ρ^0_{SATM}, and ρ^1_{SATM} are derived by fitting the high-field behaviour of the PHE using equation (1).

Layer	Thickness (nm)	Composition, x	$r = K_u/K_1$	K_1/M_s (Oe)	ρ^s_{PHE} (nΩ cm)	ρ^0_{SATM} (nΩ cm)	ρ^1_{SATM} (nΩ cm)
$Fe_{3+x}Si_{1-x}$	40 ± 1	0.39	0.0	80 ± 5	−9.9	73.8	−14
$Fe_{3+x}Si_{1-x}$	41 ± 1	0.15	−0.3	60 ± 5	−2.7	38	−7
$Fe_{3+x}Si_{1-x}$	42 ± 1	0.07	−0.3	60 ± 5	16.5	16.4	−10
$Fe_{3+x}Si_{1-x}$	46 ± 5	0.05	−0.3	45 ± 5	30.6	2.1	−8.5
$Fe_{3+x}Si_{1-x}$	47 ± 3	0.03	0.0	50 ± 5	21.9	−4.4	−8.7
$Fe_{3+x}Si_{1-x}$	42 ± 5	−0.04	−0.85	50 ± 5	36	−23.5	−8.5
Fe	26	1	0.6	200 ± 20	−9.7	−15.7	8.5
Al/Fe	1.4	1	2.34	135	−7.1	8.2	−3.5

thicknesses of 26 and 1.4 nm. The 1.4 nm Fe film corresponds to only 10 monolayers (ML) of Fe and hence an Al capping layer (20 nm) was grown to prevent oxidation of the layer. The figure shows the angular dependence of the two films with in-plane magnetic fields of $H = +2$ and $+0.5$ kOe. The calculated curves shown as solid lines are obtained by using the SW model for magnetization rotation, as discussed before. Note that the 1.4 nm-thick sample is even reversible, though it is not completely saturated even at $H = +2$ kOe, hence the curve cannot be fitted using equation (1) alone. The best fit is obtained only by calculating ρ_{xy} using the SW model and equation (1), as explained above. The behaviours of the PHE in both films are qualitatively similar. However, the sign and magnitude of the different components are

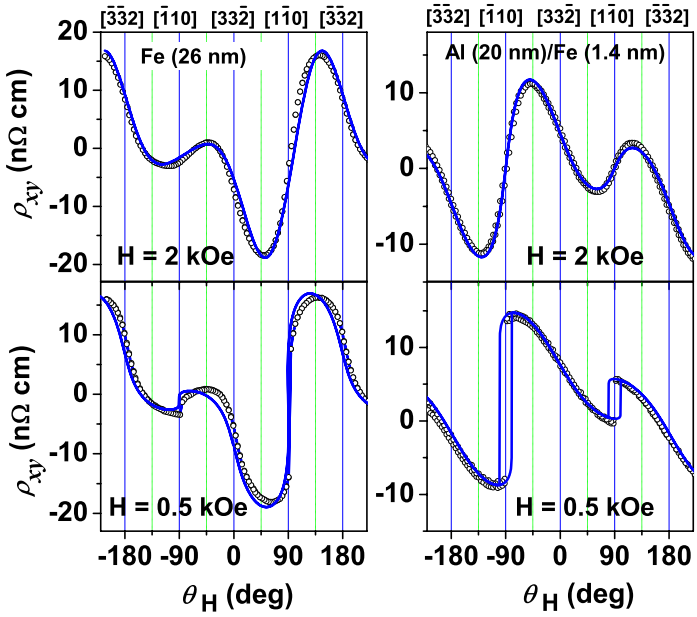

Figure 4. Experimental (symbols) and calculated (thick solid lines) angular dependence of ρ_{xy} (PHE) at magnetic fields of $H = +2$ kOe and $H = +0.5$ kOe for a 26 nm (first column) and a 1.4 nm Fe (second column) film measured at 300 K. Here, $\theta_H = 0°$ indicates the [33$\bar{2}$] direction, which is also the direction of the current. Note that the 1.4 nm Fe film is not completely saturated at $H = +2$ kOe.

different. As shown in figure 4 and table 1, the sign of ρ_{SATM} in the 1.4 nm-thick Fe film is opposite to that of the thicker films. The convention for the sign of ρ_{SATM} is defined in [6]. The opposite sign implies that the interface can play a significant role in determining the sign of the antisymmetric component. It is essential to mention that the PHE measurements of the films shown in figure 4 were performed on rectangular samples with a typical size of 2×4 mm^2. We have also compared the behaviour of the PHE on Hall bar structures with that of the large rectangular samples, in which case a small difference in the switching fields was observed. However, the shape of the PHE was found to be very similar, which indicates that the single-domain model is valid in a wide range of sample dimensions from several μm to several mm^2. The surprising validity of the single-domain model in both $Fe_{3+x}Si_{1-x}$ and Fe films was also observed in SQUID magnetometry [11] and *in situ* magneto-optic Kerr effect experiments [17]. However, consideration of multiple domains should provide more quantitative insight into the observed values of switching fields [18].

4. Discussion

Several interesting phenomena can be deduced from the results summarized in table 1. First, it reports the values of phenomenological coefficients of the PHE for a wide range of compositions of Fe_3Si and different thicknesses of Fe films. Chen *et al* have reported the values of symmetric coefficients for transition metal alloys [19, 20]. However, to our knowledge, the values of the antisymmetric coefficients are never reported in the literature even for the transition metals. The present study involving a low symmetric surface allows us to observe and report these values. It is important to mention that the symmetric amplitude is found to

be different from the anisotropic magnetoresistance. This is a result of the single-crystalline nature of the samples, in agreement with the phenomenological model discussed in [6]. Both the symmetric and antisymmetric coefficients exhibit wide changes in magnitude and sign with composition and thickness of the films. While the actual origin of these phenomena is not clearly understood, this study does provide some insight into the underlying physical origin of the sign changes. For example, stoichiometric Fe_3Si and thick Fe films exhibit the same sign of the saturated antisymmetric transverse resistivity, $\rho_{SATM} = 2(\rho^0_{SATM} + \rho^1_{SATM})$, which is a measure of the antisymmetric component. This implies a relation between the ordering of the Fe_3Si lattice near stoichiometry and the sign of ρ_{SATM}. Besides, the sign of ρ_{SATM} for the 1.4 nm Fe film is reversed compared to the thicker Fe films, which indicates that the interface can also play an important role in thin films in determining the sign of these coefficients. The sign of symmetric coefficients is found to be negative in Fe films and in off-stoichiometric Fe_3Si films. However, a detailed discussion of the physical origin of the sign changes is beyond the scope of this paper.

Table 1 also completely characterizes the magnetic anisotropy of all the samples investigated. In general, we show that the magnetic anisotropy of these samples can be understood by assuming a combination of the four-fold and a uniaxial magnetic anisotropy. The four-fold magnetic anisotropy characterized by the constant K_1, which arises from the magnetocrystalline anisotropy, is a result of the large demagnetization energy of the films [8]. Table 1 shows a positive value of K_1 over the whole composition range, similar to ordered bulk Fe_3Si with $D0_3$ crystal structure [21]. Furthermore, a decrease in K_1/M_s with the addition of Si is also found. Note that, from SQUID magnetometry, we found the saturation magnetization to decrease with the addition of Si [22]. Using the respective saturation magnetization from SQUID magnetometry, this results in $K_1 = (4.6 \pm 1.3) \times 10^5$ erg cm^{-3} for the 26 nm-thick Fe film and $K_1 = (3.0 \pm 0.6) \times 10^4$ erg cm^{-3} for the almost stoichiometric Fe_3Si film. Both values are also comparable to the bulk values of $K_1 = 4.7 \times 10^5$ erg cm^{-3} for bulk Fe and $K_1 = 5.4 \times 10^4$ erg cm^{-3} in ordered Fe_3Si [21]. The decrease in the four-fold magnetic anisotropy constant with increasing Si content can be understood from the argument of the reduced symmetry environment of the Fe atoms in the crystal lattice due to the addition of Si. Since the magnetocrystalline anisotropy arises from the spin–orbit coupling, the decrease in K_1 implies a decrease in spin–orbit coupling strength with the addition of Si.

The ratio r, which reflects the strength of the additional UMA, also exhibits several interesting phenomena. First, it is positive for Fe films, which implies an easy axis along $[33\bar{2}]$ and is found to increase with decreasing thickness, in perfect agreement with the results of SQUID magnetometry [8, 11] and anisotropic magnetoresistance [3]. As explained in [8, 11], the UMA in these Fe films is an interfacial effect and is determined by the anisotropic bonding structure at the interface. However, in Fe_3Si films, the ratio r is negative and increases in amplitude with increasing Si content (decreasing x)—with the exception of one sample with $x = 0.03$. The negative sign of r, which indicates an easy axis of the UMA along the $[\bar{1}10]$ direction, is opposite to that of the above interface-related UMA in the Fe films of [8, 11]. Hence, the UMA observed here is probably not related to the interface. Besides, the thickness range (40–50 nm) studied here may be substantially too large to observe any interface-related effect. However, for $Fe_3Si(001)$ films in this thickness range, a UMA [23, 24] of interfacial origin [25] has recently been reported. For this reason, the role of the interface should not be discarded so easily. A detailed thickness dependence study is required to confirm the role of the interface on the negative r observed in these [113]-oriented films. The surface morphology of these films does not exhibit any anisotropic roughness, thus ruling out a surface-morphology-related dipolar origin of the UMA. The other possible origin of the UMA includes the growth conditions, the presence of some additional phase, and the strain in the films. To investigate

the influence of the former, we have also studied the growth temperature dependence for the stoichiometric $Fe_{3+x}Si_{1-x}$ sample $x = 0.03$ with SQUID magnetometry. However, from these studies we only witness an increase in the coercive field H_c with $r = 0$, remaining constant when the growth temperature is increased above 250 °C. The increase in H_c is essentially due to the degradation of the layer quality. However, the preservation of $r = 0$ indicates that the four-fold magnetic anisotropy is dominant in this growth temperature range. This shows that the growth conditions do not have a significant influence on this UMA, at least in the temperature range studied. A strong UMA is actually observed for samples with high Si content (e.g. $x = -0.04$), for which the presence of some additional phase is also known from reflection high-energy electron diffraction and high-resolution x-ray diffraction experiments [7]. However, the composition of this possible phase and its relation to the UMA are not known clearly. Thus the UMA observed here is not completely understood. However, these studies indicate that it might be related to interfacial bonding like that of Fe films or some interfacial reactions at the interface. Note that strain is an unlikely origin of this UMA, since the lattice mismatch between Fe_3Si and GaAs is much smaller compared to the Fe/GaAs system, for which the UMA is known to be strain independent [26]. Besides, all the Fe_3Si films that were studied were found to be coherent, and hence no in-plane anisotropic strain is supposed to be present in these films.

5. Conclusion

In conclusion, we report an extensive study of the planar Hall effect in Fe_3Si and Fe films grown on low-symmetry GaAs(113)A substrates over a range of compositions and several thicknesses. The result of this study is two-fold. First, it completely characterizes the magnetic anisotropic properties of the films using the planar Hall effect as a tool and identifies the simple Stoner–Wolfarth model as a qualitative description for the magnetization reversal. This is possible despite the presence of the antisymmetric component in the PHE, which complicates the behaviour and the shape of the planar Hall effect. Second, the study reports the phenomenological symmetric and antisymmetric coefficients and their behaviour with the composition and thickness of the films.

Acknowledgments

The authors would like to thank E Wiebicke and A Riedel for Hall bar sample preparation. We would also like to thank M Bowen, L Däweritz, R Hey, and B Jenichen for useful discussions. Part of this work has been founded by the German Bundesministerium für Bildung und Forschung under the research program *NanoQuit* (contract no. 01BM463).

References

[1] Tang H X, Kawakami R K, Awschalom D D and Roukes M L 2003 *Phys. Rev. Lett.* **90** 107201
[2] Kreutz T C, Allen W D, Gwinn E G, Awschalom D D and Gossard A C 2004 *Phys. Rev.* B **69** 081302
[3] Friedland K J, Herfort J, Muduli P K, Schönherr H P and Ploog K H 2005 *J. Supercond.* **18** 309
[4] Wang K Y, Edmonds K W, Campion R P, Zhao L X, Foxon C T and Gallagher B L 2005 *Phys. Rev.* B **72** 085201
[5] Friedland K J, Nötzel R, Schönherr H P, Riedel A, Kostial H and Ploog K 2001 *Physica* E **10** 442
[6] Muduli P K, Friedland K J, Herfort J, Schönherr H P and Ploog K H 2005 *Phys. Rev.* B **72** 104430
[7] Muduli P K, Herfort J, Schönherr H P and Ploog K H 2005 *J. Cryst. Growth* **285** 508
[8] Muduli P K, Herfort J, Schönherr H P and Ploog K H 2005 *J. Appl. Phys.* **97** 3904
[9] Hansen M 1958 *Constitution of Binary Alloys* (New York: McGraw-Hill)
[10] Elliot R P 1965 *Constitution of Binary Alloys, Suppl. 1* (New York: McGraw-Hill)

[11] Muduli P K, Herfort J, Schönherr H P, Däweritz L and Ploog K H 2005 *Appl. Phys.* A **81** 901
[12] Gester M, Daboo C, Hicken R J, Gray S J, Ercole A and Bland J A C 1996 *J. Appl. Phys.* **80** 347
[13] Florczak J M and Dahlberg E D 1991 *Phys. Rev.* B **44** 9338
[14] Gu E, Bland J A C, Daboo C, Gester M, Brown L M, Ploessl R and Chapman J N 1995 *Phys. Rev.* B **51** 3596
[15] Riggs K T, Dahlberg E D and Prinz G A 1990 *Phys. Rev.* B **41** 7088
[16] Stoner E C and Wohlfarth E P 1948 *Phil. Trans. R. Soc.* A **240** 74
[17] Muduli P K 2006 *PhD Thesis* Humboldt University, Berlin http://edoc.hu-berlin.de/docviews/abstract.php?id=27224
[18] Daboo C, Hicken R J, Gu E, Gester M, Gray S J, Eley D E P, Ahmad E, Bland J A C, Ploessl R and Chapman J N 1995 *Phys. Rev.* B **51** 15964
[19] Chen T T and Marsocci V A 1972 *Physica* **59** 498
[20] Chen T T and Marsocci V A 1972 *Solid State Commun.* **10** 783
[21] Goto M and Kamimori T 1983 *J. Phys. Soc. Japan* **52** 3710
[22] Herfort J, Muduli P K, Friedland K J, Schönherr H P and Ploog K H 2006 *J. Magn. Magn. Mater.* at press
[23] Herfort J, Schönherr H P, Friedland K J and Ploog K H 2004 *J. Vac. Sci. Technol.* B **22** 2073
[24] Ionescu A, Vaz C A F, Trypiniotis T, Gurtler C M, Garcia-Miquel H, Bland J A C, Vickers M E, Dalgliesh R M, Langridge S, Bugoslavsky Y, Miyoshi Y, Cohen L F and Ziebeck K R A 2005 *Phys. Rev.* B **71** 094401
[25] Lenz K, Kosubek E, Baberschke K, Wende H, Herfort J, Schönherr H P and Ploog K H 2005 *Phys. Rev.* B **72** 144411
[26] Thomas O, Shen Q, Schieffer P, Tournerie N and Lépine B 2003 *Phys. Rev. Lett.* **90** 017205

Flipping of magnetic moments induced by the first-order phase transition in MnAs disks on GaAs(001)

Y. Takagaki, J. Herfort, L. Däweritz, and K. H. Ploog
Paul-Drude-Institut für Festkörperelektronik, Hausvogteiplatz 5-7, 10117 Berlin, Germany
(Received 28 June 2006; revised manuscript received 5 September 2006; published 14 December 2006)

The relaxation of magnetization in MnAs nanomagnets fabricated on GaAs(001) substrates consists of three exponential decays that are associated with the first-order phase transition between the ferromagnetic and nonmagnetic phases of MnAs and fast and slow flipping processes of magnetic moments. Not only the phase-transition component but also the fast-relaxation component become appreciable in the narrow temperature range of the thermal hysteresis of the phase transition. The magnetic moments are suggested to be rotated by virtual phase-transition processes. A brief expansion of the lattice constants of MnAs through the magnetic-field-induced phase transition is found to generate a memory effect and permanently elongate the decay times.

DOI: 10.1103/PhysRevB.74.224417 PACS number(s): 75.60.Jk, 75.60.Nt, 75.75.+a

I. INTRODUCTION

Manganese arsenide is ferromagnetic at room temperature and possesses unusual magnetic characteristics around Curie temperature $T_C \approx 315$ K. The material undergoes a simultaneous magnetic and structural first-order phase transition at T_C and a second-order structural transition at $T_s \approx 395$ K. The magnetic phase transition is accompanied by a large magnetocaloric effect, which is useful for magnetic refrigeration.[1] Although the ferromagnetic order is lost at T_C, the magnetic susceptibility follows the Curie-Weiss law only at $T > T_s$.[2] In addition, the loss of the magnetic order at T_C is discontinuous. In typical ferromagnetic materials, the magnetization M changes with temperature T as

$$M(T) = M_0 B_S\left(\frac{S^2 J_0}{k_B T}\frac{M}{M_0}\right), \tag{1}$$

where M_0 is the magnetization at $T=0$, $B_S(x)$ is the Brillouin function, and J_0 is related to T_C as $k_B T_C = (1/3)S(S+1)J_0$. One obtains T_s as the extrapolated Curie temperature for MnAs if the temperature dependence of the magnetization for $T < T_C$ is fitted by Eq. (1).[3] The peculiar magnetic properties have led to an unsettled debate whether the medium temperature phase, β-MnAs, is paramagnetic or antiferromagnetic.[4,5]

In this paper, we investigate the magnetization reversal processes in nanometer-scale MnAs disks. The thermal fluctuations in the magnetization of small magnetic particles are one of the fundamental issues of modern micromagnetics. Due to the unusual magnetic properties around T_C, the magnetization relaxation in MnAs is anticipated to be different from that in ordinary ferromagnetic particles. We find that a certain relaxation process sets in dramatically in the narrow temperature range of the thermal hysteresis associated with the first-order phase transition, providing evidence that the phase transition can enhance the flipping of magnetic moments. We also demonstrate that the application of an external magnetic field modifies the relaxation behavior through the strain imposed by the substrates.

The thermal relaxation of magnetization is also of great importance for applications. Over nearly half a century, the density of bits in magnetic storage devices has increased steadily at a rate of tenfold in six years. The so-called superparamagnetic limit resulting from thermal magnetization reversal is rapidly approaching as the magnetic energy to hold magnetic moments can no longer be much larger than the thermal energy $k_B T$.[6] There are a number of proposals to extend the superparamagnetic limit, including, for instance, perpendicular recording and heat assisted magnetic recording (HAMR). In HAMR,[7] a high-coercivity magnetic material is used to overcome thermal fluctuations. The material is heated during recording to "soften" it magnetically in order to reduce the external magnetic field required for the recording. Understanding the magnetization relaxation processes near the Curie temperature T_C is hence crucial for HAMR. There is also a practical issue. If one employs a ferromagnetic material having T_C not too far from room temperature in order to ease the heating task for HAMR, the magnetization is considerably reduced from M_0 at room temperature in accordance with Eq. (1).

The material properties of MnAs are intriguing from the viewpoint of magnetic storages and HAMR. The uniaxial magnetocrystalline anisotropy of MnAs is significantly large, giving rise to an almost square-shaped hysteresis in the magnetization curve and slow relaxation of magnetization in small disks.[8] The abrupt disappearance of the ferromagnetic order at T_C means for HAMR that the remanent magnetization of MnAs remains substantial at room temperature even though the required heating is merely a few tens degree. If β-MnAs is antiferromagnetic, the exchange-biasing effect can be utilized[9,10] to stabilize the magnetization of the ferromagnetic α phase.[11]

II. EXPERIMENT

$(1\bar{1}00)$-oriented hexagonal MnAs films were grown on GaAs(001) substrates by molecular-beam epitaxy. MnAs disks were fabricated using electron-beam lithography and Ar ion milling.[12] In the inset of Fig. 1 we show a scanning electron micrograph of a typical sample. The MnAs disks were assembled in the form of a square array stretched along the cleavage directions of the GaAs substrates in order to strengthen the magnetization signal. The number of the disks

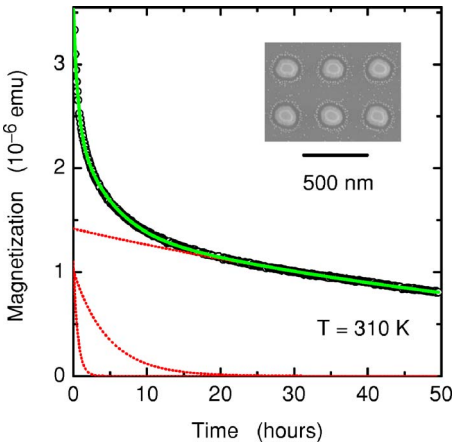

FIG. 1. (Color online) Decay of the remanent magnetization in MnAs disks No. 1 at a temperature $T=310$ K. The disks were magnetized at a magnetic field of 20 kOe prior to the time-dependence measurement. The solid curve shows a fit assuming three exponential decays with the decay times $\tau_p=0.59$ h, $\tau_f=4.65$ h, and $\tau_s=88.0$ h. The individual components are shown by the dotted curves. The inset shows a scanning electron micrograph of the MnAs disks. The diameter of the disks is 100 nm.

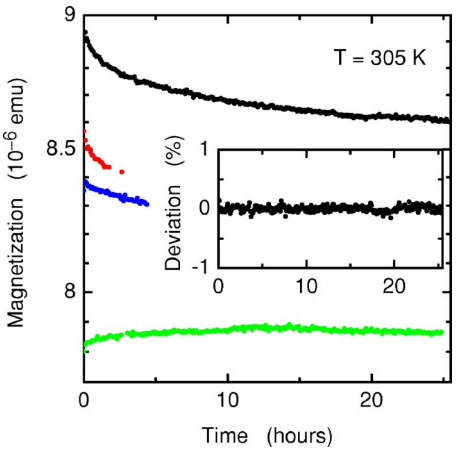

FIG. 2. (Color online) Time dependence of the remanent magnetization in MnAs disks No. 2 having a diameter of 100 nm after various thermal history. The disks were magnetized at a magnetic field of 20 kOe prior to each measurement run. The sample temperature before the measurements was higher and lower than the measurement temperature $T=305$ K for the top three and the bottom curves, respectively. The inset shows the difference between the experimental data (top-most curve) and a theoretical fit assuming $\tau_s=\infty$ ($\tau_p=0.87$ h, $\tau_f=10.5$ h, and M_p, M_f, M_s are 0.11, 0.24, 8.59×10^{-6}emu, respectively).

in a sample is on the order of 10^7-10^8. The magnetic easy axis of the MnAs films is along the $[11\bar{2}0]$ direction, which is parallel to the [110] direction of GaAs. The magnetization of the disks was measured using a superconducting-quantum-interference-device (SQUID) magnetometer (Quantum Design MPMS XL). We examined the relaxation of the remanent magnetization in samples processed from two 50-nm-thick films and one 37-nm-thick film grown under distinct growth conditions. All the samples exhibited qualitatively similar results, indicating that the phenomena we report here are generic for MnAs disks. Only the data obtained using the 50-nm-thick films are included in the present paper. In the microstructuring process, a Ti or NiCr mask was used for MnAs etching. For some samples the mask was removed at the completion of the ion milling using a HF solution, whereas, for the rest of the samples, the mask was left on the surface of the disks during the SQUID measurements. We emphasize that no essential difference was found among these different kinds of samples, indicating that the mask did not influence the magnetic properties of the MnAs disks.

III. RELAXATION OF REMANENT MAGNETIZATION

In Fig. 1, the time dependence of the magnetization at $T=310$ K in the sample shown in the inset (sample No. 1) is plotted by the circles. Prior to the measurement, the sample was magnetized in an external magnetic field of 20 kOe applied along the $[11\bar{2}0]$ direction of MnAs, i.e., the magnetic easy axis. The magnetic field was reduced to zero, at time $t=0$, at a rate of 8 kOe/min. Note that the remanence in the MnAs disks is fairly close to the saturation magnetization due to the strong uniaxial magnetocrystalline anisotropy.[8] As shown by the solid curve, the experimental behavior is described by a superposition of three exponentially decaying components

$$M(t) = M_p e^{-t/\tau_p} + M_f e^{-t/\tau_f} + M_s e^{-t/\tau_s}, \tag{2}$$

where M_i and τ_i are the magnitude and the relaxation time of the component i ($\tau_p<\tau_f<\tau_s$), respectively. The individual components are shown by the dotted curves in Fig. 1. While the magnetic relaxation is given by an exponential decay if the underlying activation-energy processes are exactly similar, the relaxation is generally found to exhibit a $\ln t$ dependence due to a distribution in the activation energy.[13,14] However, we have encountered that systematic analysis of our experimental data is possible only by assuming the three exponential decay components. We will return to this point in Sec. V.

With lowering temperature, the time dependence of the magnetization is drastically reduced. The variation at room temperature shrinks to the extent that it is barely detectable, as reported in Ref. 8. The temperatures at which the relaxation time can be evaluated are, as a consequence, in a narrow range just below T_C. As this range overlaps with that of the thermal hysteresis originating from the first-order phase transition at T_C, the relaxation characteristics critically depend on the thermal history of the samples. In Fig. 2 we show a number of the magnetization decay curves at $T=305$ K obtained from an identical sample (sample No. 2, which was fabricated from a MnAs film different from that of sample No. 1). The top three measurement runs were obtained under nominally the same thermal procedure but in different thermal cycles. The bottom curve was obtained under a thermal procedure fundamentally different from that for the top three curves. The variation in $M(t=0)$ for the differ-

ent measurement runs is a direct consequence of the thermal hysteresis. Notice that even the relaxation times change with thermal cycles. As the Néel-Brown law

$$\tau = \tau_0 \exp(E_B/k_B T) \tag{3}$$

implies that the relaxation time τ is determined by thermally activated processes over an energy barrier E_B, the latter indicates a fluctuation of E_B.

For the bottom curve in Fig. 2, the magnetization increased with t instead of a relaxation. The magnetization was maximized at $t \approx 13$ h and exhibited a slow decay afterwards. (Similar behavior at 293 K observed in the same sample was reported in Ref. 8, for which the maximum appeared at $t \approx 20$ h.) This qualitatively different behavior was reproducible under a specific thermal history. For the top three curves in Fig. 2, the sample temperature was lower than the measurement temperature of $T=305$ K prior to the measurement runs. To be specific, the sample was heated from 200 K to 305 K at a rate of 10 K/min, except when the sample temperature became less than 10 K below the measurement temperature, for which the heating rate was reduced to 1 K/min. On the contrary, the sample was cooled to the measurement temperature for the bottom curve, resulting in the distinctively small magnetization due to the thermal hysteresis. We have confirmed that solely the sample temperature immediately before the measurements determines the initial fate of the magnetization, i.e., an increase or a decrease. In addition, the magnetization decay for $t > 15$ h is a common feature regardless of the thermal history, i.e., the process associated with the component f universally reduces the magnetization. Therefore, the fastest decay when the sample was warmed to the measurement temperature (component p) and the initial increase when the sample was cooled to the measurement temperature are indicated to be associated with the first-order phase transition between the α and β phases of MnAs. In a first-order phase transition, the phase transition does not occur immediately. It takes place by surmounting a potential barrier separating the two phases, see Fig. 3, giving rise to a stochastic behavior.[15]

The initial increase of the magnetization takes place on a time scale which is considerably longer than τ_p. (We have not been able to extract the characteristic times when the magnetization initially increases.) The different time scales are ascribed to the fact that the transition from (magnetized) α-MnAs to β-MnAs always reduces the magnetization, whereas the transition from β-MnAs to α-MnAs does not have to change the magnetization. The direction of the magnetic moment in the α-MnAs disks emerged in the course of the phase transition is, in principle, random. The increase of the magnetization implies that the newly created α-MnAs disks are, at least partly, magnetized in the dominant magnetization direction of the surrounding disks, plausibly through the dipole-dipole interaction.[16] The MnAs disks in our devices are assembled in the form of a square array having a period about one order of magnitude larger than the diameter of the disks. The stray fields from the surrounding disks can be large enough to influence the magnetization direction of the newly created ferromagnetic disks. For square arrays, the dipole-dipole interaction gives rise to a ferromagneticlike coupling between adjacent disks.[17] The time scale of the magnetization increase is thus governed by the interdisk interaction.

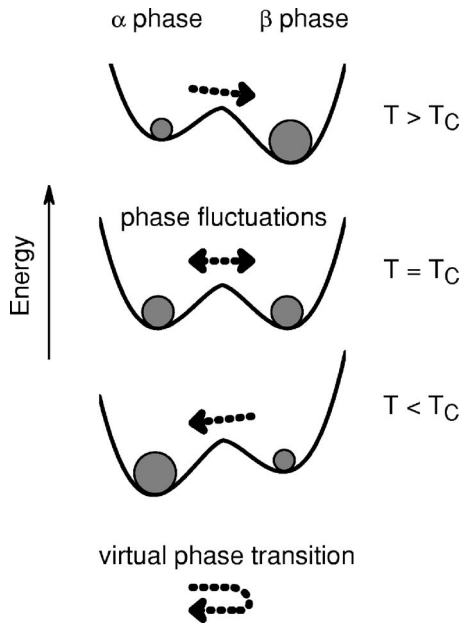

FIG. 3. Schematic energy diagram of the first-order phase transition between the α phase and the β phase of MnAs at temperatures around Curie temperature T_C. The arrows indicate the transition from the metastable state (the α phase for $T > T_C$ and the β phase for $T < T_C$) to the stable state (the β phase for $T > T_C$ and the α phase for $T < T_C$). The phase fluctuates between the α and β phases at temperature $T = T_C$. Such fluctuations may give rise to virtual phase transitions.

The two components f and s correspond to the flipping of the magnetic moments in the disks. At present, the mechanism of the two relaxation processes has not been identified. The two distinct decays may originate from the fact that the sample contains two types of disks in terms of the magnetic-domain structure in individual disks. When the diameter of MnAs disks is reduced, the magnetic-domain structure undergoes a transition from a double-domain state to a single-domain state.[15] In large disks, the double-domain state is favored as the closure flux arrangement reduces the magnetostatic energy originating from stray fields. Note that this double-domain state corresponds to the vortex state for ordinary magnetic materials. The strong uniaxial magnetocrystalline anisotropy of MnAs transforms the vortex state to the double-domain state. Below a critical diameter of the disks, the double-domain state becomes unfavorable as the cost of domain-wall energy exceeds the gain in the magnetostatic energy. The disks in the latter regime are of single magnetic domain even in the demagnetized state, the so-called nanomagnets. As the meandering of the local atomic magnetic moments along the disk boundary is fairly small, the magnetic relaxation in the two types of ferromagnetic MnAs disks can be treated as a thermodynamics of a single magnetic moment for the single-domain disks and of two magnetic moments arranged either in parallel or antiparallel configuration for the double-domain disks. (We do not refer a double-domain disk having parallel configuration as a single-

domain disk despite its effective single magnetic domain.) For the single-domain disks, the relaxation occurs by reversing the direction of the magnetic moment with respect to that of the rest of the disks. In contrast, the magnetization vanishes for the double-domain disks when the magnetic moments rearrange themselves from the parallel configuration to the antiparallel configuration, which is equivalent to a domain-wall formation. The relaxation in the double-domain disks will be faster than that in the single-domain disks, provided that all the disks have a comparable size, as only a half of the magnetic moments of the disks needs to be flipped for the former case.

Using magnetic force microscopy, we have established that the disks we examine in this paper are predominantly in the single-domain regime at room temperature.[15] If the number of the double-domain disks increases at the high temperatures where the relaxation became appreciable, the two relaxation mechanisms will coexist. However, the component f is unlikely to be associated with the domain-wall formation in the double-domain disks. First, the competition between the domain-wall energy and the magnetostatic energy is hardly influenced by temperature, and so the temperature dependence of the critical size for the transition between the single- and double-domain regimes is expected to be weak.[18] Second, the fractions of the two types of the disks will vary significantly with the mean disk diameter of the array when the disk size is comparable to the critical value. However, the three-component decay was observed generally in all the samples we examined having diameters of 70 $\sim$120 nm.

We have found that the relaxation of magnetization reveals a strong and peculiar temperature dependence. Before we proceed to discuss the temperature dependence, we note a difficulty that we had to deal with in analyzing the experimental data. That is, due to the restricted measurement duration and the extremely slow relaxation for the component s, the experimental data could not be fitted using Eq. (2) unless $\tau_s=\infty$ was assumed, except for the measurement run shown in Fig. 1. For the analyses in the remainder of the paper, we assume that the magnetization associated with the component s is time independent. In the inset of Fig. 2, we show the deviation of the experimental data from the prediction by Eq. (2) assuming $\tau_s=\infty$ for the top curve in Fig. 2. The agreement between the theory and the experiment is still excellent, indicating that $\tau_s \gg 25$ h.

In Figs. 4(a) and 4(b) we show the temperature dependence of M_i and τ_i $(i=p,f)$ from sample No. 2, respectively. The components p and f are found to exhibit similar temperature dependencies. Not only the phase-transition component p but also the fast relaxation of the magnetization emerges remarkably only in a narrow temperature range, $\Delta T \sim 15$ K, below T_C. This temperature range coincides with the range of thermal hysteresis in the disks, which was determined using x-ray diffraction.[19] Moreover, the relaxation becomes appreciable not by decreasing τ_f but by increasing M_f, as highlighted by the dotted line in Fig. 4(a). As the relaxation time is expected to be given by Eq. (3), it would be roughly constant in such a narrow temperature range around room temperature, as we indeed find in Fig. 4(b).[20] (In our devices, τ_f is typically ten times longer than τ_p.) The

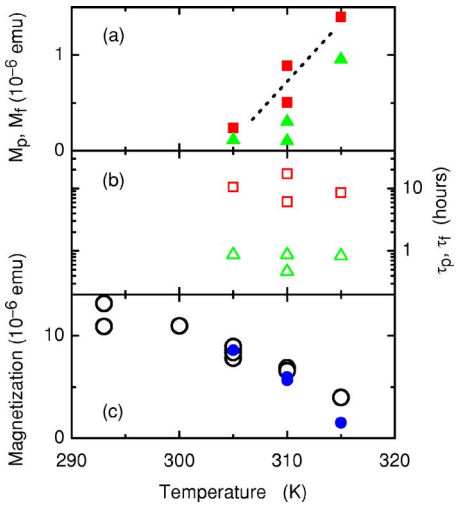

FIG. 4. (Color online) Temperature dependencies of (a) the magnitudes M_p and M_f, (b) the relaxation times τ_p and τ_f, and (c) the remanent magnetization at $t=0$ (open circles) and the magnitude M_s (filled circles) in MnAs disks No. 2. The triangles and squares correspond to the components p and f, respectively. The dotted line in (a) is a guide for the eyes.

similarity in the temperature dependence of M_f and M_p indicates that the fast relaxation of the magnetization is strongly associated with the phase transition. We emphasize that the component f cannot be due to a direct phase-transition process as the magnetization always decays regardless of the thermal history, i.e., even when the component p increases the magnetization. We propose that the fast relaxation may occur via temporally phase fluctuations from α-MnAs to β-MnAs.

Due to the nucleation initiation of the first-order phase transition, the array generally consists of those disks of α-MnAs and those of β-MnAs in the thermal hysteresis regime.[15] That is, the disks of the metastable phase are transformed to the disks of the stable phase when nuclei of the stable phase are formed in the metastable phase by surmounting a potential barrier, see the top $(T>T_C)$ and bottom $(T<T_C)$ cases in Fig. 3. Once the nuclei are formed, they grow larger and convert the phase of the entire disk to the stable one. The energy barrier for the phase transition is responsible for the relaxation behavior in the phase transition manifested by the component p. When the two phases are comparably favored for $T \approx T_C$, as illustrated by the middle case in Fig. 3, the disks will fluctuate between being in the α and β phases. Similarly, even when MnAs disks remain nominally in the α phase, they may undergo virtual transitions to the β phase. In this circumstance, the information regarding the magnetization direction when the disks are in the ferromagnetic phase will be lost while MnAs is in the nonmagnetic phase for a very brief moment. Therefore, such virtual fluctuations from the α phase to the β phase will give rise to a randomization of the magnetic moment.

In Fig. 4(c) we show evidence that the disks responsible for the component f are rather extraordinary and ordinary disks do not seem to undergo the fast relaxation process. Here, the open circles show the remanence at $t=0$ $(=M_p$

$+M_f+M_s$) at various temperatures. The temperature dependence is nearly linear and the extrapolated temperature for vanishing magnetization ($T\sim 325$ K) is unusually large for T_C of MnAs. In contrast, M_s, plotted by the filled circles in Fig. 4(c), exhibits a temperature dependence similar to that of the saturation magnetization in MnAs films. The component s hence provides ordinary magnetization that obeys Eq. (1). This may suggest that the phase transition is unstable in some disks due, for instance, to defects. While stable disks yield the magnetization decay represented by the component s, the metastable α phase "pinned" in the unstable disks may undergo the virtual phase transitions, yielding the component f. The crystal imperfections can play an important role for the phase transition between α-MnAs and β-MnAs as the transition involves a discontinuous volume change.

Another possible explanation for the two relaxation processes is that they are associated with the two types of the phase distribution, rather than the magnetic-domain structure, in the disks. When the disk size is only slightly smaller than the period of the elastic domains of α-MnAs and β-MnAs in a film, the two phases can still coexist in a disk: the stress-free surface MnAs is in the α phase and the stress-stabilized β phase is buried at the vicinity of the MnAs-GaAs interface.[15] Although most of the disks contain either α-MnAs or β-MnAs for the present disk diameter at room temperature,[15] it is likely that the core-shell-type phase coexistence occurs in a small number of disks. The fast relaxation may then take place in the disks in which the α and β phases coexist. If β-MnAs is paramagnetic, the phase coexistence will not influence the magnetic relaxation. However, a magnetic interaction should occur between the segments of the α and β phases within a disk if β-MnAs contains an antiferromagnetic order.[4,5] Unlike the magnetic-domain structure, the phase-domain structure will depend critically on temperature as it is determined by a competition between the elastic energy imposed by the substrate and the temperature-dependent free energy of the crystals. The factions of the two types of the phase-domain structures will thus vary when the temperature is increased close to T_C. This could account for the strong temperature dependence of M_f in Fig. 4. However, besides the controversy over the existence of an antiferromagnetic order in β-MnAs,[4] the coexistence is hardly expected to occur exactly in the same manner in a large number of disks to exhibit the well-defined relaxation time for the component f.

IV. STRAIN EFFECTS ON THE RELAXATION

Although M_i and τ_i remain constant as long as the sample temperature is kept unchanged, they are altered significantly with thermal cycles. The fluctuations of the decay parameters originate from the abrupt volume change of MnAs at the phase transition. The loss of the magnetic order accompanies a discontinuous expansion in the lattice constants in the C plane of MnAs by about 1%. The change in the strain between the MnAs films and the GaAs substrates when the fractions of α- and β-MnAs are varied has a memory effect as the phase transition is first order. The strain energy hence permanently modifies E_B. We have found that the decay properties of the magnetization are altered not only by thermal cycles but also by a temporary variation of an external magnetic field. Similarly, the remanence and its relaxation characteristics are permanently altered when a magnetic field is briefly applied.

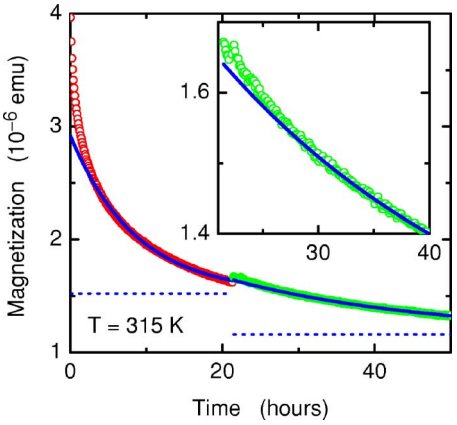

FIG. 5. (Color online) Decay of the remanent magnetization in MnAs disks No. 2 at a temperature $T=315$ K. The disks were briefly magnetized at time $t=21.4$ h in addition to the initial magnetization at $t<0$. The dotted lines show the component s. The solid curves show the contribution due to the components f and s ($\tau_p=0.84$ h, $\tau_f=8.58$ h for $t<21.4$ h and $\tau_p=0.87$ h, $\tau_f=2.66$ h for $t>26.6$ h). The decay after the remagnetization is shown with expanded scales in the inset.

In Fig. 5 the disks were magnetized again (at $t=21.4$ h) during the course of the relaxation characterization by briefly increasing the external magnetic field to 20 kOe. Although the magnetic field was applied well after the direct phase-transition contribution had vanished, the component p reemerged when the magnetic field was quickly reduced to zero, as shown in the inset of Fig. 5. Here, the solid curves show the contribution of the components f and s of the theoretically fitted decay behavior. The deviation of the experimental data (circles) from the solid curves is equivalent to the component p. The excess α phase that exhibits the phase relaxation is produced by the magnetic-field-induced phase transition from β-MnAs to α-MnAs due to magnetostriction.[21,22] In addition to the reemergence of the component p, the decay times τ_p and τ_f changed from 0.84 and 8.6 h, before the brief application of the magnetic field, to 2.7 and 27 h, after the application, respectively. The strain modification in the disks is responsible for the change of the decay times. It is noteworthy that the decay times were always elongated by applying the magnetic field, i.e., the strain modification leads to a "healing" effect. The magnitude of the component s decreased as shown by the dotted lines in Fig. 5. As the change in M_s is much larger than the magnitude of the reemerged component p, the slow-relaxation component is implied to be partly converted to the fast-relaxation component. However, at present, we cannot rule out the possibility that the reduction of M_s might be an artifact due to the necessary assumption of $\tau_s=\infty$.

V. IS THE DECAY EXPONENTIAL OR LOGARITHMIC?

As we stated earlier, magnetic materials generally exhibit a logarithmic decay of magnetization,[14] reflecting a distribu-

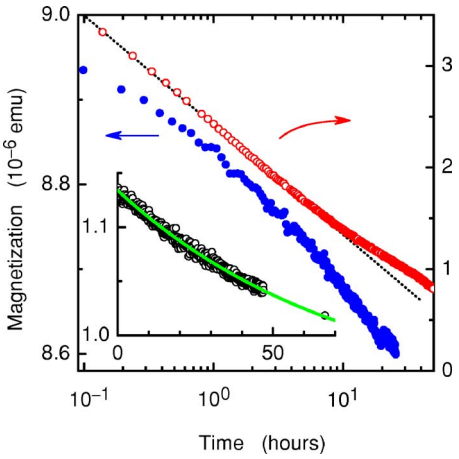

FIG. 6. (Color online) Magnetization versus the logarithm of time. The open circles are the experimental data plotted in Fig. 1. The filled circles are identical to the top curve in Fig. 2. Certain portions might be interpreted as demonstrating a logarithmic decay as shown by the dotted line. The inset shows the relaxation of the magnetization in MnAs disks No. 2 at a temperature $T=315$ K. Following an initial magnetization relaxation measurement, which dwelled about 50 h, the sample was temporarily heated to 335 K for about 10 min and re-magnetized briefly in a magnetic field of 20 kOe at 315 K. The decay obeys an exponential dependence superimposed on a constant background as shown by the solid curve.

tion of the activation energy in real devices.[13] However, the whole of our experimental data can be analyzed systematically, apart from the cases where the magnetization initially increases with time after cooling of the sample, only if we assume a relaxation in the form of Eq. (2). As an example, we plot magnetization versus the logarithm of t in Fig. 6. Here, the open and filled circles show the experimental data identical to those plotted in Fig. 1 and in Fig. 2 as the top curve, respectively. Certain portions could be interpreted as exhibiting logarithmic decays, for instance, as indicated by the dotted line. However, it is apparent between these two examples that the decay behavior is not universal: the slope at large t is gentler than that at small t for the filled circles, whereas the logarithmic decay deviates in the opposite direction for the open circles. Moreover, the open circles in Fig. 6 clearly show an increase of the slope for $t>30$ h, which corresponds to the regime where the component s becomes dominant in Fig. 1. Consequently, even a fit using a modified logarithmic decay $\ln(t+t_0)$ is unsatisfactory (not shown), in contrast to the excellent fit one finds in Fig. 1. In practice, the experimental data that were fitted assuming two exponential decays and a constant background could be fitted also using the modified logarithmic decay with comparable accuracies. However, the modified logarithmic decay cannot describe the experimental relaxation when it appears to consist of three exponential decays.

As an additional evidence for supporting our assumption of the exponential decays, we show in the inset of Fig. 6 a case in which the relaxation of magnetization exhibited a single exponential decay (plus a constance background). The experimental data were taken here at $T=315$ K following a procedure similar to that for Fig. 5: subsequent to an initial relaxation measurement, the sample was briefly heated to 335 K for about 10 min and then remagnetized by a magnetic field of 20 kOe at 315 K. The increase of the β phase by the heating and that of the α phase by the magnetic field in the component p presumably canceled each other, leaving only the exponential decay associated with the component f and the constant background associated with the component s. (The relaxation time for the fast-decay component increased and the constant magnetization value for the slow-decay component decreased after the remagnetization, similar to those shown in Fig. 5.)

We also emphasize that the magnetization deduced as corresponding to the component s using the interpretation based on the exponential decays, the filled circles in Fig. 4(c), is in reasonable agreement with the behavior of bulk MnAs. Nevertheless, as fluctuations in E_B are evidenced to be present in Fig. 2, which are the origin of the logarithmic decay observed in most of the magnetic materials,[13] further studies are needed to clarify whether the relaxation follows the exponential decay or the logarithmic decay in our disk arrays.

VI. CONCLUSION

We have investigated the reversal processes of the magnetic moments in MnAs disks on GaAs substrates. Three exponentially decaying components are found to constitute the relaxation of magnetization. The contribution due to the stochastic nature of the first-order phase transition possesses the shortest characteristic time. The component having a medium relaxation time is not a direct consequence of the thermal hysteresis of the first-order phase transition although it is strongly related to the hysteresis. This relaxation may originate from the flipping of magnetic moments by virtual phase-transition processes. All the relaxation properties are altered permanently not only by thermal cycles but also by applying a magnetic field through the magnetic-field-induced phase transition.

ACKNOWLEDGMENTS

The authors would like to thank E. Wiebicke for the assistance in the sample fabrication and C. Herrmann for the growth of the MnAs layers. Part of this work was supported by the Federal Ministry of Education and Research (nanoQUIT program).

[1] S. Gama, A. A. Coelho, A. de Campos, A. M. Carvalho, F. C. G. Gandra, P. J. von Ranke, and N. A. de Oliveira, Phys. Rev. Lett. **93**, 237202 (2004).
[2] N. Menyuk, J. A. Kafalas, K. Dwight, and J. B. Goodenough, Phys. Rev. **177**, 942 (1969).
[3] J. B. Goodenough and J. A. Kafalas, Phys. Rev. **157**, 389 (1967).
[4] M. K. Niranjan, B. R. Sahu, and L. Kleinman, Phys. Rev. B **70**, 180406(R) (2004).
[5] H. Yamaguchi, A. K. Das, A. Ney, T. Hesjedal, C. Pampuch, D. M. Schaadt, and R. Koch, Europhys. Lett. **72**, 479 (2005).
[6] A. Moser, K. Takano, D. T. Margulies, M. Albrecht, Y. Sonobe, Y. Ikeda, S. Sun, and E. E. Fullerton, J. Phys. D **35**, R157 (2002).
[7] T. W. McDaniel, J. Phys.: Condens. Matter **17**, R315 (2005).
[8] Y. Takagaki, C. Herrmann, E. Wiebicke, J. Herfort, L. Däweritz, and K. H. Ploog, Appl. Phys. Lett. **88**, 032504 (2006).
[9] S. H. Chun, S. J. Potashnik, K. C. Ku, J. J. Berry, P. Schiffer, and N. Samarth, Appl. Phys. Lett. **78**, 2530 (2001).
[10] K.-S. Ryu, D.-H. Kim, S.-C. Shin, and H. Akinaga, Phys. Rev. B **71**, 155308 (2005).
[11] V. Skumryev, S. Stoyanov, Y. Zhang, G. Hadjipanayis, D. Givord, and J. Nogués, Nature (London) **423**, 850 (2003).
[12] Y. Takagaki, E. Wiebicke, L. Däweritz, and K. H. Ploog, J. Solid State Chem. **179**, 2271 (2006).
[13] R. Street and J. C. Woolley, Proc. Phys. Soc. London **62**, 562 (1949).
[14] W. Luo, S. R. Nagel, T. F. Rosenbaum, and R. E. Rosensweig, Phys. Rev. Lett. **67**, 2721 (1991); H. Mamiya, I. Nakatani, and T. Furubayashi, *ibid.* **82**, 4332 (1999).
[15] Y. Takagaki, B. Jenichen, C. Herrmann, E. Wiebicke, L. Däweritz, and K. H. Ploog, Phys. Rev. B **73**, 125324 (2006).
[16] An increase of the magnetization in ferromagnetic films when the external magnetic field was set to be *somewhat larger than the coercive field* was reported in M. Marinescu and H. Chiriac, J. Magn. Magn. Mater. **272-276**, e1943 (2004). The anomalous behavior was attributed to the exchange and/or dipole-dipole interactions.
[17] Y. Takagaki and K. H. Ploog, Phys. Rev. B **71**, 184439 (2005).
[18] Y. Takagaki, J. Herfort, and K. H. Ploog, J. Appl. Phys. **98**, 093901 (2005).
[19] B. Jenichen, Y. Takagaki, K. H. Ploog, N. Darowski, R. Feyerherm, and I. Zizak, Appl. Phys. Lett. **89**, 051915 (2006).
[20] A substantial decrease of the magnetic moment with T near T_C can lead to a significant lowering of E_B, and thus reduction of τ. See, for example, D. A. Garanin and O. Chubykalo-Fesenko, Phys. Rev. B **70**, 212409 (2004). The effect, however, will not be significant in MnAs disks due to the abrupt disappearance of the magnetic order at T_C.
[21] V. A. Chernenko, L. Wee, P. G. McCormick, and R. Street, J. Appl. Phys. **85**, 7833 (1999).
[22] J. Mira, F. Rivadulla, J. Rivas, A. Fondado, T. Guidi, R. Caciuffo, F. Carsughi, P. G. Radaellil, and J. B. Goodenough, Phys. Rev. Lett. **90**, 097203 (2003).

Morphware – Eine anpassungsfähige Logik

Neues Anwendungsgebiet für magnetische Materialien

Der logische Aufbau von Morphware-Prozessoren ist nicht starr wie in konventioneller Hardware, sondern kann durch die Software verändert werden. Jüngste Forschungen zeigen, dass sich mit magnetoresistiven Elementen, wie sie in MRAM verwendet werden, eine Vielzahl von logischen Funktionen realisieren lassen. Im Unterschied zu einer auf Silizium-Technologie basierenden Morphware können damit elementare logische Funktionen (AND, OR, NAND, NOR) mit der Taktgeschwindigkeit des Prozessors rekonfiguriert werden. Da magnetische Information nicht flüchtig ist, übernehmen magnetologische Elemente Logik- und Speicherfunktion.

Reinhold Koch

Im Verlauf der letzten Jahrzehnte haben wir uns daran gewöhnt, dass Computer bereits zwei bis drei Jahre nach ihrer Anschaffung völlig veraltet sind. Diese beeindruckende Erfolgsgeschichte der Halbleitertechnologie manifestiert sich im viel zitierten Moore'schen Gesetz, das eine Verdopplung der Leistungsfähigkeit eines Prozessors alle 18 Monate vorhersagt. In herkömmlichen Prozessoren wird die Leistungssteigerung im Wesentlichen durch die Miniaturisierung der Transistoren erreicht, was durch die damit verbundene Verkürzung der Informationswege zu einer nominellen Geschwindigkeitserhöhung führt. Mittlerweile liegt die Grösse der Transistoren unter 100 nm und eine weitere Miniaturisierung stösst an technologische, physikalische und auch ökonomische Grenzen. Bis zum Jahr 2018 können wir noch eine Verbesserung um einen Faktor 20 erwarten [1].

Nichtsdestotrotz ist ein Ende in Sichtweite. Daher wird seit einigen Jahren intensiv an Alternativen geforscht. Beispiele sind die Entwicklung neuer und schnellerer Halbleitermaterialien, eine molekulare Elektronik, der Quanten-Computer oder die Aufwertung des Transistors durch Ausnützung des Elektronenspins in einer zukünftigen Spintronik.

Rekonfigurierbare Prozessoren

Ein anderer und viel versprechender Ansatz betrifft ein neues Prozessor-Design, das auf logischen Elementen basiert, deren Funktion durch die Software verändert werden kann – so genannte rekonfigurierbare Prozessoren. Derzeit verfügt die Mehrheit der zum Einsatz kommenden Prozessoren über eine fest verdrahtete logische Architektur. Je nach ihren Eigenschaften unterscheidet man zwei Arten von Prozessoren: Die so genannten All-Zweck-Prozessoren, zu denen der zentrale Prozessor (CPU) eines jeden Computers zählt, und die anwendungsspezifischen integrierten Schaltungen (ASICs). Erstere sind mit einem umfangreichen Befehlssatz von logischen Funktionen ausgestattet, die von der Software bei Bedarf aufgerufen werden können. So verarbeitet die CPU eines Heimcomputers Text, stellt Videosequenzen dar, löst komplizierte Gleichungssysteme oder übernimmt diverse Steuerfunktionen. Die Vielseitigkeit geht allerdings auf Kosten der Geschwindigkeit, da der Prozessor für keine dieser Aufgaben optimiert ist. Zudem ist immer nur ein geringer Teil der vorhandenen Logikfunktionen für eine Aufgabe geeignet. Im Gegensatz dazu sind ASICs einfacher strukturiert. Ihr Befehlssatz ist stark abgespeckt und für bestimmte Aufgaben optimiert. Auf Sound- oder Grafikkarten verrichten solche Chips deshalb ihren Dienst wesentlich schneller und effizienter, als der zentrale Prozessor es könnte.

Mittlerweile gibt es Hardware, deren logischer Aufbau nicht unwiderruflich festliegt, so genannte rekonfigurierbare Morphware. Ein Beispiel dafür sind die kommerziell erhältlichen FPGAs (Field-Programmable Gate Arrays). Diese bestehen aus fest verdrahteten Modulen von Transistoren, die komplexe logische Operationen ausführen. Die Verdrahtung der Module untereinander lässt sich programmieren, mithin ihr Zusammenspiel, womit die Schaltungslogik des FPGAs umgebaut wird. In der Praxis haben sich FPGAs bewährt: Sie verschlüsseln oder komprimieren Daten und erkennen Objekte in Videoaufnahmen zehn- bis hundertmal schneller als eine herkömmliche CPU [2].

Die bisherige Morphware, die auf der etablierten Siliziumtechnologie CMOS (Complementary Metal Oxide Semiconductor) basiert, bringt aber entscheidende Nachteile mit sich. Die Neuverschaltung der logischen Blöcke dauert mehr als zehn Nanosekunden, während die Taktgeschwindigkeit der FPGAs viel höher ist. Eine Rekonfiguration innerhalb eines Computertakts ist deshalb nicht möglich. Zudem ist der Platzbedarf von FPGAs hoch, was die Anzahl und Geschwindigkeit von gleichzeitig ausführbaren logischen Operationen limitiert.

Magnetische Morphware

In jüngerer Zeit arbeiten einige Forschungsgruppen [3-5] an einer neuen Art von Morphware, deren logische Elemente (Gatter, englisch gates) aus dünnen magnetischen Schichten bestehen. Da die Ummagnetisierung nur wenige Zehntel einer Nanosekunde dauert, ist die Neukonfiguration innerhalb des Prozessortaktes kein Traum mehr. Auf Grund der Nicht-Flüchtigkeit magnetischer Information haben derartige Elemente den Vorteil, dass die berechnete Information gespeichert bleibt. Sie steht damit für einen folgenden Verarbeitungsschritt zur Verfügung und muss nicht zeitaufwendig

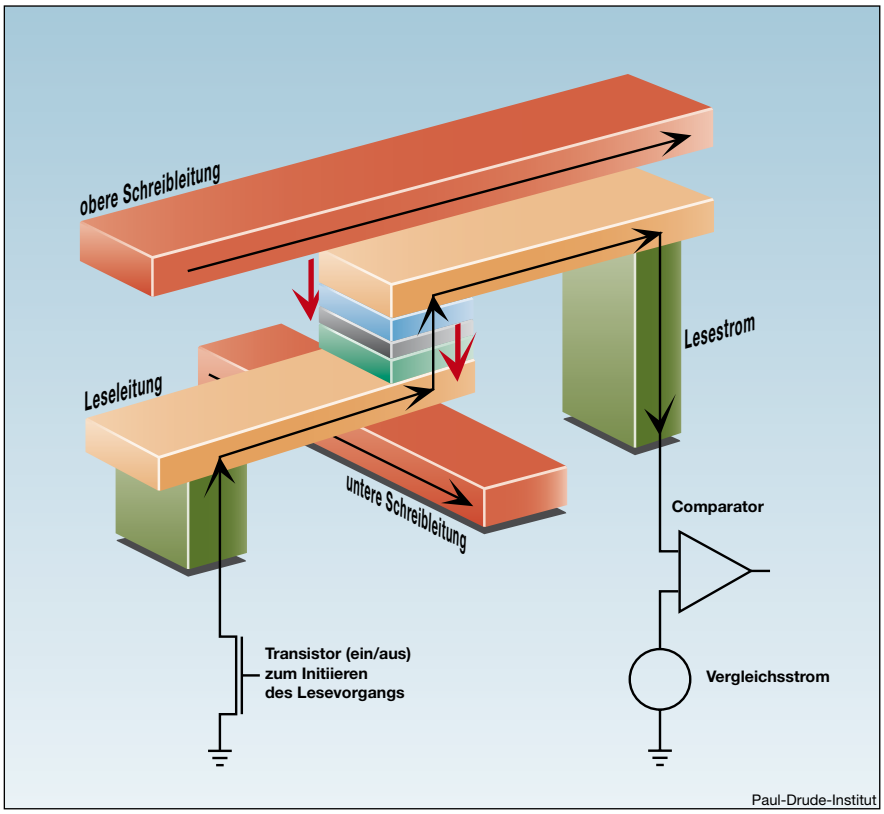

Bild 1 Prinzip einer MRAM-Speicherzelle

Das Herz einer MRAM-Speicherzelle ist ein magnetoresistives Element, bestehend aus zwei magnetischen Schichten (grün, blau), die durch eine isolierende Schicht (grau) als Tunnelbarriere getrennt sind. Je nachdem, ob die Magnetisierung der beiden Schichten parallel oder antiparallel ist, ist der elektrische Widerstand der Zelle klein bzw. gross und kann den logischen Bits ‚1' bzw. ‚0' zugeordnet werden. Das Auslesen der logischen Bits erfolgt durch die zwei Elektroden (braun) am oberen und unteren Ende des magnetoresistiven Elements. Der Transistor (links) schaltet die Zelle für den Auslesevorgang frei und garantiert selektives Auslesen. Der Comparator (rechts) vergleicht das Auslesesignal mit einem Sollwert. Das Schreiben des Bits erfolgt über die beiden Schreibleitungen (rot), mit denen das für die Ummagnetisierung der oberen Schicht erforderliche Magnetfeld (rote Pfeile) erzeugt wird. Die Magnetisierung der unteren Schicht ist fixiert. Durch die Verwendung von zwei Schreibleitungen und ihre gitterförmige Anordnung gelingt es, einzelne magnetoresistive Elemente im MRAM-Chip selektiv anzusprechen. Siehe: www.freescale.com

intern aus einem Speicher neu geladen werden. Im Gegensatz zu CMOS-Bauteilen muss sie auch nicht während des Betriebes permanent aufgefrischt werden, weshalb magnetologische Komponenten weniger Strom benötigen. Mehr noch: Selbst wenn der Rechner ausgeschaltet wird, bleibt die berechnete Information erhalten.

Die Grundlage magnetologischer Bauelemente bildet die Technologie neuer Datenspeicher, die als MRAM (Magnetic Random-Access Memory) demnächst auf den Markt kommen [6]. Ihre kleinste Baueinheit – das magnetoresistive Element – besteht aus zwei dünnen ferromagnetischen Schichten, die durch eine unmagnetische Abstandsschicht getrennt sind (Bild 1). Letztere verhindert das Übersprechen der Magnetisierung von einer Lage zur anderen. Der Wert des digitalen Bits einer Speicherzelle hängt davon ab, ob die Magnetisierungen der aktiven Schichten parallel oder antiparallel zueinander ausgerichtet sind. Im ersten Fall stellt die Speicherzelle einem elektrischen Auslesestrom nur einen kleinen Widerstand entgegen; dieser Zustand repräsentiert beispielsweise eine digitale ‚1'. Eine antiparallele Orientierung hingegen erhöht den Magnetowiderstand und das Element befindet sich im Zustand ‚0'. Der Magnetowiderstand von geschichteten Systemen ist üblicherweise deutlich höher als im Volumenmaterial, was das Auslesen der magnetischen Bits erleichtert und damit höhere Lesegeschwindigkeiten erlaubt. Diese besondere Eigenschaft wird als Riesenmagnetowiderstand oder Tunnelmagnetowiderstand bezeichnet, je nachdem, ob die Abstandsschicht elektrisch leitend oder isolierend ist. Das Schreiben des Bits erfolgt über gleichzeitigen Strom in zwei zueinander senkrechten Zuleitungen, deren Magnetfeld die Magnetisierung der oberen Lage schaltet. Die Magnetisierung der unteren Lage ist fest.

Dass magnetoresistive Elemente auch für die Darstellung von Logikfunktionen geeignet sind, zeigt die aktuelle Forschung. Wer zum Beispiel die beiden Schreibleitungen der MRAM-Zelle als die logischen Eingänge A und B verwendet, realisiert AND- und OR-Funktionen, je nachdem, ob der Strom an beiden Schreibleitungen oder nur an einer für die Ummagnetisierung der oberen Lage

ausreicht. Dies lässt sich entweder durch geeignete Wahl der Koerzitivfeldstärke[1)] oder über die Grösse der Schreibströme einstellen [3]. Wenn beide Eingänge auf eine Schreibleitung gelegt werden, kann das Magnetfeld der zweiten Schreibleitung dazu verwendet werden, zwischen der AND- und OR-Funktion umzuschalten [4]. Wie aus Bild 3 ersichtlich, können magnetoresistive Elemente in vier verschiedenen Zuständen vorliegen, zwei davon mit einer parallelen Ausrichtung der Magnetisierung der beiden magnetischen Schichten, zwei davon mit antiparalleler Orientierung. Die Forschungsgruppe Nanoakustik am Paul-Drude-Institut hat gezeigt, dass jeder dieser Zustände eine andere elementare logische Funktion repräsentiert [5], die durch den bei magnetoresistiven Elementen immer erforderlichen Setzschritt vorgegeben werden kann.

Der Aufbau des am Paul-Drude-Institut studierten magnetologischen Gatters [5] ist dem einer MRAM-Zelle sehr ähnlich. Im Zentrum steht ebenfalls ein magnetoresistives Element (Bild 2). Die parallele und antiparallele Magnetisierung der beiden Schichten mit niedrigem bzw. hohem Magnetowiderstand definieren den logischen Wert des Auslesesignals (‚1' bzw. ‚0'). Das Schreiben der Zelle erfolgt – wie in einer MRAM-Zelle – über das Magnetfeld von stromdurchflossenen Zuleitungen oder, ganz aktuell, über das Drehmoment, das ein spinpolarisierter Strom[2)] auf eine magnetische Lage ausübt. Die drei Eingänge müssen aber nicht unbedingt über drei unterschiedliche Zuleitungen geführt werden, wie in Bild 2 der Übersichtlichkeit halber dargestellt, im Prinzip wäre bereits eine Zuleitung ausreichend. Die Koerzitivfeldstärken der beiden magnetischen Schichten sind so gewählt, dass die obere Schicht nur geschaltet werden kann, wenn die beiden oberen Eingänge, A und B, adressiert sind. Für das Schalten der unteren Lage ist zusätzlich ein Strom am dritten Eingang C erforderlich. Der Logikwert des Eingangs wird über die Richtung der erzielten Magnetisierung definiert: ein positiver Strom führt zu einer positiven Magnetisierung und entspricht einer logischen ‚1', ein negativer Strom bewirkt eine negative Magnetisierung und stellt eine logische ‚0' am Eingang dar.

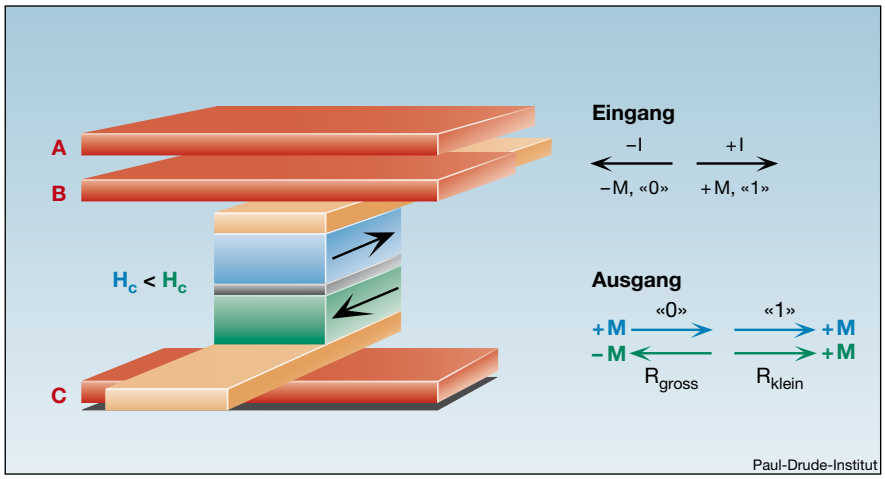

Bild 2 Prinzip eines magnetischen Logikelements

Wie in der MRAM-Speicherzelle bildet ein magnetoresistives Element das Herz des magnetologischen Elements. Je nachdem, ob die Magnetisierung der beiden Schichten (blau, grün) parallel oder antiparallel ist, ist der elektrische Widerstand (R) der Zelle klein bzw. gross und definiert den logischen Ausgangswert als ‚1' bzw. ‚0'. Die zwei Elektroden (braun) am oberen und unteren Ende des magnetoresistiven Elements dienen zum Auslesen der logischen Bits. Die Ummagnetisierung erfolgt durch einen Strom an den Eingangsleitungen A, B, und C (rot). Die Koerzitivfeldstärken der beiden magnetischen Schichten sind so gewählt, dass die obere Schicht nur dann geschaltet werden kann, wenn an den Eingängen A und B Strom mit demselben Vorzeichen anliegt. Für das Schalten der unteren Lage ist zusätzlich ein Strom am dritten Eingang C erforderlich. Definitionsgemäss führt ein positiver Strom zu einer positiven Magnetisierung und stellt eine logische ‚1' am Eingang dar. Ein negativer Strom hingegen bewirkt eine negative Magnetisierung und entspricht einer logischen ‚0'.

Elementare logische Funktionen

Für das AND-Gatter startet man vom linken Ausgangszustand in Bild 3, der einer logischen ‚0' entspricht. Die Ummagnetisierung der oberen magnetischen Lage von links nach rechts in den entsprechenden parallelen Zustand der Zelle wird nur durch einen positiven Strom an beiden Eingängen A und B erreicht. Nur dann ändert sich der Ausgabewert der Zelle von ‚0' auf ‚1', was der AND-Funktion entspricht (vergleiche entsprechende Logiktabelle in Bild 3). Für die OR-Funktion sind beide magnetischen Lagen ursprünglich nach rechts magnetisiert. Das Umschalten von diesem parallelen Ausgangszustand (‚1') in den dazugehörigen antiparallelen Zustand (‚0') wird nur durch zwei negative Ströme (‚0') erreicht. Die beiden anderen Anfangszustände der Zelle erhält man durch Ummagnetisierung der unteren Lage,

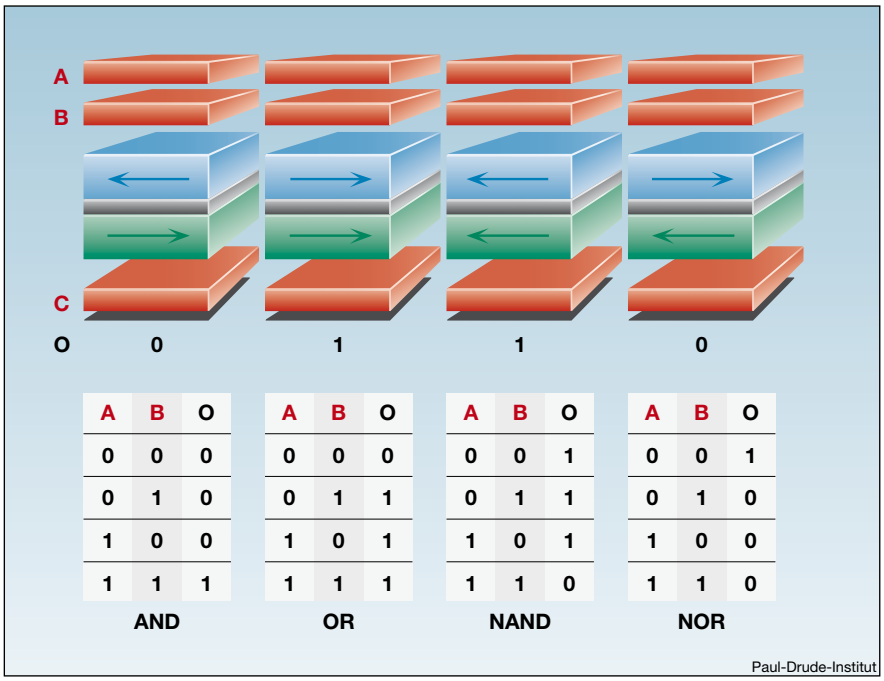

Bild 3 Elementare logische Funktionen

Zur Realisierung der vier elementaren Logikfunktionen AND, OR, NAND und NOR wird das magnetologische Element in einen seiner vier möglichen Zustände initialisiert, d.h. Magnetisierung oben/unten = links/rechts, rechts/rechts, links/links oder rechts/links. Für das AND-Gatter startet man vom linken Ausgangszustand, der einer logischen ‚0' entspricht. Die Ummagnetisierung der oberen magnetischen Lage von links nach rechts in den entsprechenden parallelen Zustand der Zelle wird nur durch einen positiven Strom an beiden Eingängen A und B erreicht. Nur dann ändert sich der Ausgabewert der Zelle von ‚0' auf ‚1', was der AND-Funktion entspricht (siehe entsprechende Logiktabelle). Für die OR-Funktion sind beide magnetischen Lagen ursprünglich nach rechts magnetisiert. Das Umschalten von diesem parallelen Ausgangszustand (‚1') in den dazugehörigen antiparallelen Zustand (‚0') wird nur durch zwei negative Ströme (‚0') erreicht. Die beiden anderen Anfangszustände der Zelle erhält man durch Ummagnetisierung der unteren Lage, was den Ausgangswert negiert und die Logikfunktionen NAND bzw. NOR generiert.

was einer Negation ihres Ausgangswertes entspricht und zu den Logikfunktionen NAND bzw. NOR führt.

Dem gemäss verläuft eine logische Operation mit einem magnetologischen Element in zwei Schritten: Zuerst erfolgt der Setzschritt, in dem die logische Funktion des Gatters programmiert wird. Für das OR und NAND werden alle drei Eingänge mit positivem bzw. negativem Strom adressiert. Um das AND und NOR zu erhalten, muss anschliessend noch die Magnetisierung der oberen Lage mit den Eingängen A und B entsprechend verstellt werden. Im zweiten Schritt wird dann die logische Operation durchgeführt, bei der nur mehr die Zuleitungen A und B mit den logischen Eingangswerten belegt werden.

Um die NOT-Funktion zu erhalten, muss nur die Magnetisierung der unteren magnetischen Schicht negativ programmiert werden (Bild 4). Für die logische Operation werden dann die beiden oberen Zuleitungen gleichzeitig mit dem zu negierenden Eingang adressiert.

Die Funktionen OR, AND und NOT bilden eine universelle Basis für die Darstellung beliebiger Logikoperationen. Auch das NAND allein sowie das NOR sind universelle Gatter. Damit stellt ein einzelnes magnetologisches Element einen äusserst komfortablen Satz an elementaren logischen Funktionen bereit, um selbst komplexe Schaltkreise aufzubauen.

XOR und XNOR

Durch eine modifizierte Ansteuerung lassen sich auch höherwertigere logische Funktionen realisieren [7] wie das XOR, das zwischen gleichen und entgegengesetzten Eingängen unterscheidet: XOR gibt eine ‚1' bei gleichen Eingängen (‚0'/‚0' oder ‚1'/‚1') aus und eine ‚0' bei komplementären (‚1'/‚0' oder ‚0'/‚1'). Das XOR ist die wichtigste Komponente eines so genannten Volladdierers. Der wiederum ist die am häufigsten benötigte Einheit in einem Prozessor [8]. Zwei magnetologische Gatter reichen dazu aus (Bild 5), in der CMOS-Technologie sind dafür 14 Transistoren nötig.

CMOS versus Magnetologik

Das auf magnetoresistiven Elementen basierende Konzept für eine magnetische Logik zeichnet sich durch eine Reihe von Vorteilen gegenüber der konventionellen, transistorgestützen Logik aus. Da ein Gatter mehrere Logikfunktionen repräsentieren kann, die durch den Setzschritt vorgegeben werden, ist sein Einsatzbereich nicht länger durch die Hardware vorherbestimmt. In CMOS wird die Logik eines normalen Transistor-Gatters durch die Verdrahtung definiert und fixiert. Ein magnetologischer Prozessor hingegen stellt nur einen quasi universellen Block von logischen Gattern bereit, von denen jedes individuell für die gewünschte Anwendung programmiert werden kann. Ein solcher Prozessor kommt daher mit viel weniger logischen Gattern aus als sein CMOS-Pendant, das immer nur wenige Prozent seiner Gatter für eine Aufgabe einsetzt. Die Flexibilität der Gatter gestattet es, neue Software leichter zu implementieren. Durch die hohe Schaltgeschwindigkeit von magnetischen Materialien (~100 ps) eröffnen sich rekonfigurierbare (sogenannte Chamäleon-)Prozessoren, die mit der Taktgeschwindigkeit des Prozessors reprogrammierbar sind. Magnetische Information ist nicht flüchtig; daher vereinigt ein magnetischer Chamäleon-Prozessor beides, Logik- und Speicherfunktion. Berechnete Bits müssen nicht länger zeit- und energieaufwändig vom Prozessor in den Speicher und zurück befördert werden. Auf Grund der Nicht-Flüchtigkeit der Information entfällt auch die Notwendigkeit zur Synchronisation beim Betrieb, was den Programmablauf vereinfacht und beschleunigt. Sogar ein vollständig asynchroner Betrieb ist denkbar. Alles zusammen ermöglicht den Einsatz effizienterer Algorithmen und Arbeitsprozesse. Somit wächst die Leistungsfähigkeit der Prozessoren ohne die in der Siliziumtechnologie zur Geschwindigkeitssteigerung nötige Miniaturisierung.

Ein Blick voraus

Das künftige Design eines magnetischen Morphware-Prozessors bleibt vorerst ein akademisches Konzept. Doch dank der grossen Ähnlichkeit zum MRAM profitiert die Magnetologik von dessen Entwicklung. Die Eingangsleitungen könnten wie im MRAM als Gitter aufgebaut werden, mit den magnetologischen Elementen in den Kreuzungspunkten. Erhalten beide Zuführungen gleichzeitig ein Steuersignal, schaltet das jeweilige Element. Eine Matrix von CMOS-Transistoren würde weiterhin als Interface fungieren und die Nachverstärkung der für die Weiterverarbeitung zu kleinen Leseströme übernehmen. Um die Technik in den Markt einzuführen, könnte

zunächst ein MRAM-Chip als Prozessor fungieren, der – weil nur eine seiner beiden Schichten schaltbar ist – über AND- und OR-, beziehungsweise NAND- und NOR-Funktionen verfügt.

Um das volle Potenzial eines magnetischen Prozessors auszuschöpfen, müssen noch diverse Probleme gelöst werden. Noch gelingt es nicht, die beiden magnetischen Lagen unabhängig voneinander zu schalten. Zudem: Da ein magnetischer Prozessor auf Grund seiner Flexibilität die meiste Zeit unter Volllast arbeiten wird, entwickelt er viel mehr Wärme als sein Siliziumpendant, was die Haltbarkeit seiner Logikelemente beeinträchtigt. Den Ingenieuren muss es gelingen, für magnetologische Gatter eine Lebensdauer von 10^{16} bis 10^{17} Schaltzyklen zu erreichen – das Hundert- bis Tausendfache der bislang erreichten Werte. Bis dahin mag es helfen, dass defekte Gatter während des Bootvorganges eines Computers entdeckt und überbrückt werden können. Zur Optimierung einer Magnetologik sind verbesserte Materialien mit höherem Magnetowiderstand gesucht, die mit Halbleitern kompatibel sind, da diese weiterhin als Verstärker gefragt sind.

Vielleicht wird es die schwierigste Hürde sein, eine geeignete Compilersprache zu entwickeln und neue Algorithmen zu finden, die alle Vorteile der in Echtzeit reprogrammierbaren logischen Gatter ausnützen. Um tatsächlich den magnetischen Chamäleon-Prozessor mit Erfolg auf den Markt zu bringen, ist ein interdisziplinärer Forschungseinsatz angesagt, der die Fachkenntnisse von Spezialisten auf den Gebieten der Materialwissenschaften, Hardware-Design, Elektronik, Computerwissenschaften und Mathematik vereint.

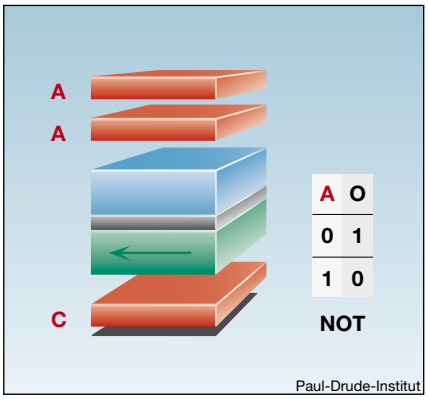

Bild 4 NOT

Für das NOT-Gatter muss nur die Magnetisierung der unteren magnetischen Schicht (grün) entsprechend programmiert werden. Für die logische Operation werden die beiden oberen Zuleitungen gleichzeitig mit dem Eingang A adressiert.

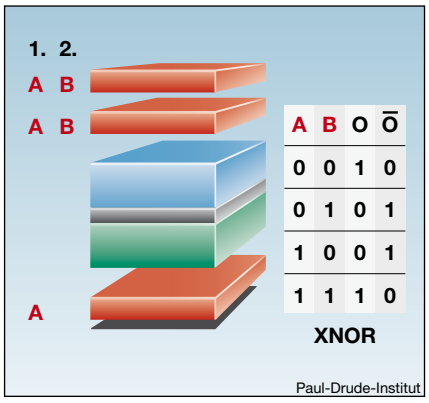

Bild 5 XNOR und XOR

Für das XNOR-Gatter wird zuerst mit dem Eingang A an allen drei Zuleitungen die Magnetisierung beider Lagen ausgerichtet. Dann wird der Eingang B nur an die beiden oberen Zuleitungen zur Magnetisierung der oberen Lage angelegt. Bei gleichen Eingängen ergibt sich eine ‚1' am Ausgang, bei komplementären eine ‚0'. Um das XOR zu erhalten, muss der Ausgang des XNORs negiert werden (rechte Spalte der Logiktabelle), z.B. mit dem NOT-Gatter.

Referenzen

[1] The International Technology Roadmap for Semiconductors
[2] K. Compton, S. Hauck, Reconfigurable Computing: A Survey of Systems and Software, ACM Computing Surveys, Bd. 34, 171 (2002)
[3] W. C. Black Jr., B. J. Das, Programmable Logic Using Giant-Magnetoresistance and Spin-Dependent Tunneling Devices, J. Appl. Phys. 87, 6674 (2000)
[4] R. Richter, H. Boeve, L. Bär, J. Bangert, U. K. Klostermann, J. Wecker, G. Reiss, J. Magn. Magn. Mater. 240, 127 (2002)
[5] A. Ney, C. Pampuch, R. Koch, K. H. Ploog, Programmable Computing with a Single Magnetoresistive Element, Nature, 425, 485 (2003)
[6] R. Cowburn, The Future of Universal Memory, Materials Today, Bd. 6, Heft 7/8, S. 32, 2003
[7] C. Pampuch, A. Ney, R. Koch, A universal gate for magnetologic computers, Euro-phys. Lett. 66, 895 (2004)
[8] C. Pampuch, A. Ney, R. Koch, Programmable magnetologic full adder, Appl. Phys. A 79, 415 (2004)

Angaben zum Autor

Reinhold Koch leitet die Forschergruppe Nanoakustik am Paul-Drude-Institut für Festkörperelektronik in Berlin. Er ist Chemiker und habilitierte 1993 an der Freien Universität in Berlin. 1994 erhielt er den Karl-Scheel-Preis für seine Arbeiten auf dem Gebiet der mechanischen Spannungen in dünnen Schichten sowie Strukturuntersuchungen mit einem Rastertunnelmikroskop.
Paul-Drude-Institut für Festkörperelektronik, D-10117 Berlin, koch (at) pdi-berlin.de

[1] Als Koerzitivfeldstärke bezeichnet man die magnetische Feldstärke, die notwendig ist, um eine ferromagnetische Substanz vollständig zu entmagnetisieren, so dass der resultierende Gesamtfluss bzw. die lokale Flussdichte gleich null ist.
[2] Bei einem spinpolarisierten Strom in einem Halbleiter haben alle Elektronen den gleichen definierten Spin. Dieser wird ausgenutzt, wenn sie auf eine ferromagnetische Schicht treffen.

Résumé

Morphware – une logique susceptible d'adaptation

Nouveau domaine d'application pour matériaux magnétiques. La constitution logique des processeurs Morphware n'est pas rigide comme dans le matériel conventionnel mais peut être modifiée par le logiciel. De récentes recherches montrent que des éléments magnétorésistants comme ceux utilisés en MRAM permettent de réaliser une multitude de fonctions logiques. Contrairement à un Morphware basé sur la technologie au silicium, ils permettent de reconfigurer des fonctions logiques (ET, OU, NON-ET, NON-OU) à la vitesse d'horloge du processeur. Etant donné que l'information magnétique n'est pas volatile, les éléments magnétologiques assument la fonction de logique et de mémoire.

IOP PUBLISHING JOURNAL OF PHYSICS D: APPLIED PHYSICS

J. Phys. D: Appl. Phys. **40** (2007) 1631–1634 doi:10.1088/0022-3727/40/6/007

Growth temperature dependent interfacial reaction of Heusler-alloy Co_2FeSi/GaAs(001) hybrid structures

M Hashimoto, J Herfort, A Trampert, H-P Schönherr and K H Ploog

Paul-Drude-Institut für Festkörperelektronik, Hausvogteiplatz 5–7, 10117 Berlin, Germany

E-mail: hashimoto@pdi-berlin.de

Received 29 November 2006, in final form 5 January 2007
Published 2 March 2007
Online at stacks.iop.org/JPhysD/40/1631

Abstract

We have studied the growth temperature dependence of the interfacial reaction of Heusler-alloy Co_2FeSi/GaAs(0 0 1) hybrid structures. The reaction proceeds dominantly by Co in-diffusion, resulting in the formation of isolated grains in the GaAs substrate starting at the growth temperature T_G of 200–250 °C. The interfacial reaction is classified into two stages: (i) intermediate T_G regime (250–300 °C), where a highly oriented single-crystalline phase, most likely ternary Co_2GaAs, is formed in the topotaxial relationship of $Co_2GaAs[1\,\bar{1}\,0](1\,1\,0)$ || $GaAs[1\,\bar{1}\,0](0\,0\,1)$; and (ii) high T_G regime (⩾350 °C) where binary CoAs is formed in the asymmetric topotaxial relationship of $CoAs[0\,0\,1](2\,1\,0)$ || $GaAs[1\,1\,0](0\,0\,1)$.

(Some figures in this article are in colour only in the electronic version)

1. Introduction

Half-metallic ferromagnets (HMF), which have 100% spin-polarized carriers at the Fermi level, are promising candidates for spintronics devices, e.g. magnetic tunnelling junction and spin injection device. The potential HMF include some diluted magnetic semiconductors, oxides and Heusler alloys. Heusler alloys such as Co_2MnSi and Co_2MnGe are especially attractive because of their high Curie temperature T_C and close lattice-matching with semiconductors [1]. In addition, a recent study suggests that Co_2FeSi, which has the highest T_C (>1100 K) and the largest magnetic moment (6 μ_B) among the Heusler alloys as well as a small lattice-mismatch with respect to GaAs (∼0.08%) [2], is indeed a HMF [3].

It is believed that the spin injection efficiency depends on the interface perfection of the ferromagnet/semiconductor (FM/SC) hybrid structures. The growth of a FM layer on SC substrates at high growth temperatures generally leads to the formation of magnetically modified interfacial compounds which could reduce the spin-polarization of injected carriers. Therefore, a thermally stable FM/SC interface is highly desirable for efficient electrical spin injection. We have demonstrated so far that Heusler-alloy/SC interfaces have a superior thermal stability to conventional FM metals such as Fe, Co and Ni [4, 5]. However, despite a number of reports concerning the growth of Heusler-alloy/SC hybrid structures, little information is available as to the detailed phase formation at the interface. Here, we report on the growth temperature dependence of the interfacial phase formation in Heusler-alloy Co_2FeSi/GaAs(0 0 1) hybrid structures.

2. Sample preparation

The Co_2FeSi layers were grown on semi-insulating GaAs(0 0 1) substrates by molecular-beam epitaxy. Before the growth of the Co_2FeSi layer, 100 nm thick GaAs templates were prepared in the III–V growth chamber using standard GaAs growth conditions. An As-terminated $c(4 \times 4)$ reconstructed GaAs(0 0 1) surface was realized by cooling the samples down to 420 °C under As_4 flux to prevent the formation of macroscopic defects on the surface similar to our studies on Fe/GaAs(0 0 1) [6] and Fe_3Si/GaAs(0 0 1) [7]. The samples were then transferred under ultrahigh vacuum (UHV) to the As-free deposition chamber which is directly connected to the III–V growth chamber via an interlock. Co, Fe and Si were codeposited from high temperature effusion cells with a base pressure of 1×10^{-10} Torr. The growth

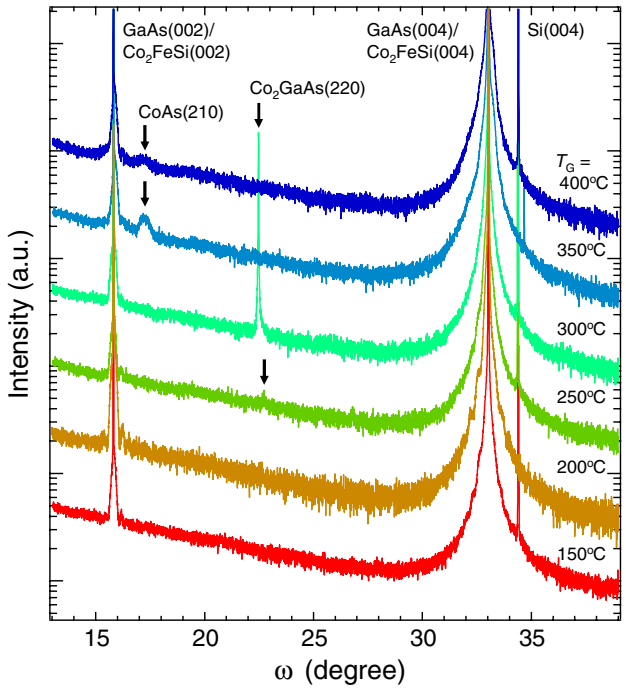

Figure 1. Wide-range XRD ω–2θ curves taken with an open-detector of the films grown in the range 150–400 °C. The sharp peaks at $\omega = 34.56°$ originate from the Si(0 0 4) reflection from the sample holder. Additional peaks are marked by arrows.

temperature T_G for the Co_2FeSi layers was varied in the range 100–400 °C. The thickness of the layers d was determined by high-resolution x-ray diffraction (HRXRD) and X-ray reflectivity (XRR) measurements to be 18.5 nm. Details of the growth and structural characterizations including the determination of the stoichiometric composition can be found elsewhere [8, 9].

The structural characterization of the Co_2FeSi/GaAs(0 0 1) interface was performed by XRD and cross-section transmission electron microscopy (TEM). The XRD ω–2θ curves were taken after growth with a PANalytical X'pert diffractometer using Cu K_α radiation with a Ge(2 2 0) monochromator. A JEM-3010 microscope was used for the conventional TEM as well as the high-resolution (HR) TEM analysis (point resolution: 0.17 nm). Thin specimens were prepared in cross-sectional configuration along both the [1 1 0] and the orthogonal [1 $\bar{1}$ 0] direction. After mechanical grinding, Ar-ion milling was applied to achieve electron transparency with thinning conditions of 2.5–2.7 keV beam energy and a beam incident angle of 2.5°–3° in order to minimize surface damage.

3. Results and discussion

Figure 1 shows the XRD ω–2θ curves measured with an open detector for Co_2FeSi films grown in the range of 150–400 °C. The GaAs(0 0 2) and (0 0 4) peaks, which overlap with the Co_2FeSi(0 0 2) and (0 0 4) peaks, respectively, are labelled. The sharp peak at $\omega = 34.56°$ originates from the Si(0 0 4) reflection of the sample holder. Another sharp peak around $\omega \simeq 23°$ was observed for the films grown in the intermediate T_G regime (250 and 300 °C), although the peak intensity is very low for the 250 °C film. This peak disappears in the higher T_G regime ($\geqslant$350 °C) and a rather broad peak at $\omega = 17.3°$ appears instead. These results indicate that the Co_2FeSi/GaAs interface goes through two stages of interfacial reaction depending on T_G. The peak at $\omega = 17.3°$ is close to that of the binary CoAs(2 1 0) and $(Fe_{1-x}Co_x)_2As$(1 1 0) ($0 < x < 0.3$) reflection [10, 11], whereas the peak at $\omega \simeq 23°$ is close to that of CoAs(2 2 0) and ternary Co_2GaAs(2 2 0). The sharp peak compared with that of the higher T_G regime indicates a highly oriented phase with respect to the GaAs substrate.

It is known that ternary Co_2GaAs is a metastable phase formed at relatively low temperatures in Co/GaAs [12–15]. Co_2GaAs is isostructural with binary CoAs and has an orthorhombic structure with a lattice parameter close to that of CoAs [10, 13, 16]. The Co_2GaAs phase is stabilized in GaAs forming two types of domains with the orientation relationship $Co_2GaAs[1\,1\,0](1\,\bar{1}\,0)$ || $GaAs[1\,\bar{1}\,0](0\,0\,1)$ and $Co_2GaAs[1\,1\,0](1\,\bar{1}\,0)$ || $GaAs[1\,1\,0](0\,0\,1)$ [15]. This relationship is consistent with our observation of the (2 2 0) peak in our symmetric ω–2θ measurements with an open detector. It should be noted, however, that the Co_2GaAs(2 2 0) is not exactly parallel to the GaAs(0 0 1) since our HRXRD ω–2θ measurements with an analyzer crystal did not detect the Co_2GaAs(2 2 0) peak. The ternary phase is subsequently decomposed into the compounds having the lowest heat of formation, namely the most stable binary CoAs and CoGa, at higher temperatures [13–16]. These facts suggest that the interfacial phase observed in the intermediate T_G regime is most likely ternary Co_2GaAs.

In order to further confirm the phase in the 250–300 °C films and to determine the orientation relationship with the substrate, we recorded XRD pole-figures of these films. Pole-figures are ϕ-scans (sample rotation) at different tilts (ψ) at a fixed Bragg condition and is often used to determine the orientation relationship. As can be seen in the reciprocal space map of Co_2GaAs in the inset of figure 2, if the Co_2GaAs(1 1 0) is parallel to the surface plane as expected from the literature, the Co_2GaAs(4 2 0) reflection spot should be observed at $\psi = 18.95°$. Figure 2 shows a XRD pole-figure of the film grown at 300 °C taken in the Co_2GaAs(4 2 0) Bragg condition. In the figure $\phi = 0$ corresponds to the GaAs[1 1 0] direction. The well-defined (4 2 0) spot indicates that the Co_2GaAs phase is single crystalline and highly oriented to the substrate. The topotaxial relationship with the GaAs substrate turned out to be $Co_2GaAs[1\,\bar{1}\,0](1\,1\,0)$ || $GaAs[1\,\bar{1}\,0](0\,0\,1)$. The observation of a single peak in the ϕ-scan is expected from the orthorhombic structure of Co_2GaAs. An additional peak at $\phi = 145°$, $\psi \simeq 24.7°$ with a smaller intensity could be an additional Co_2GaAs domain with a different orientation.

The TEM observations for the same series of films revealed the formation of interfacial compound above T_G of 250 °C [5]. The film grown at 200 °C did not show clear evidence of interfacial reaction but slight modifications of the interface were observed [5]. We consider, therefore, that the interfacial reaction starts around T_G of 200–250 °C. This is much higher than those of the elemental FM/SC structures, for which reaction temperatures of 95 °C (Fe/GaAs) and −10 °C

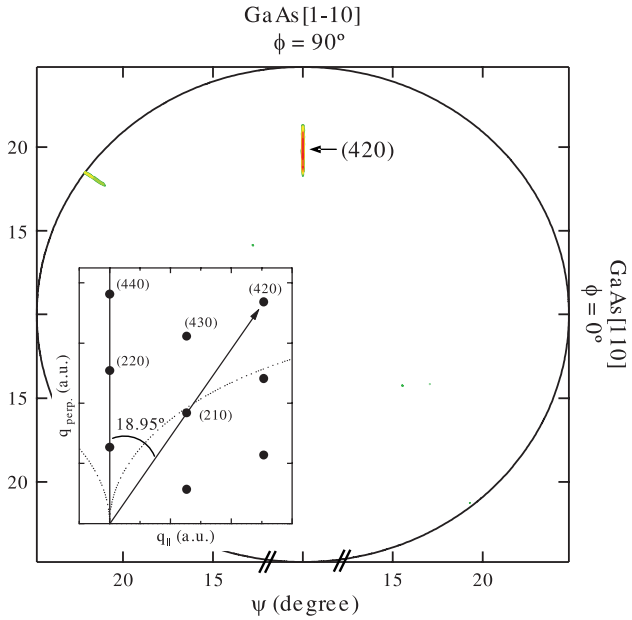

Figure 2. An XRD pole-figure for a Co_2FeSi film grown at 300 °C. $\phi = 0$ corresponds to the GaAs[1 1 0] direction. ψ was scanned in the range 14.79°–24.79°. The inset shows the reciprocal space map of Co_2GaAs.

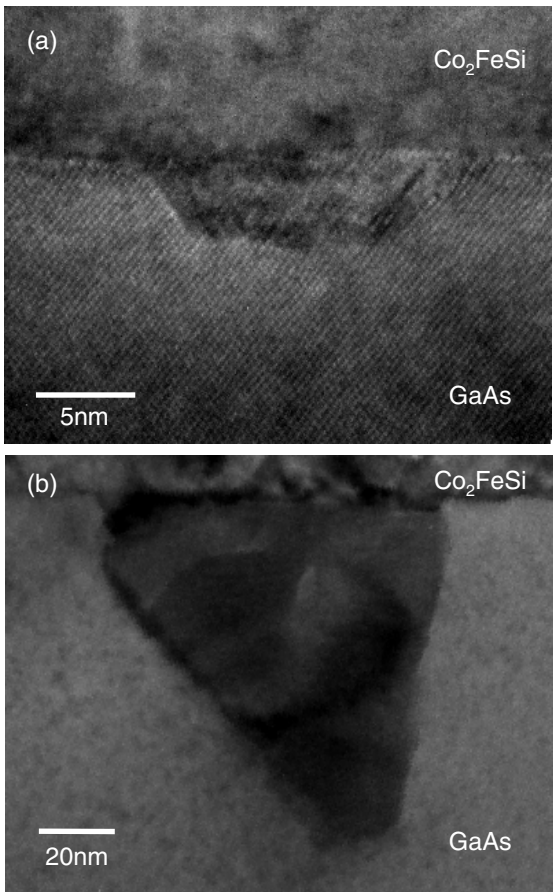

Figure 3. (*a*) A cross-section TEM micrograph around the reacted area of the Co_2FeSi/GaAs film grown at 250 °C and (*b*) a bright field image of the film grown at 400 °C obtained along the [1 1 0] zone axis.

(Co/GaAs) were reported [17,18]. Moreover, in contrast to the elemental FM/SC structures, where an extended ternary phase is formed due to their high reactivity with SC [13,19–21], the interfacial compounds are isolated inside the substrate region. This indicates the suppression of the Co in-diffusion and hence lower reactivity of Heusler-alloy/GaAs interfaces than elemental FM metals. Figure 3(*a*) shows the cross-sectional HRTEM micrograph of a typical reacted region in the film grown at the intermediate T_G of 250 °C obtained along the GaAs[1 1 0] zone axis. The grains are mainly triangle- or trapezoid-shaped. The angle between the side and the base of the grain is approximately 55°, being nearly equal to the angle of the GaAs{1 1 1} planes to the surface normal. This suggests that the interfacial reaction proceeds by Co in-diffusion along the GaAs{1 1 1} planes and the growth is diffusion-limited, resulting in the highly oriented phase with respect to the substrate. Note that since ternary Co_2GaAs is a metastable phase, it is stabilized only by epitaxial growth. This could explain the slight difference of the peak positions of the reacted phase ($\omega \simeq 23°$) between the 250 and 300 °C films, since the lattice parameter, i.e. the peak position, can be sensitive to several factors such as composition and strain in this kind of pseudomorphic phase.

Figure 3(*b*) shows the bright field image of a grain formed in the film grown in the high T_G regime (400 °C) obtained along the [1 1 0] zone axis. In contrast to the 250 °C film, the film grown in the high T_G regime shows asymmetrically shaped grains. The corresponding selected area diffraction (SAD) pattern obtained along the GaAs[1 1 0] zone axis is also shown in figure 4(*a*) together with the result of a kinematic simulation for CoAs along the CoAs[0 0 1] zone axis. The experimental pattern consists of an overlap of that from GaAs and an additional rectangular grid which is identical to the simulated pattern of CoAs. The ratio of the spot spacings in the rectangular grid $B/A = 0.91$ (cf figure 4) almost agrees with that in the simulated pattern (0.90). In addition, the presence of the CoAs(2 1 0) spot close to the GaAs(0 0 2) spot is consistent with the observation of the (2 1 0) reflection near GaAs(0 0 2) in the ω–2θ curves, and the lattice spacing $d^{\mathrm{CoAs}}_{\{2\,1\,0\}}$ obtained from the SAD pattern is 2.61 Å, which is close to that obtained from the XRD measurements (2.59 Å). Therefore, the phase formed in the higher T_G regime is binary CoAs with the topotaxial relationship CoAs[0 0 1](2 1 0) || GaAs[1 1 0](0 0 1). The angles between the surface plane and the two sides of the grain are almost equal to those between the CoAs(2 1 0) plane and the (3 1 0), (1 3 0) planes (8.7° and 44.3°, respectively). This indicates that the two sides are along the (3 1 0) and (1 3 0) planes of CoAs and the grain is no longer restricted to the GaAs lattice. Hence, the reaction process differs from that of the 250 °C film. The growth of CoAs in the high T_G regime is explained by the increased T_G, which makes it possible to dissociate Ga–As bond and nucleate the most stable binary alloy.

It should be noted that Ga- and Fe-related reaction products were not identified in our TEM and XRD studies. The absence of Fe-related compounds can be explained by the lower reactivity of Fe with GaAs compared with Co as well as its minor composition in Co_2FeSi. Further investigations are required to clarify the reaction of Ga after dissociating with As.

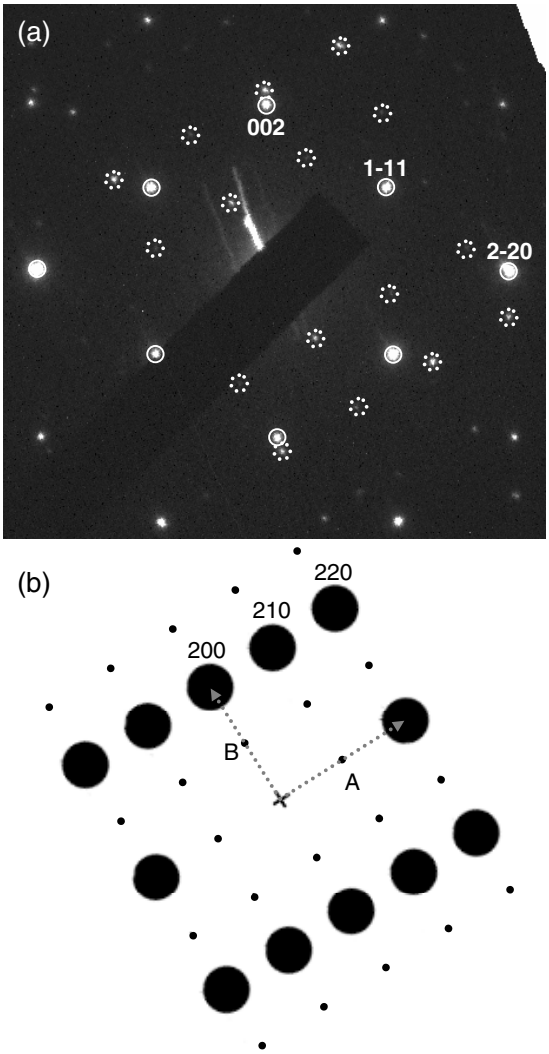

Figure 4. (*a*) SAD pattern along the GaAs [1 1 0] zone axis of a grain formed in the film grown at 400 °C and (*b*) the simulated SAD pattern for CoAs along the zone axis of CoAs[0 0 1]. The spots marked with solid circles and dotted circles belong to those from GaAs and CoAs, respectively. Some major reflections of GaAs are labelled.

4. Conclusion

We have studied the growth temperature dependence of the interfacial phase formation of Heusler-alloy Co_2FeSi/GaAs (0 0 1) hybrid structures. The reaction proceeds predominantly by Co in-diffusion and results in the formation of isolated grains in GaAs starting around 200–250 °C, indicating the lower reactivity than that of the elemental ferromagnets. In the intermediate T_G regime (250–300 °C), the reaction results in the formation of a highly-oriented single-crystalline phase, most likely ternary Co_2GaAs in the topotaxial relationship of $Co_2GaAs[1\bar{1}0](110)$ || $GaAs[1\bar{1}0]$ (0 0 1). In the high T_G regime ($\geqslant$350 °C), on the other hand, the binary CoAs phase is formed in the asymmetric topotaxial relationship $CoAs[001](210)$ || $GaAs[110](001)$. This study has shown the superiority of Co_2FeSi as a ferromagnetic electrode in spintronic devices due to its thermal stability of the interface.

Acknowledgments

This work was partly supported by the German BMBF under the research programme NanoQUIT (Contract No 01BM463). The authors would like to thank B Jenichen for useful discussions and for a careful reading of the manuscript.

References

[1] Palmstrøm C 2003 *Mater. Res. Soc. Bull.* **28** 725
[2] Niculescu V, Budnick J I, Hines W A, Raj K, Pickart S and Skalski S 1979 *Phys. Rev.* B **19** 452
[3] Wurmehl S, Fecher G H, Kandpal H C, Ksenofontov V, Felser C, Lin H-J and Morais J 2005 *Phys. Rev.* B **72** 184434
[4] Herfort J, Jenichen B, Kaganer V, Trampert A, Schönherr H-P and Ploog K H 2006 *Physica* E **32** 371
[5] Hashimoto M, Herfort J, Trampert A, Schönherr H-P and Ploog K H 2006 *J. Vac. Sci. Technol.* B **24** 2004
[6] Schönherr H-P, Nötzel R, Ma W and Ploog K H 2001 *J. Appl.Phys.* **89** 169
[7] Herfort J, Schönherr H-P and Ploog K H 2003 *Appl. Phys. Lett.* **83** 3912
[8] Hashimoto M, Herfort J, Schönherr H-P and Ploog K H 2005 *Appl. Phys. Lett.* **87** 102506
[9] Hashimoto M, Herfort J, Schönherr H-P and Ploog K H 2005 *J. Appl. Phys.* **98** 104902
[10] Wyckoff R W G 1963 *Crystal Structures* vol 1 (New York: Wiley)
[11] Önnerud P, Andersson Y, Tellgren R, Ericsson T, Nordblad P, Krishnamurthy A and Srivastava B K 1995 *J. Magn. Magn. Mater.* **147** 346
[12] Yu A J, Galvin G J, Palmstrøm C J and Mayer J W 1985 *Appl. Phys. Lett.* **47** 934
[13] Palmstrøm C J, Chang C C, Yu A, Galvin G J and Mayer J W 1987 *J. Appl. Phys.* **62** 3755
[14] Genut M and Eizenberg M 1987 *Appl. Phys. Lett.* **50** 1358
[15] Genut M and Eizenberg M 1989 *J. Appl. Phys.* **66** 5456
[16] Sands T, Keramidas V G, Yu K M, Washburn J and Krishnan K 1987 *J. Appl. Phys.* **62** 2070
[17] Schultz B D, Farrell H H, Evans M M R, Lüdge K and Palmstrøm C J 2002 *J. Vac. Sci. Technol.* B **20** 1600
[18] Lüdge K, Schultz B D, Vogt P, Evans M M R, Braun W, Palmstrøm C J, Richter W and Esser N 2002 *J. Vac. Sci. Technol.* B **20** 1591
[19] Monteverde F, Michel A, Eymery J P and Guérin P 2004 *J. Cryst. Growth* **267** 231
[20] Lépine B *et al* 1998 *J. Appl. Phys.* **83** 3077
[21] Herfort J, Trampert A and Ploog K H 2006 *Int. J. Mater. Res.* **97** 1026

Available online at www.sciencedirect.com
ScienceDirect
Journal of Magnetism and Magnetic Materials 310 (2007) 2228–2230
Journal of magnetism and magnetic materials
www.elsevier.com/locate/jmmm

Magnetic anisotropy in Heusler alloy Fe_3Si films on GaAs(1 1 3)A

J. Herfort*, P.K. Muduli, K.-J. Friedland, H.-P. Schönherr, K.H. Ploog

Paul-Drude-Institut für Festkörperelektronik Berlin, Hausvogteiplatz 5-7, 10117 Berlin, Germany

Available online 17 November 2006

Abstract

The magnetic anisotropy in thin Heusler alloy Fe_3Si films on GaAs(1 1 3)A substrates is studied using superconducting quantum interference device magnetometry. The layers exhibit a dominant four-fold magnetic anisotropy with the easy axes along $\langle 0\,3\,\bar{1}\rangle$. The magnetic anisotropy constant K_1 of stoichiometric samples is found to be $(3.0\pm0.6)\times10^4\,\mathrm{erg/cm^3}$, which agrees well with the reported values for bulk Fe_3Si and Fe_3Si/GaAs(0 0 1) films.

PACS: 75.47.−m; 73.50Jt; 73.43.Qt; 75.50.Bb

Keywords: Heusler alloy; Fe_3Si; GaAs(1 1 3)A; Magnetic anisotropy

1. Introduction

The combination of magnetic and semiconducting materials is now one of the key issues in the development of semiconductor devices utilizing the spin of the carriers [1–3]. The ferromagnetic Heusler alloy Fe_3Si is a promising material for spintronic applications because its interface with GaAs is thermally more stable than elemental ferromagnets [4–6]. So far the growth of ferromagnets on GaAs substrates has been focused mainly on low-index surfaces. Much less work is devoted to study ferromagnetic films on high-index semiconductor surfaces. The GaAs(1 1 3)A surface, in particular, is characterized by a low surface symmetry with the two major in-plane axes, namely $\langle 3\,3\,\bar{2}\rangle$ and $\langle\bar{1}\,1\,0\rangle$ being crystallographically in-equivalent. Hence, the combination of Fe_3Si with GaAs(1 1 3)A substrates allows to study the effect of a reduced surface symmetry on magnetic and magnetotransport properties. In a previous report [7], we have shown that this unique orientation results in an additional antisymmetric component (ASC) in the planar Hall effect (PHE), which manifests itself as a change in sign of the PHE when the direction of the saturating in-plane magnetic field is reversed. This ASC shows a maximum for a magnetic field applied along the $\langle 3\,3\,\bar{2}\rangle$ axes and vanishes along the $\langle\bar{1}\,1\,0\rangle$ axes. This effect results from the reduced symmetry of the $\langle 1\,1\,3\rangle$ orientation and manifests the so-called "Umkehr" effect where symmetric and antisymmetric contributions coexist [7]. In this report, we will focus on the magnetic anisotropy of these $Fe_{3+x}Si_{1-x}$/GaAs(1 1 3)A films and its dependence on the composition x.

2. Sample preparation

High-quality epitaxial Fe_3Si(1 1 3) films with the same orientation as the substrate have been achieved by molecular-beam epitaxy due to the small lattice mismatch between Fe_3Si and GaAs [8]. The growth temperature and growth rate are optimized to 250 °C and 0.13 nm/min, respectively, for producing Fe_3Si films with structural properties comparable to that of Fe_3Si on GaAs(0 0 1) [8]. The thickness of all layers is between 35 and 50 nm, which was determined from interference fringes obtained in X-ray reflectivity and high-resolution X-ray diffraction measurements.

*Corresponding author. Tel.: +49 30 20377 344; fax: +49 30 20377 201.
E-mail address: herfort@pdi-berlin.de (J. Herfort).

0304-8853/$ - see front matter © 2006 Elsevier B.V. All rights reserved.
doi:10.1016/j.jmmm.2006.10.813

3. Results and discussion

The room temperature magnetic properties of the Fe_3Si films are studied by superconducting quantum interference device (SQUID) magnetometry. All Fe_3Si films are ferromagnetic at room temperature. The magnetic anisotropy of the films exhibits a complex dependence on the growth conditions and composition x. In general, the anisotropy can be expressed in terms of two contributions, namely a four-fold magnetic anisotropy and a uniaxial magnetic anisotropy (UMA). As can be seen in Fig. 1, the easy axes of the four-fold magnetic anisotropy are close to the $\langle 0\,3\,\bar{1}\rangle$ axes. This arises from the cubic magnetocrystalline anisotropy, and is a result of the large demagnetization energy in the thin film geometry [9]. Unlike in the magnetotransport experiments [7], the two major in-plane crystallographic in-equivalent directions, $\langle 3\,3\,\bar{2}\rangle$ and $\langle \bar{1}\,1\,0\rangle$, are found to be magnetically equivalent and are intermediate axes. In some samples, a UMA is found with an easy axis along $\langle \bar{1}\,1\,0\rangle$, which is perpendicular to that observed in ultrathin Fe films on GaAs(1 1 3)A substrates. In addition, this UMA shows an increase with increasing Si content. However, the origin of this UMA is not yet completely understood and several possible origins will be discussed elsewhere [10].

The anisotropy constants are determined from fitting the magnetization curves by tracking the local minimum of the free energy as the field is swept following the method developed in Ref. [9] for Fe films on GaAs(1 1 3) A substrates. Fig. 2(a) shows a plot of K_1/M_S as a function of composition x, where K_1 and M_S denote the four-fold magnetic anisotropy constant and saturation magnetization, respectively. A positive value of K_1 is found over the whole composition range, similar to ordered bulk Fe_3Si with $D0_3$ crystal structure [11]. In addition, a decrease of K_1 with increasing Si content is observed, which arises from the reduced strength of exchange interaction between the Fe atoms due to the addition of Si in the crystal lattice.

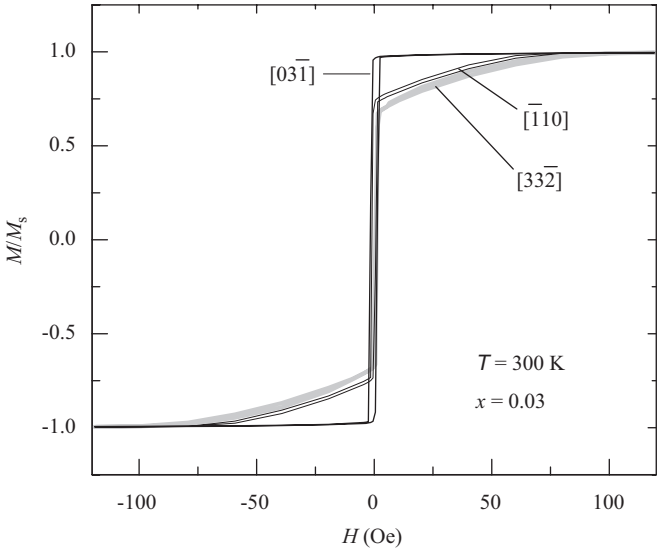

Fig. 1. SQUID magnetization curves for an almost stoichiometric $Fe_{3+x}Si_{1-x}$ layer with $x = 0.03$ along the major crystallographic directions.

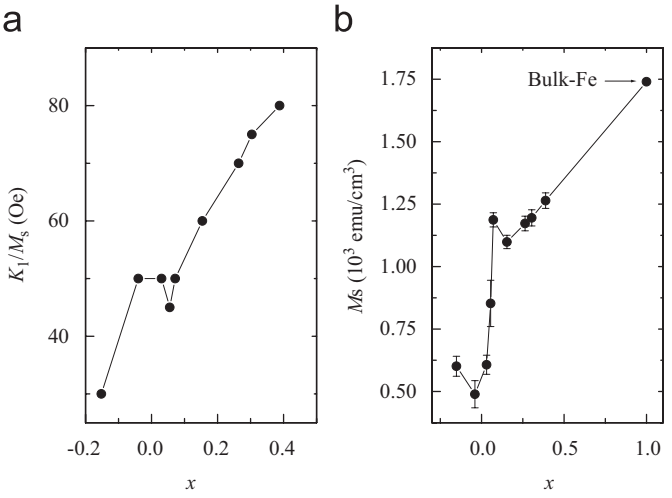

Fig. 2. Composition dependence ($T = 300\,K$) of (a) K_1/M_S and (b) M_S, where K_1 and M_S denote the four-fold magnetic anisotropy constant and saturation magnetization, respectively.

The saturation magnetisation of the $Fe_{3+x}Si_{1-x}$ films decreases with the addition of Si as shown in Fig. 2(b). By taking the saturation magnetization as $(600 \pm 50)\,emu/cm^3$ and the lattice constant as $a_{Fe3Si} = 5.652\,\text{Å}$, the average magnetic moment per atom for the stoichiometric Fe_3Si film is determined to be $(0.73 \pm 0.06)\,\mu_B$ at 300 K. This value is smaller as compared to the bulk value of $1.2\,\mu_B$ and also to the reported values for Fe_3Si films on GaAs(0 0 1) substrates [12]. For stoichiometric samples, the value of K_1 is found to be equal to $(3.0 \pm 0.6) \times 10^4\,erg/cm^3$, which agrees well with those reported for bulk Fe_3Si and Fe_3Si/GaAs(0 0 1) films [11–13].

Acknowledgment

Part of this work has been supported by the German BMBF under the research program *NanoQuit* (contract no. 01BM463).

References

[1] G.A. Prince, Science 282 (1998) 1660.
[2] S.A. Wolf, D.D. Awschalom, R.A. Buhrmann, J.M. Doughton, S. von Molnar, M.L. Roukes, A.Y. Chtelkanova, D.M. Treger, Science 294 (2001) 1488.
[3] H. Ohno, Science 281 (1998) 951.
[4] J. Herfort, H.-P. Schönherr, K.H. Ploog, Appl. Phys. Lett. 83 (2003) 3912.
[5] J. Herfort, H.-P. Schönherr, A. Kawaharazuka, M. Ramsteiner, K.H. Ploog, J. Cryst. Growth 278 (2005) 666.
[6] J. Herfort, B. Jenichen, V. Kaganer, A. Trampert, H.-P. Schönherr, K.H. Ploog, Physica. E 32 (2006) 371.
[7] P.K. Muduli, K.-J. Friedland, J. Herfort, H.-P. Schönherr, K.H. Ploog, Phys. Rev. B 72 (2005) 104430.

[8] P.K. Muduli, J. Herfort, H.-P. Schönherr, K.H. Ploog, J. Cryst. Growth 285 (2005) 514.
[9] P.K. Muduli, J. Herfort, H.-P. Schönherr, L. Däweritz, K.H. Ploog, Appl. Phys. A 81 (2005) 901.
[10] P.K. Muduli, K.-J. Friedland, J. Herfort, H.-P. Schönherr, K.H. Ploog, J. Phys. Condens. Matter 18 (2006) 9453.
[11] M. Goto, T. Kamimori, J. Phys. Soc. Japan 52 (1983) 3710.
[12] A. Ionescu, C.A.F. Vaz, T. Trypiniotis, C.M. Gurtler, H. Garcia-Miquel, J.A.C. Bland, M.E. Vickers, R.M. Dalgliesh, S. Langridge, Y. Bugoslavsky, Phys. Rev. B 71 (2005) 094401.
[13] K. Lenz, E. Kosubek, K. Baberschke, H. Wende, J. Herfort, H.-P. Schönherr, K.H. Ploog, Phys. Rev. B 72 (2005) 14411.

Available online at www.sciencedirect.com
ScienceDirect
Journal of Crystal Growth 301–302 (2007) 592–596
JOURNAL OF CRYSTAL GROWTH
www.elsevier.com/locate/jcrysgro

Growth, interface structure and magnetic properties of Heusler alloy Co_2FeSi/GaAs(0 0 1) hybrid structures

M. Hashimoto, J. Herfort*, A. Trampert, K.H. Ploog

Paul-Drude-Institut für Festkörperelektronik, Hausvogteiplatz 5-7, 10117 Berlin, Germany

Available online 30 October 2006

Abstract

We have investigated the growth, interface structure, and magnetic properties of full-Heusler alloy Co_2FeSi/GaAs(0 0 1) hybrid structures. We found that a $L2_1$-ordered Co_2FeSi layer with an atomically abrupt interface can be achieved up to the growth temperature T_G of 200 °C. The simulations of the high-resolution transmission electron microscopy interference pattern for Co_2FeSi/GaAs(0 0 1) interface suggests a 1 layer of intermixing at the interface. Both uniaxial and cubic in-plane magnetic anisotropy constants decrease above 200 °C in correspondence with the proceeding interfacial reaction, indicating degradations of the interface perfection as well as the ordering of the layer. The formation of interfacial compounds reduces the saturation magnetization of the Co_2FeSi layer in higher T_G, which can deteriorate its expected half-metallicity.

PACS: 68.35.Ct; 75.50.Cc; 81.15.Hi

Keywords: A3. Molecular beam epitaxy; B1. Heusler alloy; B2. Ferromagnet/semiconductor hybrid structure

1. Introduction

Half-metallic ferromagnets (HMF), which have 100% spin-polarized carriers at the Fermi level, are promising candidates for spintronics devices e.g. magnetic tunneling junction and spin injection device. The potential HMF include some of diluted magnetic semiconductors, oxides and Heusler alloys. Heusler alloys like NiMnSb, Co_2MnSi, and Co_2MnGe are especially attractive because of their high Curie temperature (T_C) and the close lattice-matching with semiconductors [1]. In addition, a recent study suggests that Co_2FeSi, which has the highest T_C (>1100 K) and the largest magnetic moment (6 μ_B) among Heusler alloys as well as a small lattice-mismatch with respect to GaAs (~0.08%) [2], is indeed a HMF [3].

The growth of ferromagnet(FM)/semiconductor(SC) hybrid structures is often complicated by the reaction between the layer and substrate. This can be detrimental for the efficiency of electrical spin injection. Moreover, atomic ordering of the Heusler alloy layer has a significant influence on its electronic structure and magnetic properties. Therefore, Co_2FeSi/GaAs hybrid structures with highly ordered layers and atomically abrupt interfaces are desirable. The aim of this study is to correlate growth, interface structure and magnetic properties of Co_2FeSi/GaAs(0 0 1) hybrid structures.

2. Sample preparation

The Co_2FeSi layers were grown on semi-insulating GaAs(0 0 1) substrates by molecular-beam epitaxy. Before the growth of the Co_2FeSi layer, 100 nm-thick-GaAs templates were prepared in the III–V growth chamber using standard GaAs growth conditions. An As-terminated $c(4\times4)$ reconstructed GaAs(0 0 1) surface was realized by cooling the samples down to 420 °C under As_4 pressure to prevent the formation of macroscopic defects on the surface similar to our studies on Fe/GaAs(0 0 1) [4] and Fe_3Si/GaAs(0 0 1) [5]. The samples were then transferred under ultrahigh vacuum (UHV) to the As-free deposition chamber which is directly connected to the III–V growth chamber via an interlock. Co, Fe and Si were codeposited

*Corresponding author.
E-mail address: herfort@pdi-berlin.de (J. Herfort).

0022-0248/$ - see front matter © 2006 Elsevier B.V. All rights reserved.
doi:10.1016/j.jcrysgro.2006.09.019

from high temperature effusion cells with a base pressure of 1×10^{-10} Torr. The growth temperature (T_G) for the Co_2FeSi layers was varied in the range from 100 to 400 °C. The thickness of the layers d was determined by high-resolution X-ray diffraction (HRXRD) and X-ray reflectivity (XRR) measurements to be 18 nm. Details of the growth and structural characterizations including the determination of the stoichiometric composition can be found elsewhere [6,7].

The characterization of the Co_2FeSi/GaAs(0 0 1) interface was performed by XRD and cross-sectional transmission electron microscopy (TEM). The XRD $\omega - 2\theta$ curves were taken after growth with a PANalytical X'pert diffractometer using Cu K_α radiation with a Ge(2 2 0) monochromator. Thin specimens for TEM were prepared in cross-sectional configuration along both the [1 1 0] and the orthogonal [1 $\bar{1}$ 0] direction. After mechanical grinding, Ar-ion milling was applied to achieve electron transparency with thinning conditions of 2.5–2.7 keV beam energy and a beam incident angle of 2.5°–3° in order to minimize surface damage. A JEM-3010 microscope was used for the conventional TEM as well as the high-resolution (HR) TEM analysis (point resolution: 0.17 nm).

3. Results and discussion

Fig. 1 shows the XRD $\omega - 2\theta$ curves measured with an open detector for Co_2FeSi films grown in the range of 150−400 °C. The sharp peak at $\omega = 34.56°$ originates from the Si(0 0 4) reflection of the sample holder. In addition to the substrate peaks, i.e. GaAs(0 0 2) and (0 0 4) reflections, two additional peaks are detected labeled as A (250−300 °C) and B (≥350 °C). The peaks A and B can be assigned to the ternary compound Co_2GaAs(2 2 0) and to the binary CoAs(2 1 0) reflection, respectively [8]. The result shows that the interfacial reaction starts around 200−250 °C and the main diffusing species is Co into the GaAs substrate. The details of the interfacial reaction will be described elsewhere [8].

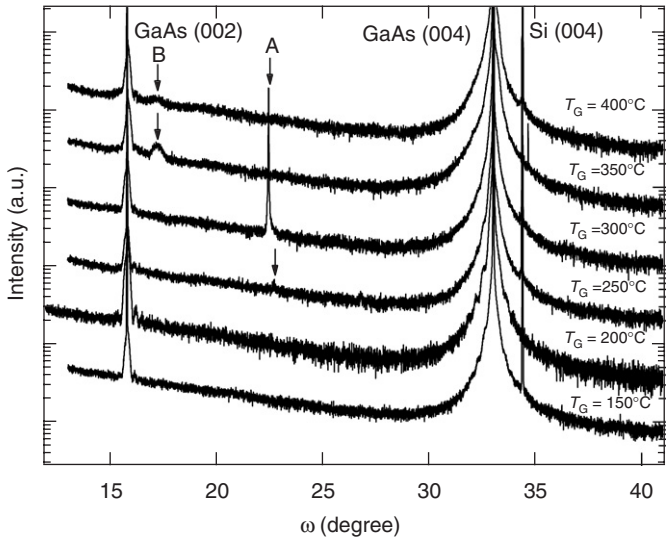

Fig. 1. Wide-range XRD $\omega - 2\theta$ curves taken with an open-detector of the Co_2FeSi/GaAs films grown in the range from 150 to 400 °C. The sharp peak at $\omega = 34.56°$ is originated from the Si(0 0 4) reflection from the sample holder. Additional peaks are labeled as A (250−300 °C) and B (≥350 °C) (see text for details).

Fig. 2(a) shows a cross-sectional HRTEM micrograph of the Co_2FeSi/GaAs(0 0 1) interface grown at 200 °C obtained along the GaAs[1 1 0] zone axis. The image has been Fourier-filtered in order to reduce the noise and to obtain a clearer contrast. The arrays of bright dots in the substrate region correspond to the tunneling positions and are related to the {1 1 1} planes. On the other hand, the interference pattern in the Co_2FeSi region shows lines running perpendicular to the interface, which correspond to the {2 2 0} planes. The Co_2FeSi{2 2 0} atomic planes perfectly match with the GaAs{2 2 0} planes ($d_{GaAs\{2\,2\,0\}} \approx 2$ Å) across the interface i.e., the layer is coherently strained. At the interface, the two bright vertical lines meet with a bright dot forming a dark dot between the lines. From the clear change in the motive of the interference pattern between the Co_2FeSi layer and GaAs substrate, we recognize that the interface is atomically abrupt within 1–2 monolayer (ML). Atomic steps can be seen at the interface as indicated by arrows in the figure. The modified layer of 1–2 ML which shows a similar pattern but a different contrast observed at the interface of the same film [9] originates either from the superpositions of these steps across the specimen along the electron beam direction or from interdiffusion of the atoms. As already revealed in a previous work [9], the Co_2FeSi/GaAs interface grown at 100 °C is atomically abrupt without reacted layers, whereas the film grown at 350 °C shows undulation and large steps at the interface due to reaction [9]. Therefore, a relatively abrupt interface can be achieved up to T_G of 200 °C.

In order to obtain further information on the atomic configuration at the interface, we performed contrast simulations of the interference pattern for the interface region. The simulations were performed using the Cerius^{TM} software [10] for three models i.e. the Co_2FeSi/As-terminated-GaAs(0 0 1) interface with (i) no-intermixing, (ii) 1-layer intermixing, and (iii) 2-layers intermixing. The experimental pattern can be best reproduced by the 1-layer intermixing model, where the top As-layer of GaAs and the bottom Co_2FeSi layer are intermixed. The 1-layer-intermixed interface model is schematically shown in Fig. 2(c) together with the corresponding result of the simulation in (b) [11]. The simulation well reproduces both the dark dots and the junctions of two vertical lines with a bright dot observed at the interface. Note that in elemental ferromagnetic metal Fe/GaAs(0 0 1) structures, two layers of Fe and GaAs are found to be intermixed at the interface already at a much lower T_G (50 °C) [12]. The more detailed analysis including the results of contrast simulations for the 2-layers-intermixing and no-intermixing interface models will be described elsewhere.

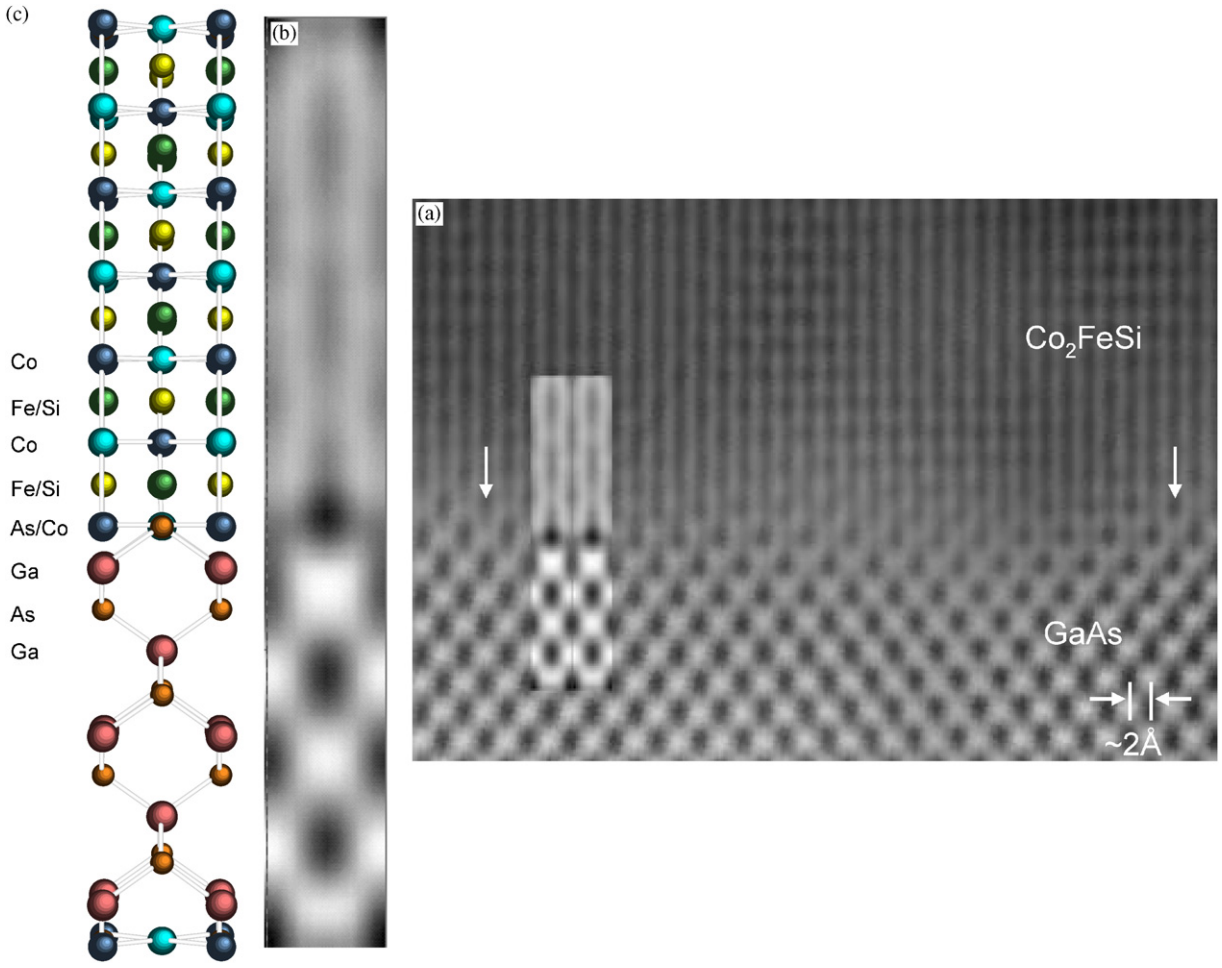

Fig. 2. (a) A cross-sectional HRTEM micrograph of the Co_2FeSi/GaAs(0 0 1) interface grown at 200 °C along GaAs[1 1 0] zone axis, the image is Fourier-filtered. The lattice spacing of GaAs $d\{2\,2\,0\} \approx 2$ Å is indicated for scaling. The steps are indicated by arrows. The result of the simulation is also shown in the inset for comparison. (b) The result of the contrast simulation for the 1-layer-intermixed Co_2FeSi/GaAs(0 0 1) interface. (c) The schematic model of the 1-layer-intermixed interface.

In order to examine the atomic ordering, we took nano-beam diffraction (NBD) patterns of the layer. Fig. 3 shows the NBD pattern of the Co_2FeSi layer grown at 100 °C together with the result of a kinematical calculation of electron diffraction pattern for Co_2FeSi along the [1 1 0] zone axis. We used an electron beam with the diameter of 3−5 nm, which is smaller than the Co_2FeSi layer thickness of 18 nm to obtain information only from the Co_2FeSi layer. For the Heusler-type $L2_1$ structure, the odd reflections e.g. (1 1 1) are the superlattice reflections, which appear when the crystal is ordered. We observed the {1 1 1} spots having an smaller intensity than the (0 0 2) spots, which is consistent with the calculation. This indicates that at least some degree of the Heusler-type $L2_1$ ordering is present in the Co_2FeSi layer despite the low T_G. This is consistent with our observations in XRD measurements [7].

Fig. 4(a) plots the two in-plane magnetic anisotropy (MA) constants, uniaxial (K_u^{eff}) and cubic (K_1^{eff}) MA constant, as a function of T_G. K_u^{eff} and K_1^{eff} are an

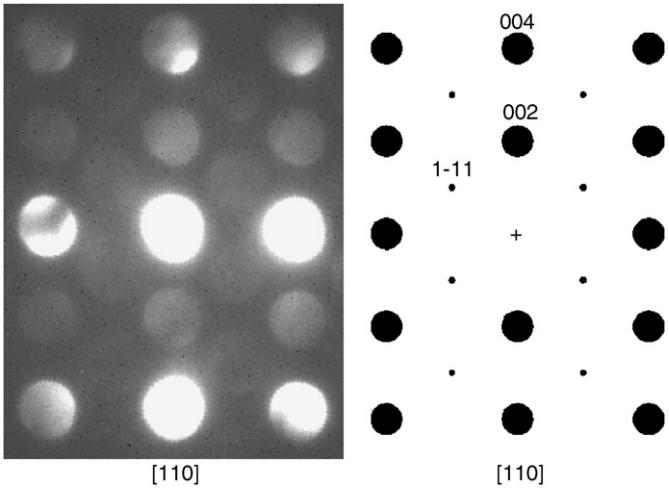

Fig. 3. A nano-beam diffraction pattern of the Co_2FeSi layer grown at 100 °C obtained along GaAs[1 1 0] zone axis (left). The result of the kinematical calculation of diffraction intensity for Co_2FeSi is also shown in the right.

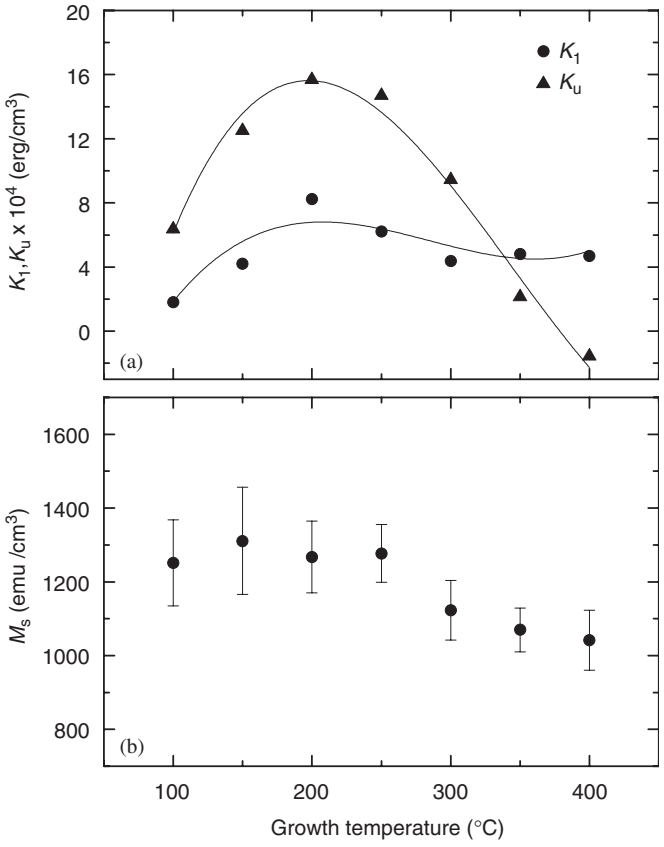

Fig. 4. Growth temperature dependence of (a) uniaxial magnetic anisotropy constant K_u^{eff} (triangle) and cubic magnetic anisotropy constant K_1^{eff} (circle) and (b) saturation magnetization M_s of Co_2FeSi/GaAs(0 0 1). The solid lines are guides for the eye.

interface-related and volume-related term, respectively, as we revealed in our previous work [7]. The uniaxial MA in *c*-FM/zinc-blende-SC systems is attributed to an anisotropic bonding at the FM/SC interface [13]. Therefore, one can presume that the formation of interface compounds and/or a modification of the interface structure results in a reduction of uniaxial MA. The MA constants can offer additional information on the interface perfection as well as atomic ordering of the layer.

The two MA constants were obtained by fitting the magnetization curve along the reversible hard axis using the expression derived from the free energy density consisting of uniaxial and cubic terms [14]:

$$H(m) = 2K_1^{eff}(2m^3 - m)/M_s + 2K_u^{eff}m/M_s, \quad (1)$$

where m is the normalized magnetization component along the applied field. For the magnetization curves above 350 °C, which do not show reversible hard axes, the Stoner–Wohlfarth model was used to fit the curves. In the latter case, the irreversible parts were not reproduced since the Stoner–Wohlfarth model does not take into account the micro-magnetic structure of the layer [15]. As can be seen in Fig. 4(a), both K_u^{eff} and K_1^{eff} have a maximum around $T_G = 200$ °C. This indicates that the optimum T_G to obtain an abrupt and ordered Co_2FeSi/GaAs interface is around 200 °C. K_u^{eff} decreases above 200 °C in correspondence with the progress of the interfacial reaction. The simultaneous decrease of K_1^{eff} above 200 °C probably originates from the atomic disordering due to the diffusion of Co into the substrate.

The saturation magnetization M_s of Co_2FeSi decreases above $T_G = 250$ °C as can be seen in Fig. 4(b). The magnetism of the reaction product Co_2GaAs (250−300 °C) is unknown, but CoAs (≥350 °C) is reported to be paramagnetic [16]. Therefore, the in-diffusion of Co and the resultant formation of these compounds at the interface most likely causes the gradual reduction of M_s with increasing T_G. Note that M_s of the films grown at 200 °C is (1260 ± 100) emu/cm^3, being approximately equivalent to $(6.2 \pm 0.5)\mu_B$/f.u. Despite the large error bar this value is relatively close to the theoretically expected integer value of 6 (μ_B/f.u.), suggesting that thin Co_2FeSi films can be a HMF. The decrease of M_s in the higher T_G regime can lead to a degradation of the half-metallicity expected for this material.

4. Conclusion

We have investigated the MBE growth, interface structure and magnetic properties of Co_2FeSi/GaAs(0 0 1) hybrid structures. Atomically ordered Co_2FeSi layers with an atomically abrupt interface were achieved up to the growth temperature of 200 °C. The simulations for the TEM interference pattern of the Co_2FeSi/GaAs(0 0 1) interface grown at $T_G = 200$ °C revealed that the bottom layer of Co_2FeSi is most likely intermixed with the GaAs substrate. Both uniaxial and cubic in-plane MA constants decrease above 200 °C in correspondence with the progress of interfacial reactions, indicating degradation of the interface perfection as well as ordering of the layer. The formation of interfacial compounds reduces the saturation magnetization of the Co_2FeSi layer at higher T_G, which can be detrimental to its expected half-metallicity.

Acknowledgments

This work was partly supported by the German BMBF under the research program *NanoQUIT* (Contract no. 01BM463). The authors would like to thank H.-P. Schönherr for his support in sample preparation and R. Hey for useful discussions and for a careful reading of the manuscript.

References

[1] C. Palmstrøm, MRS Bull. 28 (2003) 725.
[2] V. Niculescu, J.I. Budnick, W.A. Hines, K. Raj, S. Pickart, S. Skalski, Phys. Rev. B 19 (1979) 452.
[3] S. Wurmehl, G.H. Fecher, H.C. Kandpal, V. Ksenofontov, C. Felser, H.-J. Lin, J. Morais, Phys. Rev. B 72 (2005) 184434.
[4] H.-P. Schönherr, R. Nötzel, W. Ma, K.H. Ploog, J. Appl. Phys. 89 (2001) 169.
[5] J. Herfort, H.-P. Schönherr, K.H. Ploog, Appl. Phys. Lett. 83 (2003) 3912.

[6] M. Hashimoto, J. Herfort, H.-P. Schönherr, K.H. Ploog, Appl. Phys. Lett. 87 (2005) 102506.
[7] M. Hashimoto, J. Herfort, H.-P. Schönherr, K.H. Ploog, J. Appl. Phys. 98 (2005) 104902.
[8] M. Hashimoto, J. Herfort, A. Trampert, H.-P. Schönherr, K.H. Ploog, Appl. Phys. Lett., submitted.
[9] M. Hashimoto, J. Herfort, A. Trampert, H.-P. Schönherr, K.H. Ploog, J. Vac. Sci. Technol. B 24 (2006) 2004.
[10] Cerius2 Program, Molecular Simulations Incorporated, San Diego, CA.
[11] The thickness of the specimen and the defocus are assumed in the simulation to be 8 nm and −550 nm, respectively.
[12] J. Herfort, A. Trampert, K.H. Ploog, Int. J. Mat. Res. (formerly Z. Metallkd.) 97 (2006) 1026.
[13] E. Sjöstedt, L. Nordström, F. Gustavsson, O. Eriksson, Phys. Rev. Lett. 89 (2002) 267203.
[14] M. Dumm, M. Zölfl, R. Moosbühler, M. Brockmann, T. Schmidt, G. Bayreuther, J. Appl. Phys. 87 (2000) 5457.
[15] C. Daboo, R.J. Hicken, E. Gu, M. Gester, S.J. Gray, D.E.P. Eley, E. Ahmad, J.A.C. Bland, R. Ploessl, J.N. Chapman, Phys. Rev. B 51 (1995) 15964.
[16] K. Adachi, S. Ogawa, Landolt-Börnsterin New Series III/27a, Springer, Berlin, 1988.

Atomic ordering and interlayer diffusion of Co_2FeSi films grown on GaAs(001) studied by transmission electron microscopy

M. Hashimoto,[a] A. Trampert, J. Herfort, and K. H. Ploog
Paul-Drude-Institut für Festkörperelektronik, Hausvogteiplatz 5-7, 10117 Berlin, Germany

(Received 6 February 2007; accepted 5 March 2007; published 31 July 2007)

The influence of the growth temperature on the atomic ordering and interlayer diffusion of Heusler alloy Co_2FeSi films grown on GaAs(001) substrates has been studied using high-resolution transmission electron microscopy. The Co_2FeSi/GaAs(001) films grown below 200 °C show a coexistence of the Heusler-type $L2_1$ phase and the disordered $B2$ phase, which can be seen mainly near the interface, due to the low growth temperature. This phase coexistence can affect the spin polarization of the Co_2FeSi layer near the interface. On the other hand, the film grown at an elevated temperature of 300 °C shows a uniformly atomically ordered $L2_1$ phase, indicating that 300 °C is approximately the transition temperature to the atomically ordered $L2_1$ structure. The elevation of the growth temperature, however, results in the formations of interfacial compounds above 250 °C, which could be detrimental to the efficient electrical spin injection. © *2007 American Vacuum Society.* [DOI: 10.1116/1.2748413]

I. INTRODUCTION

Half-metallic ferromagnets (HMFs), which have 100% spin-polarized carriers at the Fermi level, are promising candidates for spintronics devices. The potential HMFs include some diluted magnetic semiconductors, oxides, and Heusler alloys. Heusler alloys are especially attractive because of their high Curie temperature T_C and close lattice matching with semiconductors.[1] A recent study suggests that Co_2FeSi, which has the highest T_C(>1100 K) and the largest magnetic moment ($6\mu_B$) among Heusler alloys as well as a small lattice mismatch with respect to GaAs (~0.08%),[2] is indeed a HMF.[3]

Co_2FeSi is a member of full-Heusler alloys with the cubic $L2_1$ crystal structure [see Fig. 1(a)]. The $L2_1$ structure can be considered as four interpenetrating fcc sublattices A, B, C, and D with origins at (0 0 0), (1/4 1/4 1/4), (1/2 1/2 1/2), and (3/4 3/4 3/4).[4] The A and C sublattices, which are crystallographically equivalent, are occupied by Co, and the B and D sublattices by Fe and Si, respectively. The lattice constant of bulk Co_2FeSi is 5.658 Å,[2] being closely lattice matched to GaAs (a_{GaAs}=5.653 Å). The combination of these materials gives a lattice mismatch as small as 0.08%, which enables us to grow epitaxially a high quality Co_2FeSi layer on GaAs.[5,6] The atomically ordered $L2_1$ structure is reduced to the $B2$ (CsCl) structure [cf. Fig. 1(b)], which has half the lattice constant of the $L2_1$ structure, when the Fe(B) and Si(D) sublattices are completely disordered. On the other hand, a complete disorder among all the three sublattices results in a further reduction of the crystal symmetry to the $A2$ (bcc) structure. These are considered to be the preferential disorders in full-Heusler alloys with the chemical formula X_2YZ.[4,7,8]

It has been reported that the atomic disorder in the Heusler alloy layer and/or the formation of defects have/has a significant influence on their electronic structure and magnetic properties. For example, atomic ordering influences the magnitude of the magnetic moment, the value of T_C, and also the type of magnetic order.[4,9–11] Moreover, some theoretical works revealed that the half-metallicity can be influenced by some types of atomic disorder and/or defect formation.[12–14] This can be detrimental to the spin injection efficiency using this material as an electrode. In fact, recent experimental works have attributed the contradicting observations of a low spin-polarization degree to atomic disorder in the Heusler alloy layer.[15–17] Therefore, knowing the atomic ordering of the Heusler layer is of importance for the realization of efficient electrical spin injection using Heusler alloys as an electrode. Furthermore, from an application point of view, it is highly desirable to explore ferromagnet/semiconductor structures with high interface perfection and thermal stability. In this study we examine the influence of the growth temperature on the long-range atomic ordering and interfacial reaction in Heusler alloy Co_2FeSi/GaAs(001) hybrid structures using high-resolution transmission electron microscopy.

II. EXPERIMENTS

The Co_2FeSi layers were grown on semi-insulating GaAs(001) substrates by molecular-beam epitaxy. Before the growth of the Co_2FeSi layer, 100-nm-thick GaAs templates were prepared in the III-V growth chamber using standard GaAs growth conditions. An As-terminated $c(4\times4)$ reconstructed GaAs(001) surface was realized by cooling the samples down to 420 °C under As_4 flux. This is necessary to prevent the formation of macroscopic defects on the surface similar to our studies on Fe/GaAs(001) (Ref. 18) and Fe_3Si/GaAs(001).[19] The samples were then transferred under ultrahigh vacuum to the As-free deposition chamber which is directly connected to the III-V growth chamber via an interlock chamber. Co, Fe, and Si were codeposited from high temperature effusion cells at a base pressure of 1

[a]Electronic mail: hashimoto@pdi-berlin.de

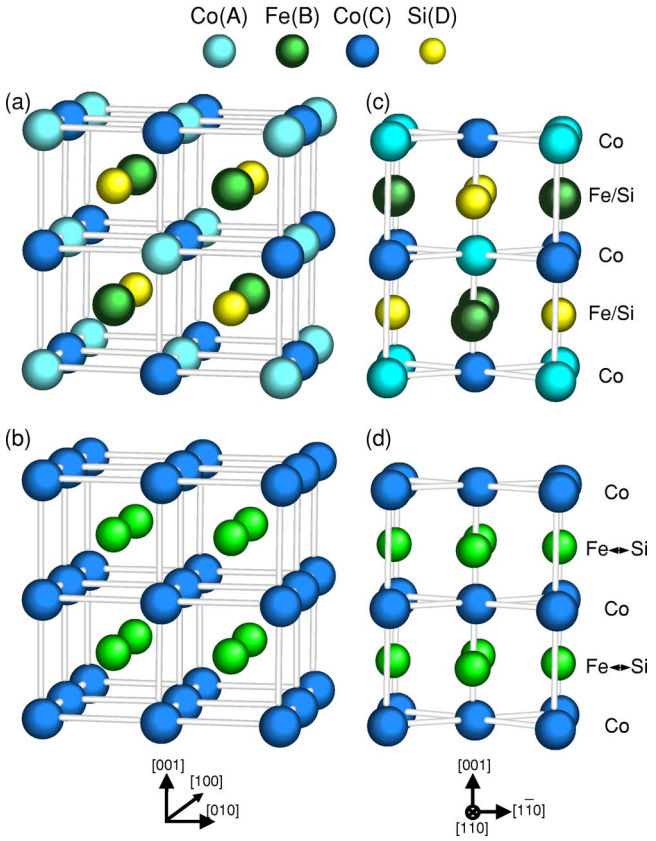

FIG. 1. (a) Schematic view of the unit cell of the Heusler-type $L2_1$ structure and (b) the disordered $B2$ structure. The crystal structure of (c) Heusler-type $L2_1$ structure and (d) the $B2$ structure viewed along the [110] direction are also displayed.

$\times 10^{-10}$ Torr. The growth temperature T_G for the Co_2FeSi layers was varied in the range of 100–400 °C. The thickness of the layers, d, was determined by high-resolution x-ray diffraction and x-ray reflectivity measurements to be 18 nm. Details of the growth and structural characterizations including the determination of the stoichiometric composition can be found elsewhere.[5,6]

The atomic ordering of the $Co_2FeSi/GaAs(001)$ interface was investigated by semiquantitative high-resolution transmission electron microscopy (HRTEM) study. A JEM-3010 microscope was used for the conventional TEM as well as the HRTEM analysis (point resolution: 0.17 nm). Thin specimens were prepared in cross-sectional configuration along both the [110] and the orthogonal [1$\bar{1}$0] directions. After mechanical grinding, Ar-ion milling was applied to achieve electron transparency with thinning conditions of 2.5–2.7 keV beam energy and a beam incident angle of 2.5°–3° in order to minimize surface damage. The contrast simulations based on the multislice method were performed with the CERIUS™ software[20] in order to analyze the HRTEM images. The spherical aberration C_s, the focus spread and the semidivergence angle used in the simulation were assumed to be 1.0 mm, 10 nm, and 1.0 mrad, respectively.

III. RESULTS AND DISCUSSION

In general, determination of the crystal structure from a lattice fringe pattern requires a careful comparison between experimental and simulated images, since it is sensitive to several factors: the image contrast varies with small changes in specimen thickness (t), the orientation of the specimen, and the defocus of the objective lens (Δf). We took the following procedures in order to determine the structure strictly. First, we simulated the thickness-defocus (t-Δf) dependent image maps of the possible crystal structures, i.e., (i) the $L2_1$ (atomically ordered), (ii) $B2$ (disordering between Fe(B) and Si(D) sublattices), and (iii) $A2$ (complete disordering) structures of Co_2FeSi as well as (iv) the substrate GaAs. Second, we compared the simulated results with the experimental results for both the Co_2FeSi layer and the GaAs substrate. In comparing the patterns, we examined if the simulated pattern which resembles the experimental pattern has realistic thickness and defocus values and if these values are nearly equal for both the Co_2FeSi layer and the GaAs substrate. By checking the values for both layers, we can obtain a more reliable assignment. Finally, we examined the maps to see if the experimental pattern agrees with other simulated patterns of our three models.

Figures 2–4 show the t-Δf maps of Co_2FeSi with $L2_1$ and disordered $B2$ structure and GaAs, respectively, along the [110] zone axis in the range of interest around the Scherzer defocus. The crystal structures along the [110] direction of the $L2_1$ and $B2$ structure are schematically shown in Figs. 1(c) and 1(d). The electron incident angle is along the [110] direction for both the Co_2FeSi layer and GaAs substrate as the straightforward cube-on-cube epitaxial relationship of $Co_2FeSi[110](001)\|GaAs[110](001)$ was confirmed by reflection high-energy electron diffraction and x-ray diffraction (XRD) in our previous work.[6] The beam tilt was assumed to be zero in the contrast simulations, since the electron beam was carefully aligned along the [110] zone axis using the diffraction pattern of the GaAs substrate. As expected from their crystal structures, the patterns of the $B2$ structure have the half unit-cell periodicity of those of the $L2_1$ structure (cf. Figs. 2 and 3). On the other hand, the simulated patterns for the $A2$ structure (not shown) show simple vertical line patterns, since the interferences involve only the beams from the fundamental reflections and the spacing of the (004) planes is beyond the point resolution of the microscope. This type of simple vertical line pattern can be found, for instance, for bcc-Fe grown on GaAs substrate.[21] We will come back to the simulated results later in the discussion of the experimental results described below.

We first discuss the experimental results of the $Co_2FeSi/GaAs(001)$ films grown at an intermediate T_G of 200 °C. From the results of XRD and magnetic measurements in our previous studies, we found that an abrupt and atomically ordered interface can be achieved at this T_G.[22,23] Figure 5 shows a cross-sectional HRTEM micrograph of the $Co_2FeSi/GaAs(001)$ interface grown at 200 °C obtained along the [110] zone axis. The image has been Fourier filtered in order to reduce the noise and to obtain a more well-

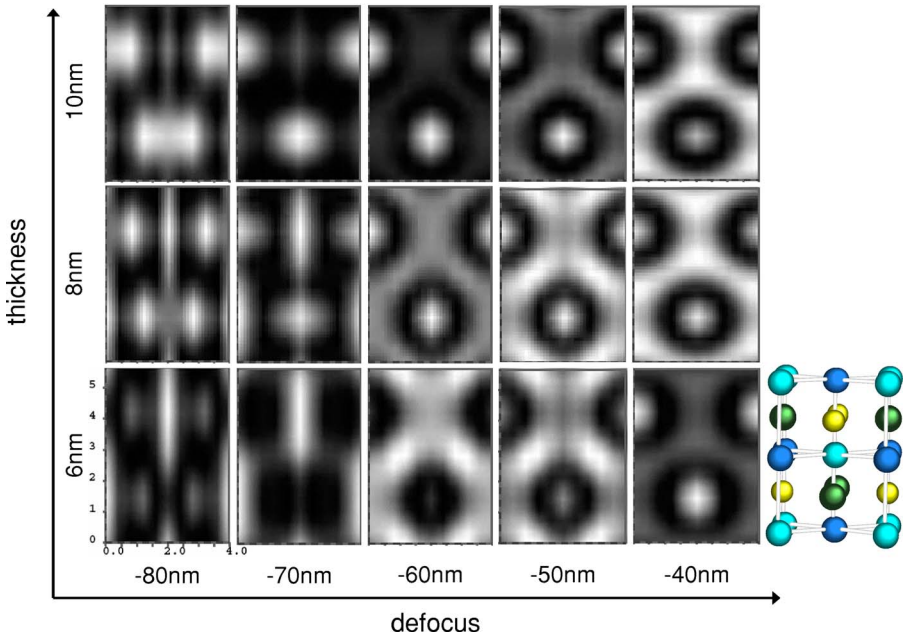

FIG. 2. Thickness-defocus map of the contrast simulations for Co_2FeSi with the $L2_1$ structure along the [110] zone axis. The crystal structure assumed in the simulation is shown in Fig. 1(c).

defined contrast. The array of bright dots in the substrate area is related to the two GaAs{111} planes. On the other hand, the lattice fringe patterns of the Co_2FeSi layer show a coexistence of two phases: (i) a line-and-ball interference pattern in the off-interface region and (ii) a gridlike interference pattern with the half unit-cell periodicity of that of the line-and-ball one, which can be seen predominantly near the interface region (Fig. 5).

In order to identify these phases, we compared these patterns with the simulated results. From careful comparisons with the t-Δf maps, we found that the line-and-ball pattern is in agreement with the simulated pattern based on the ordered Heusler-type $L2_1$ structure with $\Delta f=-70$ nm and $t=8$ nm (cf. Fig. 2). On the other hand, the grid pattern agrees with the disordered $B2$ phase with $\Delta f=-70$ nm and $t=6$ nm (cf. Fig. 3). Moreover, the arrays of GaAs patterns are also well reproduced under the conditions of $\Delta f=-70$ nm and $t=6$ nm (cf. Fig. 4). These assignments meet the requirement that all the patterns are reproduced nearly under the same conditions, i.e., the same defocus value. Moreover, all the experimental patterns cannot be attributed to other structures except the ones assigned above, e.g., we cannot find the line-and-ball pattern in the t-Δf map of the $B2$ structure. These facts justify the above assignments of the crystal structures. Note that the slightly thicker area of the $L2_1$ phase originates from the TEM foil thickness fluctuation appearing during ion beam etching. The result for the 200 °C film indicates that

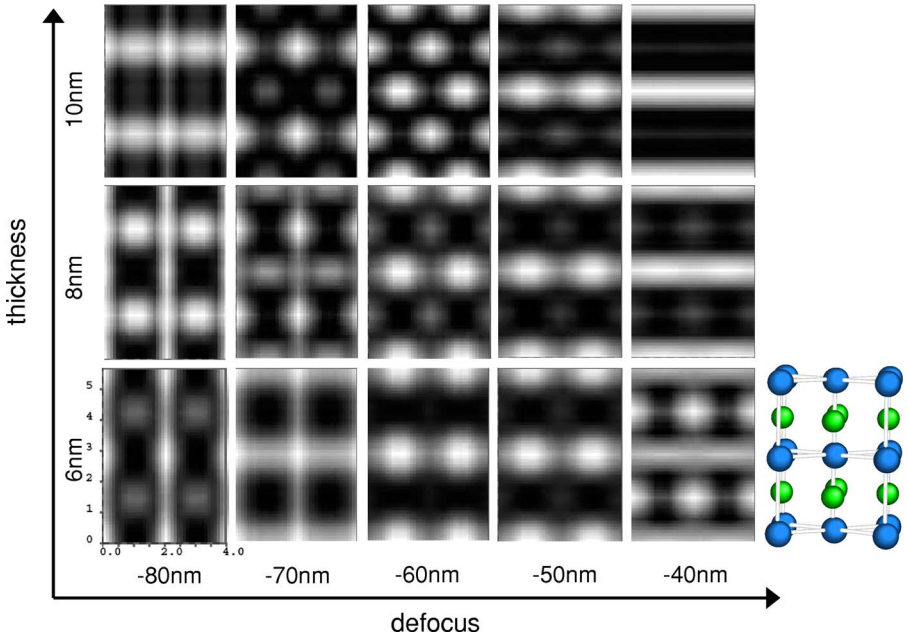

FIG. 3. Thickness-defocus map of the contrast simulations for Co_2FeSi with the $B2$ structure along the [110] zone axis. The crystal structure assumed in the simulation is shown in Fig. 1(d).

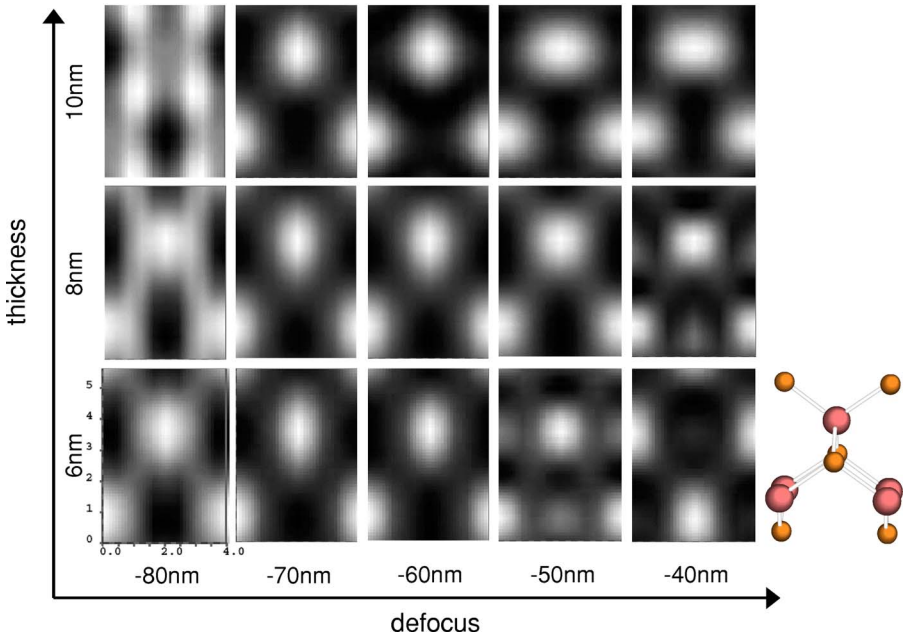

FIG. 4. Thickness-defocus map of the contrast simulations for GaAs zinc-blende structure along the [110] zone axis.

despite the abrupt and ordered interface, the atomically ordered and disordered phases coexist in the Co_2FeSi layer near the interface due to the low T_G.

Although the origin of the existence and distribution of the $B2$ phase, which extends to 6–10 monolayers (ML) near the interface in the 200 °C film are not clear, we consider two possible explanations. One is diffusion of Co atoms, which was found to be the dominant diffusing species in the $Co_2FeSi/GaAs$ system,[24] into the substrate. This causes the deviation of the composition of the Co_2FeSi layer from stoichiometry, leading to a reduction of the crystal symmetry especially near the interface. However, the Co indiffusion is supposed to be negligible at this low T_G as we did not obtain any evidence of interfacial compounds at this T_G.[24] The other explanation is based on the kinetics at the initial nucleation of the Co_2FeSi layer on the GaAs substrate. In the initial nucleation process, the adsorption energies of Fe and Si atoms for the B and D sites may be comparable when they are located on the GaAs surface in contrast to those in the bulk Co_2FeSi. This can cause a random distribution of the Fe and Si atoms on the B and D sites in the initial growth stage followed by a gradual recovery of atomic ordering during the further Co_2FeSi deposition, leading to the formation of the ordered $L2_1$ structure. Based on the observation that the interface region of films grown at the higher T_G of 300 °C is dominated by the $L2_1$ phase, as shown later, we consider that the latter reason is more plausible.

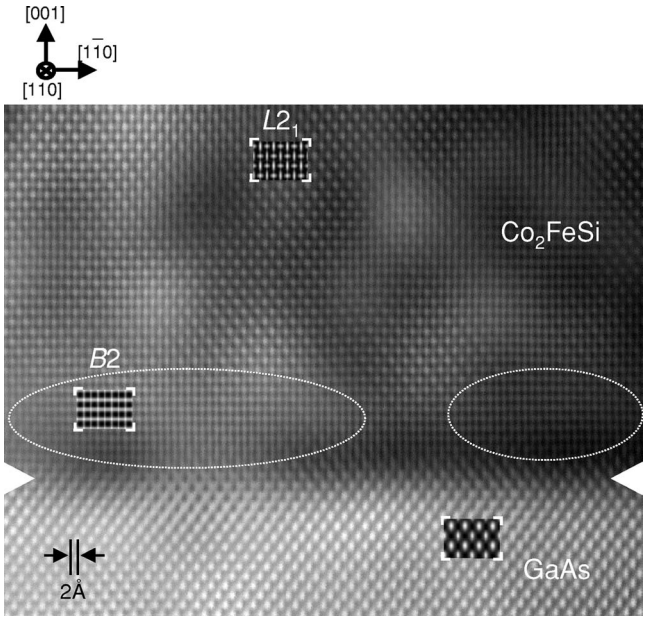

FIG. 5. Fourier-filtered cross-sectional HRTEM micrograph along the [110] zone axis of the $Co_2FeSi/GaAs(001)$ film grown at 200 °C. The simulated patterns for the $L2_1$ and $B2$ structures of Co_2FeSi and GaAs are shown for comparison as insets. The lattice spacing of GaAs $d\{220\} \approx 2$ Å is indicated for scaling.

Next we applied the same structure assignments to a film grown at lower T_G. In Fig. 6(a), we show a cross-sectional Fourier-filtered HRTEM micrograph of the Co_2FeSi layer grown at 100 °C. We revealed an atomically abrupt $Co_2FeSi/GaAs(001)$ interface and at least a certain degree of $L2_1$ ordering for the film grown at this temperature in the preceding work.[22] The $L2_1$ ordering was also revealed by our nanobeam diffraction (NBD) measurement for this film.[23] We show in Fig. 6(b) the NBD pattern of the Co_2FeSi layer grown at 100 °C together with the result of kinematical calculation of electron diffraction intensity for Co_2FeSi along the [110] zone axis. We used an electron beam with diameter of 3–5 nm for the NBD measurement, which is smaller than the Co_2FeSi layer thickness of 18 nm, in order to obtain information only from the Co_2FeSi layer. As can be seen in Fig. 6(b) the presence of the odd superlattice reflections, e.g., {111}, confirms the $L2_1$ ordering of the layer despite the low T_G. From Fig. 6(a), however, the coexistence of the line-and-

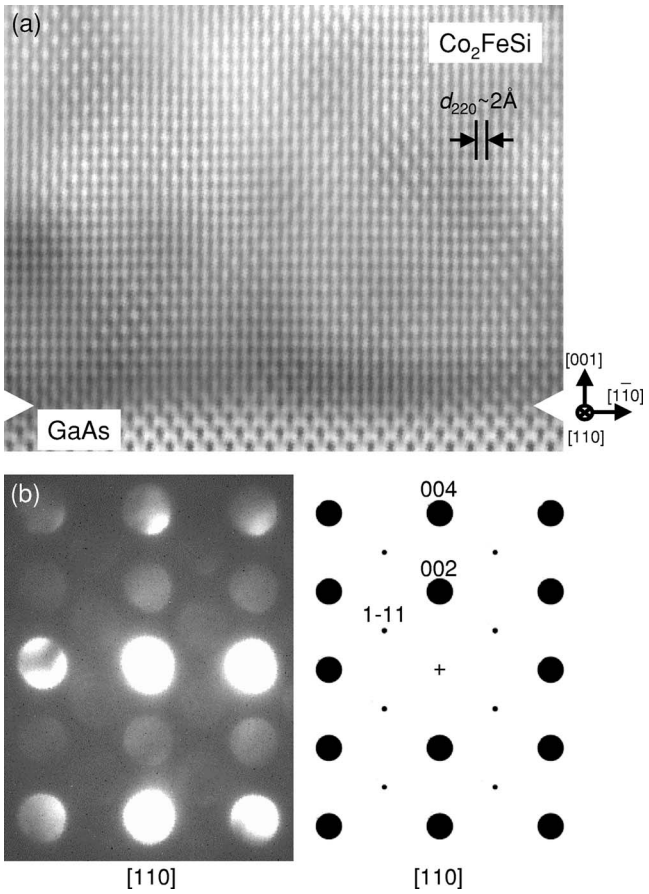

FIG. 6. (a) Fourier-filtered cross-sectional HRTEM micrograph along the [110] zone axis of $Co_2FeSi/GaAs(001)$ film grown at 100 °C. The lattice spacing of Co_2FeSi $d\{220\} \approx 2$ Å is indicated for scaling. (b) Nanobeam diffraction pattern of the Co_2FeSi layer grown at 100 °C obtained along the [110] zone axis (left). The result of the kinematical calculation of diffraction intensity for $L2_1$-Co_2FeSi is also shown in the right.

ball pattern ($L2_1$) and the grid pattern ($B2$) can be identified as in the case of the 200 °C film. The $B2$ phase extends up to approximately 14–15 ML near the interface. This indicates that the 100 °C film is also phase separated due to the low T_G similar to the 200 °C film, although the abrupt interface is achieved in this low T_G range. Therefore, the $L2_1$ atomic ordering, which was revealed by the NBD pattern and XRD asymmetric scans for the 100 °C film,[6,23] is not the proof of a long-range ordering in the whole layer. The layer indeed includes a large fraction of the disordered $B2$ phase due to the low T_G. This phase separation near the interface can hardly be identified by NBD measurement due to the small thickness of the phase-separated area compared to our electron beam diameter.

Finally, we turn to the results of a film grown at a higher temperature. Figure 7 shows a cross-sectional HRTEM micrograph after Fourier filtering for the $Co_2FeSi/GaAs(001)$ film grown at the elevated T_G of 300 °C along the [110] zone axis. The image shows a checkerboardlike rectangular pattern for the Co_2FeSi layer. As can be found in the t-Δf map of the $L2_1$ structure (cf. Fig. 2), this pattern also originates from the ordered $L2_1$ phase with the same defocus as for the line-and-ball pattern but a slightly different specimen thickness ($\Delta f = -70$ nm, $t = 6$ nm). This interference pattern cannot be simulated based on the $B2$ or $A2$ lattice structure. The uniform distribution of the $L2_1$ phase indicates that the T_G of 300 °C is sufficiently high to obtain a uniformly long-range-ordered Co_2FeSi layer, i.e., 300 °C is approximately the transition temperature into the $L2_1$ structure. This temperature almost agrees with the T_G at which the low-temperature resistivity of the Co_2FeSi films finally reaches a minimum, i.e., atomic disorder and/or defects are expected to be minimized.[6] For the lattice fringe patterns under the mentioned imaging condition, the white contrast corresponds to the atom positions. A perfect matching of the $Co_2FeSi\{220\}$ and the $GaAs\{220\}$ atomic planes ($d_{Co_2FeSi\{220\}} \simeq d_{GaAs\{220\}} \simeq 2$ Å) is visible across the interface, i.e., the layer is coherently strained in this area. The $Co_2FeSi\{004\}$ and $GaAs\{004\}$ lattice planes cannot be resolved due to the limited resolution of the microscope (0.17 nm), while the vertical length of a rectangle in the Co_2FeSi layer corresponds to the $Co_2FeSi\{002\}$ lattice planes; the lattice spacing is $d_{Co_2FeSi\{002\}} \simeq 2.82$ Å (cf. Fig. 7).

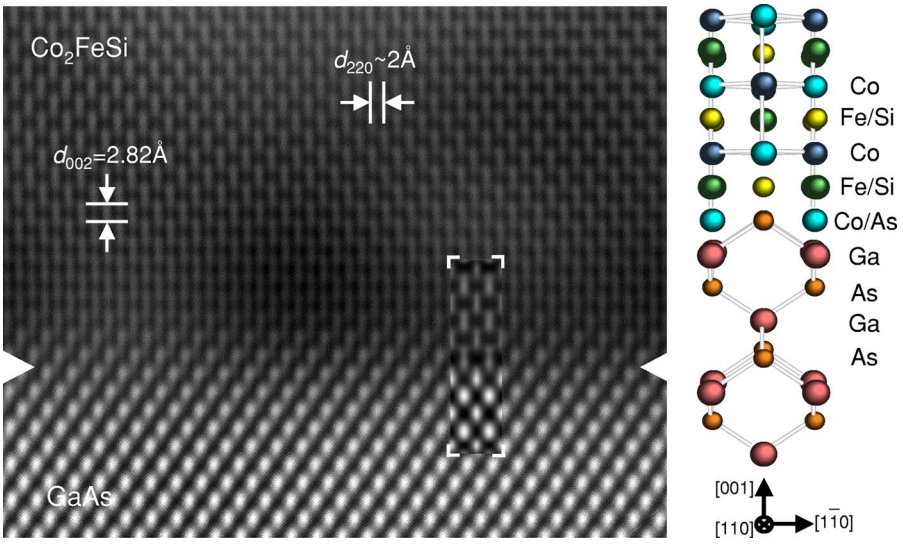

FIG. 7. Fourier-filtered cross-sectional HRTEM micrograph along the [110] zone axis of $Co_2FeSi/GaAs(001)$ film grown at 300 °C. The simulated image of the interface with the one-layer-intermixing model, which is schematically shown on the right of this figure, is embedded in the image for comparison. The lattice spacings of Co_2FeSi $d\{220\} \approx 2$ Å and $d\{002\} \approx 2.82$ Å are indicated for scaling.

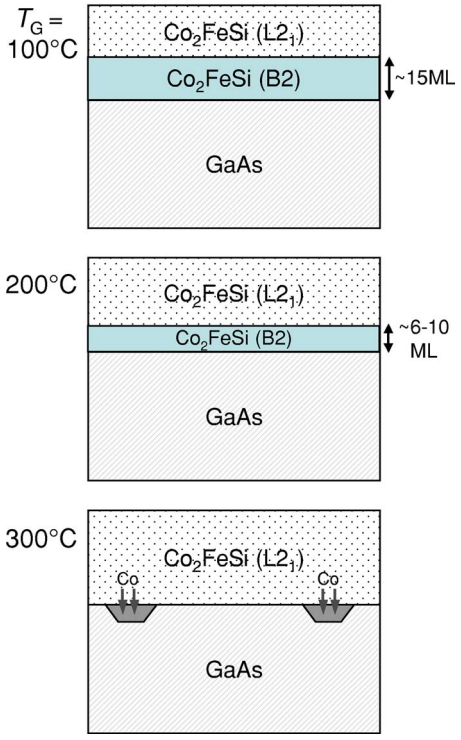

FIG. 8. Schematic illustrations of the spatial distribution of the $L2_1$ and $B2$ phases as well as the interfacial reaction in the $Co_2FeSi/GaAs(001)$ films grown at 100, 200, and 300 °C.

Despite the uniform $L2_1$ phase of the epilayer, however, further TEM observations around the near-interface area of the films have revealed the formation of interfacial compounds above a T_G of 250 °C (not shown). We found that the interfacial reaction takes place predominantly by Co indiffusion into the substrate, resulting in the formation of isolated grains in the substrate region.[24] The formation of the $L2_1$ and $B2$ phases and the interfacial reaction are schematically summarized with respect to T_G in Fig. 8. The increase of T_G suppress the formation of the $B2$ phase, leading to the formation of the uniform $L2_1$ phase together with the grains in the substrate region at 300 °C. Since the grains are isolated in the substrate region, the clear $Co_2FeSi/GaAs$ interface is preserved in the nonreacted areas, as schematically illustrated in Fig. 8 (bottom). This is in clear contrast to elemental ferromagnet/semiconductor systems, e.g., Co/GaAs and Fe/GaAs, where the reacted phase is typically extended over the interface.[21,25,26] Note that due to the Co indiffusion, the atomically ordered $L2_1$ phase observed in the 300 °C film (Fig. 7) probably does not extend throughout the whole layer. The interfacial reactions also degrade the magnetic properties. We found a reduction of the saturation magnetization as well as the in-plane magnetic anisotropy constants of the Co_2FeSi layer above the T_G of 250 °C.[22,23] Therefore, although an elevation of T_G up to 300 °C enables us to obtain an uniformly ordered layer, it induces an increased Co diffusion into the substrate, which leads to the formation of interfacial compounds. This could significantly degrade the spin injection efficiency.

The atomic arrangement of $Co_2FeSi/GaAs(001)$ interface was further examined for a nonreacted region of the 300 °C film by contrast simulation (Fig. 7). This is an additional important information since the atomic arrangement of the interface is predicted to influence the spin polarization at the interface.[27–29] We would like to note that although we have already revealed a one-layer-intermixed interface for the 200 °C film in our previous study,[23] the contrast simulations under the present conditions of $t=6$ nm and $\Delta f=-70$ nm can offer a much clearer distinction between the interface models, e.g., the period of the rectangle array, as well as the interference pattern at the interface differ in each model. Moreover, the 300 °C film offer the information on the atomic arrangement of $L2_1$-$Co_2FeSi/GaAs$ interface. The contrast simulations were performed for three Co_2FeSi/As-terminated-GaAs(001) interface models: (i) abrupt interface, (ii) one-layer-intermixed interface, where the bottom layer of Co_2FeSi is intermixed with the top As layer of the GaAs substrate and (iii) two-layer-intermixed interface, where the intermixing extends to the top (bottom) two layers of GaAs (Co_2FeSi).

From comparisons with the experimental pattern, we found that the lattice fringe pattern of the interface is best reproduced by the one-layer-intermixed interface model, which is schematically shown on the right side of Fig. 7. The simulated result of the one-layer-intermixed interface is given as an inset in Fig. 7. As can be seen in the figure, the period of the bright rectangle array perfectly matches with that in the experimental pattern, which is not the case for the other models. Moreover, the interference pattern at the interface agrees with that in the experimental pattern. The intermixing of the bottom Heusler layer with the top As layer can also modify the electronic structure, i.e., the theoretically predicted half-metallicity, near the interface. However, theoretical calculations for this interface configuration are highly desirable to account for this observation.

IV. CONCLUSIONS

In summary, we have studied the influences of the growth temperature on the atomic ordering and interlayer diffusion of the Heusler alloy Co_2FeSi grown on GaAs(001) by high-resolution transmission electron microscopy. The film grown at 200 °C shows the coexistence of the Heusler-type $L2_1$ phase and the disordered $B2$ phase near the interface due to the low growth temperature. The atomic disorder near the interface can in principle modify the electronic structure, i.e., the theoretically predicted half-metallicity of Co_2FeSi, which can degrade the spin injection efficiency. The film grown at a higher T_G of 300 °C shows a uniform $L2_1$ phase, indicating that the transition temperature into the $L2_1$ structure is around 300 °C. The elevation of the growth temperature, however, results in the formation of interfacial compounds above 250 °C, which could also be detrimental to an efficient electrical spin injection.

ACKNOWLEDGMENTS

This work was partly supported by the German BMBF under the research program NanoQUIT (Contract No. 01BM463). The authors would like to thank H.-P. Schönherr for his support in sample preparation and for useful discussions and E. Luna for a careful reading of the manuscript.

[1]C. Palmstrøm, MRS Bull. **28**, 725 (2003).
[2]V. Niculescu, J. I. Budnick, W. A. Hines, K. Raj, S. Pickart, and S. Skalski, Phys. Rev. B **19**, 452 (1979).
[3]S. Wurmehl, G. H. Fecher, H. C. Kandpal, V. Ksenofontov, C. Felser, H.-J. Lin, and J. Morais, Phys. Rev. B **72**, 184434 (2005).
[4]P. J. Webster and K. R. A. Ziebeck, *Magnetic Properties of Metals*, Landolt-Börnsterin, New Series, Group III, Vol. 19, Pt. C (Springer, Berlin, 1988), p. 75.
[5]M. Hashimoto, J. Herfort, H.-P. Schönherr, and K. H. Ploog, Appl. Phys. Lett. **87**, 102506 (2005).
[6]M. Hashimoto, J. Herfort, H.-P. Schönherr, and K. H. Ploog, J. Appl. Phys. **98**, 104902 (2005).
[7]G. B. Johnston and E. Hall, J. Phys. Chem. Solids **29**, 193 (1968).
[8]P. J. Webster, J. Phys. Chem. Solids **32**, 1221 (1971).
[9]Y. V. Kudryavtsev, Y. P. Lee, and J. Y. Rhee, Phys. Rev. B **69**, 195104 (2004).
[10]J. Rusz, L. Bergqvist, J. Kudrnovský, and I. Turek, Phys. Rev. B **73**, 214412 (2006).
[11]A. W. Carbonari, R. N. Saxena, J. Mestnik-Filho, G. A. Cabrera-Pasca, M. N. Rao, J. R. B. Oliveira, and M. A. Rizzuto, J. Appl. Phys. **99**, 08J104 (2006).
[12]S. Picozzi and A. J. F. A. Continenza, Phys. Rev. B **69**, 094423 (2004).
[13]Y. Miura, K. Nagao, and M. Shirai, Phys. Rev. B **69**, 144413 (2004).
[14]I. Galanakis, K. Özdogan, B. Aktas, and E. Sasioglu, Appl. Phys. Lett. **89**, 042502 (2006).
[15]W. H. Wang *et al.*, Phys. Rev. B **71**, 144416 (2005).
[16]H. Schneider *et al.*, Phys. Rev. B **74**, 174426 (2006).
[17]Z. Gercsi, A. Rajanikanth, Y. K. Takahashi, K. Hono, M. Kikuchi, N. Tezuka, and K. Inomata, Appl. Phys. Lett. **89**, 082512 (2006).
[18]H.-P. Schönherr, R. Nötzel, W. Ma, and K. H. Ploog, J. Appl. Phys. **89**, 169 (2001).
[19]J. Herfort, H.-P. Schönherr, and K. H. Ploog, Appl. Phys. Lett. **83**, 3912 (2003).
[20]CERIUS2, Molecular Simulations Incorporated, San Diego, CA.
[21]J. Herfort, A. Trampert, and K. H. Ploog, Z. Metallkd. **97**, 1026 (2006).
[22]M. Hashimoto, J. Herfort, A. Trampert, H.-P. Schönherr, and K. H. Ploog, J. Vac. Sci. Technol. B **24**, 2004 (2006).
[23]M. Hashimoto, J. Herfort, A. Trampert, and K. H. Ploog, J. Cryst. Growth **301–302**, 592 (2007).
[24]M. Hashimoto, J. Herfort, A. Trampert, H.-P. Schönherr, and K. H. Ploog, J. Phys. D **40**, 1631 (2007).
[25]C. J. Palmstrøm, C. C. Chang, A. Yu, G. J. Galvin, and J. W. Mayer, J. Appl. Phys. **62**, 3755 (1987).
[26]B. Lépine *et al.*, J. Appl. Phys. **83**, 3077 (1998).
[27]S. Picozzi, A. Continenza, and A. J. Freeman, J. Phys. Chem. Solids **64**, 1697 (2003).
[28]I. Galanakis, J. Phys.: Condens. Matter **16**, 8007 (2004).
[29]Y. Miura, K. Nagao, and M. Shirai, Phys. Rev. B **73**, 104447 (2006).

PHYSICAL REVIEW B **78**, 121303(R) (2008)

$Co_2FeSi/GaAs/(Al,Ga)As$ spin light-emitting diodes: Competition between spin injection and ultrafast spin alignment

M. Ramsteiner,* O. Brandt, T. Flissikowski, H. T. Grahn, M. Hashimoto,† J. Herfort, and H. Kostial
Paul-Drude-Institut für Festkörperelektronik, Hausvogteiplatz 5-7, 10117 Berlin, Germany
(Received 24 July 2008; published 18 September 2008)

Electrical injection from the Heusler alloy Co_2FeSi into (Al,Ga)As is investigated for different growth temperatures T_G of the injector layer. Depending on T_G, the spin polarization of injected electrons in the semiconductor is determined by two competing mechanisms: actual spin injection at the $Co_2FeSi/(Al,Ga)As$ interface and ultrafast spin alignment in the (Al,Ga)As layer. This layer is strongly affected by the thermally activated diffusion of Co, Fe, and Si during the growth of the Co_2FeSi layers. Despite the electrical compensation and magnetic transformation in the underlying semiconductor structure, a spin-injection efficiency of at least 50% is achieved as deduced from the analysis of electroluminescence and time-resolved photoluminescence data.

DOI: 10.1103/PhysRevB.78.121303 PACS number(s): 72.25.Hg, 72.25.Dc, 72.25.Mk, 72.25.Rb

Spin injection from ferromagnetic metals into semiconductors is an important building block for spintronic applications.[1–4] With respect to the desired high spin-injection efficiency, a very promising concept is the introduction of a spin-dependent tunnel barrier between the ferromagnetic injector and the semiconductor as demonstrated recently for the system (Co,Fe)/MgO/(Al,Ga)As.[5,6] Assuming perfect spin filtering by the tunnel barrier, a 100% spin-injection efficiency can in principle be achieved. An alternative approach is to utilize a halfmetal as spin-injector material. In this case, the complete spin polarization of electrons at the Fermi energy necessarily leads to a spin-injection efficiency of 100% without the need for a tunnel barrier acting as a spin filter. In this respect, ferromagnetic Heusler alloys are of particular interest due to the fact that some of them have been predicted to be halfmetallic. For one member of this material class, Co_2MnGe, spin injection into (Al,Ga)As has been investigated.[7] However, the spin-injection efficiency has been limited to relatively low values due to the formation of a disordered phase at the interface with the semiconductor. The Heusler alloy Co_2FeSi is also predicted to be a halfmetal and has the advantage to be closely lattice matched to GaAs allowing for the synthesis of high-quality epitaxial layers on GaAs/(Al,Ga)As spin light-emitting diodes (spin LEDs).

In this Rapid Communication, we investigate the spin injection from Co_2FeSi in GaAs/(Al,Ga)As spin LEDs. The spin LEDs with a design similar to that given in Ref. 4 (cf. Table I) were grown in a dual-chamber molecular-beam epitaxy (MBE) system. These devices comprise the following layer sequence grown in the semiconductor-MBE chamber on *p*-type GaAs(001) substrates: 400 nm *p*-GaAs ($p=1\times10^{17}$ cm^{-3}), 200 nm *p*-$Al_{0.1}Ga_{0.9}As$ ($p=1\times10^{16}$ cm^{-3}), 50 nm of undoped material containing a 10-nm-thick GaAs quantum well sandwiched between 20-nm-thick $Al_{0.1}Ga_{0.9}As$ barriers, 115 nm *n*-$Al_{0.1}Ga_{0.9}As$ (100 nm with $n=1\times10^{16}$ cm^{-3} and 15 nm linearly graded from $n=1\times10^{16}$ to 5×10^{18} cm^{-3}), and 15–25 nm *n*-$Al_{0.1}Ga_{0.9}As$ ($n=5\times10^{18}$ cm^{-3}). After the growth of the semiconductor structure, the samples were transferred to the metal-MBE growth chamber in ultrahigh vacuum, and a 9-nm-thick Co_2FeSi layer was deposited at temperatures of 100 °C (LED 1 and LED 1a), 200 °C (LED 2), and 300 °C (LED 3). For more details about the Co_2FeSi growth, we refer the readers to Ref. 8. The MBE-grown structures were subsequently processed into mesa-shaped devices with a diameter of 450 μm. The electroluminescence (EL) measurements were performed in Faraday geometry with the LEDs placed in a superconducting magnet system. The circular polarization degree of the EL signal was analyzed by using a photoelastic modulator (PEM) in combination with lock-in detection. The degree of circular polarization is determined by $P=(I_+-I_-)/(I_++I_-)$, where I_+ (I_-) is the intensity of right (left) circularly polarized light. The absolute value of the polarization degree P is identical to the spin polarization of the radiatively recombining electrons if the heavy holes are assumed to be unpolarized. Time-resolved photoluminescence (PL) measurements were performed using a synchro-scan streak camera system

TABLE I. Co_2FeSi-growth temperature T_G, postgrowth thermal annealing temperature T_A, injector material (Co_2FeSi or Ti), and type of magnetic-field dependence in a spin-injection experiment (PM=paramagnetic or FM=ferromagnetic) for the spin LEDs under investigation.

	LED 1	LED 2	LED 3	LED 1a	LED 2t	LED 3t
T_G (°C)	100	200	300	100	200	300
T_A (°C)	—	—	—	300	—	—
Injector	Co_2FeSi	Co_2FeSi	Co_2FeSi	Co_2FeSi	Ti	Ti
Type	—	PM	FM	FM	PM	—

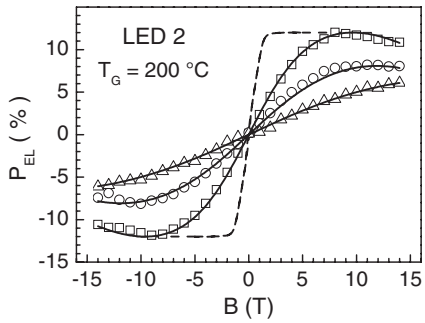

FIG. 1. Degree of circular EL polarization P_{EL} as a function of external magnetic field of LED 2 at 20 K (squares), 50 K (circles), and 100 K (triangles) together with the out-of-plane magnetization curve measured by SQUID (dashed line in arbitrary units) and the expected polarization for a paramagnetic DMS (solid lines) according to a model based on Eqs. (1) and (2).

in conjunction with a Ti:sapphire laser emitting 200 fs pulses with a repetition rate of 76 MHz. An initial spin polarization of photoexcited carriers was created by pump pulses, which were right circularly polarized by means of a quarter-wave plate. The emitted PL light was analyzed into its right (I_{++}) and left (I_{+-}) circularly polarized components.

Investigations of $Co_2FeSi/GaAs$ structures by transmission electron microscopy (TEM) as described in Ref. 9 revealed interfacial reactions at growth temperatures $T_G > 250$ °C with the conclusion that $T_G \sim 200$ °C is optimal for achieving high spin-injection efficiency from Co_2FeSi into GaAs. However, the investigated LEDs exhibit variations in their electro-optical characteristics wider than expected from the structural data obtained by the TEM study.[9] In particular, the EL intensity of LED 1 is too weak to determine its polarization. In contrast, the EL intensity of LEDs with higher Co_2FeSi growth temperature is several orders of magnitude higher, but their polarization properties are strikingly different. The EL polarization (P_{EL}) of LED 2 is shown in Fig. 1 as a function of the external magnetic field. P_{EL} of this device does not follow the out-of-plane magnetization of the Co_2FeSi injector measured by superconducting quantum interference device (SQUID) magnetometry (shown in Fig. 1 as dashed line in arbitray units and with the sign selected according to that of P_{EL}), from which a saturation at an external magnetic field of about 1 T is expected. Instead, the saturation of P_{EL} at 20 K requires a field as high as 8 T, which resembles the magnetic response of a paramagnetic material, such as a dilute magnetic semiconductor (DMS).

In contrast, the EL polarization of LED 3 clearly evidences a ferromagnetic response since it tracks the magnetization of the injector material over the whole range of magnetic fields as shown in Fig. 2 (note the different scale compared to Fig. 1). A further striking difference between LEDs 3 and 2 is the opposite sign of P_{EL}. Thermal annealing of LED 1 for 30 min at 300 °C (LED 1a in Table I) results in an EL intensity and a polarization response basically identical to the one of LED 3. It is important to note that the observed polarization degrees of 15% to 20% in the saturation range are basically one order of magnitude larger as compared to our previous spin-injection experiments using Fe, Fe_3Si, or MnAs injectors.[1,10,11]

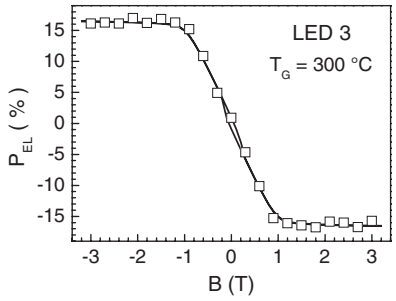

FIG. 2. Degree of circular EL polarization P_{EL} as a function of external magnetic field at 20 K of LED 3 (squares) together with the out-of-plane magnetization curve measured by SQUID (solid line in arbitrary units). For a better comparison with the EL polarization, the sign of the magnetization curve has been reversed with respect to that in Fig. 1.

The complex behavior evidenced by Figs. 1 and 2 is elucidated by secondary-ion mass spectrometry (SIMS) and TEM. Figure 3 displays the SIMS depth profiles for Co [Fig. 3(a)], Fe [Fig. 3(b)], and Si [Fig. 3(c)] in spin LEDs onto which a Co_2FeSi injector was deposited at $T_G = 100$ °C, 200 °C, and 300 °C. Note that the injector layer has been removed by selective wet chemical etching withHF prior to the SIMS depth profiling. The concentration of all elements in the upper $Al_{0.1}Ga_{0.9}As$ layer, but particularly of Co and Fe, is seen to increase drastically with increasing T_G. For $T_G = 300$ °C, the concentration of both Co and Fe exceeds several 10^{20} cm^{-3} in the topmost 20 nm of the LED structure. For the case of Fe, an Arrhenius plot of the integrated concentration yields an activation energy of 0.44 eV, while the diffusion of Co seems to be more complex and cannot be

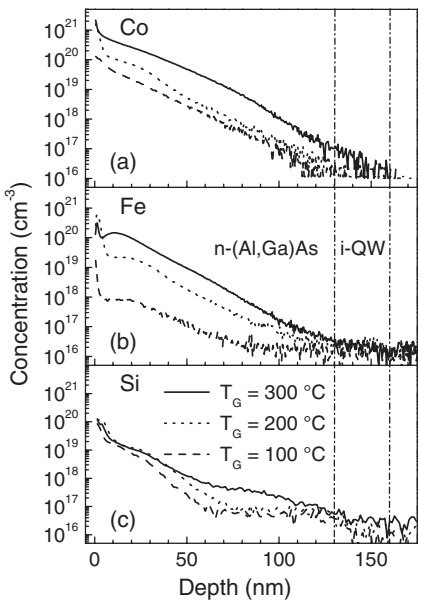

FIG. 3. Concentration depth profiles of (a) Co, (b) Fe, and (c) Si in LEDs with Co_2FeSi injectors grown at $T_G = 300$ °C (solid curves), $T_G = 200$ °C (dotted curves), and $T_G = 100$ °C (dashed curves) measured by secondary-ion mass spectrometry (SIMS). The vertical dash-dotted lines indicate the intrinsic region of the LED structures (i-QW).

described by a simple activated process. Finally, the SIMS profiles of LED 1a (cf. Table I) reveal that postgrowth thermal annealing at 300 °C does not induce significant diffusion into the semiconductor structure (not shown here).

SIMS integrates over an area of typically 60×60 μm^2 and thus does not give information about the actual lateral distribution of the diffused species. As mentioned above, previous TEM experiments in conjunction with x-ray diffraction have revealed the formation of (Co,Ga)As precipitates at growth temperatures above 250 °C.[9] At lower temperatures, no precipitates were found suggesting that both Co and Fe are incorporated as isolated impurities, which are expected to be electrically active.

With the help of these additional experiments, we are in a position to suggest a tentative yet comprehensive model for the explanation of our results. At $T_G=100$ °C, we suppose that nonradiative defects are generated at the $Co_2FeSi/Al_{0.1}Ga_{0.9}As$ interface and remain there due to their insufficient mobility at this low temperature. Consequently, the EL efficiency of LED 1 is very low. At $T_G=200$ °C, these nonradiative defects are presumably annihilated by diffusion at the interface. However, significant diffusion of Co and Fe sets in simultaneously, effectively converting the upper $Al_{0.1}Ga_{0.9}As$ layer into a DMS with paramagnetic response. Finally, at $T_G=300$ °C, bulk segregation of Co and Fe occurs causing the formation of precipitates and the depletion of Co and Fe from the DMS matrix, which is very similar to the behavior reported for Fe in GaAs.[12,13] This process effectively depletes the matrix of substitutional Co and Fe.

The observed saturation of the polarization at 8 T for LED 2 (cf. Fig. 1) is a signature of spin alignment in a paramagnetic semiconductor. Consequently, spin alignment in the upper $Al_{0.1}Ga_{0.9}As$ barrier has to be taken into account. We thus expect the following magnetic-field dependence of P_{EL} in thermal equilibrium:[14]

$$P_{EL}(B)=\tanh\left[\frac{g\mu_B(B+B_{int})}{2k_BT}\right], \tag{1}$$

where k_B is the Boltzmann factor and T is the temperature. $\Delta E(B)=g\mu_B B$ is the energy separation between the Zeeman sublevels of electrons in the upper $Al_{0.1}Ga_{0.9}As$ barrier in an external magnetic field B. For a magnetic semiconductor, we have to consider the additional splitting $\Delta E_{int}(B)=g\mu_B B_{int}$ generated by the internal field produced by the magnetic atoms given by

$$B_{int}=\frac{N_0\alpha xJ}{g\mu_B}B_J\left(\frac{g_M\mu_B JB}{k_BT}\right), \tag{2}$$

where g_M is the g factor, J is the total angular-momentum quantum number, and x is the concentration of magnetic atoms. $N_0\alpha$ is the exchange constant and $B_J(B,T)$ is the Brillouin function. We analyze the data with a rate-equation model, which takes into account spin scattering, such that thermal equilibrium according to Eq. (1) is reached when the spin-relaxation time is much shorter than the transit time of the electrons through the upper $Al_{0.1}Ga_{0.9}As$ barrier.[15] Furthermore, our model assumes a generation term, which corresponds to spin injection with a magnetic-field dependence according to the ferromagnetic out-of-plane magnetization of Co_2FeSi. Indeed, the magnetic-field dependence in Fig. 1 can be described very well by our model using a spin-relaxation time about two orders of magnitude shorter than the transit time. Since the transit time is expected to be on the order of picoseconds, this finding constitutes an ultrafast spin alignment. For the remaining parameters in Eqs. (1) and (2), we assume values which are typical for GaAs-based DMS.[15] The observed temperature dependence between 20 and 100 K is characteristic for a paramagnetic DMS and can be simulated consistently with our DMS-related model (cf. Fig. 1; for details see Ref. 15) The sign of P_{EL} due to spin alignment depends on the sign of the g factors of free electrons and holes in the semiconductor structure. These signs and, exclusively for a DMS, the sign of the exchange constant $N_0\alpha$ define the ordering of the Zeeman levels. We verified that the spin alignment due to Zeeman thermalization in LEDs without ferromagnetic injector leads to the opposite sign of P_{EL} as compared to that of LED 2. The corresponding contribution to P_{EL} from Zeeman thermalization inside or below the active region is observed in Fig. 1 for $T=20$ K at very large magnetic fields as a slight decrease of P_{EL}. Thus, the observed sign of P_{EL} strongly supports our model.

The experimental observation for LED 3 (cf. Fig. 2) provides evidence for spin injection from Co_2FeSi with the preferential spin orientation opposite to that in thermal equilibrium in the DMS-like $Al_{0.1}Ga_{0.9}As$ barrier of LED 2. This result is explained by the effective depletion of the upper $Al_{0.1}Ga_{0.9}As$ barrier of substitutional Co and Fe so that spin alignment is rendered ineffective. Our model is confirmed by the results obtained from LEDs after the replacement of the Co_2FeSi injectors by a nonmagnetic Ti injector. After the exchange of a Co_2FeSi injector grown at 300 °C (LED 3t in Table I) neither paramagnetic nor ferromagnetic behavior is obtained. On the contrary, after removal of a Co_2FeSi injector grown at 200 °C (LED 2t in Table I) we still observe a clear paramagnetic signature with the absolute value of P_{EL} remaining nearly unchanged. The situation for Co_2FeSi growth at 200 °C is particularly interesting, since spin injection from ferromagnetic Co_2FeSi presumably coexists with the competing ultrafast spin alignment in the underlying paramagnetic semiconductor. In order to explain the complete absence of a remaining ferromagnetic signature in the EL polatization (cf. Fig. 1), we have to assume a very strong spin scattering in the topmost $Al_{0.1}Ga_{0.9}As$ layer leading to a complete relaxation of spins into thermal equilibrium as given by Eq. (1). Considering the large concentration of magnetic impurities in that layer, this strong spin scattering is not surprising.

Another interesting point we would like to stress is the high EL polarization measured for LED 1a. Apparently, the annealing effectively removes nonradiative defects but does not induce a diffusion of Co and Fe into the semiconductor. Consequently, MBE growth at low temperatures combined with postgrowth annealing seems to be a potentially attractive strategy to produce efficient spin-injection devices without strong interdiffusion at the ferromagnet/semiconductor interface.

For obtaining the actual spin-injection efficiency S at the

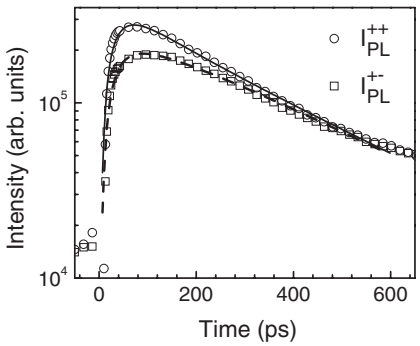

FIG. 4. Right (circles: I_{++}) and left (squares: I_{+-}) circularly polarized PL transients of the reference sample upon right circularly polarized excitation in the barrier at 20 K. The lines indicate the simultaneous fit of the data by the model mentioned in the text.

ferromagnet/semiconductor interface, we examine the carrier recombination and spin dynamics in the active region of our spin LEDs.[10] For this aim, we perform time-resolved PL on a reference *n-i-n* structure with an active region identical to that of the spin LEDs under investigation. Figure 4 shows the right and left circularly polarized PL transients from this sample for excitation at an energy above the band gap of the $Al_{0.1}Ga_{0.9}As$ barriers at 20 K. We analyzed the data with a model which takes into account not only the spin flip of excitons (τ_x) but also the spin flip of electrons (τ_e) and holes (τ_h) and thus the participation of dark exciton states.[16] A simultaneous fit of the data for both polarizations by this model (cf. Fig. 4) yields τ_x=250, τ_e=800, τ_h=20, and the radiative lifetime τ_r=150 ps. With these values, the measured circular polarization P_{EL} of 17% corresponds to an actual value for S of 51%. While this value is lower than the desired one (100%), one has to bear in mind the efficient scattering of spin-polarized electrons by the magnetic impurities in the upper $Al_{0.1}Ga_{0.9}As$ layer as mentioned above. This scattering reduces the initial spin polarization of the electrons prior to their capture by the GaAs quantum well. Therefore, the value deduced for S is still a lower limit for the actual spin-injection efficiency at the ferromagnet/semiconductor interface. This result leaves us with the open question of whether or not Co_2FeSi is indeed a halfmetallic spin injector. In this context, it is interesting to note that the sign of P_{EL} observed for LED 3 (cf. Fig. 2) is opposite to that of our previous spin-injection experiments using Fe, Fe_3Si, or MnAs injectors[1,10,11] reflecting a qualitatively different electronic band structure in Co_2FeSi.

Finally, let us stress that the diffusion of Co and Fe not only leads to a *magnetic* modification of the topmost semiconductor part in our spin LEDs but also to an *electrical* one. Since both Co and Fe are deep acceptors in (Al,Ga)As and are both present in very large concentrations (cf. Fig. 3), the topmost $Al_{0.1}Ga_{0.9}As$ layer in our LEDs is unlikely to be *n* type as intended but is probably entirely compensated by the huge concentration of deep acceptors present in the material. Thus, the topmost layer is expected to be depleted, which is actually confirmed by capacitance-voltage measurements (not shown here). Consequently, the formation of a Schottky barrier at the ferromagnet/semiconductor interface cannot take place, and tunneling should not play a significant role for the injection process. At the same time, we observe a rather large spin-injection efficiency, which casts doubt onto the common belief that tunneling is a prerequisite for spin injection from a metal into a semiconductor.

In summary, we have studied the electrical injection from the Heusler alloy Co_2FeSi into (Al,Ga)As. The magnetic and electrical properties of the semiconductor part in the investigated spin LEDs have been found to be strongly modified by thermally activated diffusion during MBE growth. The corresponding polarization of the EL reflects the competing mechanisms of spin injection and ultrafast spin alignment. Despite the strong diffusion of magnetic acceptor species, a large spin-injection efficiency of at least 50% has been achieved. Our results demonstrate the potential of Co_2FeSi for being a halfmetallic spin injector and indicate that tunneling is not necessarily an important process for spin injection at metal/semiconductor interfaces.

We acknowledge expert technical assistance by Edith Wiebicke and Gerd Paris as well as comments and a careful reading of the manuscript by Paulo Santos.

*ramsteiner@pdi-berlin.de

†Present address: Department of Electrical and Computer Engineering, University of California, Santa Barbara, CA 93106, USA.

[1] H. J. Zhu *et al.*, Phys. Rev. Lett. **87**, 016601 (2001).
[2] A. T. Hanbicki *et al.*, Appl. Phys. Lett. **80**, 1240 (2002).
[3] V. F. Motsnyi *et al.*, Phys. Rev. B **68**, 245319 (2003).
[4] C. Adelmann *et al.*, Phys. Rev. B **71**, 121301(R) (2005).
[5] X. Jiang *et al.*, Phys. Rev. Lett. **94**, 056601 (2005).
[6] R. Wang *et al.*, Appl. Phys. Lett. **86**, 052901 (2005).
[7] X. Y. Dong *et al.*, Appl. Phys. Lett. **86**, 102107 (2005).
[8] M. Hashimoto *et al.*, J. Appl. Phys. **98**, 104902 (2005).
[9] M. Hashimoto *et al.*, J. Vac. Sci. Technol. B **25**, 1453 (2007).
[10] M. Ramsteiner *et al.*, Phys. Rev. B **66**, 081304(R) (2002).
[11] A. Kawaharazuka *et al.*, Appl. Phys. Lett. **85**, 3492 (2004).
[12] S. Hirose *et al.*, Thin Solid Films **371**, 272 (2000).
[13] R. Moriya *et al.*, Physica E (Amsterdam) **10**, 224 (2001).
[14] W. Heimbrodt *et al.*, Physica E (Amsterdam) **10**, 175 (2001).
[15] O. Brandt *et al.* (unpublished).
[16] M. Z. Maialle *et al.*, Phys. Rev. B **47**, 15776 (1993).

Composition dependent properties of Fe_3Si films grown on GaAs(113)*A* substrates

P. K. Muduli,[a] K.-J. Friedland, J. Herfort, H.-P. Schönherr, and K. H. Ploog
Paul-Drude-Institut für Festkörperelektronik, Hausvogteiplatz 5-7, D-10117 Berlin, Germany

(Presented 13 November 2008; received 17 September 2008; accepted 27 November 2008; published online 5 March 2009)

Structural, electrical, and magnetic properties of Fe_3Si/GaAs(113)*A* hybrid structures are studied, dependent on the layer composition varying from 15 to 26 at. % Si. The presence of superlattice reflections in x-ray diffraction and lower resistivity confirms the long-range atomic ordering in the stoichiometric Fe_3Si films, reflecting the $D0_3$ crystal structure. The observed atomic ordering is also found to influence the sign and magnitude of the antisymmetric component of the planar Hall effect observed in this orientation. However a finite disorder is observed even in nearly stoichiometric samples. © *2009 American Institute of Physics*. [DOI: 10.1063/1.3072832]

Ferromagnet/semiconductor heterostructures are important for spin-electronic devices.[1] In order to achieve higher spin injection efficiency, the interface structure between the semiconductor and ferromagnet must be controlled carefully.[2] This is often performed by careful low temperature growth and processing. Growth or postgrowth annealing at modest temperatures can lead to interdiffusion and the formation of some interfacial compounds. For Fe or Co on GaAs, interaction and interdiffusion occur at moderate temperatures of about 200 °C.[3] Therefore, it is highly desirable to obtain alternative ferromagnets that show improved interfacial quality as well as a higher thermal stability. Fe_3Si is one such alternative material that exhibits better thermal stability[4,5] compared to Fe and other elemental ferromagnets. It is known to be ferromagnetic up to 840 K, and it has a cubic $D0_3$ crystal structure with a lattice constant of 5.653 Å, which is close to the lattice constant of GaAs. It is also regarded as a Heusler alloy, which is a promising candidate for spintronic applications due to its high Curie temperatures of 200–1100 K and its high degree of spin polarization[6] though calculated density of states for bulk Fe_3Si does not predict a half-metallic behavior.[7] For these reasons, Fe_3Si films epitaxially grown on semiconducting substrates such as GaAs (Refs. 8–11) and Si (Refs. 12 and 13) have promoted strong interests recently. Another striking advantage of Fe_3Si is the easy growth control compared to complex ternary Heusler alloys. This is not only due to its binary nature but also due to the broad phase stability of the Fe_3Si alloy, with Si contents ranging from 9.5 to 26 at. % Si.[14]

In this work, we present a study of the structural, electrical, and magnetic properties of Fe_3Si/GaAs(113)*A* hybrid structures dependent on the layer composition, with special focus on the influence of atomic ordering on these properties. Here we have chosen the GaAs(113)*A* surface, which is characterized by a low-surface symmetry, as the substrate for the growth of Fe_3Si films. Due to this low-surface symmetry, a unique antisymmetric contribution to the planar Hall effect (PHE) in the Fe(113) and Fe_3Si(113) films has been observed.[15] We will show that this antisymmetric component exhibits a sensitive dependence on atomic ordering. The properties will be compared with the Fe_3Si films grown on the GaAs(001) substrates.[8,10,11]

The high quality Fe_3Si films are grown on GaAs(113)*A* substrates by molecular-beam epitaxy.[9] The structural and crystalline qualities of these $Fe_{3+x}Si_{1-x}$ films show smooth surface morphology as well as a sharp interface with GaAs, as discussed elsewhere.[9] The high resolution x-ray diffraction (HRXRD) measurements are performed *ex situ* with a PANalytical X'pert diffractometer using Cu $K\alpha$ radiation with a Ge(220) monochrometer and a triple-bounce analyzer crystal. The magnetic properties of these films are studied *ex situ* using a commercial Quantum Design MPMS XL superconducting quantum interference device magnetometry. The transport measurements are performed on layers with lithographically patterned Hall bars aligned along the $[33\bar{2}]$ direction. The width of the Hall bar is 30 μm, and the separation between the voltage leads is 22.5 μm.

The cubic $D0_3$ structure of Fe_3Si is considered as four interpenetrating fcc sublattices *A*, *B*, *C*, and *D* with origins at $A(0,0,0)$, $B(0.25,0.25,0.25)$, $C(0.5,0.5,0.5)$, and $D(0.75,0.75,0.75)$. In the ordered Fe_3Si crystal, Fe atoms occupy the three sublattices *A*, *B*, and *C*, while Si atoms fill the sublattice *D*. In HRXRD measurements, Bragg reflections for this structure are obtained for planes with either all odd or all even Miller indices (h,k,l). The reflections for which *h*, *k*, and *l* are all even with $(h+k+l)=4n$ are fundamental reflections and are unaffected by the state of ordering. The reflections for which *h*, *k*, and *l* are all even with $(h+k+l)=4n+2$ are sensitive to an $(A,C)\leftrightarrow D$ disorder, whereas the reflections with odd *h*, *k*, and *l* are sensitive to both $B\leftrightarrow D$ and $(A,C)\leftrightarrow D$ disorder.[16,17] The relative intensities of these two classes of superlattice reflections depend on the state of ordering. But for a perfectly ordered lattice, the intensities should be equal.[16] For example, the (002) and (113) reflections should have the same intensity for a perfectly ordered Fe_3Si lattice. Hence to investigate the atomic

[a]Electronic mail: muduli@kth.se. Present address: Department of Microelectronics and Applied Physics, Royal Institute of Technology, Electrum 229, 164 40 Kista, Sweden.

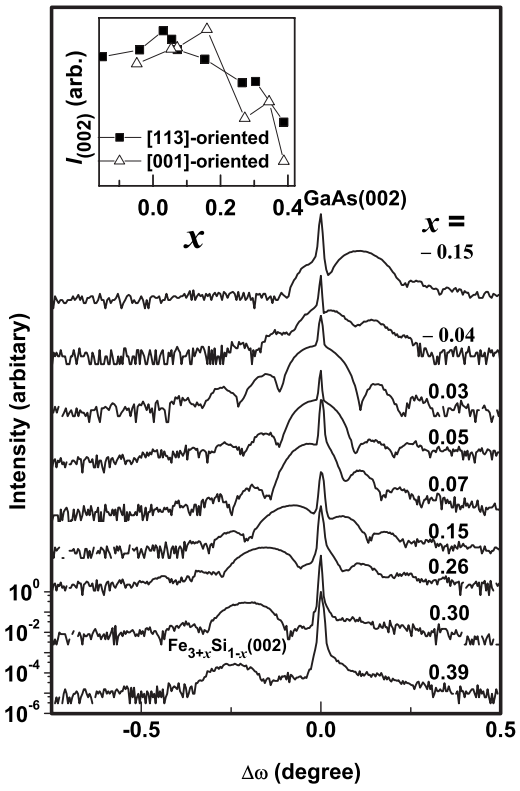

FIG. 1. Normalized *skew-symmetric* ω-2θ scans of Fe_3Si/GaAs(113)*A* near the superlattice (002) reflection. The curves are normalized to the GaAs(002) reflection and are shifted with respect to each other for clarity. The inset shows a plot of intensity of (002) reflection $I_{(002)}$ as a function of the composition x for [113]- and [001]-oriented films.

ordering of the Fe_3Si films, we analyze these two different superlattice reflections. The results are summarized in Figs. 1 and 2 as a function of composition x of the $Fe_{3+x}Si_{1-x}$ films, where x denotes the deviation from stoichiometry.

We found an increase in the intensity of the (002) reflection with increasing Si content toward stoichiometry, as shown in Fig. 1. This is more clearly seen in the inset in Fig.

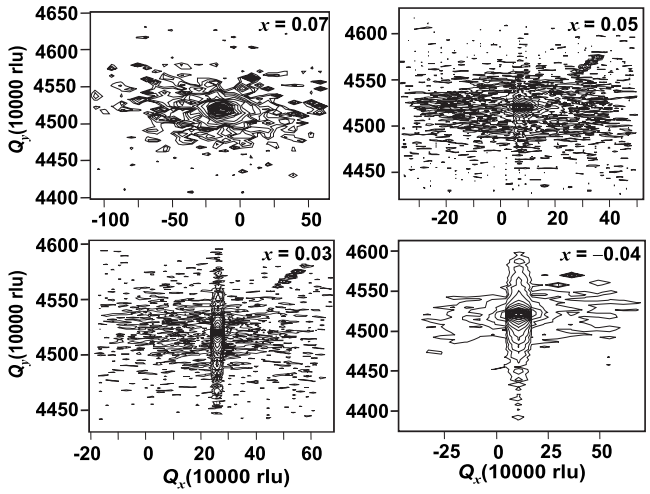

FIG. 2. X-ray reciprocal space maps of stoichiometric Fe_3Si films grown on GaAs(113)*A* substrates for the symmetric and superlattice (113) reflection. The reciprocal lattice unit (rlu) is $\lambda/2d$, where λ is the wavelength of Cu $K\alpha 1$ radiation and d is the lattice plane spacing of the corresponding reflection.

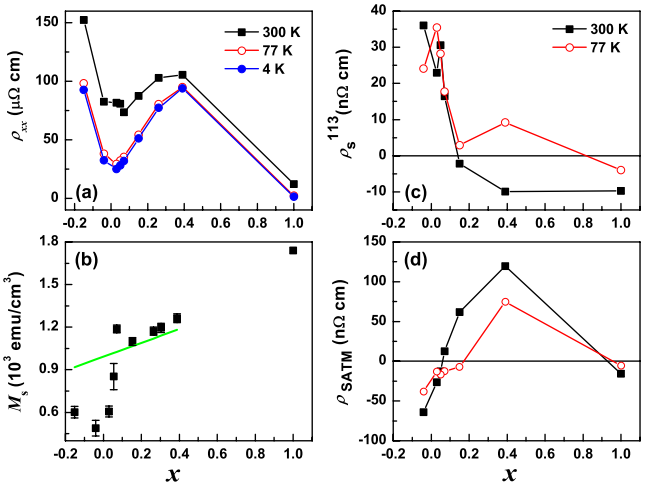

FIG. 3. (Color online) (a) Resistivity ρ_{xx} as a function of composition x for the $Fe_{3+x}Si_{1-x}$ alloys at 300, 77, and 4 K. (b) Saturation magnetization M_s as a function of composition x. Open rectangles are experimental points, whereas the solid line is the behavior according to Eq. (2). Composition dependence of the (c) symmetric PHE amplitude ρ_s^{113} and (d) antisymmetric amplitude ρ_{SATM} obtained from the fitting of transverse resistivity at a saturating field. In these figures $x=1$ represents a 20-nm-thick Fe film grown on GaAs(113)*A* substrates.

1, where intensity $I_{(002)}$ of the (002) layer reflection is plotted as a function of composition. The substrate reflection GaAs(002) is used as a reference to scale the intensity $I_{(002)}$. For comparison, the intensities of the Fe_3Si/GaAs(001) films are also shown. The behavior for both orientations is qualitatively similar, though in some cases, [113]-oriented samples exhibit slightly higher $I_{(002)}$. The superlattice and symmetric (113) reflections with odd h, k, and l are detectable only for the most stoichiometric samples with $x=0.05$, 0.03, and -0.04, as shown in Fig. 2. A slight increase in the intensity of the (113) reflection is also observed from $x=0.05$ to -0.04. Here, we show reciprocal space maps around the (113) reflection since the layer peak was not detected in normal symmetric ω-2θ scans. In Fig. 2, the distinction of the layer peak from the substrate peak (for $x=0.05$, 0.03, and -0.04) is not very clear. This is because the GaAs(113) reflection itself is rather broad and the layer peak is very close to that of the substrate peak. However, the interface fringes can be identified from the elongation along Q_y, indicating the presence of the layer reflection. Thus we observe an improvement in the long-range ordering of the lattice with increasing Si content toward stoichiometry. The observation of the (002) and (113) superlattice reflections for the nearly stoichiometric samples indicates the formation of the $D0_3$ crystal structure. However, the intensity of the (113) reflection of the layer was found lower compared to the (002) reflection in all samples, indicating a finite disorder even in the nearly stoichiometric samples.[11]

The effect of atomic ordering on electrical and magnetic properties is discussed in Fig. 3. For all studied temperatures, the resistivity ρ first increases with increasing Si content until $x=0.3$. However with further increase in the Si content, ρ shows a strong decrease, and a minimum is reached around the stoichiometry. For even higher Si contents ρ increases again. This behavior is very similar to that in bulk,[18]

$Fe_3Si(001)$ films[19] and can be understood from the Fe-Si site disorder. The electrical resistivity to a first approximation is given by:

$$\rho_{xx}(T) = \rho_0 + \rho_p(T), \tag{1}$$

where ρ_0 is the temperature independent residual resistivity due to impurity or alloy scattering mechanisms and $\rho_p(T)$ is the temperature dependent resistivity due to scattering by phonons. The residual resistivity ρ_0 is assumed to be temperature independent. In $Fe_{3+x}Si_{1-x}$, ρ_0 reflects the alloy scattering from the randomly distributed Si sites. As discussed above, the long-range order in Fe_3Si strongly depends on the Si content. Near stoichiometry, the layers are found to be ordered, and hence a decrease in the residual resistivity is observed. When randomly distributed Si atoms are added to pure Fe, the resistivity rapidly increases due to the enhancement of alloy scattering. The increase in the resistivity is suppressed for $x > 0.3$ when atomic ordering begins to occur. While the ordering is established, the resistivity turns from the local maximum at around $x=0.3$ to the minimum at the perfect ordering for stoichiometric Fe_3Si since in this case alloy scattering is strongly reduced and phonon scattering, which depends strongly on temperature, comes into play. For higher Si content or $x < 0$, the Si atoms replace the Fe atoms, randomly resulting in higher resistivity.

The effect of atomic ordering on saturation magnetization is shown in Fig. 3(b). As the Fe–Si composition is varied around stoichiometry, an excess of Fe will substitute into the Si sites, while any excess of Si replaces Fe in the sublattice B.[17] Thus the composition dependence of saturation magnetization (μ_B/cm^3) can be described by the following equation:

$$M_s = [(4+x)\mu_{\mathrm{Fe}}(B) + (4-x)\mu_{\mathrm{Si}}(D) + 8\mu_{\mathrm{eff}}(A,C)]/V, \tag{2}$$

where V denotes the volume of the unit cell, which is determined from the measured lattice constant. We use the magnetic moment of Fe at sublattice B $\mu_{\mathrm{Fe}}(B)=2.2\mu_B$ and the magnetic moment of Si at sublattice D $\mu_{\mathrm{Si}}(D)=-0.07\mu_B$. Fe at sublattices A and C has an average magnetic moment $\mu_{\mathrm{eff}}(A,C)$ that varies linearly with Fe concentration and has particular values of $1.35\mu_B$ for 75 at. % Fe and $2.2\mu_B$ for 100 at. % Fe.[17] The solid line in Fig. 3(b) shows the behavior of M_s according to Eq. (2), which qualitatively agrees with experiment for $x > 0.2$. For nearly stoichiometric samples, a significant decrease in saturation magnetization is observed in the experiment, which seems to be related to the finite disorder observed in HRXRD measurements. This behavior of M_s with composition is found to be different from the corresponding (001)-films, for which a linear behavior was observed.[19] This is most likely related to a different ordering in stoichiometric (113)-films.

We found the impact of ordering also in the earlier investigations of the so called PHE.[15] The PHE on [113]-oriented films exhibits an antisymmetric component, which is sensitive to the crystal symmetry,[15] and hence we examine the composition dependence of PHE in Figs. 3(c) and 3(d). The PHE on this orientation is the sum of a symmetric ρ_s^{113} and an antisymmetric component ρ_{SATM}.[15] The symmetric component ρ_s^{113} is negative for Fe and off-stoichiometric Fe_3Si samples and then increases with decreasing x. The behavior of the symmetric component is different compared to the [001]-oriented films,[20] which is because in [113]-films it corresponds to a different component of magnetoresistivity tensor.[15] Unlike the symmetric component, the antisymmetric component exhibits an identical sign for Fe and the nearly stoichiometric Fe_3Si films, which is expected because of the same crystal class for Fe and $D0_3$-ordered Fe_3Si.

In conclusion, we have studied structural, electrical, and magnetic properties of $Fe_3Si/GaAs(113)A$ hybrid structures dependent on the layer composition. The presence of superlattice reflections and lower resistivity confirms the long-range atomic ordering in the stoichiometric Fe_3Si films, reflecting the $D0_3$ crystal structure. A finite disorder was found even for the nearly stoichiometric films.

Part of this work has been supported by the German BMBF under the research program NanoQUIT (Contract No. 01BM463). The authors would like to thank B. Jenichen, O. Brandt, and M. Hashimoto for useful discussions and R. Ranchal for a critical reading of the manuscript.

[1] G. A. Prinz, Science **282**, 1660 (1998).
[2] T. J. Zega, A. T. Hanbicki, S. C. Erwin, I. Žutić, G. Kioseoglou, C. H. Li, B. T. Jonker, and R. M. Stroud, Phys. Rev. Lett. **96**, 196101 (2006).
[3] J. R. Waldrop and R. W. Grant, Appl. Phys. Lett. **34**, 630 (1979); H.-P. Schönherr, R. Nötzel, W. Ma, and K. H. Ploog, J. Appl. Phys. **89**, 169 (2001).
[4] J. Herfort, H.-P. Schönherr, A. Kawaharazuka, M. Ramsteiner, and K. Ploog, J. Cryst. Growth **278**, 666 (2005).
[5] Y. Hsieh, M. Hong, J. Kwo, A. Kortan, H. Chen, and J. Mannaerts, in *GaAs and Related Compound*, IOP Conference Proceedings Series No. 120, edited by G. B. Stringfellow (Institute of Physics, London, 1992), Vol. 154, p. 95.
[6] R. A. de Groot, F. M. Mueller, P. G. van Engen, and K. H. J. Buschow, Phys. Rev. Lett. **50**, 2024 (1983).
[7] J. Kudrnovsky, N. E. Christensen, and O. K. Andersen, Phys. Rev. B **43**, 5924 (1991).
[8] J. Herfort, H.-P. Schönherr, and K. H. Ploog, Appl. Phys. Lett. **83**, 3912 (2003).
[9] P. K. Muduli, J. Herfort, H.-P. Schönherr, and K. H. Ploog, J. Cryst. Growth **285**, 514 (2005a).
[10] A. Ionescu, C. A. F. Vaz, T. Trypiniotis, C. M. Gurtler, H. Garcia-Miquel, J. A. C. Bland, M. E. Vickers, R. M. Dalgliesh, S. Langridge, Y. Bugoslavsky, Y. Miyoshi, L. F. Cohen, and K. R. A. Ziebeck, Phys. Rev. B **71**, 094401 (2005).
[11] B. Jenichen, V. M. Kaganer, J. Herfort, D. K. Satapathy, H.-P. Schönherr, W. Braun, and K. H. Ploog, Phys. Rev. B **72**, 075329 (2005).
[12] F. Lin, D. Jiang, X. Ma, and W. Shi, Thin Solid Films **515**, 5353 (2007).
[13] T. Sadoh, H. Takeuchi, K. Ueda, A. Kenjo, and M. Miyao, Jpn. J. Appl. Phys., Part 1 **45**, 3598 (2006).
[14] M. Hansen, *Constitution of Binary Alloys* (McGraw-Hill, New York, 1958).
[15] P. K. Muduli, K.-J. Friedland, J. Herfort, H.-P. Schönherr, and K. H. Ploog, Phys. Rev. B **72**, 104430 (2005).
[16] V. Niculescu, K. Raj, J. I. Budnick, T. J. Burch, W. A. Hines, and A. H. Menotti, Phys. Rev. B **14**, 4160 (1976).
[17] W. A. Hines, A. H. Menotti, J. I. Budnick, T. J. Burch, T. Litrenta, V. Niculescu, and K. Raj, Phys. Rev. B **13**, 4060 (1976).
[18] W. B. Muir, J. I. Budnick, and K. Raj, Phys. Rev. B **25**, 726 (1982).
[19] J. Herfort, H.-P. Schönherr, K.-J. Friedland, and K. H. Ploog, J. Vac. Sci. Technol. B **22**, 2073 (2004).
[20] M. Bowen, K.-J. Friedland, J. Herfort, H.-P. Schönherr, and K. H. Ploog, Phys. Rev. B **71**, 172401 (2005).

Epitaxial Heusler alloy Co_2FeSi films on Si(111) substrates

M. Zander[a], J. Herfort, K. Kumakura[b], H.-P. Schönherr, and A. Trampert
Paul-Drude-Institut für Festkörperelektronik, Hausvogteiplatz 5–7, 10117 Berlin, Germany

Well ordered, epitaxial Co_2FeSi layers on Si(111) grown by molecular beam epitaxy can be obtained in an optimized growth temperature range 150 °C$< T_G <$ 200 °C. From double crystal x-ray diffraction measurements and transmission electron microscopy, it was shown that the films crystallize in the Heusler-type $L2_1$ structure. All layers are ferromagnetic and well-ordered films show high magnetic moments with an average value of (1140 ± 250) emu/cm^3, which is in good agreement with the value of bulk Co_2FeSi at 300 K. The magnetic anisotropy is correlated to the structural properties of the layers.

PACS numbers: 68.35.Ct, 75.50.Cc, 81.15.Hi

Spintronic devices are making use of the spin degree of freedom of the electron and are expected to offer new perspectives to semiconductor device technology. One of the key issues for the realization of spintronic devices is the efficient electrical injection of spin-polarized carriers into semiconductors. Therefore, epitaxial ferromagnet/semiconductor (FM/SC) heterostructures have attracted considerable attention. In particular, Heusler alloys are promising candidates for a spin injection source into semiconductors, because of their high Curie temperature and half-metallicity predicted for some Heusler alloys.[1–5] To date, mainly the fabrication of ferromagnetic Heusler alloy/III-V semiconductor hybrid structures has been reported.[6–10] On the other hand, there have been so far only few attempts to grow ferromagnetic Heusler alloys on group-IV semiconductors,[11–13] despite the fact that these semiconductors are important for an integration of spintronic devices into Si large-scale integrated circuits. In addition to its importance in electronics, Si is a highly attractive semiconductor for spintronic devices due to an enhanced spin relaxation time and a large transport length of the electrons.[14] Only recently, spin injection into Si was demonstrated.[15] In the past, growth of binary Heusler alloy Fe_3Si on Si substrates was reported.[12] However, Fe_3Si does not exhibit 100% spin polarization at the Fermi level.

Co_2FeSi is one member of full-Heusler alloys with the cubic $L2_1$ crystal structure consisting of 4 interpenetrating fcc sublattices.[16] The lattice constant of bulk Co_2FeSi is 5.658 Å and has a lattice mismatch of 4% relative to the Si(001) substrate. Bulk Co_2FeSi with a large magnetic moment ($\approx 6\ \mu_B$)[5,17] is ferromagnetic up to more than 1100 K.[5] In addition, Co_2FeSi is expected to exhibit halfmetallic behaviour.[5] Recently, electrical spin injection from an epitaxial Co_2FeSi thin film into GaAs was demonstrated.[18] In this letter, we present our results on the fabrication and characterization of epitaxial Heusler alloy Co_2FeSi/Si(111) hybrid structures grown by molecular beam epitaxy (MBE) at various growth temperatures T_G.

Co, Fe and Si are codeposited from high-temperature effusion cells at growth temperatures varied between 100 and 300 °C, at a growth rate of 0.1 nm/min with a base pressure of 1×10^{-10} Torr. The evaporation rates are controlled by the cell temperatures and are in accordance with the optimized fluxes for the growth of stochiometric Co_2FeSi films on GaAs(001) substrates.[19] The thickness of the layers is between 15 and 42 nm as determined by x-ray reflectivity measurements. The growth is initiated on a Si(111)-(7×7) reconstructed surface for providing well-defined surface conditions. The growth was monitored *in-situ* using reflection high energy electron diffraction (RHEED). After a few monolayers streaky pattern

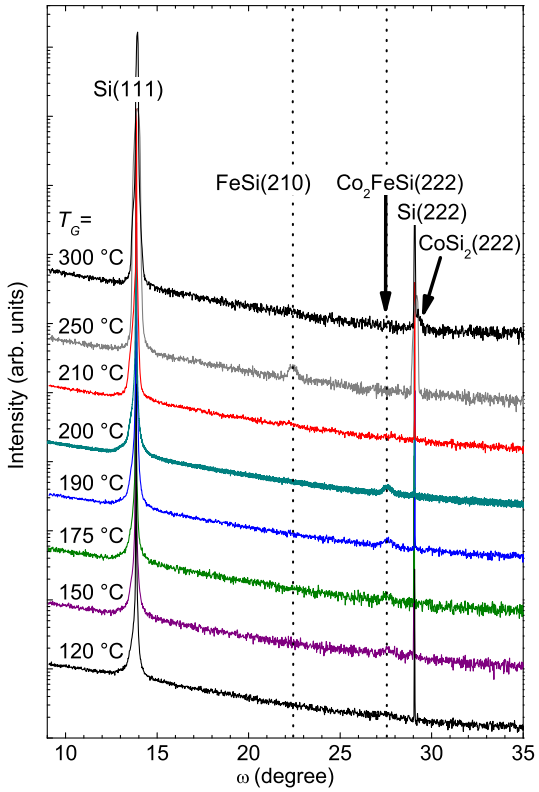

FIG. 1: DCXRD curves of the symmetric (111) and (222) reflections for different values of T_G. For samples grown between $T_G = 150$ and 200 °C, Co_2FeSi(222) reflections are observed. For films grown at $T_G \geq 250$ °C, interfacial reactions set in. The thickness of the films is $d \approx 18$ nm.

[a] Electronic mail: zander@pdi-berlin.de
[b] Permanent address: NTT Basic Research Laboratories, 3-1 Morinosato Wakamiya, Atsugi-shi, Kanagawa 243-0198, Japan.

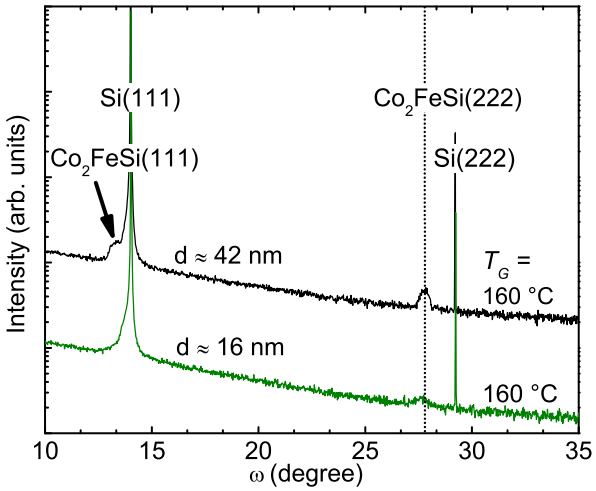

FIG. 2: DCXRD curves of the symmetric (111) and (222) reflections for two different values of d at $T_G = 160$ °C. The appearance of the $Co_2FeSi(111)$ reflection indicates that an ordering in the $L2_1$ structure could be obtained.

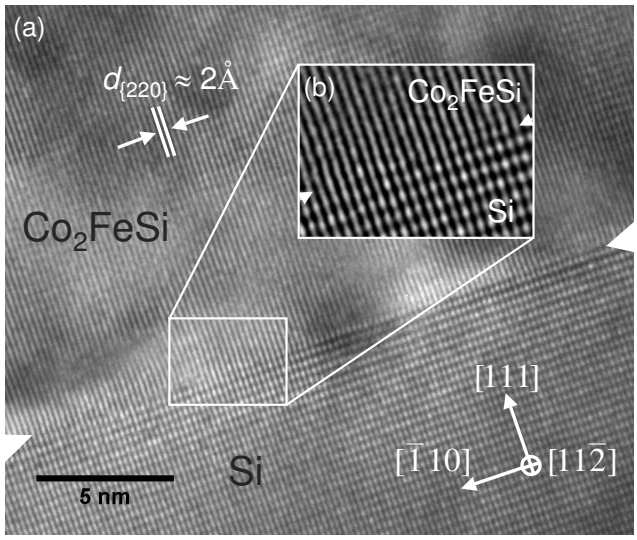

FIG. 3: (a) A cross-sectional high-resolution TEM image of the Co_2FeSi film grown at $T_G = 160$ °C with $d \approx 42$ nm along the Si-$[11\bar{2}]$ zone axis. (b) Noise-reduced (Fourier-filtered) HRTEM image of the interface. The white triangles mark the position of the interface.

are observed implying the formation of smooth Co_2FeSi layers on the Si(111) substrate. The observed RHEED pattern is symmetric for electron beam direction along the Si $[11\bar{2}]$ azimuth and for any multiple of 60°. An identical RHEED pattern is seen every 120°. From the analysis of the RHEED pattern we found that (111)Co_2FeSi||(111)Si, giving a first evidence that epitaxially grown films are obtained.

Figure 1 shows double crystal x-ray diffraction (DCXRD) $\omega - 2\theta$ scans measured with an open detector ranging from Si(111) to Si(222) reflections for different T_G. Pronounced peaks due to the $Co_2FeSi(222)$ layer reflection were only obtained in a relatively narrow temperature range between $T_G =$ 150 and 200 °C. At higher T_G, strong interfacial reactions set in, which are derived from the observation of the FeSi(210) and $CoSi_2(222)$ reflections for the films grown at $T_G = 250$ and 300 °C, respectively. This is in agreement with atomic force microscopy measurements showing a strong degradation of the surface for $T_G \geq 210$ °C with a root mean square (rms) roughness ≥ 3 nm, where for well-ordered films with 150 °C$< T_G <$ 200 °C a rms-roughness of (0.4 ± 0.1) nm was found. For $T_G \leq 120$ °C, no diffraction peak of the layer could be observed, which indicates the absence of a structural order of the Heusler alloy. The measured difference between the $Co_2FeSi(222)$ and Si(222) reflections is $\Delta\theta_B \approx 1.43°$ which is smaller than the theoretical difference of 1.6° for a fully strained layer, implying that the layers are partially relaxed. This also explains the absence of fringes in the $\omega - 2\theta$ scans despite the smooth surface of the films, which is different to the case of Co_2FeSi films on GaAs(001) substrates.[19] In addition, the apperarance of the $Co_2FeSi(222)$ reflection suggests that at least the $B2$ structure is formed. However, for the confirmation of the $L2_1$ structure, which is required to obtain 100% spin polarization in the film, additional reflections with all odd Miller indeces like the $Co_2FeSi(111)$ reflection need to be observed. Figure 2 compares DCXRD $\omega - 2\theta$ scans measured with an open detector ranging from Si(111) to Si(222) reflections for films grown at $T_G = 160$ °C with $d \approx 16$ nm and $d \approx 42$ nm, respectively. For the 16 nm thick film only a weak shoulder peak due to the $Co_2FeSi(111)$ reflection is observed. However, for the 42 nm thick sample the $Co_2FeSi(111)$ peak as well as the $Co_2FeSi(222)$ peak are clearly more pronounced indicating an ordering in the $L2_1$ structure. The pronounced observation of the $Co_2FeSi(111)$ reflection in thicker films can be either due to the enhanced intensity of the reflection and/or a thickness dependent improvement of the long-range atomic ordering as observed in Co_2FeSi films on GaAs(001) substrates.[10]

The cystallinity and interface properties were investigated using cross-sectional transmission electron microscopy (TEM). Figure 3 (a) shows a high-resolution TEM (HRTEM) image along the Si-$[11\bar{2}]$ zone axis for the well-ordered film grown at $T_G = 160$ °C with $d \approx 42$ nm near the Co_2FeSi/Si(111) interface. Despite the lattice mismatch, a very sharp Co_2FeSi/Si(111) interface and an atomic scale abruptness could be obtained. This is more clearly seen in Figure 3 (b) where the noise-reduced (Fourier-filtered) enlarged HRTEM image of the interface is shown. Furthermore, Co_2FeSi grows epitaxially on Si(111) with (111)Co_2FeSi||(111)Si and crystallizes in the $L2_1$ structure, which is derived from the analysis of the diffraction pattern and is in good agreement with the RHEED and XRD measurements. In the HRTEM image [Fig. 3 (a)] additionally, relatively strong differences in brightness can be seen. As the lattice mismatch between the Co_2FeSi layer and the Si substrate is relatively large, the contrast differences at the interface are most likely due to local strain variations. We also found from HRTEM images the existence of a few misfit disloca-

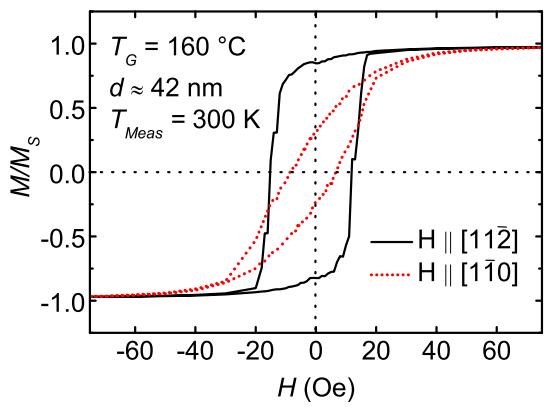

FIG. 4: The magnetization curves of a Co_2FeSi film grown at $T_G = 160$ °C with $d \approx 42$ nm. The external magnetic field was applied along the $[11\bar{2}]$ and $[1\bar{1}0]$. The diamagnetic contribution of the substrate has been substracted.

tions (not shown here), which explains the partial relaxation of the Co_2FeSi layer as observed by XRD measurements. For the sample with $T_G = 200$ °C TEM measurements revealed the existence of an interlayer at the interface (not shown here) which is explained by the initiation of interfacial reactions at this temperature.

The magnetic properties of the layers were measured using superconducting quantum interference device magnetometry (SQUID) at 300 K. Figure 4 shows the hysteresis loop for the sample with $T_G = 160$ °C and $d \approx 42$ nm. The external magnetic field was applied along the $[11\bar{2}]$ and $[1\bar{1}0]$ directions. The layer is ferromagnetic at room temperature, where the relatively easy axis of magnetization is in the film plane along the $[11\bar{2}]$ direction and the hard axis along the $[1\bar{1}0]$ direction, indicating the presence of an uniaxial magnetic anisotropy in the film plane. This is in good agreement with the investigation of Co_2FeSi/GaAs(001) hybrid structures.[19] Ando *et al.* recently showed an uniaxial magnetic anisotropy in Fe_3Si films on Ge(111), where the magnetic easy axis is oriented randomly for each of the samples.[11] For the Co_2FeSi films on Si(111) we found that the relatively easy axis was oriented along the $[11\bar{2}]$ direction for all films. The presence of an uniaxial magnetic anisotropy is most likely correlated with the high crystal quality of the Co_2FeSi layer at the interface.[20] The coercive fields $H_C = 10 - 20$ Oe are rather small for all examined orientations, but are higher than in the case of Co_2FeSi layers on GaAs(001), which is explained by the existence of defects pinning magnetic domains.[21] For well-ordered Co_2FeSi films on Si(111) with 150 °C$< T_G <$ 200 °C the magnetic moment is almost constant within the error limit. The average magnetic moment for these films amounts to (1140 ± 250) emu/cm^3, which is close to the bulk value of Co_2FeSi.[5,17] For higher $T_G \geq 210$ °C the magnetic moment is decreased implying the formation of magnetic modified compounds due to interfacial reactions in agreement with the results of the XRD, AFM and TEM measurements.

In summary, ferromagnetic and well-ordered Co_2FeSi films can be grown epitaxially by MBE in a narrow T_G range between 150 and 200 °C on Si(111) substrates. The results are promising for the application of Co_2FeSi/Si(111) hybrid structures for future spintronic devices.

This work was partly supported by the German BMBF under the research program NanoQUIT (Contract No. 01BM463). The authors would like to thank B. Jenichen, L. Geelhaar, and H. Riechert for useful discussions and B. Jenichen for a careful reading of the manuscript.

[1] C. Palmstrom, MRS Bull. **28**, 725 (2003).
[2] R. A. de Groot, F. M. Mueller, P. G. van Engen, and K. H. J. Buschow, Phys. Rev. Lett. **50**, 2024 (1983).
[3] I. Galanakis, P. H. Dederichs, and N. Papanikolaou, Phys. Rev. B **66**, 174429 (2002).
[4] S. Fujii, S. Sugimura, S. Ishida,and S. Asano, J. Phys.: Condens. Matter **2**, 8583 (1990).
[5] S. Wurmehl, G. H. Fecher, H. C. Kandpal, V. Ksenofontov, C. Felser, H. J. Lin, and J. Morais, Phys. Rev. B **72**, 184434 (2005).
[6] T. Ambrose, J. J. Krebs,and G. A. Prinz, Appl. Phys. Lett. **76**, 3280 (2000).
[7] J. Lu, J. W. Dong, J. Q. Xie, S. McKernan, C. J. Palmstrom, and Y. Xin, Appl. Phys. Lett. **83**, 2393 (2003).
[8] Y. J. Chen, D. Basiaga, J. R. O'Brien, and D. Heiman, Appl. Phys. Lett. **84**, 4301 (2004).
[9] W. H. Wang, M. Przybylski, W. Kuch, L. I. Chelaru, J. Wang, Y. F. Lu, J. Barthel, H. L. Meyerheim,and J. Kirschner, Phys. Rev. B **71**, 144416 (2005).
[10] M. Hashimoto, A. Trampert, J. Herfort, and K. H. Ploog, J. Vac. Sci. Techn. **25**, 1453 (2007).
[11] Y. Ando, K. Hamaya, K. Kasahara, K. Ueda, Y. Nozaki, T. Sadoh, Y. Maeda, K. Matsuyama, and M. Miyao, J. Appl. Phys. **105**, 07B102 (2009).
[12] K. Hamaya, K. Ueda, Y. Kishi, Y. Ando, T. Sadoh, and M. Miyao, Appl. Phys. Lett. **93**, 132117 (2008).
[13] T. Sadoh, M. Kumano, R. Kizuka, K. Ueda, K. Kenjo, and M. Miyao, Appl. Phys. Lett. **89**, 182511 (2006).
[14] I. Appelbaum, B. Q. Huang, and D. J. Monsma, Nature **447**, 295-298 (2007).
[15] B. T. Jonker, G. Kioseoglou, A. T. Hanbicki, C. H. Li, and P. E. Thompson, Nature Phys. **3**, 542-546 (2007).
[16] For the details of $L2_1$ structure, see P. J. Webster and K. R. A. Ziebeck, *Landolt-Börnstein New Series III/19c*, (Springer, Berlin, 1988), p.75.
[17] V. Niculescu T. J. Burch, K. Raj, and J. I. Budnick, J. Magn. Magn. Mater. **5**, 60-66 (1977).
[18] M. Ramsteiner, O. Brandt, T. Flissikowski, H. Grahn, H. T. Hashimoto, J. Herfort, and H. Kostial, Phys. Rev. B **78**, 121303 (2008).
[19] M. Hashimoto, J. Herfort, H.-P. Schönherr, and K. H. Ploog, Appl. Phys. Lett. **87**, 102506 (2005).
[20] M. Hashimoto, J. Herfort, A. Trampert, and K. H. Ploog, J. Cryst. Growth. **301**, 592 (2007).

[21] J. Herfort, H.-P. Schönherr, K.-J. Friedland, and K. H. Ploog, J. Vac. Sci. Technol. B **22**, 2073 (2004).